

LONG WAVELENGTH EXTENSION OF DIAMOND RAMAN LASERS

By

Alexander Sabella

A THESIS SUBMITTED TO MACQUARIE UNIVERSITY

FOR THE DEGREE OF

DOCTOR OF PHILOSOPHY

DEPARTMENT OF PHYSICS AND ASTRONOMY

SEPTEMBER 2016



MACQUARIE
University
SYDNEY · AUSTRALIA

Except where acknowledged in the customary manner, the material presented in this thesis is, to the best of my knowledge, original and has not been submitted in whole or part for a degree in any university.

Alexander Sabella

Contents

Abstract	xi
Acknowledgements	xiii
List of Symbols	xv
Acronyms	xix
1 Introduction	1
1.1 Raman lasers	2
1.1.1 Raman laser technology review	4
1.1.2 Extending Raman lasers to the mid-IR	7
1.2 The case for diamond	9
1.3 Status of diamond Raman lasers	12
1.4 Thesis summary	13
2 Properties of CVD grown diamond	15
2.1 Fundamental properties of diamond	16
2.1.1 Crystal structure	16
2.1.2 Raman Linewidth	18
2.1.3 Transmission and multiphonon absorption	20
2.1.4 Raman gain coefficient	22
2.1.5 Thermal properties	26

2.1.6	Damage thresholds	26
2.2	Diamond growth imperfections	27
2.3	Raman properties comparison	29
3	Polarisation properties of diamond Raman lasers	31
3.1	The tensor properties of Raman scattering in diamond	32
3.1.1	Analysis of DRL polarisation using Mueller calculus	33
3.2	Polarisation properties of first Stokes DRLs with linear pump polarisation	36
3.2.1	Experiment	36
3.2.2	Results	36
3.2.3	Dependence of g_R on propagation direction	39
3.3	Polarisation properties of first Stokes DRLs with elliptical pump polarisation	41
3.4	Application of DRL polarisation effects	44
3.5	Chapter summary	46
3.5.1	Publications arising from the work in this chapter	47
4	Near-IR diamond Raman lasers	49
4.1	External-cavity Raman lasers	50
4.1.1	Modelling external cavity Raman lasers	52
4.2	First Stokes, 1.240 μm laser	54
4.2.1	Experiment	54
4.2.2	Results	55
4.2.3	Performance comparison with other Raman crystals	60
4.3	Second Stokes, 1.485 μm laser	62
4.3.1	Results	63
4.3.1.1	Polarisation properties	68
4.3.2	Comparison with other Raman crystals	69
4.4	Conversion of 1 μm lasers to eye-safer wavelengths	69
4.5	Implications for future DRL designs	74
4.5.1	Output power	74

4.5.2	Pulse duration	77
4.5.3	Wavelength	78
4.6	Chapter summary	78
4.6.1	Publications arising from the work in this chapter	79
5	Mid-IR Raman gain coefficient of diamond	81
5.1	Measurement techniques for g_R	82
5.1.1	SRS threshold technique	83
5.1.2	Pump-probe technique	84
5.1.3	Pump-probe measurements with multi-mode beams	85
5.1.3.1	Linewidth correction factor	86
5.1.3.2	The validity of the linewidth correction factor - corre- lations	87
5.2	Improving the pump-probe technique	88
5.2.1	Modelling of multi-longitudinal-mode Raman amplification . . .	88
5.2.1.1	Model Description	89
5.2.1.2	Modelling results	92
5.2.2	Broadband pump-probe experiment	97
5.2.3	Broadband pump-probe results	100
5.2.3.1	Correlation measurement	100
5.2.3.2	Probe amplification and g_R measurement	102
5.2.3.3	Implications for published g_R measurements using the pump-probe technique	105
5.2.3.4	Implications for published g_R measurements using the SRS threshold technique	107
5.2.3.5	Implications for laser thresholds	108
5.3	Measurement of g_R using coherent Stokes Raman scattering	110
5.3.1	Raman Susceptibility	110
5.3.2	Third order background electronic susceptibility	114
5.3.3	Experiment	116

5.3.4	Results	117
5.3.5	Application of the CSRS technique to other crystals	119
5.4	Chapter Summary	119
5.4.1	Publications arising from the work in this chapter	121
6	Mid-IR diamond Raman laser	123
6.1	Potential mid-IR wavelengths	124
6.2	Pump laser selection for 3.75 μm output	126
6.2.1	Pump laser options	126
6.2.2	OPO output parameters	127
6.3	3.70 μm diamond Raman laser	128
6.3.1	Concentric cavity results	129
6.3.2	Hemispheric cavity results	131
6.3.3	Effect of multiphonon absorption loss	133
6.3.4	Tuneable output	135
6.3.5	Threshold reduction through four-wave-mixing	136
6.3.5.1	SRS modelling with four-wave-mixing	136
6.3.5.2	Results with FWM	138
6.3.6	Laser induced damage of the diamond crystal	139
6.3.7	Mid-IR DRL performance comparison	140
6.4	Wavelengths longer than the two-phonon absorption region	143
6.4.1	7.30 μm laser experiment	145
6.5	Current limits of mid-IR performance	148
6.6	Chapter Summary	150
6.6.1	Publications arising from the work in this chapter	150
7	Strategies for improving mid-IR performance	153
7.1	Modification of the diamond crystal	154
7.1.1	$\langle 111 \rangle$ Brewster cut crystal	154
7.1.2	Anti-reflecting microstructures	158
7.1.3	Waveguides	159

7.1.4	Carbon-13 crystal	161
7.1.5	Cryogenic cooling	161
7.2	Coherent Raman mixing	163
7.3	Chapter Summary	165
8	Conclusion	167
A	Classical stimulated Raman scattering theory	173
A.1	Raman Susceptibility	174
A.2	Coupled Raman Intensity Equations	177
A.3	Modelling parameters	179
B	Tensor form of the third order susceptibility	181
C	OPO development	185
D	Related Publications	191
	References	195

Abstract

Ideal wavelengths for laser applications often do not align with commonly available laser sources, particularly in the mid-infrared, where there are reduced laser options. Raman lasers are a means of simultaneously extending the spectral coverage and enhancing the brightness of existing laser technology. Historically, average powers in crystalline Raman lasers have been restricted by poor thermal handling of the deposited heat, which is intrinsic to the frequency shifting process. In addition, solid-state Raman lasers traditionally are only reported in the visible and near-infrared, with operation at longer wavelengths limited by material absorption and reduced Raman gain coefficients. Synthetic diamond is a nonlinear frequency conversion material that has the potential to challenge these limitations, with a high Raman gain coefficient, excellent thermal properties and broad transmission. This thesis investigates the performance of pulsed diamond Raman lasers across the near and mid-infrared regions.

Conversion of a 1.064 μm Nd:YAG laser to first (1.240 μm) and second (1.485 μm) Stokes wavelengths was studied, with the quantum conversion efficiencies achieved equivalent to, or exceeding, other Raman or optical-parametric-oscillator materials. Mueller matrix modelling was used to determine the optimal crystal orientation and pump polarisation. In particular, aligning the pump polarisation with a $\langle 111 \rangle$ crystal axis produced a 33% enhancement in the Raman gain coefficient, compared to previously utilised crystal orientations.

Knowledge of the Raman gain coefficient of diamond in the mid-infrared is vital for designing long wavelength Raman lasers, due to the reduced gap between laser and

damage thresholds. Detailed investigations consider two measurement methods. The first is a refinement of the pump-probe technique that examines the effect of correlating intensity structure and laser linewidth. The second is a novel approach based on four-wave-mixing, which removes the need to accurately characterise the spatial, temporal and spectral properties of the lasers involved.

Extending the wavelength of diamond Raman lasers to the mid-infrared necessitates overcoming the challenges of a diminished Raman gain coefficient, increased crystal absorption and weaker optical coatings. Demonstrations of tuneable first Stokes output from 3.4-3.8 μm and second Stokes output at 7.3 μm represent the longest wavelengths reported from a solid state Raman laser. Cavity losses restrict the obtainable conversion efficiencies, and several methods, including four-wave-mixing and microstructured facets, are considered as means to improve performance.

Acknowledgements

There have been many people who have provided invaluable support since I embarked on this research journey many years ago. The support from my work colleagues at the Defence Science and Technology Group has been excellent. The generous time I have been provided to undertake research has made this experience more fulfilling and led to many interesting discoveries. Thank you Dr Olivia Samardzic and Dr John Haub for encouraging me to start a PhD, your efforts getting the initial paperwork in place, providing feedback on my publications and presentations, and your continuing support throughout. Thank you to the rest of the Laser Technologies group. I won't go through the names as I think that almost everyone has provided assistance at some stage (Optics and laser discussions, loan of equipment, electronics designs, CAD drawings, reading journal/thesis drafts).

I am also very grateful to the researchers at Macquarie University who have been involved with my PhD. I would like thank Associate Professor Rich Mildren for his continued technical guidance and mentoring over the course of this PhD. It has been a privilege to be involved with you studying diamond Raman lasers since the early days. Professor Jim Piper, your sagely advice was always appreciated. Associate Professor David Spence, thank you for helping me understand the intricacies of Raman gain. Without your clear explanations, Chapter 5 would be in a much weaker state. To Ondra, Aaron and Rob, thank you for your assistance over the years. From diamond discussions, to help with some of the administrative aspects of PhD enrolment, to your hospitality during my all to infrequent visits to campus. Not being in an environment

with other researchers working on the same topic was definitely the main drawback of undertaking an off-campus PhD.

Finally, a big thank you to my wife, Cassie, for your continued support and understanding, especially during the times I was working at home or while I was away at conferences or on campus.

List of Symbols

Crystallographic notation

$[xxx]$ Crystal direction vector

$\langle xxx \rangle$ Family of direction vectors related by symmetry
e.g. $\langle 100 \rangle$ covers $[100]$, $[010]$, $[001]$, $[\bar{1}00]$, $[0\bar{1}0]$, and $[00\bar{1}]$

(xxx) Crystal plane

$\{xxx\}$ Family of planes related by symmetry

Frequently used subscripts

AS Anti-Stokes

P Pump

R Raman

S Stokes

S1 First Stokes

S2 Second Stokes

Symbols

A_{eff} Effective area

a_0	Crystal unit cell edge length
α	Polarisability
$\alpha_{P,S1-3}$	Loss coefficient
α_T	Thermal expansion coefficient
C	Heat capacity
C_r, C_ϕ	Photoelastic stress tensor components
c	Speed of light
$c.c$	Complex conjugate
D	Degeneracy factor
d	Single independent element of the Raman scattering tensor of diamond
d_{1-4}	Effective susceptibility coefficients
E	Electric field, Young's modulus
e_P, e_S	Normalised polarisation vectors for the pump and Stokes
ϵ_0	Permittivity of free space
g_R	Raman gain coefficient
η	Linewidth correction factor
I	Intensity
J	Pulse energy
k	Wavenumber
κ	Thermal conductivity

L	Crystal length
λ	Wavelength
λ_g	Wavelength of the lowest direct band gap
M^2	Beam quality factor
m	Reduced mass
N	Density of Raman scatterers
n	Refractive index
n_2^I	Intensity based nonlinear refractive index
ν	Poisson's ratio
P	Polarisation
Q	Normal mode of vibration coordinate, Cavity quality factor
R_{1-3}	Raman scattering matrices
$R_{P,S1-3}$	Mirror reflectivity
$R(\omega)$	Raman profile (intensity)
$R^E(\omega)$	Raman profile (electric field)
r_0	Spot size
ρ	Density
σ_{SP}	Spontaneous scattering coefficient
T_2	Phonon decay time
t_{eff}	Effective pulse width
$\chi^{(2)}$	Second order susceptibility

$\chi_E^{(3)}$ Third order electronic susceptibility

$\chi_F^{(3)}$ Four-wave-mixing susceptibility

$\chi_R^{(3)}$ Raman susceptibility

Ω Longitudinal mode spacing

ω Angular frequency

$\Delta\omega$ FWHM linewidth

Acronyms

AM	Amplitude modulation
AR	Anti-reflection
ARMS	Anti-reflecting microstructured
BBO	β barium borate (nonlinear crystal)
BHG	Bettis-House-Guenther (Scaling law)
CARS	Coherent anti-Stokes Raman spectroscopy
CPFS	Co-planar folded slab (laser)
CSRS	Coherent Stokes Raman spectroscopy
CVD	Chemical vapour deposition
CW	Continuous wave
DRL	Diamond Raman laser
FCC	Face centred cubic
FM	Frequency modulation
FSR	Free spectral range
FTIR	Fourier transform infrared

FWHM Full width half maximum

FWM Four wave mixing

HPHT High pressure high temperature

HR High reflectivity

HT High transparency

HWP Half waveplate

IC Input coupler

IR Infrared

KTP Potassium titanyl phosphate (nonlinear crystal)

MPE Maximum permissible exposure

OC Output coupler

OPO Optical parametric oscillator

OSA Optical spectrum analyser

PPLN Periodically polled lithium niobate (nonlinear crystal)

PER Polarisation extinction ratio

PR Partial reflection

QWP Quarter waveplate

ROC Radius of curvature

SLM Single longitudinal mode

SRS Stimulated Raman scattering

TEM Transverse electro-magnetic

UV Ultraviolet

YAG Yttrium aluminium garnate (laser crystal)

ZGP Zinc germanium phosphide (nonlinear crystal)

1

Introduction

Since the invention of the laser, the demand for higher power, broader spectral coverage and increased efficiency has fostered development of numerous optical materials. Progress in rare earth ions hosted in Yttrium Aluminium Garnate (YAG) or silica fibres, for example, has yielded high average power and high beam quality laser output in several wavelength bands from 1-2 μm [1]. Access to longer mid-IR wavelengths is typically more challenging and research into transition-metal-doped chalcogenide compounds is an example of an optical material that has enabled moderate laser power from 2-5 μm [2]. However, directly emitting lasers, such as the examples above, may not deliver the required laser parameters at the desired wavelength. This has led to the need for nonlinear optical materials, such as lithium niobate, potassium titanyl phosphate (KTP), and zinc germanium phosphide (ZGP), to transfer laser power to shorter or longer wavelengths.

High optical quality synthetic diamond is a ‘new’ nonlinear optical material that has the potential to extend the wavelength of existing lasers into new spectral regions with high efficiency, excellent beam quality and unmatched average power. Facilitating the enhanced performance are a range of exceptional properties, such as unparalleled thermal conductivity, broad transmission and extraordinary robustness [3, 4].

Despite the well known properties of diamond, for decades it has remained underexploited in laser applications due to the variable quality and high cost of natural stones, limited quality and size of synthetic samples, and an inability to host large rare-earth ions. The recent development of high purity, low birefringence, chemical vapour deposition (CVD) grown single crystals [5] has unlocked its potential for a range of photonic applications. Early use of CVD diamond in lasers was in a passive role, such as high performance windows or intracavity heat spreaders [6, 7]. Employing diamond as an active part of the laser generation process, by exploiting its high cross-section for Raman scattering, enables wavelength conversion devices with unprecedented attributes. The research presented herein describes seminal work in efficient near-IR diamond Raman lasers (DRLs) and the first extension of the output wavelength to the mid-IR, where there is great demand for new solid-state sources.

1.1 Raman lasers

Raman lasers employ Stimulated Raman Scattering (SRS) to convert the wavelength of a pump laser. Focussing the pump laser into a Raman active material with sufficient intensity excites longer wavelength Stokes photons, with a frequency difference, ω_R , corresponding to a phonon mode of the crystal lattice (or a molecular vibration for gases and liquids). Depending on the Raman laser characteristics and pump intensity, energy may flow to higher order Stokes wavelengths or shorter ‘anti-Stokes’ wavelengths (see Fig. 1.1). Unlike weak spontaneous Raman scattering (1 in $\sim 10^6$ photons), SRS produces an intense coherent beam that is capable of depleting a large fraction of the pump. The pump intensity required to initiate SRS is proportional to the Raman gain coefficient, g_R , which decreases with increasing wavelength.

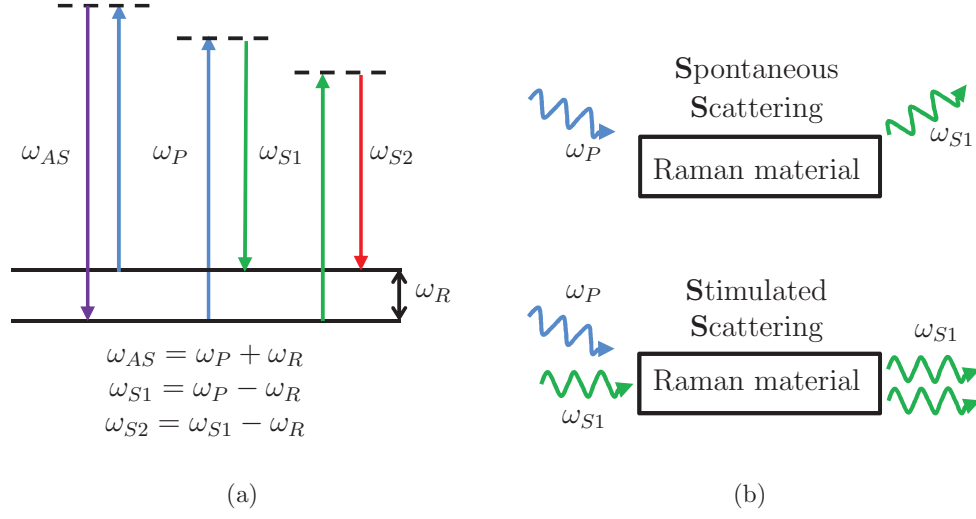


FIGURE 1.1: (a) Energy diagram for an anti-Stokes (ω_{AS}) and two Stokes (ω_{S1} , ω_{S2}) shifts. (b) Schematic of spontaneous and stimulated Raman scattering.

Raman lasers enable generation of wavelengths insufficiently serviced by direct lasing techniques. Direct laser action with the required efficiency, average/peak power, linewidth and beam quality suitable for many applications is only available for limited ranges of wavelengths, such as high beam quality, multi-kilowatt output near $1\ \mu\text{m}$ from Yb^{3+} or Nd^{3+} doped hosts [1]. Other wavelength regions are not as well serviced, and Raman lasers are able to efficiently transition many of the key pump laser properties to a new spectral region.

There is a natural comparison between Raman lasers and optical parametric oscillators (OPOs) as nonlinear methods for extending the wavelength of a pump laser. OPOs require $\chi^{(2)}$ nonlinear materials, which in practical terms are limited to the class of crystals that lack inversion symmetry (e.g. LiNbO_3 , KTP and BBO). The generation of a pair of signal and idler photons in an OPO from a pump photon is analogous to the pairs of Stokes photons and phonons of a Raman laser. Efficient conversion necessitates mounting the crystals at specific orientations and temperatures to ensure phase matching between the different wavelengths. Tuning the crystal angle or temperature changes the phase matching conditions and thus changes the output wavelength, which is the primary advantage of OPOs. Free running OPO spectral outputs are typically

quite broad, spanning several to hundreds of wavenumbers, unless specific linewidth narrowing elements are included in the cavity. Raman shifted linewidths, however, are bounded by the pump linewidth or the Raman linewidth of the material, whichever is broader. The Raman linewidth in diamond, for example, is $\sim 1.5 \text{ cm}^{-1}$ [8].

Unlike OPOs, Raman shifting does not require phase matching between the pump and output beams for efficient conversion. Any phase mismatch is automatically compensated for by the phonon field and precise temperature/angular control is not required. The absence of phase matching requirements also contributes to a process called ‘Raman beam clean up’ [9, 10]. Phase distortions in an aberrated pump beam are not transferred to the Stokes beam during amplification [11] and the resultant gain profile in an oscillator converges towards a Gaussian distribution [9]. Thus high quality Stokes outputs have been demonstrated from poor quality pump lasers [9, 11, 12]. Similarly, the absence of phase matching means that it is possible to spatially combine several pump beams in a Raman laser or amplifier to produce a single high beam quality Stokes output [13]. In contrast, the beam quality of OPOs is often degraded relative to the pump [14–17].

At high average powers, OPOs and Raman lasers both suffer from degraded efficiency and beam quality due to thermal lensing effects, and in the case of OPOs, phase matching instabilities [18, 19]. Detrimental thermal loads in OPOs are largely due to parasitic absorption, as the frequency conversion process does not intrinsically generate heat. The deposition of heat in Raman lasers however, is an intrinsic part of the conversion process. The creation of a Stokes photon in a Raman laser generates a corresponding phonon (vibration), which manifests as heat. Thermal aberrations counter the beneficial properties of Raman beam clean-up [18, 20] and as such, good thermal properties are critical for high average power Raman lasers.

1.1.1 Raman laser technology review

Unlike the $\chi^{(2)}$ active materials required for OPOs, all materials have a $\chi^{(3)}$ Raman response. Thus it is unsurprising that Raman shifting of pump lasers has been demonstrated in many gases, liquids and solids. The earliest research, in 1962, consisted of

placing organic liquids in a ruby laser cavity [21]. In the following year, experiments with gases [22] and crystals (including diamond) [23] focussed a ruby laser beam into external Raman generators, where conversion occurred during a single pass of the pump through the Raman gain material. Very high peak powers are required to reach the SRS threshold in Raman generators (100s of MW cm^{-2}) and multiple Stokes and anti-Stokes orders are often observed in rings around the pump beam (the rings arise from phase matching of four-wave-mixing processes between pump and Stokes wavelengths). In the following years, Stokes generation using cells filled with gasses such as hydrogen and methane dominated investigations [24–27]. These enabled large changes in wavelength from high peak power pulsed lasers. Although good conversion efficiencies were obtained, there are several drawbacks that limit their practicality. Device sizes are typically of the order of 1 m as the Raman gain coefficient of gases is low and optical breakdown limits the pump focus intensity. Gas Raman generators are also limited to repetition rates at the Hertz level unless the gas is cycled to reduce thermal blooming.

Since the 1990s, research into Raman lasers transitioned to the solid state regime, with crystalline and optical fibre technologies receiving significant research interest [28–30]. Crystalline Raman lasers are a compact means of extending the spectral coverage of CW or pulsed lasers. Incorporating crystals with strong Raman responses allows greatly reduced device sizes compared to gas cells, while improved thermal conductivity permits increased average powers. Raman lasers have been demonstrated in a large selection of crystals, including nitrates ($\text{Ba}(\text{NO}_3)_2$), iodates (LiIO_3), vanadates (YVO_4 and GdVO_4) and tungstates ($\text{KGd}(\text{WO}_4)_2$, SrWO_4 , BaWO_4 , CaWO_4 , and PbWO_4) [28].

Solid state Raman laser designs typically resonate the Stokes wavelength, with single-pass Raman generators often reported in the context of material characterisation or broadband frequency generation [31, 32]. Placing the Raman crystal in a cavity separate to, or shared with, the pump laser gain medium (external-cavity or intracavity conversion, respectively) reduces the SRS threshold intensity and enables a degree of control over the modal quality and the dominant Stokes output wavelength. Both cavity configurations have demonstrated greater than 50% conversion of pump photons

to a specific Stokes wavelength [28]. Historically, thermal deformation in the Raman crystal has limited average powers to less than 20 W [33]. Thermal rollover is a particularly challenging problem in CW lasers, where small spot sizes in the Raman crystal, and small out-coupling fractions enhance the sensitivity to cavity distortions.

Extending beyond Raman conversion in bulk materials has the potential to further reduce thresholds and permit integration with photonic chip concepts. Ring-resonators, whispering gallery mode devices and photonic crystal micro-cavities combine small mode volumes with very high cavity Q-factors to greatly enhance the Raman amplification process. Pump thresholds for a CW CaF_2 whispering gallery mode Raman laser are as low as $3\text{ }\mu\text{W}$ [34] and a similarly low $1\text{ }\mu\text{W}$ threshold is demonstrated in a silicon nano-cavity [35]. These thresholds are more than six orders of magnitude lower than bulk CW external cavity Raman lasers [36].

Linear waveguide structures also reduce Raman thresholds by tightly confining the pump and Stokes light over longer distances than otherwise possible through geometric focussing. Optical fibres are the classic example, where the low gain coefficient and poor thermal conductivity of silica are overcome by interaction lengths of tens to hundreds of metres in single mode fibre. In fact, a silica fibre Raman amplifier holds the record for the highest reported average power from a Raman device. Up to 1.5 kW first Stokes CW average power at $1.12\text{ }\mu\text{m}$ is demonstrated from a 2 kW ytterbium pump laser [37]. The same factors that make fibre Raman lasers feasible also create challenges with competing nonlinear effects. Induced spectral broadening limits higher Stokes order efficiencies and the achievable peak power for pulsed applications. Hollow-core photonic crystal fibres redesign the gas Raman laser by combining the Raman shifting capability of gases with the high power, high beam quality, strengths of optical fibre. A high power 55 W hydrogen filled fibre converted essentially all ($>99.9\%$) of the coupled pump light to Stokes, with waveguide losses (100 dB/km) limiting the output conversion efficiency to 70% [38].

1.1.2 Extending Raman lasers to the mid-IR

The mid-IR and longwave-IR are regions of intense interest for laser research and a compact, high brightness laser source is beneficial for many applications. Atmospheric transmission bands at 3-5 μm and 8-12 μm are extensively used for imaging thermal signatures and are subsequently targeted by laser countermeasures [39]. Laser based remote sensing also takes advantage of good atmospheric transmission to enable long range detection of chemicals. The mid-IR fundamental absorption bands of many molecular species are stronger than overtones at shorter wavelengths and thus aid in detection of lower concentrations [40]. Similarly, stronger absorption in many compounds is valuable for laser materials processing, as ablation is achieved with reduced power and absorption depth.

The maturity and range of lasers in the mid-IR is far less than in its near-IR neighbour. Only a limited number of wavelengths are accessible via rare earth ions, for instance 2.9 μm (Er^{3+}) and 3.9 μm (Ho^{3+}). While diode laser technology, particularly quantum cascade lasers, has progressed substantially in recent years, the available average and peak powers are limited, especially at room temperature [41]. Transition metal doped chalcogenides, such as Cr:ZnSe (2-3.3 μm) and Fe:ZnSe 4-5 μm , have attracted significant recent attention as tuneable mid-IR lasers. Pulse energies greater than 1 J and average powers up to 57 W have been demonstrated, with higher average powers limited by strong thermal lensing [2, 42].

To access the mid-IR region from available near-IR laser technology, nonlinear frequency conversion is often employed. OPO conversion is the most common approach, and generates wavelengths spanning large segments of the mid-IR from efficient pump sources such as Nd:YAG (1.06 μm) and Ho:YAG (2.1 μm). For wavelengths up to 4 μm , several materials, including KTA and periodically polled LiNbO₃, allow conversion directly from 1 μm lasers. Accessing wavelengths beyond 4 μm from 1 μm pumps requires materials like AgGaS₂, which have very poor thermal conductivity (0.015 W/m/K) and low damage thresholds ($\sim 25 \text{ MW/cm}^2$) [43]. Orientation patterned GaAs is an engineered crystal that has a large $\chi^{(2)}$ nonlinear response and is transparent from 0.9 to 17 μm . Two photon absorption however, restricts efficiency using 1 μm and 1.5 μm

pump sources. When pumping with wavelengths longer than $2\text{ }\mu\text{m}$, ZGP (Zinc Germanium Phosphide) is a suitable material, with demonstrated tunable output from a single device of $3.8 - 12.9\text{ }\mu\text{m}$ [44] and good thermal conductivity (35 W/m/K). The maximum reported average power of a ZGP OPO is 41 W [45], with the free running spectra spanning several hundred nanometres ($3.7\text{--}4\text{ }\mu\text{m}$ and $4.4\text{--}4.8\text{ }\mu\text{m}$) and a degraded beam quality ($M^2 = 4$).

Raman conversion into the mid-IR has received far less attention, primarily due to the limited range of materials with sufficiently large g_R and good mid-IR transparency. Until recently, examples were almost exclusively bulky gas Raman lasers [25, 46, 47]. For example, the large Raman frequency of hydrogen (4155 cm^{-1}) allows access to the mid-IR from two shifts of a near-IR pump source.

Practical and compact solid-state mid-IR Raman converters are limited to a few select materials. Silicon is in the same periodic table group as carbon and shares many physical properties with diamond due to an identical crystal structure. It has a high g_R , high damage threshold and good thermal conductivity. Like diamond, it has no long wavelength absorption edge, but does have mild multiphonon absorption from 6.5 to $30\text{ }\mu\text{m}$. There have been numerous proposals for mid-IR Raman lasers using silicon [48–51], most of which seek to leverage extensive wafer fabrication capabilities to create a range of on-chip devices. Despite the seemingly good properties for Raman lasers and mature manufacturing capability, experimental demonstrations of mid-IR silicon Raman lasers are limited to Raman amplification of a $3.4\text{ }\mu\text{m}$ HeNe beam in a bulk silicon sample [49, 52].

Despite the transparency of tungstates such as BaWO_4 and KGW out to $5\text{ }\mu\text{m}$, the longest wavelength Raman lasers are $2.5\text{ }\mu\text{m}$ [53] and $2.9\text{ }\mu\text{m}$ [54], respectively. Fourth order cascaded SRS has been demonstrated out to $3.7\text{ }\mu\text{m}$ in a BaWO_4 Raman generator [55], indicating that, with appropriate mirrors, a Raman laser would be feasible.

As is the case with silica, long interaction lengths have enabled Raman lasers in fibres drawn from mid-IR transmitting chalcogenide glasses. First and second Stokes lasers at $3.34\text{ }\mu\text{m}$ and $3.77\text{ }\mu\text{m}$ were demonstrated in 3 m of As_2S_3 fibre using a $3\text{ }\mu\text{m}$ Er^{3+} doped fibre laser pump [56, 57]. The slope efficiency of the first Stokes laser was

39% of launched pump power. The second Stokes laser had a reduced slope efficiency of 8.7%, which was attributed to spectral broadening of the first Stokes and background losses. Third Stokes conversion of a 1.88 μm thulium fibre to 2.35 μm was also demonstrated in a As_2S_3 micro-sphere resonator, but output powers were less than 1 μW [58]. Chalcogenide glass devices are suited to low average power CW applications due to low melting points and poor robustness. This is a consequence of low phonon energies, which are also the source of their increased mid-IR transparency.

1.2 The case for diamond

The strongly bonded lattice of low mass carbon atoms in diamond gives rise to a range of properties capable of greatly expanding the parameter space of Raman lasers. Combining the physical properties of diamond, with Raman beam clean-up and the developing capability to manufacture advanced photonic structures potentially enables a range of devices with high peak and/or average powers, good beam quality, small footprints and new wavelengths.

Diamond is a versatile Raman laser material because its broad transmission spectrum enables laser operation across several important spectral bands (see Fig. 1.2). Without phase matching requirements, it is possible in principle to operate Raman lasers wherever the material is transparent. There is no long wavelength absorption edge in diamond and the only features are a set of mild multi-phonon absorption peaks spanning 2.5 μm to 6.5 μm . Providing the multi-phonon peaks can be negotiated, there is the opportunity to build solid-state Raman lasers beyond the traditional near-IR region, into the application rich, but laser source poor, mid-IR region. This has not previously been demonstrated using alternative crystalline Raman materials.

Extending existing pump laser sources into new spectral regions often requires a large change in wavelength. The single Raman line in diamond at 1332 cm^{-1} is the largest frequency shift of all crystals, reducing the required number of Raman shifts to transition a given spectral span. Figure 1.3 shows two potential applications that utilize the large spectral shift in diamond. Conversion of common 1 μm laser sources,

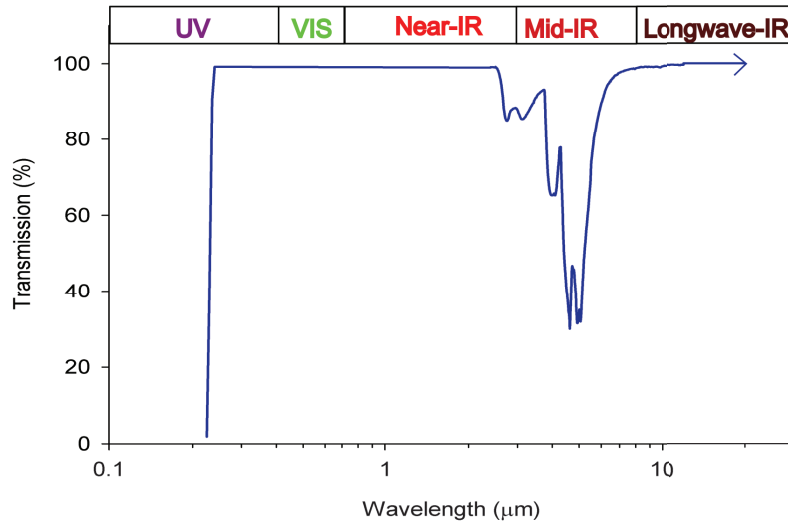


FIGURE 1.2: Internal transmission through a 1 mm CVD diamond crystal. Wavelengths longer than $2\mu\text{m}$ are measured using an FTIR spectrometer. Data for shorter wavelengths is extracted from [3].

such as Nd:YAG, to less hazardous wavelengths is beneficial to outdoor applications such as lidar and remote sensing. This is explored in more depth in Chapter 4. The second example is a first Stokes DRL pumped by a high power Ho:YAG laser. The emission at $2.9\mu\text{m}$ is strongly absorbed in liquid water and hydroxyapatite (a major component in bones and teeth) and thus is attractive for several surgical procedures [59]. In addition, the high peak power and short pulse lengths typical of pulsed DRLs are desirable to reduce collateral thermal damage to tissues [60]. Current medical $2.9\mu\text{m}$ pulsed lasers use Er:YAG, which suffers from strong thermal lensing and poor beam quality at high average power [61].

High quality diamond crystals cannot be grown as large as other common Raman crystals ($\sim 1\text{ cm}$ cf. $\sim 5\text{--}7\text{ cm}$). This would typically be disadvantageous as the higher pump intensities and tighter focussing required to reach threshold would increase the susceptibility to damage and thermal lensing. The outstanding physical properties of diamond however, eliminate any disadvantage associated with small crystal sizes. The Raman gain coefficient, g_R , is amongst the largest of all crystals [63], reducing the pump intensities required to reach threshold. This is particularly important for

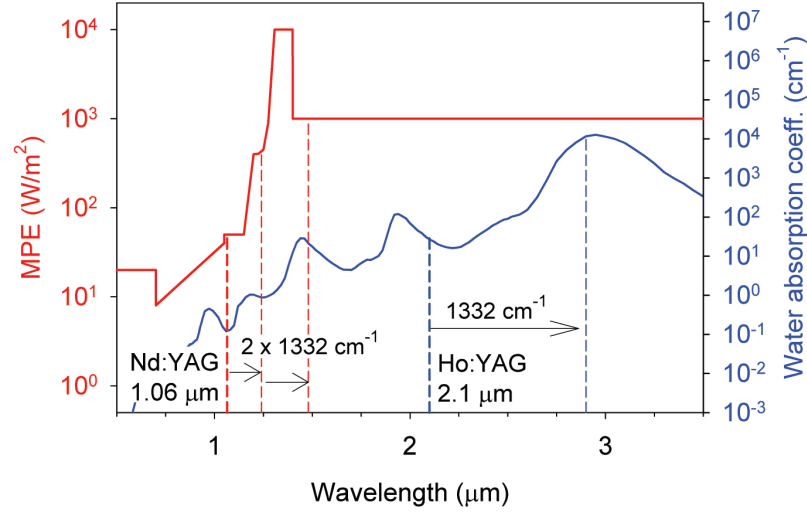


FIGURE 1.3: (Red lines) Increase in maximum permissible exposure (MPE) after Raman shifting a 1.064 μm Nd:YAG laser in diamond. (Blue lines) Increase in water absorption after Raman shifting a 2.1 μm Ho:YAG laser. MPE data is calculated using the AS/NZS IEC 60825.1:2014 standard and a 10 kHz laser with 10 ns pulses. The water absorption coefficient data is from [62].

longer wavelength Raman lasers, where g_R is diminished. Thermal management is a critical issue for Raman lasers of even moderate average powers [28]. The thermal conductivity of diamond is the highest of any material at room temperature and 142 times greater than YAG, a laser material that traditionally is associated with good thermal performance. As such, adverse thermal effects are not expected in diamond Raman lasers until output powers are 2-3 orders of magnitude higher than achievable in other Raman crystals [64]. Finally, the damage threshold is similar to other high performing optical materials [65]. The combination of a high g_R , high damage threshold and exceptional thermal conductivity enables efficient high power Raman conversion from compact devices.

‘On-chip’ photonic devices are an active research area where linear and nonlinear optical interactions are confined within waveguide structures. Combining the excellent properties of bulk diamond with waveguides, enables DRLs with lower thresholds and the ability to integrate with photonic chip components [66–68]. Compared to Raman waveguide lasers etched into silicon, the larger bandgap of diamond eliminates the

multi-photon and free-carrier absorption losses present for near-IR wavelengths [48]. Diamond also has advantages over silica micro-cavities, as a factor of 100 increase in g_R reduces the cavity Q requirements. Despite the hardness and chemical inertness of diamond, fabrication of micro-structured features is possible using a range of processing tools, such as reactive ion etching and focused ion beam milling [66].

1.3 Status of diamond Raman lasers

At the commencement of the research outlined in this thesis, diamond Raman lasers (DRLs) were in their infancy and the first efficient DRL had just been reported [69]. Despite extensive prior research into diamond, several fundamental properties were not well understood in the context of Raman laser design. Polarisation effects of DRLs had not been studied, largely due to restrictions placed on experiments from Brewster facets [69–71] or the chosen crystal orientation [72, 73]. The Raman gain coefficient had been measured by several authors [72, 74, 75], but reported values were clustered in the visible and near-IR, and varied by more than a factor of two.

Most prior experiments on Raman conversion in diamond consisted of Raman generators, where there is no cavity feedback and the conversion occurs with a single pass of the pump. Multiple Stokes and anti-Stokes lines were reported in a natural diamond sample pumped with a Ruby laser in 1963, not long after the invention of the laser [23]. Arguably, the first DRL was reported in 1970 by McQuillan et al. [72]. The Fresnel reflections from the facets provided weak feedback to form a laser cavity and the estimated conversion efficiency was 0.25%. After a gap of several decades, a patent was filed by Spectra Systems in 2004 detailing a basic Raman generator and external cavity Raman laser [76]. The results listed in the patent indicate that only a Raman generator had been demonstrated experimentally. A year later, a 2005 conference abstract mentioned a microchip laser with intracavity Raman conversion using diamond, but minimal details could be found on this work [77]. The first detailed report of a DRL was published in 2008 using a square crystal tilted at Brewster’s angle [70]. It was pumped by a Q-switched 0.532 μm laser and predominantly generated a first Stokes

output at $0.573\mu\text{m}$. Significant birefringence within the crystal was reported to have restricted performance and the total conversion efficiency was 22%. Improvements to the crystal growth process led to the development of low birefringence samples [78], which greatly enhanced laser performance. Research I conducted prior to the current PhD research, demonstrated a $0.573\mu\text{m}$ DRL with a slope efficiency of 75% and a conversion efficiency of 63.5% [69]. At the peak of the pump pulse, the instantaneous conversion of photons was measured to be 91%. These values were commensurate with the best performing crystalline Raman lasers published to that date. No thermal effects were observed, as was expected for an average output power of 1.2 W. The same low birefringence crystal was also incorporated into a synchronously pumped picosecond DRL [71]. The laser generated 2.2 W average power at $0.573\mu\text{m}$ with 21 ps pulse durations. In parallel, a research effort into intracavity DRLs was commencing at the University of Strathclyde, with the first Stokes light reported in 2009 [73].

Over the course of conducting research for this thesis, DRL technology has advanced on many fronts including; high power CW and pulsed IR lasers [79–81], deep UV output [82], femtosecond output pulses [83], tuneable output wavelength [84], monolithic cavities [85] and low threshold waveguide structures [67]. Further details on these advancements are presented, where relevant, within the subsequent chapters.

1.4 Thesis summary

This thesis examines the capability of synthetic diamond as a new frequency conversion material, with a view to assessing its potential in the mid-IR. The following chapter examines the intrinsic and growth induced properties of diamond, relevant to Raman lasers, in more detail. Understanding attributes such as multiphonon absorption and the Raman gain coefficient is vital for optimising DRL designs.

The effect of pump polarisation on laser threshold had not been previously considered and Chapter 3 describes the first experimental and theoretical investigations on this topic. Mueller matrix modelling calculates the highest Raman gain crystal orientations for both linear and elliptical pump polarisations. Several conclusions from

the polarisation analysis are utilised in Chapter 4, which presents the first reported efficient first and second Stokes infrared DRLs. The results are compared to existing solid-state Raman and OPO materials and the implications for future DRL designs are considered.

Existing measurements of the Raman gain coefficient, g_R , in diamond vary significantly and are concentrated in the visible and near-IR. Chapter 5 reports on g_R measurements relevant to the mid-IR, using both pump-probe and four-wave-mixing experiments. The previously unconsidered influence of longitudinal mode beating on pump-probe experiments is examined experimentally and through numeric modelling.

The lessons learnt in the near-IR, combined with mid-IR g_R results are then applied to developing a mid-IR DRL. Chapter 6 firstly examines feasible mid-IR wavelengths and pump sources, before outlining the construction of a DRL with tuneable output near $3.7\text{ }\mu\text{m}$. Mixing of two pump wavelengths is investigated to reduce the threshold of the DRL. Cascading the Raman process enables a $7.3\text{ }\mu\text{m}$ DRL operating on the long wavelength side of the two phonon absorption region. Finally, several options to improve mid-IR performance are examined in Chapter 7.

Alongside some technical calculations and tables, the appendices contain several supplementary chapters. Firstly, Appendices A and B summarise the classical Raman theory and derive several of the relationships underpinning the research in earlier chapters. Secondly, the design of the OPO pump source used in the mid-IR experiments is covered in Appendix C. In this chapter, linewidth narrowing using a diffraction grating in Littman-Metcalf and Littrow configurations is analysed in the context of their suitability for pumping DRLs.

2

Properties of CVD grown diamond

The exceptional properties of diamond have been studied for decades, but due to the cost and imperfections of natural crystals, using diamond in Raman lasers remained virtually non-existent. It is only since 2009 that synthetic crystals of sufficient size and quality have become available [78]. This chapter briefly outlines several of the material properties and growth defects of diamond particularly relevant to Raman lasers. The interest in diamond for use in lasers arises due to the many properties that are unmatched by alternative materials. A table comparing several important properties in diamond with other Raman materials is listed at the end of the chapter (Table 2.1).

2.1 Fundamental properties of diamond

2.1.1 Crystal structure

The remarkable attributes of diamond are directly linked to the three dimensional arrangement of strongly bonded carbon atoms. Each carbon atom is covalently bonded to four neighbours in a tetrahedral form (sp^3 hybridisation). The resulting lattice can be interpreted as inter-penetrating face-centred-cubic (FCC) sub-lattices. Each FCC sub-lattice is diagonally offset by $[x, y, z] = [0.25a_0, 0.25a_0, 0.25a_0]$, where a_0 is the cube edge length (≈ 0.178 nm). The unit cell of diamond is shown in Fig. 2.1(a) and consists of a face centred cube (outlined in red) that also includes four additional carbon atoms from an adjoining FCC cell. The arrangement of the carbon atoms along several directions of high symmetry is presented in Figs. 2.2(a) to 2.2(c). Of particular relevance for this thesis is the hexagonal pattern along the $\langle 110 \rangle$ direction and the subsequent polarisation effects in DRLs (Chapter 3) (see the list of symbols prior to the introduction chapter for axes nomenclature).

The first order Raman spectrum of diamond was first observed in 1930 [86] and consists of a single peak at 1332.3 cm^{-1} at room temperature. The Raman frequency, ω_R , originates from the rigid vibration between FCC sub-lattices along the $\langle 111 \rangle$ directions connecting the carbon atoms. Figure 2.1(b) illustrates the vibration between two isolated sub-lattices. Strong covalent bonding combined with the small atomic mass for carbon results in an ω_R larger than other crystalline materials (see Table 2.1 at the end of this chapter). Incident electromagnetic radiation with a small wavevector compared to the Brillouin zone, i.e. $\lambda \gg a_0$, as is the case in later experiments, will excite a triply degenerate phonon mode and thus ω_R is independent of the direction of propagation [87].

The strength of the Raman response is proportional to the change in polarisability, $\partial\alpha/\partial Q$, of the material as the atoms are displaced during vibration (Q is a coordinate describing displacement during normal modes of vibration). Only the triply degenerate phonon mode at 1332 cm^{-1} has a first order Raman response. Evidence of phonon modes which are not Raman active (i.e. $\partial\alpha/\partial Q = 0$), can be observed in the second

order Raman spectrum. Here, various two phonon interactions induce a change in polarisability and create a continuous, multi-peak spectrum that spans 2130 cm^{-1} to 2664 cm^{-1} . The strength of the second order response is two orders of magnitude weaker than the 1332 cm^{-1} first order mode and thus is not considered further.

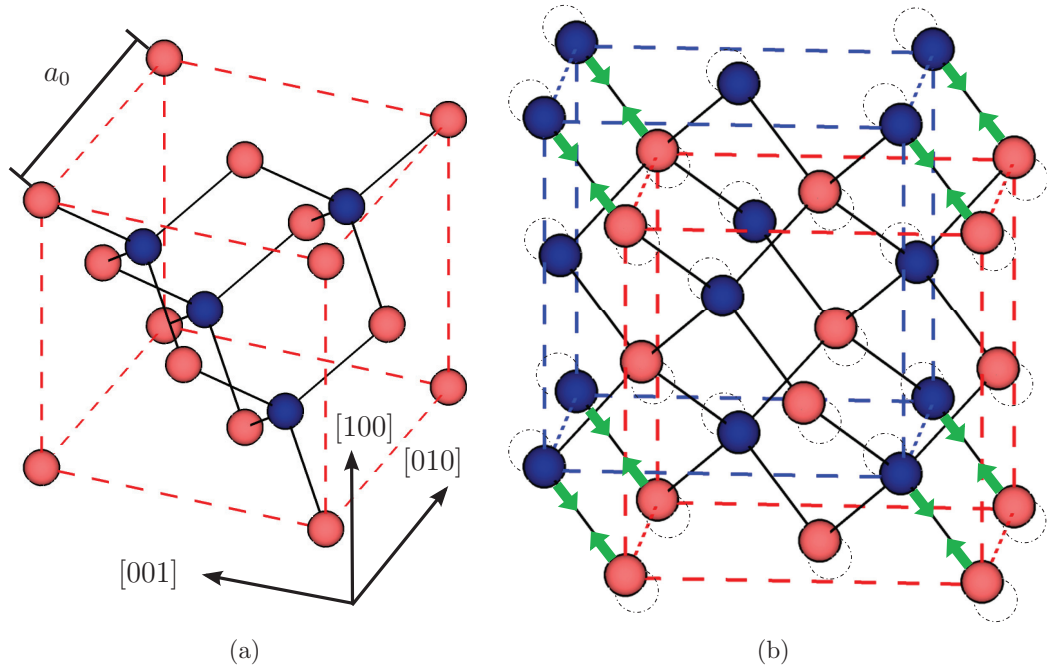


FIGURE 2.1: (a) The unit cell of diamond. The red carbon atoms highlight the FCC Bravais lattice. The internal blue carbon atoms are contributed by a second FCC sub lattice. The remainder of the blue FCC atoms are not shown. (b) Vibration of two inter-penetrating FCC sub-lattices against each other along a $\langle 111 \rangle$ direction.

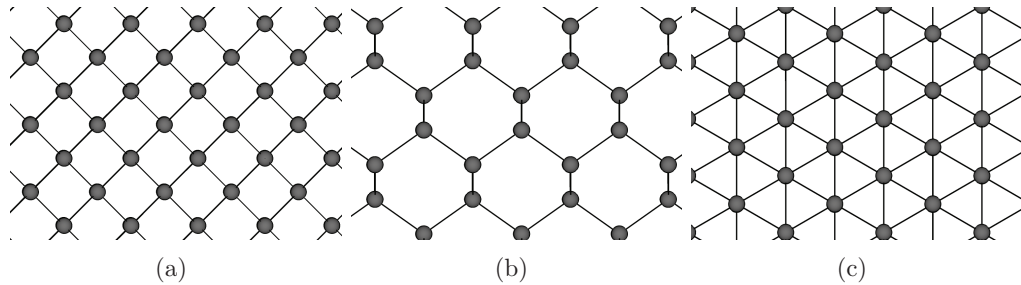


FIGURE 2.2: (a-c) Diamond lattice viewed along the $\langle 100 \rangle$, $\langle 110 \rangle$, and $\langle 111 \rangle$ directions, respectively.

2.1.2 Raman Linewidth

The 1332 cm^{-1} Raman mode has a finite linewidth, $\Delta\omega_R$, resulting in an equivalent spectral distribution in the spontaneously scattered light. Knowledge of $\Delta\omega_R$ is important for designing pump lasers since the Raman laser threshold increases when the pump laser linewidth approaches or exceeds $\Delta\omega_R$, as will be shown in Chapter 5. Similarly, $\Delta\omega_R$ is also required in Chapter 5 to measure the Raman gain coefficient.

When illuminated by a single frequency laser, the FWHM linewidth of Raman scattered light is inversely proportional to the dephasing time of the lattice phonons, T_2 .

$$\Delta\omega_R(\text{cm}^{-1}) = \frac{1}{\pi c T_2} \quad (2.1)$$

The linewidth can therefore be considered as the damping rate of the lattice vibrations. Modelling the vibrations as a weakly damped oscillator returns a Lorentzian spectral profile, which is consistent with measurements of high quality single crystals [88–90].

$$R(\omega) = \frac{\Delta\omega_R/2}{(\omega - \omega_R)^2 + (\Delta\omega_R/2)^2} \quad (2.2)$$

Reported values of $\Delta\omega_R$ vary significantly and range from 1.1 to 4 cm^{-1} [91, 92]. The range of measurements is caused by experimental limitations, and variation in the sample quality. The linewidth resolution of the spectrometers used is often a significant proportion of the measured Raman linewidth, e.g. 0.2 cm^{-1} in [88] and 0.53 cm^{-1} in [89], and the instrument contribution needs to be de-convolved from the measurement. An alternative technique is to measure the decay rate of the coherent phonons in the time domain. Such measurements are not limited by the slit-widths of spectrometers and thereby claim a higher resolution, e.g. 0.07 cm^{-1} in [8].

Imperfections within the crystal reduce phonon lifetimes and lead to a broadening of the Raman profile. Imperfections may arise from impurities, dislocations and boundaries in the crystal. Measurements of CVD samples with nitrogen impurities increasing from 1 ppm to 827 ppm showed an increasing linewidth of 1.57 to 2.84 cm^{-1} , respectively [89]. Measuring phonon decay, the linewidth of a single CVD crystal

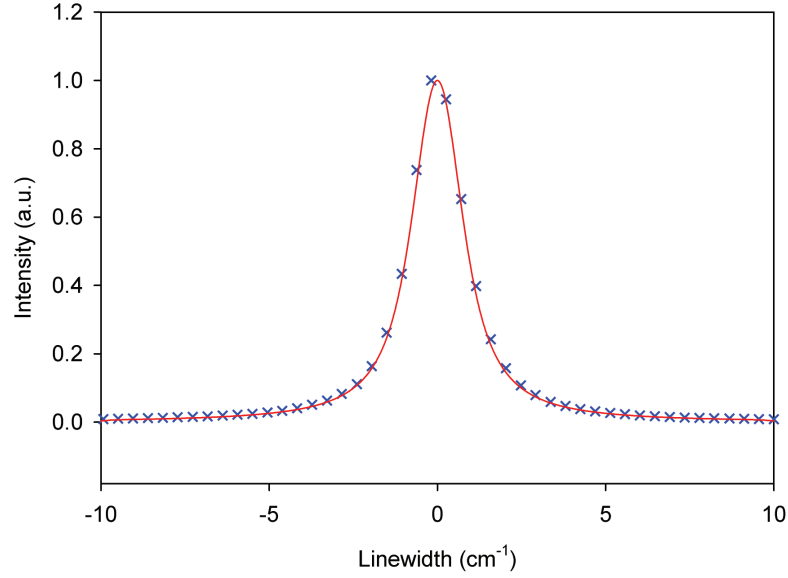


FIGURE 2.3: Spontaneous Raman scattering profile for 0.532 μm excitation. The fit is a Voigt profile, where the Gaussian instrument linewidth is 0.72 cm^{-1} and the Lorentzian Raman linewidth is 1.5 cm^{-1} .

with <1 ppm nitrogen impurity and low dislocation density was 1.5 cm^{-1} [8]. In the same experiment, a natural type IIa sample with low impurities, but a high number of dislocations and a HPHT (high pressure high temperature) sample with low dislocation density, but 10-100 ppm nitrogen were both measured with a broader 1.9 cm^{-1} linewidth. Kirilov et al. measured a 1.68 cm^{-1} linewidth for a high nitrogen content (type Ib) HPHT single crystal, which was narrower than the low nitrogen content type IIa natural crystals also measured ($1.87\text{-}2.16 \text{ cm}^{-1}$) [88]. The density of dislocations was not mentioned in the article, but can be quite high in natural crystals [93]. Polycrystalline diamond typically shows broader linewidths, with the degree of broadening increasing with reduced grain sizes [88].

The crystals used in this work have low nitrogen content (<0.1 ppm) and have very low birefringence ($\Delta n < 10^{-6}$), which indicates a low dislocation density [78]. Given these properties, the Raman linewidth is expected to be consistent with the narrowest reported results. Figure 2.3 shows spontaneous-scattering linewidth measurements on a

diamond crystal of similar quality to those used in this thesis. The spectrometer (Horiba Instruments, LabRAM HR Evolution) had an instrument linewidth of 0.72 cm^{-1} (Gaussian FWHM), resulting in a deconvolved linewidth of 1.5 cm^{-1} . This result agrees with the phonon decay measurements on high quality crystals [8], and correspondingly, the calculations throughout this thesis assume a linewidth of 1.5 cm^{-1} , or equivalently $T_2 = 7 \text{ ps}$.

2.1.3 Transmission and multiphonon absorption

The transmission spectrum of diamond is one of the broadest of all solids, facilitating the potential development of DRLs from the UV to mid-IR wavelengths. Unlike many alternative Raman crystals, there is no first order phonon absorption, and thus diamond is transparent in the longwave-IR band. A region of multiphonon absorption from 2.5 to $6.5 \mu\text{m}$ is the only feature in the transmission spectrum beyond the UV band gap absorption at $0.236 \mu\text{m}$. In the process of developing a long wavelength DRL it is inevitable that multiphonon absorption will be encountered, by either a pump wavelength or one of the Stokes wavelengths.

The measured multiphonon absorption spectrum is presented in Fig. 2.4. The wavelengths marking the start of the two and three phonon absorption regions are clearly visible and correspond to two times and three times the first order Raman frequency of diamond, respectively.

There is minimal absorption at single phonon frequencies due to the inversion symmetry of the crystal structure. The symmetry properties of the diamond crystal dictate that no net dipole moment is formed between the atoms when the unit cells vibrate against each other. As such, light is not absorbed at single phonon frequencies. However, a second order dipole can form on the creation of two phonons, which may lead to light absorption. Absorption takes place when the frequency of the incident light is equal to the sum of the frequencies of the two phonons. Phonon dispersion curves in Fig. 2.5 show the range of available frequencies for optical (LO, TO, ΣO) and acoustic (LA, TA, ΣA) phonon modes. Unlike the first order Raman effect, which is only active

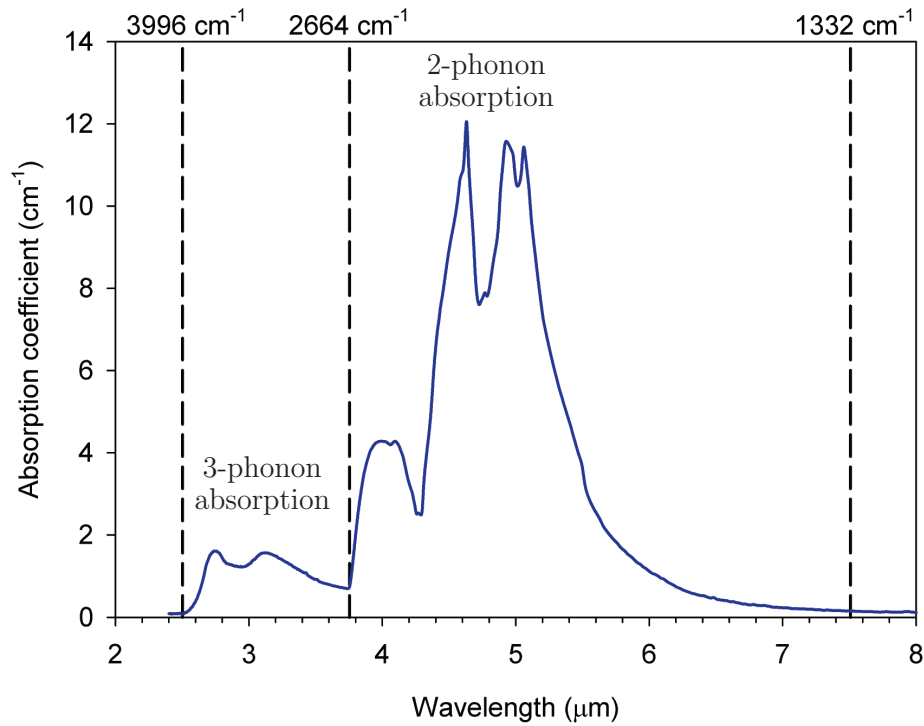


FIGURE 2.4: Multiphonon absorption region of CVD diamond measured using a FTIR spectrometer.

at 1332 cm^{-1} , phonons from anywhere on the dispersion curve can participate in multiphonon events. Selection rules govern the combinations of the frequencies that are allowed. In particular, the two phonons cannot be from the same branch in the phonon dispersion curves, hence the minima in absorption at multiples of 1332 cm^{-1} . Modelling the density-of-states of the phonon modes along the dispersion curves predicts many of the features seen in Fig. 2.4, with the strongest absorption peaks produced by combinations of high density regions [95, 96].

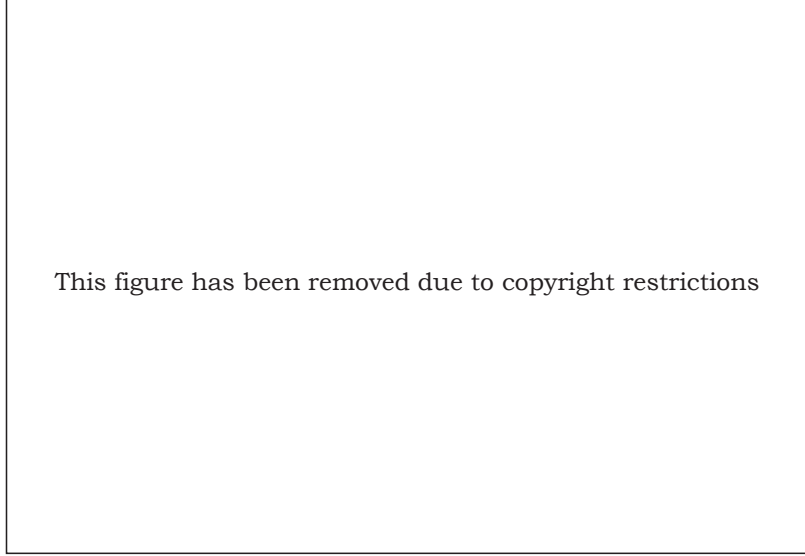


FIGURE 2.5: Phonon dispersion curves along the $\langle 100 \rangle$, $\langle 110 \rangle$ and $\langle 111 \rangle$ directions, respectively. The figure is copied from [94]

2.1.4 Raman gain coefficient

The Raman gain coefficient, g_R , describes the strength of the coupling between the pump and Stokes photons. All else being equal, a larger g_R lowers the SRS threshold intensity and thus is a key parameter in Raman laser design. The strong Raman response of diamond is comparable or exceeds other high performing Raman crystals (see Table 2.1) [97], and facilitates efficient conversion from short crystal lengths.

The high g_R observed in diamond arises from the low mass of carbon atoms and the strong bonding between them. An equation calculating its magnitude is derived in the appendix (Eq. (A.16)) and repeated here.

$$g_R = \frac{\omega_S N (\partial\alpha/\partial Q)^2}{2n_P n_S c^2 \Delta\omega_R m \epsilon_0^2 \omega_R} \quad (2.3)$$

N is the number of Raman oscillators per unit volume, which for diamond is the number of primitive cells per unit volume ($8.81 \times 10^{22} \text{ cm}^{-3}$). $\Delta\omega_R$ is the FWHM linewidth of the Raman mode (1.5 cm^{-1}), n_P and n_S are the refractive indices at the pump and Stokes wavelength, ω_R is the Raman frequency, ω_S is the Stokes frequency and m is the reduced mass ($9.989 \times 10^{-24} \text{ g}$). $\partial\alpha/\partial Q$ is the change in polarisability as the lattice

is displaced. For the $\langle 100 \rangle$ cubic axes $\partial\alpha/\partial Q = d$, where d is the single independent component of the Raman scattering tensor. The variation of $\partial\alpha/\partial Q$ and hence g_R with pump polarisation is explored in more depth in Chapter 3. Across infrared wavelengths, d is approximately constant and g_R varies proportional to the Stokes frequency. As the band gap is approached, d increases and its dispersion was measured to fit

$$|d| = 6.5 \times 10^{-16} \left(\frac{\lambda_g}{\lambda} \right)^{-2} \left(2 - \left(1 - \frac{\lambda_g}{\lambda} \right)^{-0.5} - \left(1 + \frac{\lambda_g}{\lambda} \right)^{-0.5} \right) \quad (2.4)$$

where d is in cm^2 and λ_g is the lowest direct band gap energy ($0.206 \mu\text{m}$) [74]¹. This fit agrees with recent computational modelling of the Raman polarisability [98]. The increase in d and the refractive index in the visible and UV gives rise to a faster than $1/\lambda$ change in g_R . Although this resonant enhancement to g_R is not relevant for the infrared wavelengths investigated in this thesis, it is worth considering when comparing diamond to silicon as a mid-IR Raman material. Several very high g_R values have been published for silicon [99–101], but these have been reported at wavelengths close to the $1 \mu\text{m}$ band gap.

Measurements of g_R or $|d|$ for diamond have been reported over several decades in time and use a variety of techniques. The majority of the reported values are at wavelengths less than $1.1 \mu\text{m}$ due to the availability of suitable lasers and the stronger Raman response. Comparison of g_R calculated from Eq. (2.3) with published values is presented in Fig. 2.6. While the overall trend of decreasing gain with wavelength is evident in the published data, results at the same wavelength vary by up to a factor of five.

Many of the early studies were based on spontaneous scattering (solid squares) and require accurate accounting of the collected light. Accuracies better than a few tens of percent are challenging. To overcome this limitation, Grimsditch et al. calibrated Raman scattering cross-sections (i.e. $|d|$) against Brillouin scattering cross-sections, which can be independently calculated via elasto-optic constants [107]. More recent

¹To convert $\partial\alpha/\partial Q$ from cgs (cm^2) to SI (C m/V) units multiply by $1/9 \times 10^{-13}$

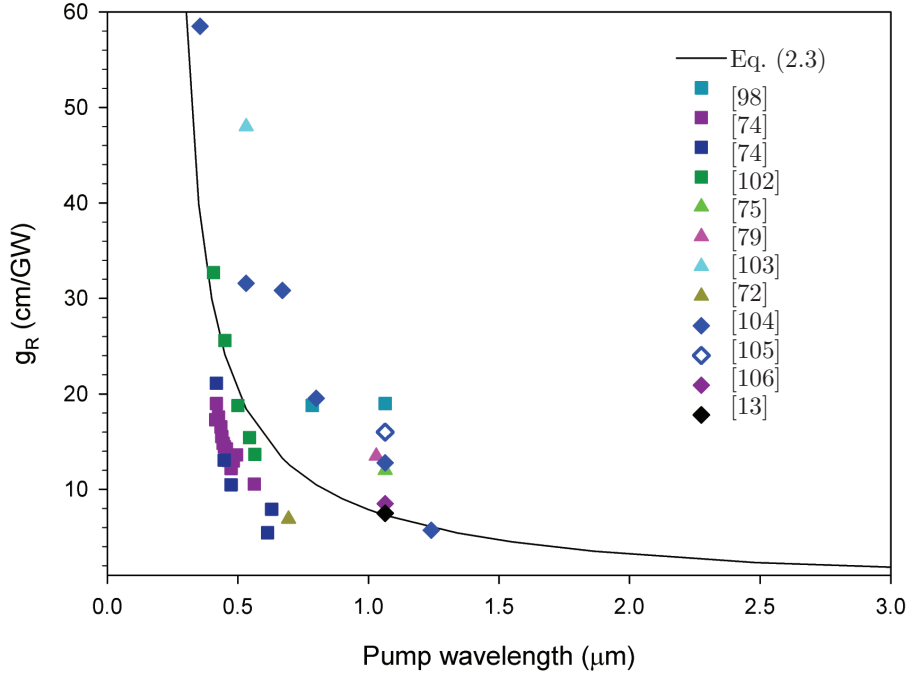


FIGURE 2.6: Reported g_R values as a function of wavelength for pump polarisation aligned with a $\langle 100 \rangle$ axis. Measurements are made using the following techniques: squares – spontaneous Raman scattering; triangles – SRS threshold; diamonds – pump probe.

measurements of g_R are based on SRS thresholds (triangles) and pump-probe amplification (diamonds), which require good spatial, temporal and spectral knowledge of the lasers used. McQuillan et al. obtained 6.9 cm/GW at $0.694 \mu\text{m}$ from separate spontaneous Raman scattering and SRS threshold measurements in a natural diamond plate [72]. The propagation through the crystal was along a $\langle 111 \rangle$ axis, which is different to subsequent published measurements that use $\langle 100 \rangle$ or $\langle 110 \rangle$ axes. Analysis conducted using the methods described later (Chapter 3), reveal that g_R for linearly polarised light propagating along a $\langle 111 \rangle$ axis should be the same as for a $\langle 100 \rangle$ axis. Using the SRS threshold method, Kaminskii et al. recorded $g_R = 12.5 \text{ cm/GW}$ for a CVD grown single crystal [75]. This result used a threshold comparison with an alternate Raman material, $\text{C}_{15}\text{H}_{19}\text{N}_3\text{O}_2$, which in turn was compared against a lead tungstate crystal [108]. The cascade of comparisons aggregates uncertainties in the final value. In addition, the result appears to have been influenced by the diamond sample behaving as a resonator. In SRS threshold measurements, $g_R I_{PL} \approx 25$ is often used as a

rough threshold benchmark to calculate g_R [109, 110]. 45% conversion is claimed for 1.5 GW/cm^2 pump intensity, which corresponds to a much lower $g_R I_P L = 1.2$. This indicates that cavity enhancement from facet reflections is significant and the accuracy of the measurement therefore depends on the cavity effects of the reference $\text{C}_{15}\text{H}_{19}\text{N}_3\text{O}_2$ crystal being similar to the diamond sample. Jelínková et al. measured 64 cm/GW and 48 cm/GW for $0.532 \mu\text{m}$ pumping by observing the SRS threshold for two unspecified crystal orientations [103]. It is implied that birefringence is the source of the difference, but the factor of 1.33 difference is precisely equal to the g_R enhancement observed when the pump polarisation is aligned with a $\langle 111 \rangle$ axis [111]. A study investigating the spectral variation of g_R from the UV to the near-IR measured absolute g_R values using the pump-probe technique for six wavelengths between $0.355 \mu\text{m}$ and $1.280 \mu\text{m}$ [104]. Relative g_R values from the SRS threshold technique were also made from $0.355 \mu\text{m}$ to $1.450 \mu\text{m}$. While the overall trend of g_R decreasing with wavelength is apparent, the difficulty of obtaining accurate absolute values is highlighted. There are several data points that don't fit the trend, even after factoring in the reported error bars. Firstly the measured gain coefficients from the pump probe experiment for $0.532 \mu\text{m}$ and $0.670 \mu\text{m}$ are very similar ($(42 \pm 4) \text{ cm/GW}$ and $(41 \pm 4) \text{ cm/GW}$, respectively), despite the 28% increase in Stokes wavelength. Similarly, when using the SRS threshold technique, the relative gain measurement for $0.450 \mu\text{m}$ is slightly lower than the value obtained for $0.532 \mu\text{m}$, when it should be higher. Finally, the linear trend presented for g_R indicates zero Raman gain for a pump wavelength of $2 \mu\text{m}$, which if true, would preclude the operation of a mid-IR DRL.

Analysis of published data highlights the challenge associated with making accurate measurements of g_R and the difficulty in accounting for all the experimental parameters that influence the result. The large variation in reported values at visible and near-IR wavelengths decreases the confidence in extrapolating results to longer wavelengths. It is because of this uncertainty that additional measurements at longer wavelengths relevant to mid-IR DRLs are conducted in Chapter 5.

2.1.5 Thermal properties

Thermal power handling is an essential property in high average power Raman lasers because the energy difference between the pump and Stokes photons manifests as heat. Crystalline Raman laser performance is degraded under excessive heat loads due to thermally induced lensing, birefringence or fracture [28, 33]. Diamond has exceptional thermal properties and is widely used in high power optical [112, 113] and electrical [114] applications. The thermal conductivity, κ , of diamond exceeds all other bulk materials. At room temperature, κ for a high quality diamond crystal is five times greater than copper (2000 W/(m K) c.f. 400 W/(m K)) and two to three orders of magnitude greater than other laser and Raman crystals (see Table 2.1 for examples). Heat transport in diamond is facilitated by phonons and the high stiffness of the *sp*³ bonding, low mass of carbon atoms and long mean-free-path of phonons in high purity crystals, ensure rapid heat dissipation. Diamond also has a low thermal expansion coefficient ($\alpha_T = 1 \times 10^{-6} \text{ K}^{-1}$) and a moderate thermo-optic coefficient ($dn/dT = 9.6 \times 10^{-6} \text{ K}^{-1}$). Given that detrimental thermal effects are typically proportional to $(dn/dT)/\kappa$ or α_T/κ [28], average powers unprecedented in crystalline Raman lasers are expected. Section 4.5 discusses the potential power limits of DRLs in more depth.

2.1.6 Damage thresholds

To minimise laser thresholds, Raman crystals are almost always placed at the waist of the pump beam and resonator modes. Damage initiated by the high field strengths present often limit output energy, particularly for Q-switched lasers. Since pumping with a confocal parameter less than the crystal length produces no overall increase in Raman gain [110], laser intensities are similar throughout the crystal and damage tends to occur on the weaker surfaces rather than in the bulk.

Klein reviewed published diamond laser damage thresholds for 0.532 μm , 1.064 μm and 10.6 μm for a variety of pulse lengths and spot sizes [115]. After normalising the laser parameters to a 1 ns pulse with a 100 μm spot using the Bettis-House-Guenther

scaling law ² the laser damage thresholds for 0.532 μm , 1.064 μm and 10.6 μm were 2 GW/cm², 8 GW/cm² and 11 GW/cm², respectively. These results are broadly consistent with damage thresholds reported in high quality CVD samples (\approx 6 GW/cm² for 5 ns pulses at 1.450 μm [104] and 2.480 μm [116]).

Coating damage will likely be the limiting factor if the crystal is antireflection (AR) coated to reduce Fresnel reflections. Calculated peak intensities in the vicinity of 1 GW/cm² damaged the AR coating for the DRL in Chapter 4. Actual intracavity intensities are difficult to accurately measure due to rapid spikes in Raman intensity. Interestingly, AR coatings in CW diamond Raman lasers survived intracavity intensities substantially beyond damage thresholds reported for conventional substrates (220 MW/cm² cf. 1 MW/cm² on silica) [81]. This was attributed to diamond acting as a very efficient heat sink for the coating.

2.2 Diamond growth imperfections

Imperfections formed in the carbon lattice during the growth of the diamond crystals may influence DRL performance. The samples used throughout this research were single crystals grown using chemical vapour deposition (CVD). While CVD gives a high degree of control over the growth process, producing large, low loss, defect free diamonds is challenging.

Depolarisation through birefringence in the diamond crystal can be detrimental to the efficiency of diamond Raman lasers [7]. Although diamond is fundamentally isotropic, the presence of defects within the lattice creates stress birefringence. For high quality single crystal CVD diamond, the primary source of stress arises from line dislocations formed during growth. These can either originate at the interface between the substrate and the deposited layer or from the continuation of defects contained in the substrate [78]. In both cases, the defect will propagate in the direction of crystal growth. It has been shown that the careful preparation of the substrate surface is crucial

² $I_{\text{damage}} = \text{Constant} * \text{spot size} * \text{pulse width}^{0.5}$

to obtaining low defect density and thus low birefringence [78]. Propagation perpendicular to the growth direction also significantly reduces the birefringence experienced (see Fig. 2.7). The diamond samples used for this project had measured birefringence values less than 5×10^{-6} , with large areas of the crystals less than 5×10^{-7} . As a point of reference, 1% single pass depolarisation loss is calculated for a birefringence of 5×10^{-6} , a crystal length of 7 mm and a wavelength of $1.064 \mu\text{m}$.

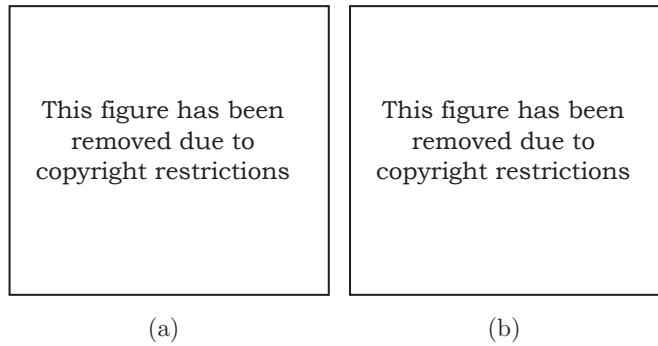


FIGURE 2.7: Birefringence images for a CVD single crystal measured using crossed polarisers (a) parallel and (b) perpendicular to the growth direction. The figure is copied from [78].

The effect of birefringence on DRL performance, to a large degree, depends on the cavity Q of the laser. For high cavity Q CW lasers, depolarisation losses approaching 1% per pass can cause significant degradation in output power [7] due to the many passes through the crystal. The birefringence also induces interesting effects on the Stokes polarisation. The output polarisation behaviour does not follow the selection rules outlined in Chapter 3, but instead demonstrates a much more complex behaviour [117]. For lower Q cavities, typical for pulsed DRLs, the sensitivity to depolarisation is substantially less. Output coupling factors are typically tens of percent and the effects of birefringence on polarization modes are insignificant.

There are numerous elements such as boron and silicon that can be incorporated, deliberately or otherwise, in the diamond lattice during the CVD growth process. For high quality, single crystal samples, designed for use in Raman lasers, nitrogen is the main impurity of concern as it is used to speed up the growth process. The increased concentration of nitrogen has been linked to an absorption ramp that increases from the

near-IR to the UV [118]. At a wavelength of 1.064 μm , increasing the nitrogen concentration from 20 to 100 ppb increased the absorption coefficient from $\sim 5 \times 10^{-4} \text{ cm}^{-1}$ to $\sim 5 \times 10^{-2} \text{ cm}^{-1}$ [5]. A calorimetry experiment, similar to [119], conducted on the crystal used in Chapter 4, returned an absorption coefficient of $2 \times 10^{-3} \text{ cm}^{-1}$ at 1.064 μm . This is less than 1% loss per pass and will have a negligible impact on the low average power pulsed DRLs considered here.

2.3 Raman properties comparison

Throughout this thesis, comparisons are made between diamond and alternative materials, with regards to their suitability for Raman lasers. Table 2.1 compares several of the properties discussed in this chapter, for a selection of materials that are referenced in this thesis. Across the optical and thermal parameters listed, the performance of diamond is similar to, or exceeds, other materials.

	Crystal				Glass fibre		Gas	
	Diamond	Silicon	Ba(NO ₃) ₂	BaWO ₄	KGW	Silica	As ₂ S ₃	H ₂
Transmission (μm)	0.23-2.5, >6.5	1.1-6, >50	0.35-1.8	0.3-5	0.35-5.5	0.2-2.1	0.8-11	broad
Raman shift (cm^{-1})	1332	521	1047	926	901,768	400	340	4155
Raman linewidth (cm^{-1})	1.5	3.5	0.4	1.6	5.9,7.8	170	87	0.02
Raman gain coefficient (1.064 μm) (cm/GW)	7.5-16 for $\langle 100 \rangle$	9.5-37 at 1.5 μm	11	8.5	6	0.01	0.5 at 1.5 μm	1
Thermal conductivity (W/m/K)	2000	149	1.17	3	2.5-3.4	1.3	0.24	0.035
Thermo-optic coefficient (10^{-6}K^{-1})	9.6	215	-20	<-9	-11.8,-17.3	9	9	
Damage threshold 10ns pulses (GW/cm^2)	6-10	1-4	0.4	5	10	5	3	
Typical Length (cm)	0.8	3	3	3	3	10s of m	300	100
								30

TABLE 2.1: Parameters important to Raman laser design for a selection of Raman materials

3

Polarisation properties of diamond Raman lasers

The polarisation state of early DRLs was not a design parameter that was studied in detail. Initial studies of SRS and Raman lasers used a variety of crystal cuts and orientations, but without careful consideration of directions that are best suited for optimizing performance [70, 72, 120]. DRLs either used Brewster's angle facets to minimise reflections [69, 70] or crystals cut with (100) orientated faces [121], which prevented a thorough investigation of the polarisation properties. This chapter contains the first detailed analysis of the relationship between pump polarisation and DRL performance. The polarisation properties of diamond are briefly examined using Jones matrices, which are commonly used to describe Raman scattering in crystals [122]. Following is a comprehensive study of DRL behaviour using Mueller matrix analysis,

which has the advantage of being inherently capable of handling the depolarisation effects observed in the Stokes output.

3.1 The tensor properties of Raman scattering in diamond

The polarisation dependence of Raman scattering has been studied for decades as a means of identifying materials and characterising the nature of the atomic and molecular bonding [123]. Diamond was one of the earliest materials to be studied in depth, due to a simple crystalline structure and strong Raman line [124, 125]. The variation in the strength of the Raman response is governed by the relative change in polarisability, $\partial\alpha/\partial Q$, of the carbon atoms as they become displaced during vibration. As outlined in Eq. (2.3), the Raman gain coefficient, g_R , and hence laser thresholds, are directly proportional to $(\partial\alpha/\partial Q)^2$.

Three tensors corresponding to the three degenerate phonon modes describe the connection between the polarisation of the incident light and the Stokes light via $\partial\alpha/\partial Q$.

$$R_1 = \begin{bmatrix} 0 & 0 & 0 \\ 0 & 0 & d \\ 0 & d & 0 \end{bmatrix}, \quad R_2 = \begin{bmatrix} 0 & 0 & d \\ 0 & 0 & 0 \\ d & 0 & 0 \end{bmatrix}, \quad R_3 = \begin{bmatrix} 0 & d & 0 \\ d & 0 & 0 \\ 0 & 0 & 0 \end{bmatrix} \quad (3.1)$$

where d is equivalent to $\partial\alpha/\partial Q$ and is weakly wavelength dependent for infrared light. The basis for the tensors in Eq. (3.1) is the cubic unit cell principal axes, which are designated by the red arrows in Fig. 3.1(a). The crystals used in experiments here are cut with four $\{110\}$ facets, as drawn in the same figure. For a given combination of incident polarisation, e_P , and scattered polarisation, e_S , the sum of the contributions from each of the tensors defines g_R [122].

$$g_R = \frac{\omega_S N}{2n_P n_S c^2 \Delta\omega_R m \epsilon_0^2 \omega_R} [|e_S^T R_1 e_P|^2 + |e_S^T R_2 e_P|^2 + |e_S^T R_3 e_P|^2] \quad (3.2)$$

Table 3.1 lists three examples for propagation along the $[011]$ axis, as per the

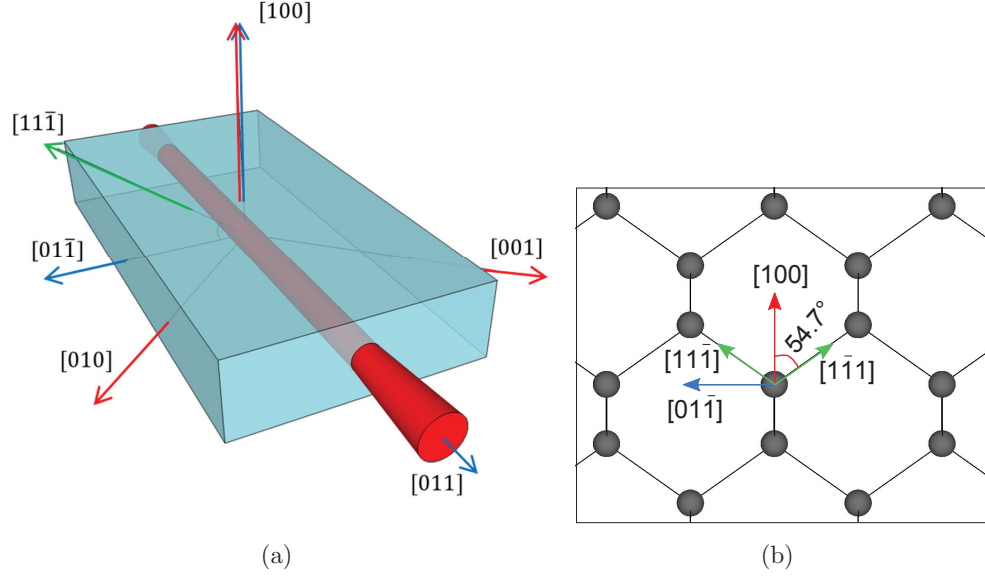


FIGURE 3.1: (a) The cut of the diamond crystals used in the experiments in this thesis, with respect to the cubic unit cell basis (red arrows) (b) The diamond crystal lattice viewed along the $[011]$ direction.

experiments detailed in Section 3.2. Pumping with $[100]$ polarisation gives orthogonally polarised first Stokes, while $[01\bar{1}]$ pumping results in equal horizontal and vertical g_R . Finally, a $4/3$ enhancement in g_R is calculated for $[11\bar{1}]$ pumping.

Pump Polarisation	g_R	
	\parallel to pump	\perp to pump
$[100]$	0	d^2
$[01\bar{1}]$	d^2	d^2
$[11\bar{1}]$	$4/3 d^2$	$1/3 d^2$

TABLE 3.1: Relative g_R parallel and perpendicular to the pump polarisation for propagation along the $[011]$ axis

3.1.1 Analysis of DRL polarisation using Mueller calculus

Although the three Raman scattering tensors were used to investigate numerous polarisation properties of DRLs, for many scenarios a Mueller matrix representation is more informative. Mueller calculus is a powerful technique for determining polarisation states through an optical system, including those that include a Raman scattering

medium. Unlike the Jones matrix representation in Eqs. (3.1) and (3.2), Mueller matrices enable the inclusion of partially polarised or unpolarised pump and Stokes states. In Mueller calculus, the input and output intensity and polarisation states are described by ‘Stokes¹ parameters’. Table 3.2 lists the ‘Stokes parameters’, I_0, I_1, I_2, I_3 , along with related equations describing the polarisation state and purity.

Total Intensity	I_0
Linear horizontal (vertical) intensity	$I_1 \quad (< 0)$
Linear +45° (-45°) intensity	$I_2 \quad (< 0)$
Right-hand (Left-hand) circular intensity	$I_3 \quad (< 0)$
Polarised Intensity, I_{pol}	$\sqrt{I_1^2 + I_2^2 + I_3^2}$
Unpolarised Intensity, I_{unpol}	$I_0 - I_{pol}$
Stokes polarisation angle, θ_S	$^{1/2} \arg(I_1 + iI_2)$
Polarisation ellipse major axis, A	$\sqrt{0.5(I_{pol} + I_1 + iI_2)}$
Polarisation ellipse minor axis, B	$\sqrt{0.5(I_{pol} - I_1 + iI_2)}$

TABLE 3.2: ‘Stokes parameters’ and derived polarisation properties

It is proposed here that g_R is proportional to the total intensity in the calculated polarisation state. The Mueller calculus splits out the unpolarised output, but half the unpolarised intensity will pass through a polariser and thus equivalently will contribute to g_R . The revised version of Eq. (3.2) becomes

$$g_R = \frac{\omega_S N (\partial\alpha/\partial Q)^2}{2n_P n_S c^2 \Delta\omega_R m \epsilon_0^2 \omega_R} [I_{pol} + 0.5I_{unpol}] \quad (3.3)$$

For a Raman scattering system, the scattered Stokes polarisation state is calculated from

$$\begin{bmatrix} S_0 \\ S_1 \\ S_2 \\ S_3 \end{bmatrix} = \mathbf{M} \begin{bmatrix} P_0 \\ P_1 \\ P_2 \\ P_3 \end{bmatrix} \quad (3.4)$$

where P_{1-4} and S_{1-4} are the ‘Stokes parameters’ for the pump and Stokes polarisation state respectively, and \mathbf{M} is the Mueller matrix describing the Raman scattering

¹The Stokes parameters are not mathematically related to the scattered Stokes light. There is an overlap in naming conventions.

process. The Mueller matrix for Raman scattering in diamond was derived by Chandrasekharan [126], and when considering only forward scattering, is given by

$\mathbf{M} =$

$\cos^4(\theta)$ $(-2 + 0.5 \sin^2(2\psi))$ $+ 2 \cos^2(\theta) + 1$	$\cos^4(\theta)$ $(2 - 0.5 \sin^2(2\psi))$ $- \cos^2(\theta)(1 + \cos^2(2\psi))$	$-0.5 \sin(4\psi)$ $\sin(\theta) \cos^2(\theta)$	0
$\cos^4(\theta)$ $(2 - 0.5 \sin^2(2\psi))$ $- \cos^2(\theta)(1 + \cos^2(2\psi))$	$\cos^4(\theta)$ $(-2 + 0.5 \sin^2(2\psi))$ $+ 2 \cos^2(\theta) - 1 + 2 \sin^2(2\psi)$ $- 2 \sin^2(2\psi) \cos^2(2\theta)$	$-0.5 \sin(4\psi) \sin(\theta)$ $(1 + \sin^2(\theta))$	0
$-0.5 \sin(4\psi)$ $\sin(\theta) \cos^2(\theta)$	$-0.5 \sin(4\psi) \sin(\theta)$ $(1 + \sin^2(\theta))$	$1 - 2 \sin^2(\theta) \sin^2(2\psi)$	0
0	0	0	-1

TABLE 3.3: Mueller matrix for forward Raman scattering in diamond and other cubic crystals with the same lattice structure. The angles θ and ψ are the elevation and azimuth of the propagation direction with respect to the $\langle 100 \rangle$ cubic basis. Note that the formula contained within [126] for element (2,2) is incorrect and has been updated here.

For two of the commonly used crystal orientations the matrix reduces to:

$$\langle 100 \rangle \text{ propagation: } \theta=0^\circ, \psi=0^\circ \text{ gives } \mathbf{M}_{\langle 100 \rangle} = \begin{bmatrix} 1 & 0 & 0 & 0 \\ 0 & -1 & 0 & 0 \\ 0 & 0 & 1 & 0 \\ 0 & 0 & 0 & -1 \end{bmatrix}$$

$$\langle 110 \rangle \text{ propagation: } \theta=0^\circ, \psi=45^\circ \text{ gives } \mathbf{M}_{\langle 110 \rangle} = \begin{bmatrix} 1.5 & 0.5 & 0 & 0 \\ 0.5 & -0.5 & 0 & 0 \\ 0 & 0 & 1 & 0 \\ 0 & 0 & 0 & -1 \end{bmatrix}$$

3.2 Polarisation properties of first Stokes DRLs with linear pump polarisation

3.2.1 Experiment

An external cavity Raman laser was used to measure the polarisation properties of DRLs. The layout of the laser is shown in Fig. 3.2 and further details of the laser design are in Chapter 4. The polarisation and power of the first Stokes output was monitored while rotating the pump polarisation via a half waveplate. Pump powers required to reach threshold for different polarisation orientations were normalised against the $[100]$ axis result and inverted to provide a measurement of the relative Raman gain. Rotating a polariser prior to the power meter determined the polarisation angle of the Stokes output with respect to the $[100]$ axis.

3.2.2 Results

An excellent fit between the Mueller matrix model using Eq. (3.3) and Table 3.3, and the measured change in g_R is seen in Fig. 3.3. Compared to the $[100]$ axis, there is a $4/3$ factor of improvement in g_R when the pump polarisation aligned with the $[11\bar{1}]$ or $[1\bar{1}1]$ axes, as also predicted by the earlier Raman tensor analysis in Table 3.1. Aligning the pump polarisation with either the $[11\bar{1}]$ or $[1\bar{1}1]$ axes also yielded the only orientations where the pump and Stokes polarisation align. The higher g_R is therefore maintained

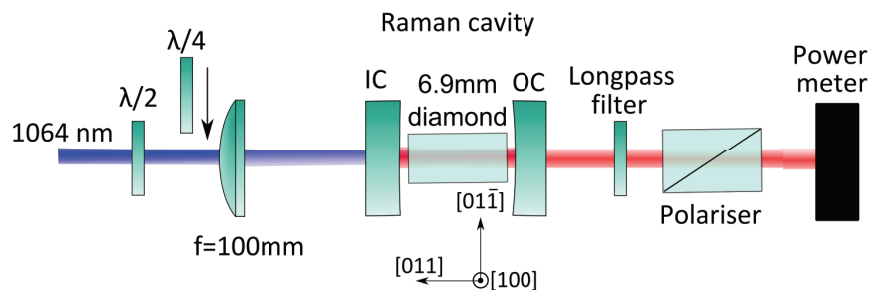


FIGURE 3.2: The external cavity DRL used for investigating the relationship between pump polarisation and Stokes output. The quarter waveplate was inserted in the case of elliptically polarised pumping.

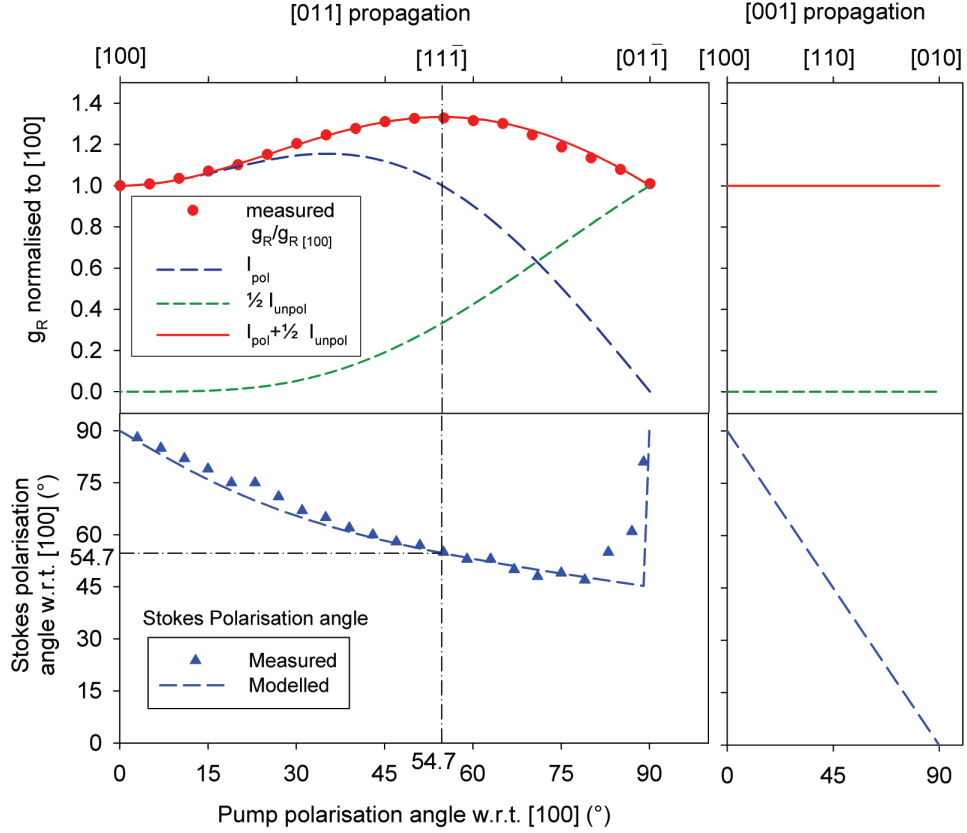


FIGURE 3.3: (Upper left) The measured and modelled relative g_R for $[011]$ propagation as the pump polarisation is rotated. Also included are the polarised and unpolarised components of the calculations. (Lower left) The measured and modelled Stokes polarisation angle with respect to the $[100]$ axis. The right hand plots are equivalent calculations for propagation along the $[001]$ axis.

for second and higher Stokes DRLs. The same calculations are also displayed in Fig. 3.3 for a cubic cut diamond, with all facets perpendicular to $\langle 100 \rangle$ axes, as used in [121]. The gain is constant for all pump polarisations, and the Stokes polarisation linearly transitions between perpendicular and parallel to the pump. There is no depolarised content as only one of the three phonon modes is excited at any time.

The angle of the Stokes polarisation becomes undefined when the pump polarisation is aligned with the $[01\bar{1}]$ axis and the modelling indicates a purely unpolarised state. Here, the combined response of the three phonon modes results in equal gain for all Stokes orientations. Measurements of the relative transmitted and rejected pulse

amplitudes from a polarising-cube-beamsplitter give a ratio that varies from pulse to pulse (see Fig. 3.4). Individual pulses were measured as horizontally polarised, vertically polarised or a combination of both. The output of each pulse is therefore not unpolarised, but averaged over many pulses, the laser output is randomly polarised. It is postulated that with no preferential orientation for gain, the random noise that seeds the Stokes output determines the final polarisation state on a pulse-by-pulse basis. If a polarising element is placed in the cavity, such as the Brewster facets in [69], or if the Stokes is seeded by an external source, the DRL will run polarised without any reduction in performance.

For most pump polarisation and crystal orientations there is Raman gain perpendicular to the dominant Stokes polarisation, e.g. where $I_{unpol} > 0$ in Fig. 3.3. Only propagating along a $\langle 100 \rangle$ axis, or pumping with the polarisation aligned with a $\langle 100 \rangle$ axis produces g_R without a depolarising component. This may manifest as a reduction in the polarisation purity of the DRL, and in the extreme case, the Stokes output is ‘randomly polarised’. The degree of depolarisation in the output will depend on the relative strength of the perpendicular gain (see Fig. 3.5(a)), but since the dominant polarisation will strongly deplete the pump pulse the relationship is highly biased. The polarisation extinction ratio (PER) of a DRL operating at approximately 2.5 times threshold (700-800 mW output) is shown in Fig. 3.5(b). For the majority of the pump polarisations the PER is around 15 dB, with an improved purity approaching 20 dB for $[100]$ pumping. It is only once the gain of the perpendicular polarisation is very close to the gain of the dominant polarisation that there is an appreciable reduction in PER.

The ability to generate linearly polarised output despite a significant perpendicular g_R component is relevant to unpolarised pumping of DRLs. Pumping with either $[100]$ or $[01\bar{1}]$ polarisations produces Stokes gain in the $[01\bar{1}]$ direction. Therefore an unpolarised pump will produce Stokes output with a preference for $[01\bar{1}]$ polarisation. Using Mueller calculus, the ratio of the horizontal to vertical gain is 2:1 and Fig. 3.5(b) indicates good polarisation purity is likely.

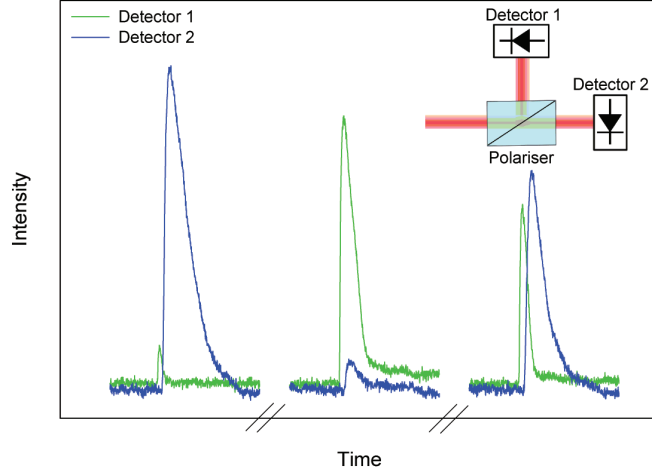


FIGURE 3.4: $[100]$ (vertical) and $[01\bar{1}]$ (horizontal) polarisation content for three different Stokes pulses in the case of pump polarisation aligned with $[01\bar{1}]$.

3.2.3 Dependence of g_R on propagation direction

Discussion in the prior section restricted analysis to propagation along a $\langle 110 \rangle$ or $\langle 100 \rangle$ direction in the crystal. To determine if alternative propagation directions allow access to higher g_R values, modelling was performed over all crystal orientations. The modelled crystal orientation was changed by varying θ and ψ in Table 3.3 from 0° to 90° . For each orientation, the linear pump polarisation was rotated through 180° and the maximum g_R recorded. The resultant surface plot is shown in Fig. 3.6, and confirms that propagating along a $\langle 110 \rangle$ axis gives access to the highest g_R value. There is a triangular ring of propagation directions that also have the same g_R enhancement. All of these directions are perpendicular to a $\langle 111 \rangle$ axis (not the $[111]$ axis drawn) which allows alignment with the electric field of the pump. The $\langle 111 \rangle$ directions align with the C-C bonds in the diamond lattice (recall Fig. 3.1(b)) and the vibrations between atoms. Co-aligning the pump polarisation in this direction maximises $\partial\alpha/\partial Q$.

The advantage of aligning the pump polarisation with a $\langle 111 \rangle$ axis has also been identified for silicon [127] and GaP [128] waveguide Raman lasers, which both share the same cubic crystal structure as diamond. The experiments described however, only used $\langle 100 \rangle$ or $\langle 110 \rangle$ polarised pumping.

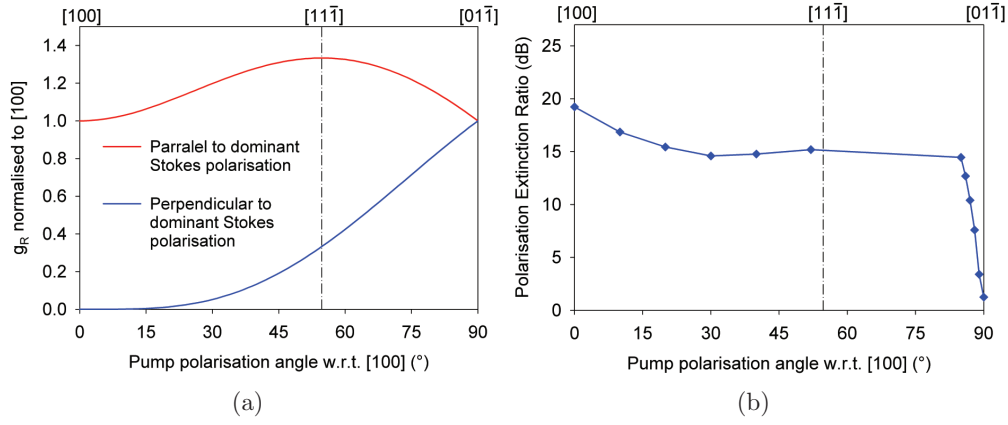


FIGURE 3.5: (a) Relative gain parallel and perpendicular to the dominant Stokes polarisation for [011] propagation. (b) Polarisation extinction ratio for a first Stokes DRL operating 2.5 times above threshold as the pump polarisation is rotated.

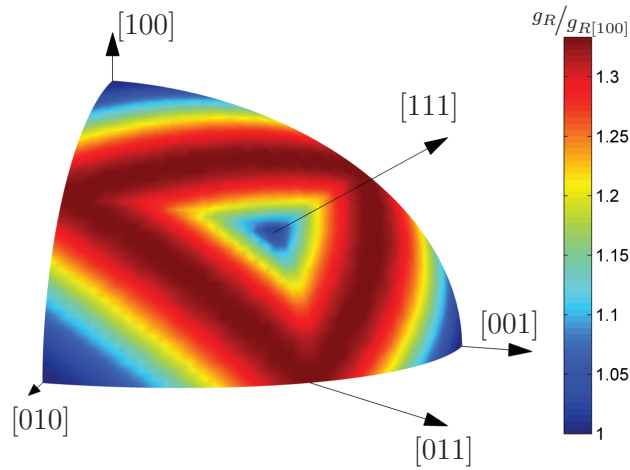


FIGURE 3.6: Maximum obtainable g_R , normalised to the [100] direction, as a function of propagation directions. Note that only linear polarisation is considered.

3.3 Polarisation properties of first Stokes DRLs with elliptical pump polarisation

The Mueller matrix approach is also applicable to elliptically polarised states. Circularly polarised pumping is a specific case that has applications in high power external-cavity DRLs. Isolating the pump laser from undepleted light reflected from the output coupler is critical to ensuring pump laser stability and potentially survival. Standard Faraday rotating isolators capable of handling up to kilowatt average powers are very large, expensive and subject to thermal lensing and depolarisation [129]. A polariser followed by a quarter-waveplate (QWP) aligned to produce circularly polarised light is a compact alternative that is less susceptible to thermal effects. The handedness of the circularly polarised light changes upon reflection and after passing back through the QWP, the light is orthogonally polarised to the input and thus rejected by the polariser.

To confirm that the modelling accurately predicts performance for elliptical polarisations, the DRL output was investigated as a function of elliptically polarised pumping. Rotating a QWP placed prior to the DRL cavity generated a selection of elliptically polarised pump states, transitioning from linear to circular and back to linear. This process was repeated for three initial linear polarisations.

Figure 3.7 shows that there are additional elliptical pump polarisations where a factor of $4/3$ increase in g_R is achieved, and that the modelled $I_{pol} + 0.5I_{unpol}$ relationship holds. Several cases of interest are highlighted in Table 3.4. As with the linearly polarised case, optimal gain is obtained when the pump and Stokes polarisation align. The measured angle and ellipticity of the output (θ_S , A, B from Table 3.2) also agree with the Mueller calculations as shown in the middle and lower plots of Fig. 3.7. A Soleil-Babinet compensator set to act as a QWP at $1.240\mu\text{m}$ was able to re-linearise the Stokes output, thus confirming the polarisation was elliptical and not just randomly polarised with an elliptical intensity distribution. Importantly for high power DRLs, pumping with circularly polarised light produces high gain, with g_R 98% of the maximum.

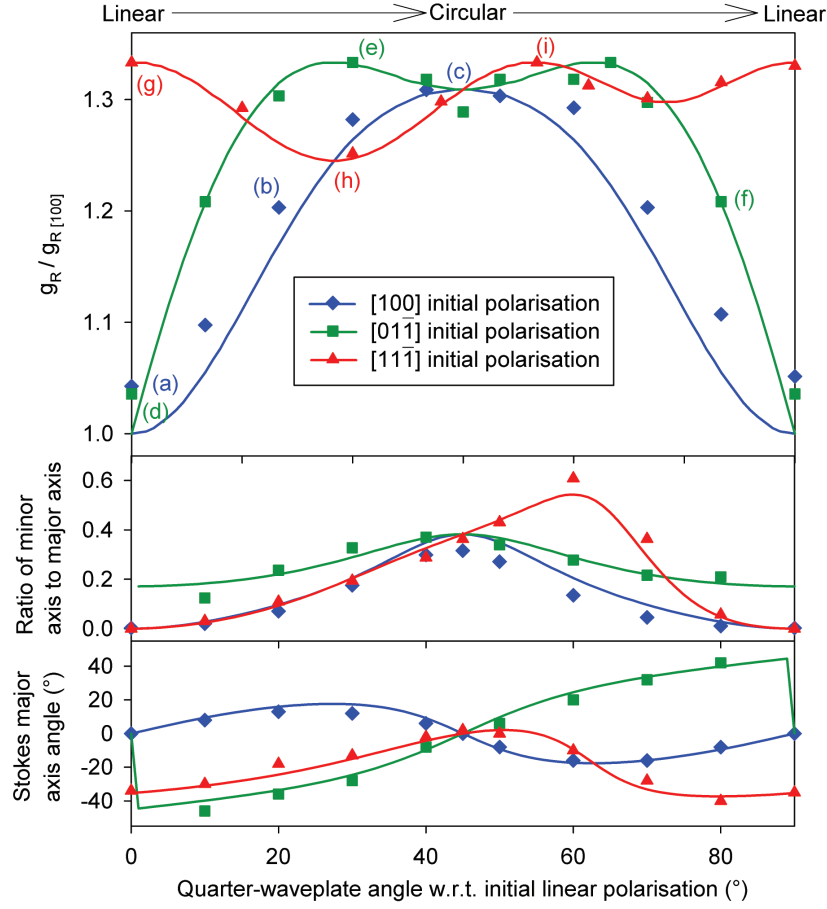


FIGURE 3.7: Top: Measured (points) and modelled (lines) relative g_R for a selection of elliptically polarised pump inputs. The polarisation states labelled (a)-(i) are displayed in Table 3.4. Middle: Power ratio between the minor and major elliptical axes. Bottom: Angle between the major axis and the $[01\bar{1}]$ axis.

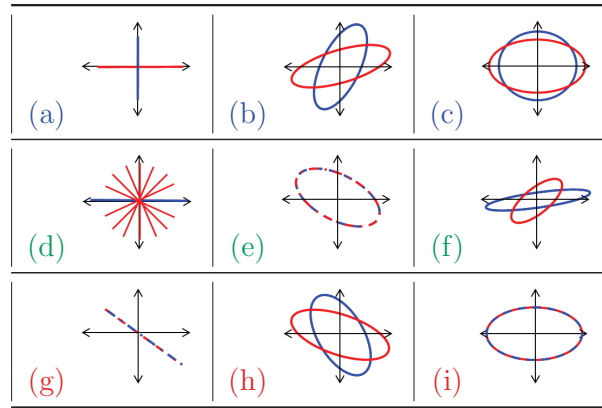


TABLE 3.4: Pump (blue) and Stokes (red) polarisation states listed in Fig. 3.7. The Stokes output for (e), (g) and (i) perfectly overlaps the pump, while (d) represents the 'randomly polarised' output described in Section 3.2.

Figure 3.7 only displays a selection of polarisations and calculations of g_R for all elliptical polarisation states are mapped onto the Poincaré sphere in Fig. 3.8. When the input is linear (the black equator) a maxima at $\pm 35.3^\circ$ from horizontal, i.e. aligned with either the $[11\bar{1}]$ or $[1\bar{1}1]$ axes, is obtained as expected. It is found that there is a band of elliptically polarised pump states that also achieve the same enhanced gain. Entries (e) and (i) in Table 3.4 are two examples. The band of high gain corresponds to polarisation states where $S_1 = \frac{1}{3}S_0$. Converting the Stokes polarisation vector to Jones vector notation, the origin of the band is more clearly observed. The Jones vector form is given by

$$\frac{1}{\sqrt{2}} \begin{bmatrix} \sqrt{1+S_1} \\ \sqrt{1-S_1}e^{i\delta} \end{bmatrix} = \frac{1}{\sqrt{3}} \begin{bmatrix} \sqrt{2} \\ e^{i\delta} \end{bmatrix}, \text{ where } \delta = \tan^{-1} \left(\frac{S_3}{S_2} \right) \quad (3.5)$$

This is a vector with the same horizontal and vertical components as one aligned with the $[11\bar{1}]$ axis, but with an arbitrary phase between them. Thus any elliptically polarised state, where the ellipse major axis has horizontal and vertical components in a ratio of $\sqrt{2} : 1$, experiences maximum Raman gain when propagating along a $\langle 110 \rangle$ direction.

The Poincaré sphere analysis was also applied to other crystal orientations. Propagation along a $\langle 100 \rangle$ axis shows no variation in gain for all polarisation states, while propagating along a $\langle 111 \rangle$ axis reveals increasing g_R , towards a $\frac{4}{3}$ factor of enhancement, as the polarisation becomes circular.

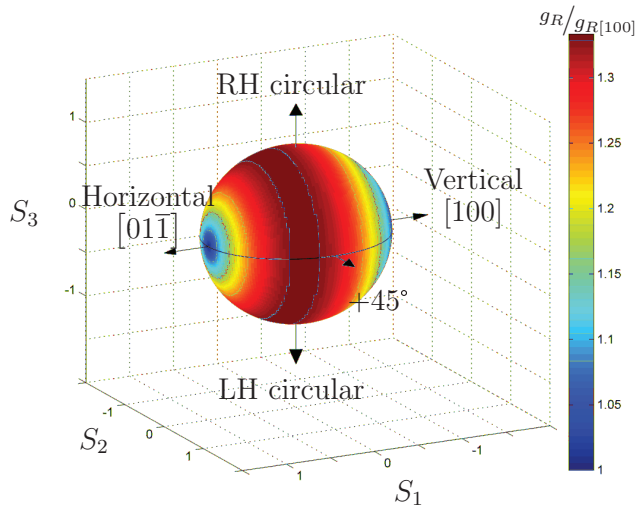


FIGURE 3.8: Relative g_R over all elliptically polarised states for $[011]$ propagation mapped onto a Poincaré sphere.

3.4 Application of DRL polarisation effects

The work outlined in this chapter was the first detailed investigation into DRL polarisation effects and the concepts shown have been applied to subsequent DRL research. Optimising thresholds, polarisation conversion and the use of high power isolators are three areas where the understanding of polarisation properties of DRLs has been pivotal to their design. Following publication of the variation in g_R with linear pump polarisation [111], polarisation studies by other researchers began emerging. Using a pump-probe experiment, Savitskii et al. measured g_R parallel and perpendicular to the pump polarisation for both $\langle 100 \rangle$ and $\langle 110 \rangle$ propagation [105] and replicated the Stokes output behaviour shown in Fig. 3.3. Fève et al. measured the polarisation properties of spontaneous Raman scattering from a diamond sample in a high Q cavity [130]. Although the overall trends in [130] agree with the theory in Section 3.1, some variation due to birefringence was seen as the sample was translated. The high number of round trips, and low gain per pass through the crystal, amplified the influence of birefringence compared to the experiment in Fig. 3.2. A study on the effect of birefringence on thresholds and Stokes polarisations in high-Q CW DRLs by Kitzler et al. revealed threshold variations that did not precisely replicate the theory and abrupt 90°

shifts in Stokes polarisation angle [117]. The shifts in polarisation angle were linked to the laser transitioning between the fast and slow axis of birefringence, depending on which axis had the highest gain.

The DRL threshold benefit associated with aligning the pump polarisation with a $\langle 111 \rangle$ axis has been widely adopted. In contrast to earlier devices [69, 121], subsequent pulsed [80, 131], CW external cavity [36, 81] and CW intra-cavity [84, 132] DRLs have employed $\langle 111 \rangle$ pumping to improve performance.

Recent progress in high power DRLs has utilised circularly polarised pumping to protect the high power CW pump laser from feedback [81]. Feedback protection using a QWP isolator demonstrated significant advantages over geometric isolation, where a slight angle (1 mrad) between the optical axes of the pump and Stokes was introduced. SRS thresholds with the QWP isolator were a factor of four lower and the beam quality improved from ‘TEM₂₀-like’ to TEM₀₀.

Consideration of the relative polarisations and crystal orientations is likely to be important in on-chip DRLs with curved waveguides, such as the racetrack structures in [67]. As the beams propagate around corners, and thus along different crystal orientations, the gain will vary. Incorporating the full Mueller matrix defined in Table 3.3 into DRL models is likely to improve model accuracy.

In conjunction with spatial improvements through Raman beam clean-up, the crystal properties of diamond offer a means of improving polarisation purity. This is particularly advantageous in high power applications where thermal depolarisation degrades the output from solid state lasers [133]. Fibre lasers are also able to emit higher powers prior to detrimental nonlinear effects if not restricted to running on a single polarisation. The conversion of an unpolarised pump laser to polarised Stokes output discussed in Section 3.2 has recently been demonstrated [134]. An average PER of 23.9 dB was obtained with a slope efficiency and threshold similar to linearly polarised pumping.

Applying Mueller matrix analysis to the first CVD DRL [70] reveals additional insights into the laser performance. The poor performance of the DRL was attributed to high birefringence within the crystal in conjunction with Brewster angled facets. Differences in g_R between the high loss s-polarisation and the low loss p-polarisation

may also be a factor. If it is assumed that the crystal was cut with $\{100\}$ faces, then at Brewster's angle the pump is propagating at 22.6° to a $\langle 100 \rangle$ axis. Applying Table 3.3, the Mueller matrix for this orientation is

$$\mathbf{M}_{22.5^\circ \text{ to } \langle 100 \rangle} = \begin{bmatrix} 1.25 & 0.25 & 0 & 0 \\ 0.25 & -0.75 & 0 & 0 \\ 0 & 0 & 1 & 0 \\ 0 & 0 & 0 & 1 \end{bmatrix}$$

For a p-polarised pump, the calculations reveal that g_R for the higher loss s-polarisation is twice the magnitude of the low loss p-polarisation. Repeating the experiment with a low birefringence crystal will reveal the effect of the g_R mismatch on laser performance.

3.5 Chapter summary

This chapter explores the polarisation properties of DRLs as a function of pump polarisation. Mueller matrix modelling is able to accurately predict the observed change in g_R with varying pump polarisation for both linearly and elliptically polarised cases. For the linear case, maximum g_R is accessed when the pump polarisation is parallel to a $\langle 111 \rangle$ axis. In this case, the pump electric field is aligned with the C-C bonds which leads to an enhanced change in polarisability, $\partial\alpha/\partial Q$. If the phase between the horizontal and vertical components of the $\langle 111 \rangle$ polarised pump is varied, the range of elliptically polarised states will also experience maximum g_R . High Stokes polarisation purity was obtained, except for the specific case where the pump polarisation aligned with the $[01\bar{1}]$ axis, and the output was on average 'randomly polarised'. Seeding the Stokes or inserting a polarising element will re-establish polarised output.

Understanding the polarisation properties of DRLs aids in optimising their performance, and several of the concepts have been applied in subsequent DRL designs. $\langle 111 \rangle$ polarised pumping is widely employed across many DRL architectures [36, 69, 80, 81, 84, 121, 131, 132] and circularly polarised pumping has demonstrated advantages in high power external cavity DRLs [81]. In addition to the beam quality

and wavelength transformation capability of Raman lasers, utilising the polarisation properties of diamond gives the ability to convert an unpolarised pump source into linearly polarised Stokes output [134].

3.5.1 Publications arising from the work in this chapter

Peer reviewed journal articles

Sabella, A., Piper, J. A., and Mildren, R. P., “1240 nm diamond Raman laser operating near the quantum limit”, *Optics letters*, **35**(23), 3874-3876, (2010).

Book chapter

Mildren, R. P., Sabella, A., Kitzler, O., Spence, D. J., and McKay, A. M., “Diamond Raman laser design and performance”, *Optical Engineering of Diamond*, 239-276, (2013).

Conference presentations

Sabella, A., Piper, J. A., and Mildren, R. P., “84% slope efficiency 1240 nm diamond Raman laser”, at Europhoton, Hamburg, Germany, (2010). *Oral Presentation*

Sabella, A., Piper, J. A., and Mildren, R. P., “Impact of pump polarisation and linewidth on the Raman gain coefficient of diamond”, at AIP congress, Sydney, Australia, (2012). *Poster Presentation*

Sabella, A., Piper, J. A., and Mildren, R. P., “Polarisation dynamics of diamond Raman lasers”, at MMI-Harvard Diamond Photonics Symposium, Melbourne, Australia, (2012). *Poster Presentation*

4

Near-IR diamond Raman lasers

Having established the polarisation dependence of the Raman gain, this chapter investigates the performance of a DRL pumped by a Q-switched $1.064\mu\text{m}$ laser. The high g_R and low loss of this regime provides a convenient platform to establish the design principles for efficient operation. Nd:YAG lasers operating at $1.064\mu\text{m}$ are a mature technology with a long history in scientific, industrial and defence applications. Correspondingly, there are many published examples of Raman and parametric conversion with which to compare the performance of diamond (e.g. [28, 133] and references therein). Compared to CW lasers, using high peak power Q-switched pulses gives high round trip Raman gain and thus reduced sensitivity to lossy optical components. This provides increased flexibility for trialling laser designs. Understanding Q-switched pumped DRLs is also particularly relevant in transitioning to the mid-IR region, in which high peak powers are anticipated to be necessary for overcoming

reduced Raman gain and increased crystal absorption.

Experiments and modelling are used to investigate design parameters for optimising the efficiency of external-cavity DRLs, operating primarily at either the first or second Stokes wavelengths ($1.240\text{ }\mu\text{m}$ or $1.485\text{ }\mu\text{m}$). After evaluating the performance of diamond, the chapter concludes with a discussion of applications for near-IR DRLs and the implications for future DRL development.

4.1 External-cavity Raman lasers

External-cavity Raman lasers offer several practical advantages over other possible architectures for Raman conversion (Fig. 4.1). Resonating the Stokes wavelengths significantly reduces SRS thresholds, compared to a Raman generator. For example, a cavity with a 50% output coupling can reduce the threshold by over an order of magnitude [28]. Cavity optics also provide additional control over the output Stokes wavelength and modal properties. In contrast to intracavity Raman lasers, an external-cavity device is a simple addition to any pump laser. No modification of the pump is generally required and the Raman laser is easily adaptable between different pump lasers. Furthermore, the separation of the pump and Raman cavities simplifies the analysis of diamond, compared to the highly interactive behaviour intrinsic to intracavity designs.

External-cavity configurations have been demonstrated with quantum conversion efficiencies of more than 60% to multiple Stokes orders for bulk Raman crystals pumped by solid state lasers [135, 136] and for optical fibre Raman lasers [137, 138]. Research into micro-resonator designs is also making progress in lowering Raman thresholds to milliwatt power levels [34, 35]. The physical separation of the pump and Raman cavities provides greater design freedom for optimisation and is a key reason why external-cavity architectures report the highest average powers from CW [81] and pulsed [79, 80, 139] crystalline Raman lasers.

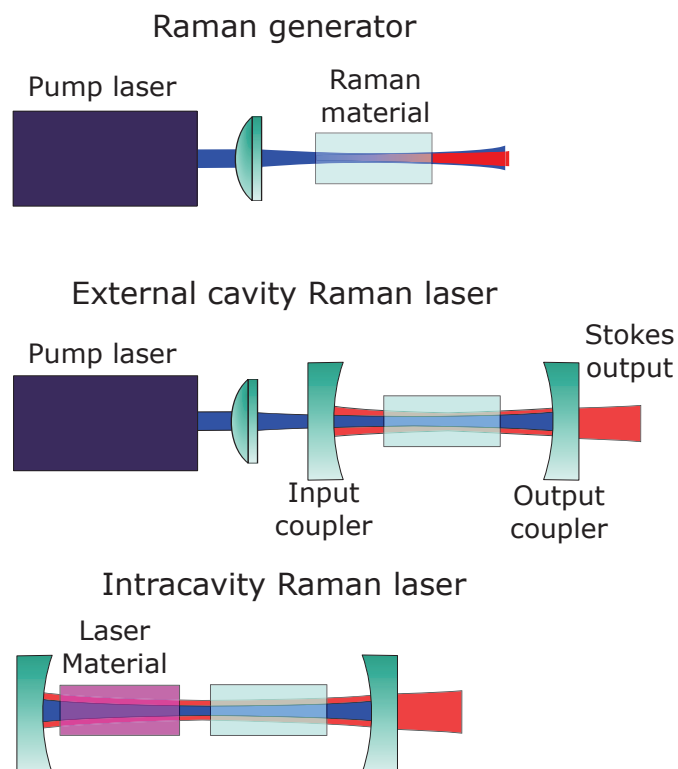


FIGURE 4.1: Simplified Raman laser architectures.

4.1.1 Modelling external cavity Raman lasers

Modelling of external cavity DRLs using the coupled Raman intensity equations [109, 140] aided in understanding the Raman dynamics and optimising cavity designs. Appendix A derives the underlying form of the equations, and extending the result to a scenario with a pump beam (I_P) and three Stokes orders (I_{S1} , I_{S2} and I_{S3}), gives

$$\begin{aligned}
\frac{dI_P^\pm}{dz} &= -g_P I_P^\pm (I_{S1}^+ + I_{S1}^-) - \alpha'_P I_P^\pm \\
\frac{dI_{S1}^\pm}{dz} &= g_{S1} I_{S1}^\pm [(I_P^+ + I_P^-) - (I_{S2}^+ + I_{S2}^-)] - \alpha'_{S1} I_{S1}^\pm + \sigma'_{SP} (I_P^+ + I_P^-) \\
\frac{dI_{S2}^\pm}{dz} &= g_{S2} I_{S2}^\pm [(I_{S1}^+ + I_{S1}^-) - (I_{S3}^+ + I_{S3}^-)] - \alpha'_{S2} I_{S2}^\pm + \sigma'_{SP} (I_{S1}^+ + I_{S1}^-) \\
\frac{dI_{S3}^\pm}{dz} &= g_{S3} I_{S3}^\pm [(I_{S2}^+ + I_{S2}^-)] - \alpha'_{S3} I_{S3}^\pm + \sigma'_{SP} (I_{S2}^+ + I_{S2}^-)
\end{aligned} \tag{4.1}$$

with boundary conditions:

$$\begin{aligned}
I_{P,S1,S2,S3}^+(IC) &= I_{P,S1,S2,S3}^-(IC) \cdot R_{IC(P,S1,S2,S3)} \\
I_{P,S1,S2,S3}^-(OC) &= I_{P,S1,S2,S3}^+(OC) \cdot R_{OC(P,S1,S2,S3)} \\
I_{S1,S2,S3}^{output} &= I_{S1,S2,S3}^+(OC) \cdot (1 - R_{OC(S1,S2,S3)})
\end{aligned}$$

and gain and loss parameters given by:

$$g_{P,S1,S2,S3} = \frac{\omega_{P,S1,S2,S3}}{\omega_{S1}} \eta g'_R$$

$$g_{P,S1,S2,S3}(z), \sigma'_{SP}(z), \alpha'(z) = \begin{cases} g_{P,S1,S2,S3}, \sigma'_{SP}, \alpha' & \text{in the crystal} \\ 0 & \text{in the air} \end{cases}$$

The equations are solved numerically for an arbitrary pump input pulse using either the Euler or Runge-Kutta methods for both forward (+ superscript) and backward (- superscript) travelling waves (see Fig. 4.2). σ_{SP} is the spontaneous scattering coefficient and $\alpha_{P,S1,S2,S3}$ is the loss coefficient for each wavelength. The Raman gain coefficient, $g_{P,S1,S2,S3}$ incorporates a scaling factor, η , to account for the finite linewidth of the

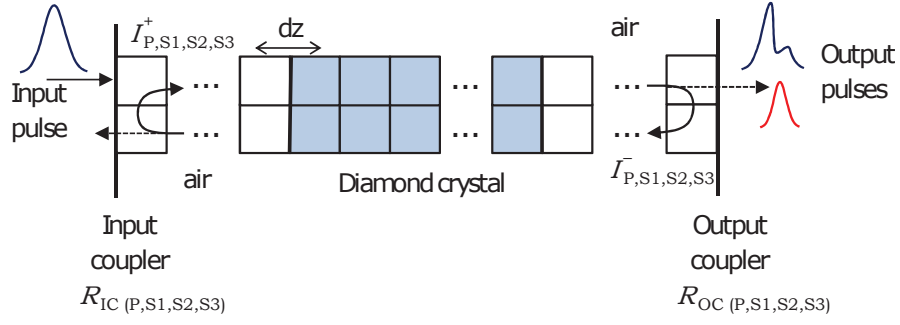


FIGURE 4.2: Conceptual diagram of the Raman modelling.

pump beam and is discussed later in Chapter 5. The reflectivity of the cavity input and output coupling mirrors, R_{IC} and R_{OC} , define the boundary conditions. The Raman cavity is modelled in terms of optical path length, z , which allows the different velocities of light in the air and diamond to be accounted for, i.e. a 1 cm diamond is modelled as a 2.38 cm crystal. The diamond properties such as gain and loss are marked with a prime to indicate that they are scaled down by the refractive index to compensate for the lengthening of the modelled diamond. Energy accumulates at a given wavelength from stimulated and spontaneous Raman scattering of the prior Stokes order. Depletion arises from energy cascading into the next Stokes wavelength and other losses such as crystal absorption. Anti-Stokes wavelengths are generally not observed with any appreciable power in collinear external cavity Raman lasers and are not included in the model.

The model, as written, assumes plane wavefronts and matched Gaussian beam profiles. The plane wavefront assumption is valid as the pump confocal parameter in experiments exceeded the crystal length. Any expansion of the beam spot size in the air filled parts of the cavity is inconsequential as g_R is zero. The assumption of matched mode sizes is typically not met because the pump spot under-filled the cavity mode and determining the Stokes beam size is complicated. Stokes growth will largely occur in the central region of the pump beam, which is smaller in area than the lowest order mode of the resonating Stokes field. The effective Stokes spot size will likely evolve during the pulse. The profile of the pump beam will also evolve as the high intensity regions are preferentially depleted. Where the relative pump and Stokes

intensity profiles are known, the effective area of the interaction is

$$A_{eff} = \frac{\int I_P dA \int I_S dA}{\int I_P I_S dA} \quad (4.2)$$

Incorporating temporally evolving variations in the spatial overlap adds to the model complexity and computation time. The agreements seen here, and in the literature [79, 141], between models assuming constant spot sizes and experimental results, is sufficient for designing and optimising pulsed external cavity Raman lasers. Further details on the modelling and variables are presented in Appendix A.

4.2 First Stokes, 1.240 μm laser

4.2.1 Experiment

The first and second Stokes laser experiments used the external-cavity architecture shown in Fig. 4.3. The dimensions of the CVD grown single diamond crystal were $6.9 \times 5 \times 1 \text{ mm}$, with the long edge orientated along a $\langle 110 \rangle$ axis. The $5 \times 1 \text{ mm}$ facets were AR coated with the reflection minimum centred at $1.240 \mu\text{m}$. The coating reflectivity at $1.064 \mu\text{m}$, $1.240 \mu\text{m}$ and $1.485 \mu\text{m}$ was 2%, 0.5% and 1%, respectively. Input and output coupling mirrors were placed as close as practical to the ends of the diamond (1-2 mm air gaps were typical). Reducing the cavity length lowers the laser threshold, primarily by ensuring the spot size for the reflected pump has not diverged significantly. A secondary benefit arises from the reduced cavity round trip time leading to a more rapid accumulation of amplified Stokes photons [110]. For first Stokes operation, the initial input couplers had high transparency (HT) at $1.064 \mu\text{m}$ and high reflectivity (HR) at $1.240 \mu\text{m}$ and $1.485 \mu\text{m}$, while the output couplers were HR at $1.064 \mu\text{m}$, 50% reflective at $1.240 \mu\text{m}$ and 3% reflective at $1.485 \mu\text{m}$. Modelling of the first Stokes output showed that 50% reflectivity is within the band of optimal values and further details are presented in Section 4.3.

The pump laser was a linearly polarised co-planar folded slab (CPFS) Nd:YAG laser similar to that described in [142]. It operated with up to 4.5 W average power

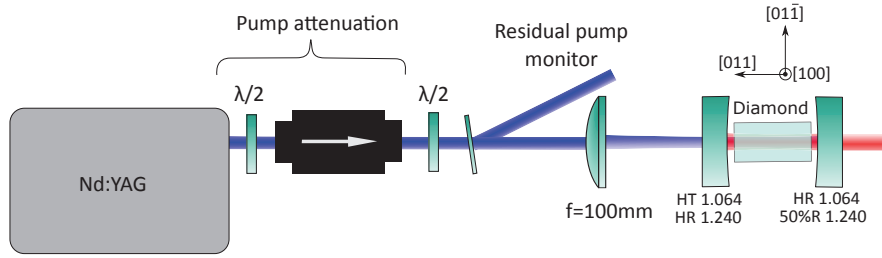


FIGURE 4.3: Experimental layout of the first Stokes DRL.

with 5 kHz, 10 ns pulses and an M^2 of 1.5. The pump beam passed through an isolator to protect the laser from back reflections from the Raman cavity output coupler. A half waveplate prior to the isolator attenuated the power incident on the Raman cavity, eliminating the need to adjust the pump laser during experiments. A second half waveplate after the isolator adjusted the polarisation of the pump beam prior to focussing into the Raman laser.

4.2.2 Results

The initial experiments were aimed at investigating the dependence of cavity and input beam parameters on first Stokes output power and efficiency. Pump focussing lenses with focal lengths of 75, 100, 125 and 150 mm were investigated to determine their influence on threshold and slope efficiency. The resultant pump spot sizes and laser performance is shown in Fig. 4.4(a). The 100 mm focal length lens offered the best performance. Longer focal lengths resulted in higher thresholds, while the shorter focal length only provided negligible threshold improvement and resulted in damage to the input coupler at high powers. For the three shorter focal length lenses, the slope efficiencies were similar, as the pump spot sizes under-filled the cavity mode. For the 150 mm lens, the pump spot size was similar to the cavity mode size and the slope efficiency decreased by 9%.

The Raman cavity mode size was adjusted by changing the radius of curvature (ROC) of the input and output coupler. Input and output mirrors with 50, 200 and 1000 mm ROC resulted in calculated cavity mode diameters of 140 μm , 200 μm and 300 μm , respectively, for a wavelength of 1.240 μm . Figure 4.4(b) shows that while there

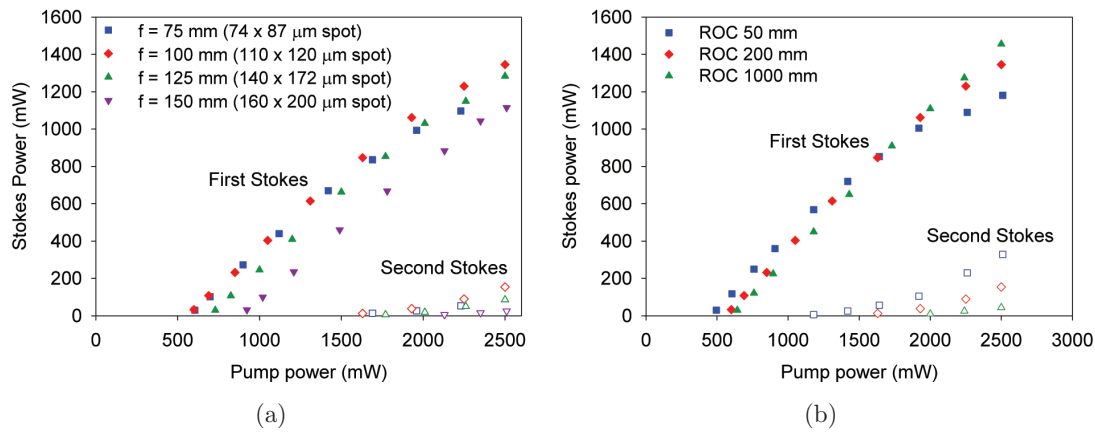


FIGURE 4.4: (a) DRL performance as a function of pump focus spot size. The input and output mirror ROC was 200 mm. (b) Performance for cavity mirror ROCs of 50-1000 mm. Both input and output coupler ROCs are matched. The pump lens focal length was 100 mm. In both figures the solid and hollow symbols are first and second Stokes power levels, respectively.

is a small reduction in the first Stokes threshold from tighter cavity mode confinement, there is a substantial penalty at higher powers due to a lower threshold for cascading to second Stokes. This issue is exacerbated by input couplers that were highly reflective at both the first and second Stokes. Ideally the cavity Q at the second Stokes should be as low as possible to prevent any build-up of power. For all further first Stokes experiments, a plano input coupler with 50% reflectivity at 1.485 μm was used, which reduced the rate of second Stokes conversion.

The third parameter that was varied was the pump polarisation. As detailed in the previous chapter, there is a 25% reduction in laser threshold for a pump polarisation aligned with a $\langle 111 \rangle$ axis, compared to the $\langle 100 \rangle$ or $\langle 011 \rangle$ axes. Aligning the pump polarisation with a $\langle 111 \rangle$ axis gives a co-polarised Stokes output, facilitating lower thresholds for higher Stokes orders. This effect is shown in Fig. 4.5 where a $\langle 111 \rangle$ pump polarisation results in a lower first and second Stokes threshold. As a result, the maximum first Stokes power is reduced due to increased conversion loss to the second Stokes.

For both $\langle 100 \rangle$ or $\langle 111 \rangle$ pump polarisations, a maximum of 2.2 W total Stokes output was generated, limited by available pump power. The total conversion efficiency

was 65%, with a maximum 61% conversion to the first Stokes. Factoring in the ratio of power in each Stokes wavelength, the quantum conversion efficiency peaks at 80%. Prior to the onset of the second Stokes, the slope efficiency was 84% and close to the quantum limit of 85.8%. To further investigate pump conversion efficiency, the double passed residual pump was observed using the reflection from a slightly-tilted ($\sim 10^\circ$) AR coated window (refer to Fig. 4.3). Figure 4.5 shows that below threshold the residual pump increases linearly, as expected. Above threshold it rolls over with a slight negative slope prior to the second Stokes threshold. In this range, each additional pump photon results in the generation of fractionally more than one Stokes photon on average. In the absence of parasitic losses in the cavity, the Stokes slope efficiency would be greater than the quantum limit. Modelling shows that this effect arises due to the rate dependence of Raman conversion on both the pump and first Stokes intensity. As the Stokes intensity increases, the pump pulse is more effectively converted to Stokes. Above the second Stokes threshold, reduced intracavity intensity of the first Stokes power due to the cascade to the second Stokes, leads to a reduction in the rate of pump depletion. Hence, the slight positive slope observed in the depleted pump after the second Stokes threshold. This interaction between the different wavelengths is explored in more depth in the description of the second Stokes laser in Section 4.3.

There is a good agreement between the modelled and measured first and second Stokes thresholds and output powers. The modelled residual pump also shows a negative slope, but there is greater depletion of the pump than observed experimentally. This effect was also seen in modelling of CW Raman lasers [143] and is attributed to the model not accounting for the evolving spatial properties of the beams.

The temporal profiles were recorded using a fast InGaAs detector (Thorlabs DET-01CFC) and a 1 GHz oscilloscope. Figure 4.6(a) shows the pulse shapes just after the second Stokes output reaches threshold (1.2 W first Stokes output). The first Stokes pulse width is 8 ns and, aside from the rapid rise in intensity when threshold is reached, largely follows the pump profile. Correspondingly, the residual pump intensity is rapidly depleted when the first Stokes reaches threshold. At the peak of the pulse, greater than 85% of the pump is depleted by the Raman interaction.

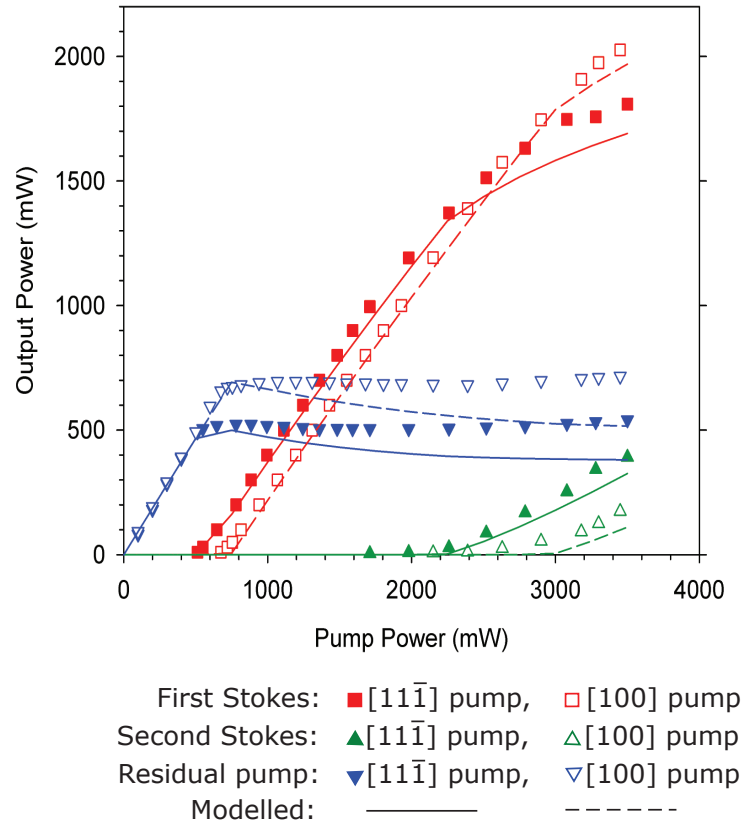


FIGURE 4.5: Stokes power and residual pump power for pump polarisation aligned with the $[11\bar{1}]$ axis and $[100]$ axis.

Beam quality measurements were performed using Gaussian fits to images recorded on a CCD beam profiler (Fig. 4.6(b)). Even though $1.240\text{ }\mu\text{m}$ is nominally beyond the specified detection band of silicon, beam profiles were visible with sufficient incident power. Insertion of multiple longpass filters confirmed that the signal was not the result of pump leakage. The output was circular and near diffraction limited. In comparison the Nd:YAG pump operated with a mildly elliptical beam and an M^2 of 1.5. Increasing the pump power did not produce any observable thermal distortions.

Output spectra were measured with an optical spectrum analyser (Advantest Q8384 OSA - 0.19 cm^{-1} instrument linewidth at $1.240\text{ }\mu\text{m}$) and a scanning Fabry-Perot interferometer (Thorlabs SA210-8B - 0.002 cm^{-1} resolution and 0.33 cm^{-1} free spectral range (FSR)). A longitudinal mode spacing of 0.24 cm^{-1} was recorded with the interferometer, which equates to a 20.8 mm cavity length (Fig. 4.7(a)), in agreement with

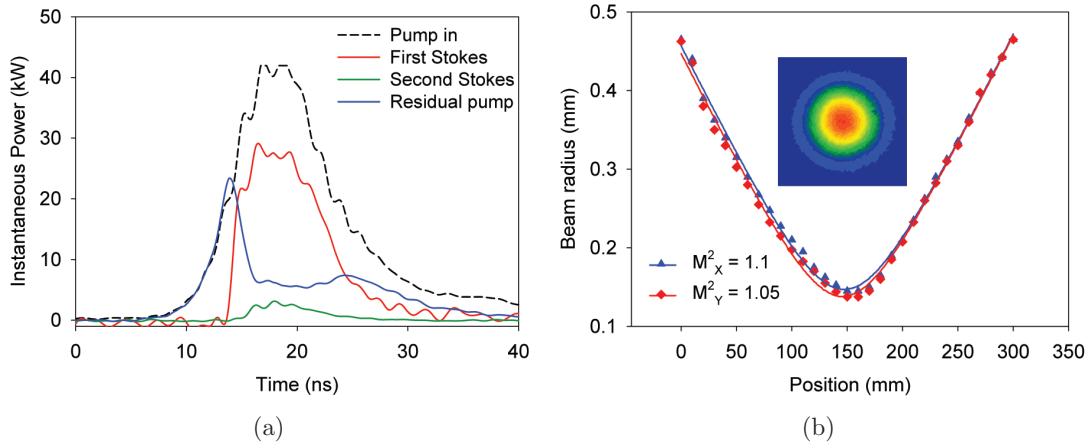


FIGURE 4.6: (a) Temporal profile of the pump, first Stokes and second Stokes for 1.2 W first Stokes output. (b) M^2 measurement for 1 W first Stokes output and an image of the focused beam profile.

the measured optical path length of the cavity. The 0.24 cm^{-1} mode spacing presented some challenges in taking accurate readings of the laser spectra. The OSA resolution was only sufficient to partially resolve the Raman laser modes (see Fig. 4.7(b)), whereas the Fabry-Perot easily resolved the modes, but if more than two modes were present the total linewidth exceeded the FSR. For output powers just prior to the detection of second Stokes light (1 W output, ~ 3 times threshold), 2-5 longitudinal modes were observed, usually with two dominant modes.

The results above describe the first efficient infrared DRL and the maximum output power of 2.2 W was equal with the highest power DRL reported at the time [71]. The total conversion of pump photons (80%) exceeds all prior DRL demonstrations. Prior to this, the highest reported quantum conversion efficiency was 68% from a $0.532\text{ }\mu\text{m}$ pumped DRL using a Brewster cut crystal [69]. Increased losses, potentially from birefringence and the Brewster facets, reduced the slope efficiency to 88% of the quantum limit, compared to $\sim 100\%$ here. Brewster facets also expand the pump and Stokes beams in one plane, leading to increased thresholds.

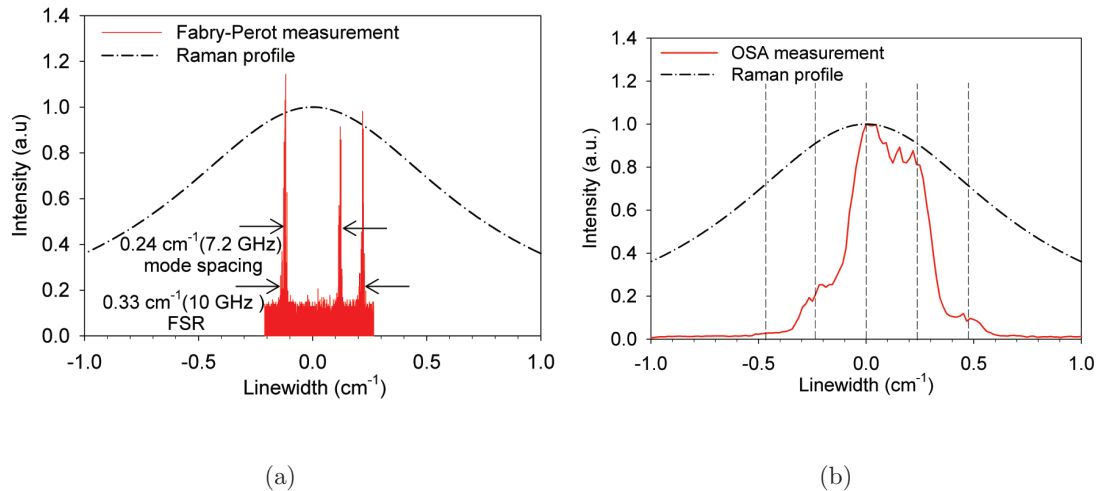


FIGURE 4.7: (a) Scanning Fabry-Perot trace for first Stokes at 1 W output power. (b) OSA spectrum for the same pump and cavity conditions showing partially resolved modes. Dashed lines indicate the longitudinal modes observed.

4.2.3 Performance comparison with other Raman crystals

Table 4.1 shows a comparison of the present results with other external-cavity first Stokes Raman lasers pumped by Q-switched 1.064 μm lasers. Conversion efficiencies for diamond are similar to alternative crystals, and slightly better when taking the larger wavelength shift of diamond into account. Pump pulse energies, crystal lengths, and focussing conditions vary substantially between experiments. Many are operating with higher energy (tens of millijoules per pulse) and with beam diameters in the Raman crystal larger than 1 mm to avoid damage. Repetition rates and average powers are not always reported, suggesting studies were conducted with long pulse periods and negligible thermal loads.

Higher average power examples operate in a regime in which thermal lensing becomes important [33, 136, 139]. Up to 17 W at 28% conversion efficiency has been demonstrated using $\text{Ba}(\text{NO}_3)_2$ [139]. The induced thermal lens distorted the pump and Stokes intensity profiles and the laser operated with degraded Stokes beam quality ($M^2 = 4 - 5$). The $\text{Ba}(\text{NO}_3)_2$ laser reported by Pask et al. used a pump laser with

similar pulse parameters, and thus offers an opportunity for a direct performance comparison [144]. The conversion efficiency with $\text{Ba}(\text{NO}_3)_2$ was lower (45% c.f. 61%) and, unlike the case with diamond, the beam quality of the Raman output degraded from an M^2 of 1.4 at 0.63 W to 3.0 at 1.32 W.

Using diamond, Fève et al. demonstrated a pulsed first Stokes DRLs with average powers up to 24.5 W (two output beams of 12.7 W each) [79]. No thermal degradation was observed at this power level. The conversion efficiency of 13% is much lower than achieved here and is due primarily to operation at input powers only 1.5 times threshold. The observed slope efficiency was 57.6%, which suggests higher conversion efficiencies for operation further above threshold, provided that damage can be avoided.

Thermal lensing is suggested by the authors of a recent report as the mechanism for the reduction in observed efficiency of a first Stokes DRL operating with millijoule pulse energy [145]. However, analysis of their results indicates that thermal effects are unlikely to be the cause. There is no correlation between the thermal load and the point at which the first Stokes rollover occurs. In addition, no rollover is observed for the second Stokes lasers, despite a much higher thermal load. The cavity mirror combinations used for the first Stokes DRLs are susceptible to cascading energy into the second Stokes, which I suggest may be the actual cause for the loss of first Stokes efficiency (the input coupler is highly reflective at 1.485 μm and the output couplers have 8 to 99.9% reflectivity at 1.485 μm). Comparing the mirror reflectivity at the first and second Stokes wavelengths with the rollover thresholds supports this hypothesis.

Material	Length (mm)	Average Power (W)	Pulse Energy (mJ)	Conversion efficiency %		Ref.
				Energy	Quantum	
Diamond	6.9	2.0	0.4	61	71	this, [111], 2010
Diamond	8	24.5	0.61	13	15	[79], 2011
Diamond	7.8	0.036	1.2	28	33	[145], 2016
Ba(NO ₃) ₂	51	—	22	60	68	[146]
Ba(NO ₃) ₂	50	1.3	0.33	45	51	[144]
Ba(NO ₃) ₂	70	1.5	150	59	66	[135]
Ba(NO ₃) ₂	70	17	14	28	32	[139]
Ba(NO ₃) ₂	70	11	10	22	25	[33]
BaWO ₄	46	—	40	61	68	[147]
BaWO ₄	95	7.5	30	30	33	[136]
SrWO ₄	49	—	11	47	52	[148]
KGW	45	—	11	45	50	[141]
PbWO ₄	90	0.35	7	20	22	[108]

TABLE 4.1: Summary of results for first Stokes external-cavity crystalline Raman lasers pumped by Q-switched 1.064 μm lasers. The diamond references also include the year of publication.

4.3 Second Stokes, 1.485 μm laser

Adapting the DRL for second Stokes output was achieved by exchanging the two cavity mirrors to provide resonance at first and second Stokes wavelengths. All other aspects remained consistent with the cavity presented in Fig. 4.3. The input coupler was highly transmissive at 1.064 μm , highly reflective at the first and second Stokes wavelengths and had a ROC of 100 mm. Several output couplers were investigated, all highly reflective at the first Stokes wavelength, but with a range of reflectivity values at the second Stokes (see Table 4.2).

Output coupler	Pump	First Stokes	Second Stokes	ROC
M1	>99%	>99%	61%	Plano
M2	>99%	>99%	31%	Plano
M3	>99%	98%	16%	500 mm
M4	53%	>99%	8%	Plano

TABLE 4.2: Reflectivity values of the output couplers at the pump and Stokes wavelengths.

4.3.1 Results

The effect of output coupling on performance is shown in Fig. 4.8(a). The highest second Stokes average power of 1.63 W was obtained using output coupler M3 and was limited by available pump power. The output power increased linearly with pump power above threshold. The slope efficiency was 56% and the conversion efficiency at maximum pump power was 51% (quantum conversion efficiency of 71%). No significant third Stokes power ($<1\text{ mW}$) was observed as expected due to the low reflectivity ($<10\%$) of the cavity mirrors at 1.852 μm . There is little change in the threshold for each mirror, except for a slight increase for M4 due to its lower pump reflectivity. The small variation arises from the rapid build-up in intensity of the first Stokes in the high-Q cavity. Seeding of the second Stokes through four-wave-mixing between the pump and first Stokes intracavity fields is also likely to contribute to the similar thresholds [149]. The slope efficiency thus becomes the main determinant of laser conversion efficiency. With output coupler M3, the slope efficiency was 5% higher than with M2 and M4. If M4 had a higher pump reflectivity the slope efficiency would be further improved. When using the highest reflectivity output coupler, M1, the slope efficiency is 9% lower again. Improved slope efficiency for the lower reflectivity output couplers corresponds to an increase in measured pump depletion (Fig. 4.8(b)). Unlike the first Stokes DRL, the residual pump traces have positive slopes above threshold, which is consistent with the lower second Stokes slope efficiencies ($<56\%$ compared to the quantum limit of 72%).

To find the optimal output coupler reflectivity, modelled values ranging from 1% to 90% are compared to experimental results in Fig. 4.9. For reference, the modelling was also conducted for a laser cavity designed for first Stokes operation. In contrast to the first Stokes optimised laser, there is a narrower band of output coupler reflectivity values that provide efficient output. Efficient second Stokes output couplers are also skewed towards lower reflectivity values. The model reveals that this is due to the competition between power transfer from the pump to the first Stokes and from first to second Stokes. A higher second Stokes mirror reflectivity increases the second Stokes intracavity intensity and Eq. (4.1) shows that this increases the rate of first Stokes

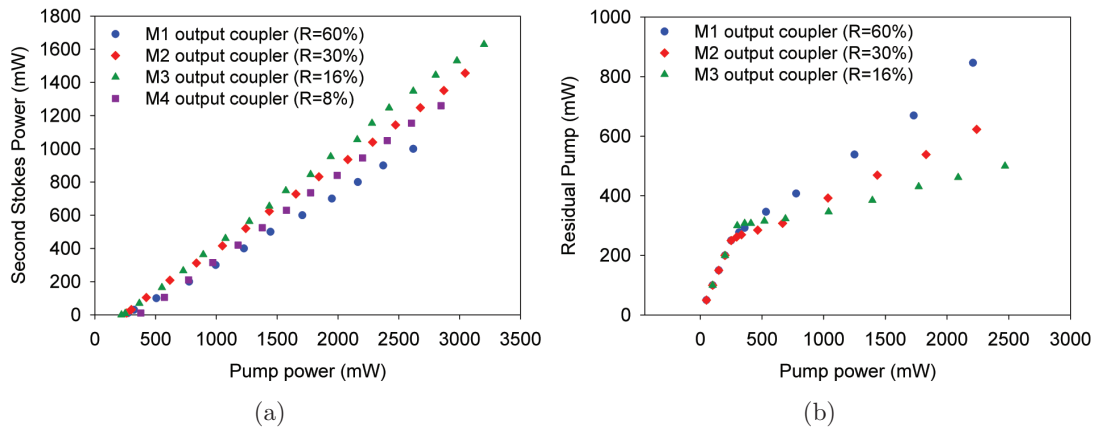


FIGURE 4.8: (a) Second Stokes output for the output couplers M1-4 listed in Table 4.2. (b) Residual pump for M1-3.

depletion. It follows that a lower first Stokes intensity will reduce the rate of pump depletion. The improvement in second Stokes performance using low reflectivity output couplers was previously predicted [150], but without experimental confirmation.

The measured and modelled pulse profiles of the pump and Stokes wavelengths in Fig. 4.10 support this explanation for the high optimal output coupling. A rapid turn-on of the first Stokes is clearly seen, followed by an equally rapid decay coinciding with the onset of the second Stokes pulse. The first Stokes then settles to a constant intensity whereby any additional photons are converted to the second Stokes. With higher intracavity second Stokes fields, a lower constant first Stokes intensity level reduces the rate of conversion from the pump field and therefore reduces the conversion efficiency.

The output beam profile was measured using a phosphor coated CCD camera (Newport LBP-4-USB), calibrated for the nonlinear response and scattered phosphorescence. The second Stokes beam quality was also excellent with an M^2 of 1.05 (Fig. 4.11(a)).

The output spectrum of the second Stokes laser reveals up to 10-12 distinct longitudinal modes under the envelope of the Raman profile (Fig. 4.11(b)), and largely follows the first Stokes spectrum. This is substantially higher than the 2-5 modes seen in the laser designed for first Stokes output, and reflects the higher Q of the first Stokes

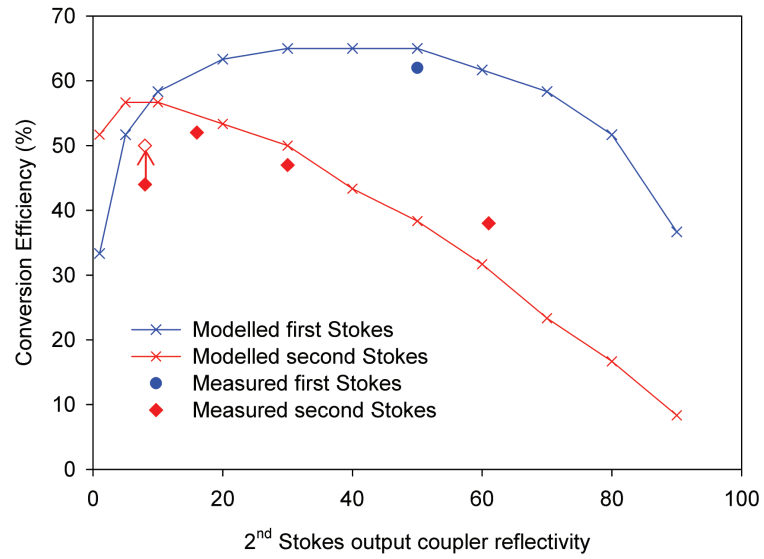


FIGURE 4.9: Measured and modelled conversion efficiency dependence on output coupler reflectivity for Raman cavities designed for first and second Stokes operation. The modelled values are for 3 W of pump power. The upper data point for mirror M4 ($R=8\%$) shows an adjusted point (hollow diamond) for the more ideal case of an output coupler that is highly reflective at the pump wavelength.

cavity as well as operation of the laser further above threshold.

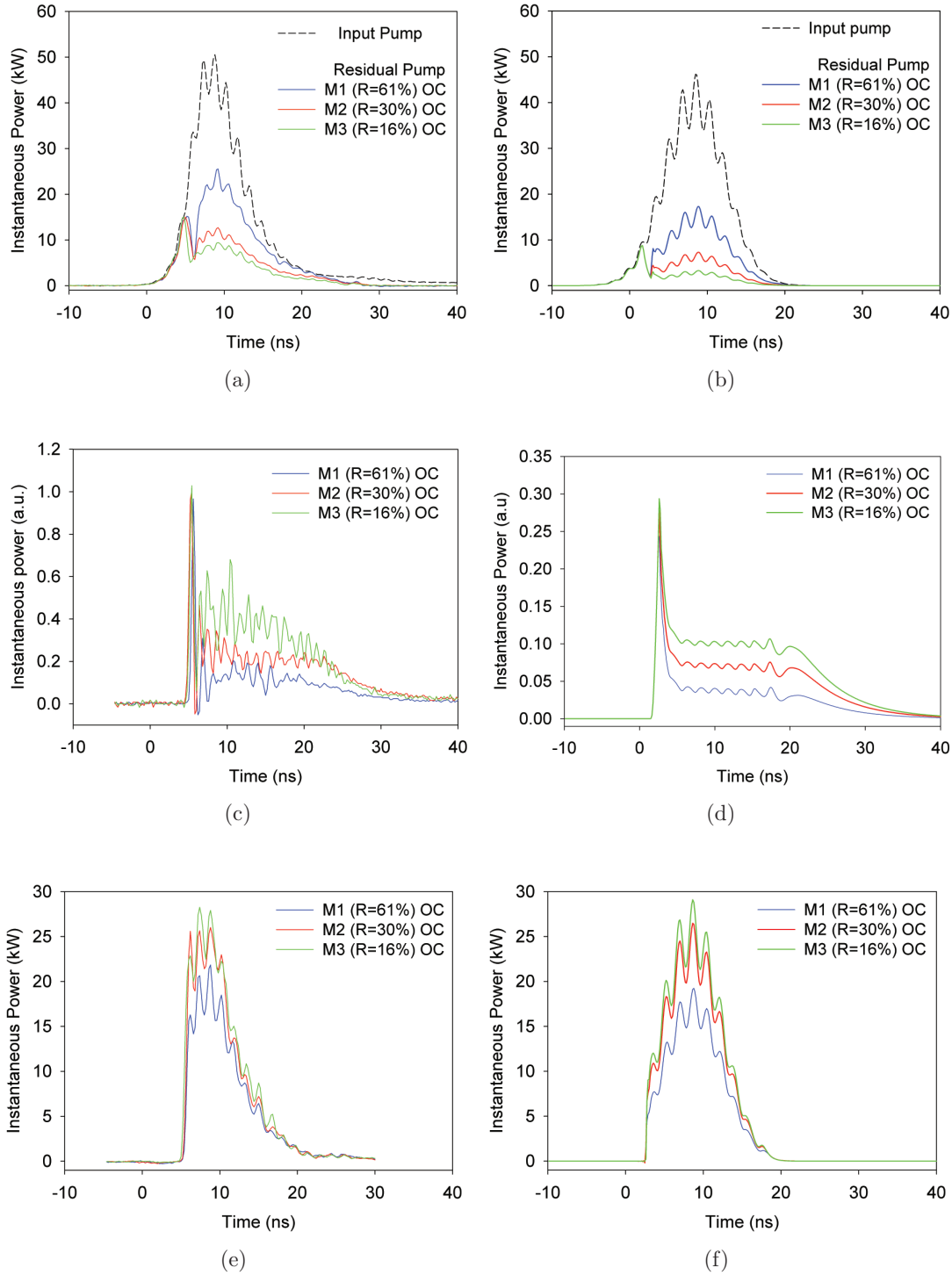
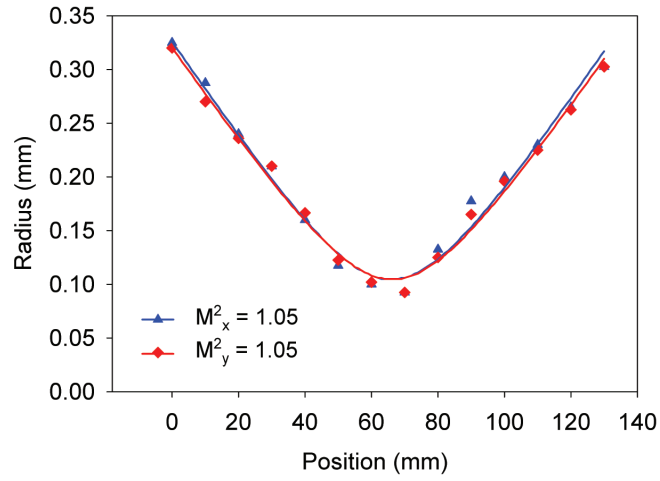
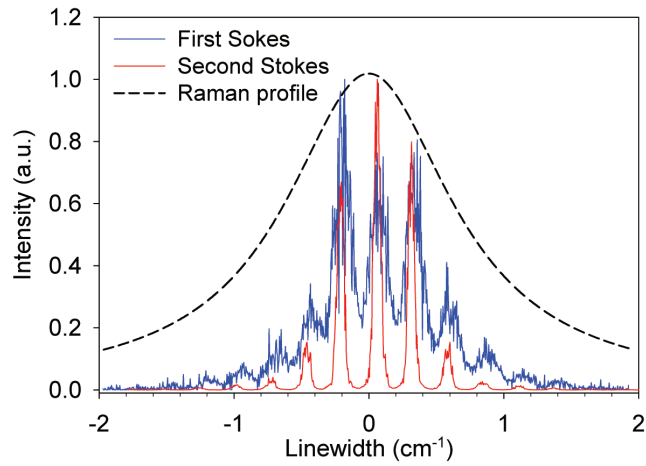


FIGURE 4.10: Measured (LHS) and modelled (RHS) temporal traces for (a,b) residual pump, (c,d) first Stokes and (e,f) second Stokes pulses. Pulses are shown for output couplers M1-3 at 2 W of pump power.



(a)



(b)

FIGURE 4.11: (a) M^2 measurements for 1.5 W second Stokes output. (b) Overlay of first and second Stokes spectra with the Raman profile for 800 mW output power (output coupler M3). The improved clarity of the second Stokes peaks is due to the higher resolution of the OSA at 1.485 μm .

4.3.1.1 Polarisation properties

Intuitively, calculating the polarisation state of a second Stokes DRL would involve applying the Raman tensors with the first Stokes laser in the place of the pump laser. In particular, if the pump laser was $[100]$ polarised, the first Stokes would be $[01\bar{1}]$ polarised, which would then lead to a randomly polarised second Stokes output. Experimentally this was not the case and the second Stokes output was strongly $[100]$ polarised.

Table 4.3 compares the tensor calculations and the experimental measurements for the three main polarisations discussed. It is hypothesised that four-wave-mixing (FWM) between the pump and first Stokes is seeding the second Stokes leading to a strong preference for linearly polarised output. Calculations outlined in Appendix B show that for the crystal class of diamond, mixing between $[100]$ and $[01\bar{1}]$ polarised beams indeed produces a seed with $[100]$ polarisation.

For the case when the pump is aligned with $[01\bar{1}]$, the first Stokes will be ‘randomly polarised’. FWM calculations show that both horizontal and vertical first Stokes polarisations lead to a $[01\bar{1}]$ polarised FWM seed, which enhances the polarisation purity of the second Stokes output.













	Pump	1 st Stokes	Predicted 2 nd Stokes	Measured 2 nd Stokes
$[100]$				
$[01\bar{1}]$				
$[11\bar{1}]$				

TABLE 4.3: Stokes polarisations predicted using only the Raman tensors compared to measured second Stokes polarisation for $[100]$, $[01\bar{1}]$ and $[11\bar{1}]$ pumping.

Material	Length (mm)	Output λ (μm)	Average Power (W)	Pulse Energy (mJ)	Conversion efficiency %		Ref.
					Energy	Quant.	
Diamond	6.9	1.485	1.63	0.33	51	71	this, [131], 2011
Diamond	8	1.485	16.2	0.45	40	56	[80], 2013
Diamond	7.8	1.485	0.021	0.7	16	22	[145], 2016
Ba(NO ₃) ₂	140	1.369	1.04	104	34	44	[135]
Ba(NO ₃) ₂	70	1.369	9.5	8	16	21	[139]
BaWO ₄	60	1.325	—	22.8	35	44	[147]
BaWO ₄	95	1.325	2.4	10	9	11	[136]
KGW	45	1.316	—	24	48	59	[141]
KGW	45	1.316	7.5	0.19	16	20	[151]
SrWO ₄	49	1.325	—	22	48	60	[148]

TABLE 4.4: Comparison of second Stokes, external-cavity crystalline Raman lasers pumped by Q-switched 1.064 μm lasers. The diamond references also include the year of publication.

4.3.2 Comparison with other Raman crystals

The results represent the first reported DRL designed to primarily output at the second Stokes wavelength. Comparisons to other second Stokes Raman lasers pumped at 1 μm in Table 4.4 show that the conversion efficiency obtained is higher than all other materials, as also seen for the first Stokes laser. Furthermore, no thermal degradation was seen, in contrast to multi-watt Raman lasers in other crystalline materials including KGW [18], Ba(NO₃)₂ [33, 139] and BaWO₄ [136]. A further distinction is that the wavelength shift of the DRL (2666 cm^{-1}) is notably larger than other crystals (1500–2000 cm^{-1}), and is the only crystal that enables a second Stokes wavelength beyond 1.4 μm .

4.4 Conversion of 1 μm lasers to eye-safer wavelengths

Although 1 μm laser technology is efficient, power scalable and versatile, a drawback is the potential high degree of retinal hazard. This limits its use in applications where eye

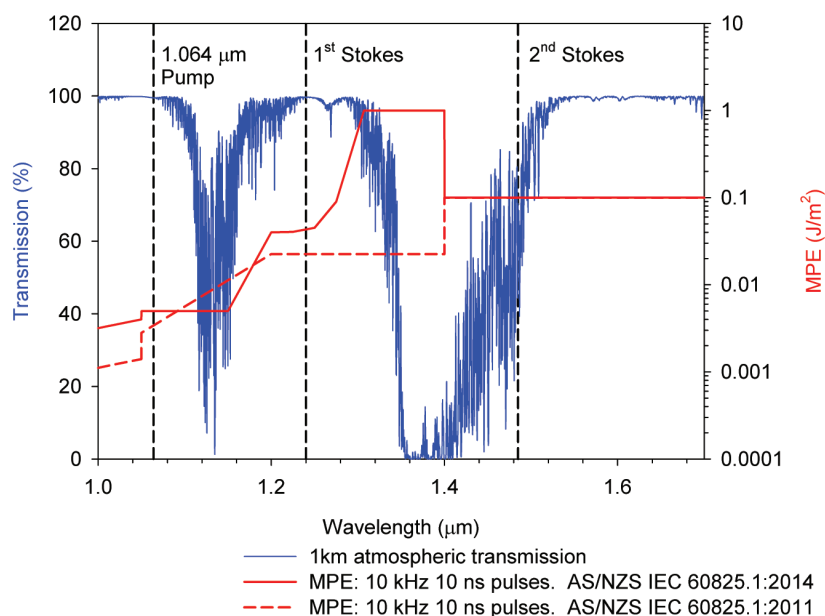


FIGURE 4.12: Maximum permissible exposure (MPE) and atmospheric transmission for a Nd:YAG laser and the first two Stokes wavelengths from a DRL. The MPE data is from the current AS/NZS IEC 60825.1:2014 standard and the previous 2011 edition for a laser with 10 ns pulses at a 10 kHz repetition rate. The atmospheric transmission data is generated by MODTRAN 5 for a 1 km horizontal path, 2 m above the ground.

exposure is likely, such as rangefinding, lidar and remote sensing. Throughout the history of Raman laser development, conversion of Nd:YAG lasers to safer wavelengths is a persistent theme [135, 152–154]. Traditionally, the so-called ‘eye-safe’ region spanned 1.5 - 1.8 μm , where the defined safe energy densities were the largest [155] and light propagates with excellent atmospheric transmission. Under the new 2014 laser safety standard [156], the 1.3 - 1.4 μm wavelength region has the highest permissible energy densities for lasers with repetition rates $>1\text{ Hz}$, but in practical terms is limited by numerous atmospheric absorption features. In either case, conversion of 1 μm lasers to 1.240 μm first Stokes and 1.485 μm second Stokes wavelengths results in a substantial increase in eye safety.

A first Stokes DRL is a simple and efficient means of converting 1 μm lasers to a less hazardous wavelength. The degree of hazard reduction given by the laser safety standard depends on the repetition rate of the laser. As an example, Fig. 4.12 shows

a 9 times increase in maximum permissible exposure (MPE) is obtained for a 10 kHz Q-switched first Stokes DRL. Figure 4.12 also shows that the first Stokes wavelength of diamond is in a region of excellent atmospheric transmission and thus suitable for long range applications. First Stokes Raman lasers using other Raman crystals ($\lambda_{S1} = 1.15 - 1.2 \mu\text{m}$) are attenuated by water vapour.

A second Raman shift results in a further 2.2 times increase in MPE, however $1.485 \mu\text{m}$ is attenuated by water vapour and thus less suited to multi-kilometre propagation. The use of a slightly longer pump wavelength, such as $1.080 \mu\text{m}$ from a Nd:YAP laser, places the second Stokes wavelength in a region of high transmission ($1.516 \mu\text{m}$) as well as high allowable MPE.

Material	Length (mm)	Pump λ (μm)	Output λ (μm)	Stokes Order	Average Power (W)	Pulse Energy (mJ)	Conversion		Ref.
							efficiency %	Quantum	
Diamond	6.9	1.064	1.485	2nd	1.63	0.33	51	71	this, [131], 2011
Diamond	8	1.064	1.485	2 nd	16.2	0.45	40	56	[12], 2014
Diamond	5	1.34	1.63	1 st	—	0.047	1.6	1.9	[157], 2012
Ba(NO ₃) ₂	140	1.064	1.599	3 rd	1.16	116	42	63	[135]
Ba(NO ₃) ₂	70	1.064	1.599	3 rd	5.0	4.5	12.5	19	[33]
Ba(NO ₃) ₂	70	1.064	1.599	3 rd	5.5	4.58	13	20	[139]
Methane	>300?	1.064	1.54	1 st	0.115	115	55	80	[154]
Ba(NO ₃) ₂	51	1.338	1.556	1 st	—	3.38	52	70	[146]
BaWO ₄	80	1.340	1.53	1 st	0.085	17	60	69	[158]
BaWO ₄	80	1.319	1.502	1 st	0.0085	8.5	47	54	[159]
KTP OPO	20	1.047	1.54	—	0.9	9	44	67	[14]
PPLN OPO	40	1.064	1.47	—	46	6.6	42	58	[17]

TABLE 4.5: A comparison of current results to a selection of external-cavity converters of Q-switched Nd³⁺ lasers to output wavelengths between 1.4 and 1.6 μm .

For a second Stokes DRL, the 71% quantum conversion efficiency achieved here compares favourably with alternative approaches for converting 1.064 μm Nd:YAG lasers to the $\sim 1.5 \mu\text{m}$ ‘eye-safe’ transmission window (Table 4.5). The highest previously reported quantum conversion efficiency in a solid state laser was 63%, obtained for a 1.599 μm third Stokes Raman laser in $\text{Ba}(\text{NO}_3)_2$ [135]. Since the quantum defect to wavelengths longer than 1.4 μm is substantial, there is significant deposition of heat when increasing average power. In $\text{Ba}(\text{NO}_3)_2$, efficiencies are reduced at powers above several watts due to the emergence of substantial thermal effects, even when using thermal lens compensation, and mitigation through the use of large pump diameters [33, 139]. In contrast, much higher powers are likely using diamond. Indeed, investigations subsequent to this work have demonstrated 16 W average power with no observed saturation of output power and degradation in beam profile [12].

Included in the 1.064 μm conversion results in Table 4.5 are several crystalline Raman examples shifting either the 1.319 μm or 1.338 μm Nd:YAG laser lines. Although pumping at 1.3 μm simplifies the design of the Raman conversion stage, several important advantages are obtained by using the higher gain 1.064 μm laser line. In addition to being more widely available, the design of efficient pump lasers with short pulsed Q-switched output, which is crucial for many applications, is typically simpler as a result of the larger emission cross section at 1.064 μm . Moreover, Raman shifting from 1.064 μm transfers a larger proportion of the total thermal load from the laser crystal into the Raman crystal (when considering the change in photon energy from the diode/flashlamp to eye-safe output). Although this is normally a disadvantage, as most Raman crystals have poorer thermal properties than the pump laser material, it becomes an advantage when using diamond in the Raman stage.

A second Stokes DRL has advantages compared to non-Raman technologies such as OPOs and Er:YAG. The conversion efficiency is similar to external-cavity OPOs operating at 1.5 μm [14, 17, 160] (Table 4.5). Absorption of the idler wavelength at 3.4 μm in OPOs may lead to thermal degradation in output efficiency and beam quality, particularly with commonly employed non-critically phase matched KTP crystals [14, 161]. OPO crystals such as KTA and LiNbO_3 have reduced idler absorption, but beam

quality is still degraded at high power. As examples, an M^2 of 30 was measured for a 33 W KTA OPO from a Nd:YAG pump laser with an M^2 of 5 [19] and a 46 W PPLN OPO produced an M^2 of 2×6 from a Nd:YAG pump with an M^2 of 2 [17]. Narrower free-running output spectrum is another advantage of DRLs. For DRLs, the linewidth is bounded by the Raman profile and the measured FWHM is 0.62 cm^{-1} . For a similarly pumped OPO, the free-running output linewidth is typically several cm^{-1} [162].

Resonantly pumped Er:YAG lasers are a technology capable of generating multi-watt average power, Q-switched output at $1.617 \mu\text{m}$ or $1.645 \mu\text{m}$. In Q-switched operation, the highest reported average powers are limited to the 10 W level [163, 164]. Energy transfer upconversion degrades efficiency at high powers, necessitating the use of low Er^{3+} doping levels [165] and thus high brightness pump sources. The reduced gain from low doping levels also leads to longer pulse durations at kHz repetition rates, compared to Nd^{3+} doped lasers ($>40 \text{ ns}$ [163] cf. $\sim 5 \text{ ns}$ [166]) .

4.5 Implications for future DRL designs

The versatility of the external-cavity architecture presents opportunities for extending the capability of the DRL designs presented above. Power, pulse duration and wavelength are three fundamental output parameters that have substantial potential to be extended.

4.5.1 Output power

Stokes output powers at the 1-2 W level are clearly well below the level to induce observable thermal effects in diamond. Scaling the average powers of crystalline Raman lasers is primarily limited by heat deposition from the inelastic Raman scattering process. Increased heat loads degrade the efficiency and beam quality of Raman lasers through thermally induced lensing, stress birefringence and eventually stress fracture of the crystal (e.g. [33]). Considering the contribution of each of these effects provides an estimation of the maximum average power of a DRL.

Thermal lensing changes the size of cavity modes and potentially leads to the excitation of higher order modes, reduced pump/Stokes overlap and unstable cavities. The focal length of the lens depends on the temperature gradient, end face curvature and photoelastic stress. Assuming the heat is deposited uniformly along the length of the crystal, analysis derived for end pumped laser crystals gives [167]

$$f = \frac{2\pi\kappa r_0^2}{P_{dep}} \left(\frac{dn}{dT} + (n-1)(\nu+1)\alpha_T + n^3\alpha_T C_{r,\phi} \right)^{-1} \quad (4.3)$$

where κ is the thermal conductivity (2200 W /m /K), r_0 is the $1/e^2$ beam radius, P_{dep} is the heat deposited, dn/dT is the thermo-optic coefficient (7.9×10^{-6} /K), ν is Poisson's ratio (0.069) and α_T is the coefficient of thermal expansion (1×10^{-6} /K). C_r and C_ϕ are the radial (0.015) and tangential (-0.032) components of the photoelastic stress tensor adapted from analysis of Nd:YAG, which also has a cubic crystal structure [64]. For diamond, α_T is small compared to many materials and dn/dT is the largest contributor to the lens strength. To destabilise the cavity in Fig. 4.3 requires a thermal lens with a focal length < 12 mm, which equates to 1.6 kW first Stokes average power for a 120 μ m beam diameter. This value must be treated as a rough approximation, as an underlying assumption of Eq. (4.3) is that the focal length is much longer than the crystal length. In comparison, similar plano-concave cavities using $\text{Ba}(\text{NO}_3)_2$ and KGW crystals reported modal instabilities beyond ~ 0.7 W first Stokes [144] and ~ 3 W second Stokes [151], respectively.

A second assumption in the lens calculation is that the pulse repetition rate is fast compared to the thermal gradient relaxation time,

$$\tau = \frac{r_0^2 C \rho}{\kappa} \quad (4.4)$$

where C is the heat capacity (0.5 J /g /K) and ρ is the density (3.51×10^6 g /m³). For a 120 μ m diameter spot size, the high thermal conductivity leads to settling times in diamond of 3 μ s. The thermal lens calculation therefore only applies for repetition rates in excess of ~ 500 kHz. At lower repetition rates the thermal gradients in diamond will

almost completely relax between pulses and damage to the crystal and coatings are likely to be the limiting factors. Increasing the pump and Stokes mode sizes to avoid damage will increase the relaxation time, but also reduce the strength of the thermal lens.

Stress birefringence reduces the polarisation purity of the DRL output, which may be important in certain applications. Similar to the photoelastic stress component of the thermal lens, the birefringence is given by [133]

$$\Delta n = \frac{n^3 \alpha_T Q C_B r_0^2}{\kappa} \quad (4.5)$$

where C_B is a photoelastic coefficient (-0.023) and Q is the heat deposited per unit volume. To achieve stress birefringence levels comparable to the background material birefringence (10^{-6}) requires first Stokes average powers in excess of 1.5 kW.

Increasing average powers further, the stress will eventually exceed the fracture limit of the material. Adapting analysis of an end pumped laser crystal, the Stokes output power at the stress fracture limit is [168]

$$P_{max} = \frac{4\pi R}{\alpha_P} \frac{1}{\lambda_S/\lambda_P - 1}, \text{ where } R = \frac{\kappa \sigma_{max}}{\alpha_T E} \quad (4.6)$$

where α_P is the pump absorption coefficient, E is Young's modulus (1100 GPa) and σ_{max} is the stress fracture limit (2.8×10^9 GPa). R is the 'thermal shock parameter' and indicates the ability of a material to withstand thermal loading without failure. The thermal shock parameter of diamond (5.6×10^6 W/m) is almost four orders of magnitude higher than YAG (800 W/m). Assuming the majority of the pump depletion occurs over a distance of 5 mm ($\alpha_P \approx 4 \text{ cm}^{-1}$), the calculated maximum first Stokes power is of the order of 10 MW.

The above analysis indicates that thermal lensing and stress birefringence require consideration for Stokes powers above the kilowatt level. This power is orders of magnitude higher than that obtainable using other Raman crystals and similar to CW fibre Raman lasers [37]. Defects within the crystal or on the surface are not considered, but

are likely to reduce the maximum achievable power by causing a weakness in the diamond lattice or absorbing energy. Catastrophic failure will result if absorption raises local temperatures in excess of the graphitisation temperature of diamond (~ 2000 K or ~ 1000 K on a surface in contact with air).

Subsequent publications have reported up to two orders of magnitude increases in average power over that demonstrated here. Pulsed external-cavity DRLs with 24 W dual ended first Stokes [79] and 16.2 W second Stokes output [12] observed no thermal effects, as expected. Interestingly, 154 W CW and 381 W QCW DRLs also exhibited no thermal degradation, despite thermal lens calculations suggesting otherwise [81]. It is suggested by the authors that the dispersion of acoustic phonons before they contribute to the thermal load increases the effective volume of the heat deposition zone.

4.5.2 Pulse duration

The external cavity architecture is applicable to pump lasers with pulse durations longer and shorter than the nanosecond regime demonstrated here. Longer pulse durations, up to the CW limit, implies reduced peak powers. Since SRS is intensity dependent, pump and Stokes spot sizes need to be reduced, and cavity lifetimes increased (higher Q factors). As shown in Eq. (4.3) smaller beam spot sizes increase the susceptibility to thermal lensing. This is the main reason why diamond is the only bulk material to demonstrate appreciable CW Stokes powers in an external cavity architecture [36, 81]. The reduced Raman gain per pass, and hence increased number of cavity round trips, increases the influence of intracavity loss and birefringence. Absorption due to high nitrogen content severely degrades efficiency [143] and birefringence leads to Stokes polarisation behaviour dependant on crystal position [117].

Transitioning to shorter pulses introduces a different set of challenges. As cavity round trip times approach the pulse duration, there is reduced overlap between the pump pulse and the build up of the Stokes photons in the cavity. Maintaining the temporal overlap requires synchronous pumping, where the pump repetition rate matches the cavity round trip time. Slight detuning of the cavity round trip time can lead to increased compression of the Stokes pulse duration [71]. Pulse durations approaching

the phonon lifetime (7 ps in diamond) reduce the effective g_R as the Raman interaction is no longer in the steady state regime.

Initial demonstrations of picosecond visible [71] and UV [82] DRLs have been followed by a 1.064 μm pumped DRL with 59% first Stokes and 21% second Stokes conversion efficiency [169]. The second Stokes demonstrated similar behaviour to that described in Section 4.3, where minimal cavity feedback is required to operate efficiently. Recently, DRLs have progressed to the femtosecond regime. 194 fs pulses from a Ti:sapphire pump laser generated 362 fs first Stokes pulses, which were compressed to 65 fs in an external prism compressor [83].

4.5.3 Wavelength

The broad transparency of diamond invites consideration of DRLs across many spectral bands. Initial research using CVD diamond was in the visible, where g_R is high. Q-switched [69] and modelocked [71] 0.532 μm pump sources were efficiently converted to 0.573 μm . UV DRLs have been demonstrated in the deep UV (0.273 μm) where operation is complicated by two-photon absorption and an unresolved UV-induced damage mechanism to the diamond [82]. Wavelengths longer than 1.6 μm [157] have not been investigated. Adapting designs to longer wavelengths and into the mid-IR is the subject of the following chapters.

4.6 Chapter summary

This chapter has investigated two 1.064 μm pumped DRLs configured for generating first and second Stokes wavelengths. Both wavelengths provide a large increase in maximum permissible eye exposures and are therefore attractive options for conversion of high power 1 μm lasers to less hazardous wavelengths for lidar and remote sensing applications. Each laser demonstrated over 70% quantum conversion efficiency at power levels of approximately 2 W. These efficiencies are slightly higher than other high performing Raman crystals and commensurate with external-cavity pumped OPOs. It was found that the optimisation of output coupling is markedly different for the two lasers.

For the second Stokes laser, the coupling of the pump with two Stokes wavelengths necessitates reducing the second Stokes intracavity intensity to allow efficient power transfer from the pump to the second Stokes output. As a result, the optimal output coupling is much higher for the second Stokes laser. No thermal effects were observed in either laser and beam qualities remained near diffraction limited. A simplified analysis suggests that output powers above 1 kW are feasible with similar cavity architectures, which is significantly higher than obtainable with other Raman crystals.

4.6.1 Publications arising from the work in this chapter

Peer reviewed journal articles

Sabella, A., Piper, J. A., and Mildren, R. P., “1240 nm diamond Raman laser operating near the quantum limit”, *Optics letters*, **35**(23), 3874-3876, (2010).

Sabella, A., Piper, J. A., and Mildren, R. P., “Efficient conversion of a 1.064 m Nd: YAG laser to the eye-safe region using a diamond Raman laser”, *Optics express*, **19**(23), 23554-23560, (2011).

Book chapter

Mildren, R. P., Sabella, A., Kitzler, O., Spence, D. J., and McKay, A. M., “Diamond Raman laser design and performance”, *Optical Engineering of Diamond*, 239-276, (2013).

Conference presentations

Sabella, A., Piper, J. A., and Mildren, R. P., “84% slope efficiency 1240 nm diamond Raman laser”, at Europhoton, Hamburg, Germany, (2010). *Oral Presentation*

Sabella, A., Piper, J. A., and Mildren, R. P., “Efficient diamond Raman lasers operating at 1240 nm and 1485 nm”, at AIP congress, Melbourne, Australia, (2010). *Oral Presentation*

Sabella, A., Piper, J. A., and Mildren, R. P., “Efficient 1064 nm conversion to the eye-safe region using an external cavity diamond Raman laser”, at CLEO PacRim, Sydney, Australia, (2011). *Oral Presentation*

5

Mid-IR Raman gain coefficient of diamond

In extending the operation of DRLs to longer wavelengths, the expected decrease in g_R makes Raman laser design more challenging. The resulting increases in intensities required to achieve laser threshold narrow the gap between the laser and damage thresholds and thus reduce the maximum achievable conversion efficiency. An accurate knowledge of g_R becomes crucial to modelling and optimisation. Chapter 2 discussed several limitations of reported values and although extrapolation of near-IR values provides an indication of the expected mid-IR values, the uncertainty is large. As can be seen from Fig. 5.1, the projected mid-IR values of g_R differ by approximately a factor of five.

This chapter aims to increase the accuracy of our knowledge of g_R at wavelengths in the mid-IR. Potential errors resulting from mode beating when using multi-longitudinal-mode lasers are examined in detail and used to enhance the accuracy of the pump-probe

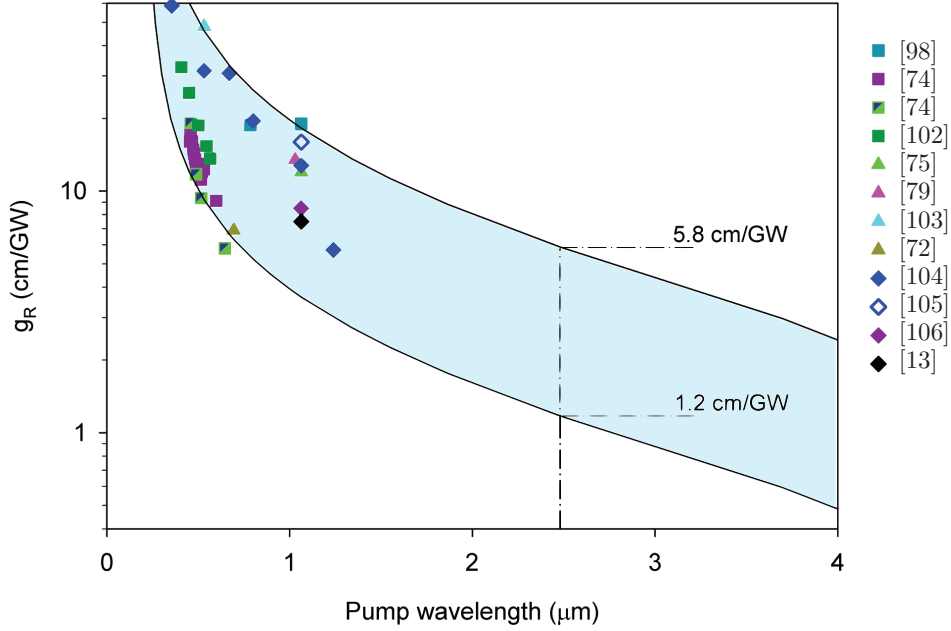


FIGURE 5.1: Extrapolation of near-IR g_R measurements for $\langle 100 \rangle$ pump polarisation. The boundaries of the shaded area are defined by scaling Eq. (2.3) to encompass the reported data.

technique. An alternative method is also developed based on four-wave-mixing. This novel technique potentially offers improved accuracy by removing the requirements to accurately characterise the beam spatial, spectral and temporal properties.

5.1 Measurement techniques for g_R

Methods for determining g_R are based on spontaneous and stimulated Raman scattering. Measurements of spontaneous Raman scattering cross sections require accurate accounting of collected light and accuracies better than a few tens of percent are challenging. Stimulated Raman scattering measurements of g_R are a more direct approach and are based on examining the growth of Stokes beam from an initial seed or from a spontaneous seed.

Prior to the onset of significant depletion of the pump, the amplification of Stokes light within a lossless Raman medium is exponential for monochromatic beams. As

derived in Appendix A, the calculated Stokes output after propagating a distance L through a Raman material is given by

$$I_S(L) = I_S(0)e^{g_R I_P L} \quad (5.1)$$

where I_S and I_P are the Stokes and pump intensities. $I_S(0)$ is the initial seed intensity at the start of the Raman medium. Equation (5.1) forms the basis for the SRS threshold and pump-probe methods for measuring g_R .

5.1.1 SRS threshold technique

The SRS threshold method involves focussing a high-peak-intensity pump laser into the material of interest and measuring the intensity required to obtain a Stokes intensity 1% of the pump. The Stokes signal grows from amplified spontaneously scattered photons and, assuming a spontaneous scattering rate for diamond of the order of 10^{-14} [4], an amplification factor of 10^{12} is required. Solving Eq. (5.1), this corresponds to $g_R I_P L = 27.6$, which is similar to the $g_R I_P L = 25$ rule of thumb used for determining g_R from threshold intensities [109, 110]. The extremely large degree of amplification leads to measurements that are very sensitive to any unwanted feedback, such as facet reflections. Numerical modelling indicates that introducing just 0.1% feedback on a 1 mm sample will reduce the SRS threshold by a factor of two.

The spatial and temporal properties of the pump laser also need to be well known to accurately calculate I_P . To remove some of the experimental uncertainties, the threshold intensity is often compared to a known material and a relative g_R value is derived. A concern with this approach is that comparisons often cascade over several materials, leading to cumulative errors. For example, the diamond g_R measurement in [75] was made relative to a $\text{C}_{15}\text{H}_{19}\text{N}_3\text{O}_2$ crystal, which in turn was measured against a lead tungstate crystal [170].

A further drawback of this technique is that the required pump intensities are typically very high and potentially exceed the damage threshold of the Raman crystal. The required pump intensity for a 1cm crystal is of the order of $25/g_R$ GW/cm² which

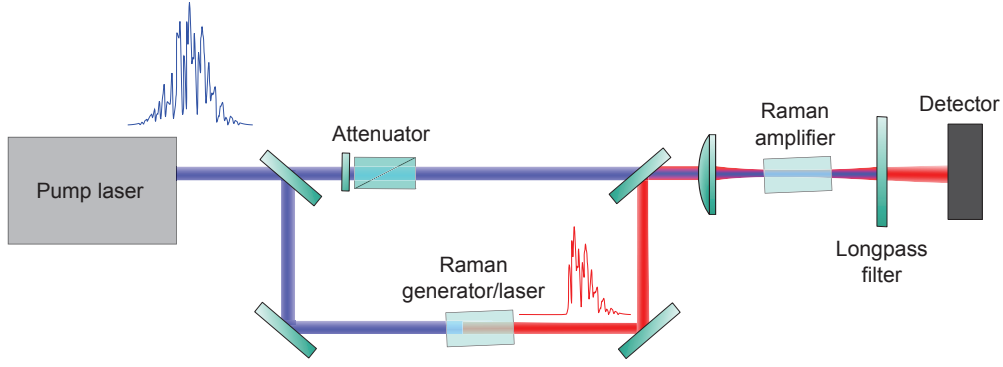


FIGURE 5.2: A standard configuration for measuring g_R using the pump-probe technique.

corresponds to multiple GW/cm^2 for most Raman crystals. Savitskii et al. were unable to measure the g_R at wavelengths longer than $1.450\text{ }\mu\text{m}$ using the threshold technique due to damage of the crystal (8 ns pulses) [104]. This technique cannot be applied in the mid-IR using the available nanosecond laser source.

5.1.2 Pump-probe technique

The pump-probe technique, a standard configuration of which is shown in Fig. 5.2, records the small signal amplification of a probe source at the Stokes wavelength as the pump intensity is increased. In this case $I_S(0)$ is known and the probe is typically only amplified by a few tens of percent, compared to $\sim e^{25}$ in the previous case. This makes the measurement much less susceptible to reflections. The required intensity of the pump beam is also much lower, allowing the measurement of smaller values of g_R or the use of thinner crystal samples. The main disadvantage is the requirement for two laser wavelengths, separated by the Raman frequency of the material.

Accurate knowledge of the spectral, spatial and temporal properties of both lasers is required. In a practical pump-probe experiment, the spatial and temporal profiles of the Stokes and pump beams are unlikely to be matched. To account for the actual overlap of the two beams an effective area, A_{eff} , and pulse width, t_{eff} , are given by [171].

$$A_{eff} = \frac{\int I_P dA \int I_S(0) dA}{\int I_S(0) I_P dA}, \quad t_{eff} = \frac{\int I_P dt \int I_S(0) dt}{\int I_S(0) I_P dt} \quad (5.2)$$

Calculating the integrals numerically using measured profiles is particularly important when the pump and probe beams are not spatially and temporally Gaussian. By inserting A_{eff} and t_{eff} into Eq. (5.1), g_R can now be expressed in terms of pump and probe pulse energies, J_P and J_S , respectively.

$$g_R = \frac{\ln\left(\frac{J_S(L)}{J_S(0)}\right)}{J_P} \frac{A_{eff} t_{eff}}{L} \quad (5.3)$$

Several published pump-probe measurements [104, 171–173] assume a small factor of amplification, with negligible pump depletion, and use the approximation $e^x \approx 1 + x$ to linearise Eq. (5.1). The linear approximation of Eq. (5.1) leads to significant errors (>10%) for amplification factors as small as 20%. This effect may have led to reported g_R values being inflated by 10% [172] and up to 18% [104].

5.1.3 Pump-probe measurements with multi-mode beams

Lasers with multiple longitudinal modes contain fluctuations in the phase (FM noise) and amplitude (AM noise) due to mode beating. A broader linewidth laser will have higher frequency (shorter duration) fluctuations.

Ideally, pump-probe measurements are performed using single longitudinal mode (SLM) lasers, since this avoids the effects of amplitude and phase fluctuations on gain. However, SLM sources are often complex and expensive and it is generally much more convenient to perform experiments with more readily available multi-longitudinal-mode lasers. In addition, the most common method of generating a probe beam is to build a Raman laser from a second sample of the Raman material under test, e.g. [13, 104, 105, 171]. Even if the pump is SLM, it is unlikely the generated probe will be, unless line-selective elements or cavity stabilisation is used to restrict the number of modes.

In principal, the multi-mode lasers may be CW, Q-switched or modelocked. Unless the average power exceeds several hundred Watts, the single pass amplification from CW beams is too low to accurately measure over typical crystal lengths. Modelocked lasers have the advantage of having a well defined pulse structure and high peak power,

but if the laser pulse durations are not longer than the phonon decay time, T_2 , the Raman amplification will be reduced. Q-switched lasers have suitable peak powers and pulse durations, but often suffer from strong phase and amplitude noise from mode beating. The remainder of this section considers the influence of mode beating on pump probe measurements.

5.1.3.1 Linewidth correction factor

It is often assumed, although not always correctly, that for pump and/or probe linewidths similar to, or larger than, the Raman linewidth, the measured Raman gain coefficient, g_{meas} , is reduced according to a correction factor, $g_{meas} = \eta g_R$. A calculation of η is presented in [174]

$$\eta = \frac{g_{meas}}{g_R} = \frac{\Delta\omega_R}{\Delta\omega_R + \Delta\omega_P + \Delta\omega_S} \quad (5.4)$$

where $\Delta\omega_R$, $\Delta\omega_P$ and $\Delta\omega_S$ are the FWHM of the Raman profile, pump and probe beams, respectively. Several authors have used variants of this equation to scale g_{meas} [99, 104, 171]. Equation (5.4) is based on the assumption that the lineshape of the Raman, pump and probe spectral profiles are Lorentzian. This is often invalid for the pump and probe and a general formula involving the convolution of arbitrary spectral profiles is more appropriate [175],

$$\eta = \int [R(\omega) \otimes P(\omega)] S(\omega) d\omega \quad (5.5)$$

where $S(\omega)$, $P(\omega)$ and $R(\omega)$ are the Stokes, pump and Raman spectra, respectively. Equation (5.5) reduces to Eq. (5.4) in the case of Lorentzian profiles. To highlight the importance of considering actual spectral profiles, the difference in η approaches a factor of two when comparing Lorentzian and Gaussian laser profiles with the same FWHM. This is due to the comparatively larger area in the wings of the Lorentzian profile. The actual lineshape of the laser spectra are typically not reported with published g_R results. Note that it is important here to distinguish between amplitude and phase noise. The reduction in Raman gain accounted for in Eqs. (5.4) and (5.5) is the result of linewidth broadening due to phase fluctuations.

5.1.3.2 The validity of the linewidth correction factor - correlations

On the basis of the linewidth correction factor, it might be expected that broadening the pump linewidth will increase the threshold intensity for SRS. The validity of η however, depends on the more subtle assumption that the fine structure in the electric fields, arising from mode beating in the pump and probe beams, is uncorrelated.

Correlations between the pump and probe structure result in Raman amplifications in excess of what otherwise would have been predicted. Early Raman experiments showed SRS thresholds were uniform for a range of pump to Raman linewidth ratios. Bocherov et al. observed a constant SRS threshold for a liquid nitrogen Raman generator despite the pump laser linewidth changing by five orders of magnitude [176]. Trutna et al. demonstrated that the threshold energy for a hydrogen Raman generator was similar for pumping with a 0.003 cm^{-1} or 0.5 cm^{-1} linewidth Nd:YAG laser [177]. Thresholds for both pump linewidths followed the same trend as the gas pressure was varied to change the Raman linewidth from 0.008 cm^{-1} to 0.02 cm^{-1} . The independence of threshold with pump linewidth arises from the pump beam driving the phase of very weak initial Stokes noise into correlation well before threshold is reached. Correlations in phase between the pump and Stokes beams increase the observed gain up to the SLM value [178]. Experimental verification of such enhancement was neatly demonstrated by Stappaerts et al. using a pump-probe experiment similar in design to Fig. 5.2, but with the addition of a variable delay line [179]. Diverting a fraction of the pump to generate the probe in a hydrogen Raman generator created a pump-probe pair with correlating phase structure. When the pump and probe path lengths were matched, g_{meas} was close to the SLM value for both 0.86 cm^{-1} and 0.33 cm^{-1} pump linewidths. Delaying the probe relative to the pump reduced the small signal Raman amplification by up to 90%. The broader linewidth pump tolerated less path length mismatch due to the more rapid variations in the phase structure. For large amplification factors however, the pump imparted its phase structure on the probe and the measured gain increased to near monochromatic values, regardless of the path mismatch.

The experiments of Trutna et al. and Stappaerts et al. in the previous paragraph were conducted using hydrogen, which has a narrow Raman linewidth (0.013 cm^{-1} to

0.13 cm^{-1} for gas pressures from 8 atm to 60 atm, respectively [177]). The bandwidth of the Raman response was smaller than the pump laser and in this case only phase noise is important [180]. In contrast, for Raman linewidths similar to, or broader than, the laser field linewidths, as is generally the case with most crystal Raman lasers, correlations in amplitude fluctuations are expected to significantly affect the Raman gain. In the temporal picture, a broader Raman linewidth translates into the phonon field more rapidly reaching its equilibrium value and as such a greater proportion of amplitude variations are in the steady state regime. As a result, amplification factors for correlated amplitude spikes increase above the SLM value [181–183]. In such cases the application of a linewidth correction factor only exacerbates the error in the pump-probe measurement.

Correlations are only a concern if the fine structure is not resolved and included in Eq. (5.2). Resolving the structure is generally challenging as the time-scale of the of the modulation is usually too fast to be directly captured by photodetectors. For a Lorentzian frequency distribution with a FWHM linewidth of $\Delta\omega_P$, the time-scale of the fluctuations is of the order of $2/\Delta\omega_P$ which, for example, corresponds to 10 ps (100 GHz) for a typical 1 cm^{-1} linewidth Nd:YAG laser.

5.2 Improving the pump-probe technique

5.2.1 Modelling of multi-longitudinal-mode Raman amplification

Numeric modelling of multi-mode Raman interactions overcomes some of the restrictions in studying probe amplification caused by the inability to directly measure the high frequency intensity structure. There are several approaches to modelling broadband Raman amplification. In essence, the difference between the models is whether the pump and probe lasers contain only phase noise or both phase and amplitude noise.

Several authors have used a ‘phase diffusion’ model where the pump laser linewidth is modelled by continuous variations in phase, with no change in amplitude [178, 184].

Whilst this does predict the phase locking of the pump and probe at high gains to produce thresholds independent of laser bandwidth, amplitude noise is not included. As a result the model is not capable of predicting the enhancement of gain in excess of the SLM value that occurs with correlated amplitude structure when $\Delta\omega_R \gtrsim \Delta\omega_P$.

Chaotic models describing broadband Raman interactions include both phase and amplitude noise [185, 186], but the assumption that $\Delta\omega_R \gg \Delta\omega_P$ is not applicable here.

Considering the pump and Stokes spectra as a series of longitudinal modes with randomly distributed phases is an alternative approach that captures both phase and amplitude noise of a pump laser [177, 180, 181, 187–190] and is suitable for the expected experimental conditions.

5.2.1.1 Model Description

The electric field of the probe and pump are described by sums of monochromatic modes with initial phases, ϕ_m and ϕ_n , and longitudinal mode spacing, Ω .

$$\begin{aligned} E_S(0) &= \sum_m S_m e^{i(m\Omega t + \phi_m)} \\ E_P(0) &= \sum_n P_n e^{i(n\Omega t + \phi_n)} \end{aligned} \quad (5.6)$$

S_m and P_n are the slowly varying complex amplitudes of the probe and pump beam, respectively. The interference between the randomly phased modes causes intensity and phase fluctuations on timescales shorter than the pump cavity round trip time, $2\pi/\Omega$. It is assumed that the individual modes vary slowly and thus the intensity pattern repeats every cavity round trip. With multiple longitudinal modes present, there are numerous routes to the excitation of a given Stokes mode. Considering the SRS as a FWM process, the rate of change for a given Stokes mode is

$$\frac{\partial S_B}{\partial z} \propto P_B(S_A P_A^*) \cdot R^E(\omega) \quad (5.7)$$

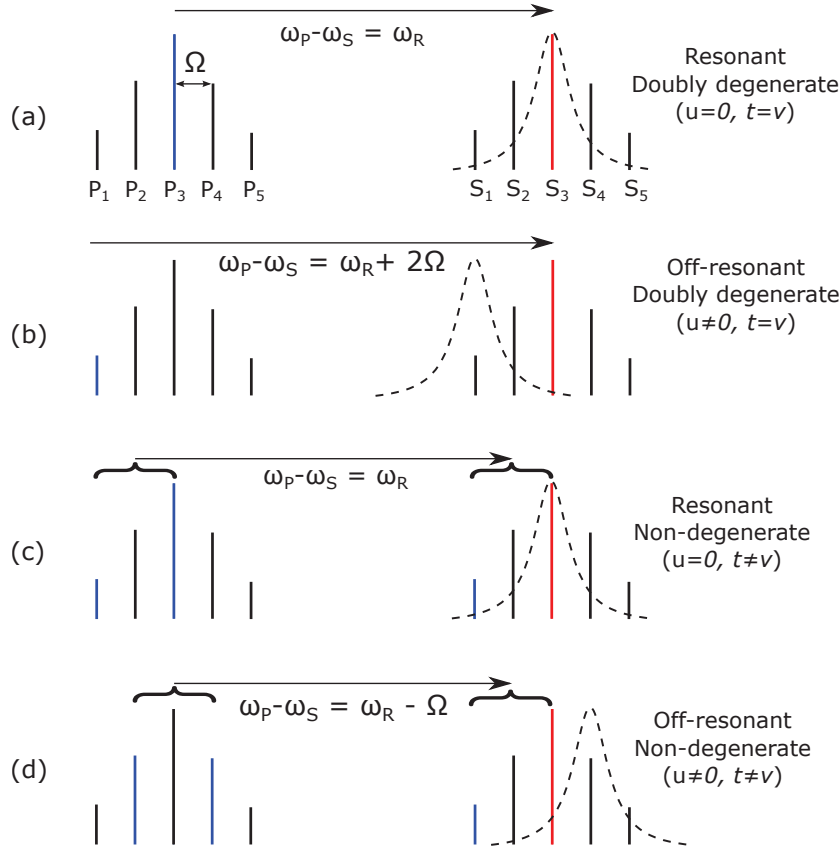


FIGURE 5.3: Four of the possible 25 routes for generating light at Stokes mode S_3 from five pump longitudinal modes.

where P_A and P_B are the electric fields of two pump modes and S_A and S_B are two Stokes modes. The pairs of modes may be degenerate (i.e. $P_A = P_B$ and/or $S_A = S_B$). $R^E(\omega)$ describes the Raman response when the frequency difference between the interacting electric fields is detuned from the Raman resonance.

The first route for generation of a particular Stokes mode is the resonant, doubly degenerate case ($P_A = P_B$, $S_A = S_B$, $\omega_P - \omega_S = \omega_R$), which is the trivial case corresponding to SLM pumping. Here a single pump mode interacts with a single Stokes mode that is separated by the Raman frequency (Fig. 5.3(a)). If the frequency separation between the pump mode and the Stokes mode under consideration is not equal to the Raman frequency, the induced vibration is detuned and the Raman interaction is weakened according to $R^E(\omega)$ (Fig. 5.3(b)). From a FWM perspective, the pump and Stokes are both doubly degenerate in the previous two examples. Mixing of

two different pump modes with an additional Stokes mode may also excite the Stokes mode under consideration. Just as with the degenerate cases, the interactions are either resonant (Fig. 5.3(c)), or off-resonant (Fig. 5.3(d)) with the Raman frequency. The combined effect on a given Stokes mode, S_t , from all the previously considered interactions is captured in the following equation [179, 187]

$$\frac{\partial S_t}{\partial z} = c\epsilon_0 g_R \sum_u \sum_v P_{t-u}(S_v P_{v-u}^*) \frac{(\Delta\omega_R)}{\Delta\omega_R - iu\Omega} e^{i(k_{P(t-u)} - k_{P(v-u)} + k_{S(v)} - k_{S(t)})z} \quad (5.8)$$

Similarly, the evolution of each pump longitudinal mode is described by

$$\frac{\partial P_t}{\partial z} = -c\epsilon_0 g_R \frac{\omega_P}{\omega_S} \sum_u \sum_v S_{t-u}(P_v S_{v-u}^*) \frac{(\Delta\omega_R)}{\Delta\omega_R - iu\Omega} e^{i(k_{S(t-u)} - k_{S(v-u)} + k_{P(v)} - k_{P(t)})z} \quad (5.9)$$

The calculations are performed with t , u and v spanning the number of modes modelled. When $u \neq 0$ the interaction is off-resonant and the multiplication is reduced by the Raman profile, $(\Delta\omega_R)/(\Delta\omega_R - iu\Omega)$, which is a Lorentzian when converted from electric field amplitude to intensity. The final terms in Eqs. (5.8) and (5.9), in the form of $e^{i(\Delta k)z}$, describe the effect of group velocity dispersion on the travelling pump and Stokes waves. If dispersion is strong, walk-off occurs between amplitude and phase features in the pump and Stokes beams. In particular, correlations imparted on the probe by the pump desynchronise and reduce the effective gain. The approximate propagation length before which the structure in the pump and probe are no longer overlapped is given by [188]

$$l_{dephase} = \frac{2}{\Delta\omega_P} \left(\frac{c}{n_P - n_S} \right) \quad (5.10)$$

where n_P and n_S are the group refractive indices of the pump and Stokes, respectively. For the experimental conditions considered in this chapter, the pump and probe wavelengths of 1.86 μm and 2.48 μm have maximum linewidths of 3 cm^{-1} , yielding a dephasing length in diamond greater than 20 cm. As the crystals studied are less than 1 cm long the dispersion component of Eqs. (5.8) and (5.9) is not implemented, to reduce computation time. If the pump and Stokes beams are non-collinear, such as in

a Raman beam combination experiment, then the group velocity mismatch is larger and dispersion may need to be considered. For counter-propagating beams the dephasing length is short (200 μm for the previous example) and only the doubly degenerate modal interactions generate significant contributions (i.e. Fig. 5.3(a),(b)).

Many prior applications of the longitudinal mode model studied hydrogen Raman lasers [177, 180, 187–190] and care must be taken when analysing the outcomes in the context of diamond. To simplify the mathematical analysis the authors assume that the pump laser longitudinal mode spacing is greater than the Raman linewidth ($\Omega > \Delta\omega_R$). This assumption is partially valid in the context of hydrogen gas Raman lasers at low pressures, where the Raman linewidth is similar in magnitude to the longitudinal mode spacing of the flashlamp pumped Nd:YAG lasers used. In this case each pump longitudinal mode forms a pair with a corresponding Stokes mode, with minimal off-resonance contribution from other pump modes. This removes the sum over ‘ u ’ from Eqs. (5.8) and (5.9) and allows several analytical relationships to be derived. The Raman linewidth of diamond is 10 to 100 times broader than hydrogen, depending on the gas pressure, and typically $\Delta\omega_R \gg \Omega$. This dictates that the off-resonant contributions must be considered and a full numerical calculation is required.

5.2.1.2 Modelling results

The effect of multi-longitudinal-mode beams on pump-probe measurements was investigated for the cases where the pump and probe linewidths ($\Delta\omega_{P,S} = 1 \text{ cm}^{-1}$) are broader, equal to and narrower than the Raman linewidth ($\Delta\omega_R = 0.01, 1$ and 10 cm^{-1} , respectively). The pump and probe lasers have 71 longitudinal modes with $\Omega = 0.083 \text{ cm}^{-1}$ under a Lorentzian spectral profile (Fig. 5.4(a)). The phases of each of the pump longitudinal modes were randomly generated. The phases of the probe were either randomly generated, or set to be the same as the pump, depending on whether the run was for uncorrelated or correlated beams, respectively. The average initial intensity of the pump beam was 100 times that of the probe. An example of an uncorrelated pump and probe intensity profile for one cavity round trip is shown in Fig. 5.4(b) and as expected the minimum width of the amplitude spikes is approximated by $2/\Delta\omega_{P,S}$.

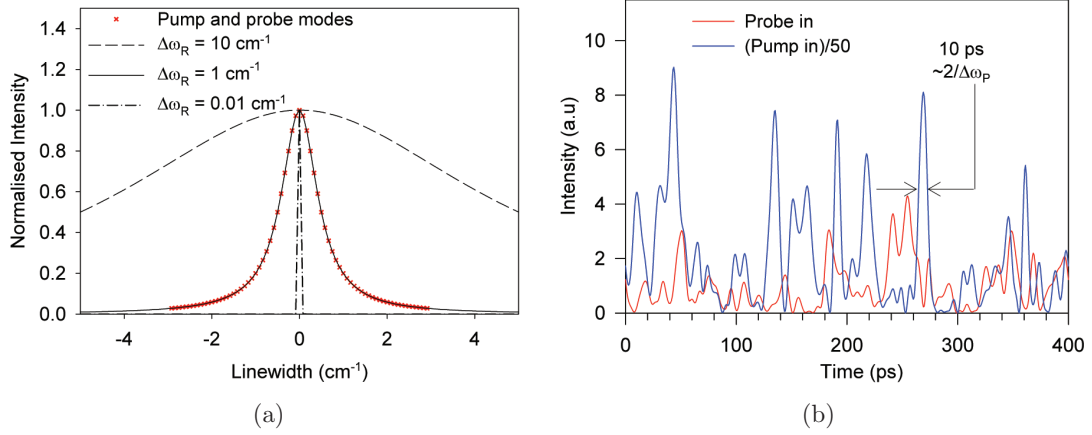


FIGURE 5.4: (a) Normalised Raman and laser spectral profiles. (b) An example of temporal pump and probe intensity profiles for uncorrelated beams with spectra as shown in (a).

The relative linewidths of the Raman and laser spectra determine the gain response to the instantaneous intensity structure. Figure 5.5 shows that when $\Delta\omega_R \ll \Delta\omega_P$ and for initially correlated beams, the amplification factor is constant across the probe structure. Broadening the Raman linewidth decreases the steady state phonon field response time and the amplification of the probe becomes proportional to the instantaneous pump and probe intensity. Subsequently, the peaks in Fig. 5.5 are amplified exponentially more than the troughs and the probe becomes an exaggerated copy of the pump.

For the case of an initially uncorrelated probe, correlations develop as the stronger pump defines the amplification of the probe. Figure 5.6(a) shows the amplified probe structure more closely resembling the pump structure for both narrow and broad Raman linewidths. The three largest peaks in the pump intensity are highlighted in the figure as examples. Again, when $\Delta\omega_R \gtrsim \Delta\omega_{P,S}$, enhanced amplification of high intensity features, such as the spike near 40 ps in Fig. 5.6(a), result in a distorted copy of the pump.

The strong dependence of instantaneous Raman gain to the size and relative position of high intensity features in the pump and probe produces noise in the amplified

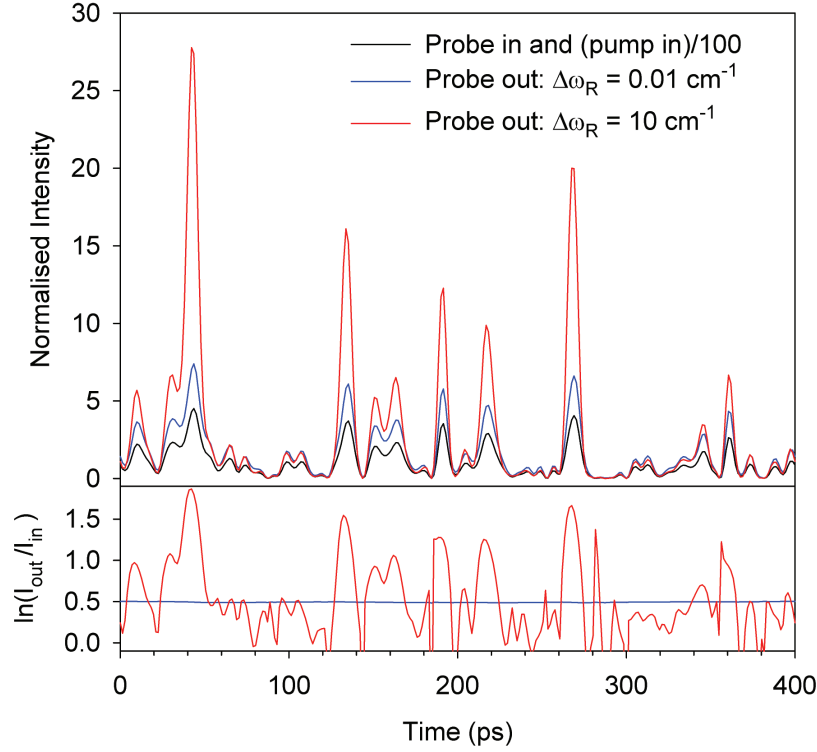


FIGURE 5.5: Gain dynamics for correlated beams: (top) Intensity of the probe temporal structure after amplification for $\Delta\omega_R = 0.01 \text{ cm}^{-1}$ and $\Delta\omega_R = 10 \text{ cm}^{-1}$. The input pump and probe intensities are 1 and 0.01 GW/cm, respectively, g_R is 5 cm/GW and the crystal length 0.1 cm (i.e. $g_R I_{Pz} = 0.5$). The pump and probe are initially correlated and thus the input pump perfectly overlays the probe after scaling. Traces are normalised to the average input probe intensity. (bottom) Instantaneous amplification of the probe.

beam. Even when the pump and probe are fully correlated, there is variation in the amplification, as shown in Fig. 5.6(b). The two outlying runs that have the highest initial slopes represent cases that contain a particularly large intensity spike (i.e. accidental partial mode-locking). The spread in the traces is greater for the uncorrelated runs due to the range of spike sizes coupled with the varying overlap of the intensity spikes between the pump and probe. There is substantial literature on the noise statistics of SRS [191, 192] which is not explored in any depth here. To enable comparisons with experimental observations, the modelled data contained in Figs. 5.7, 5.8, 5.11, 5.13(b), 5.14 and 5.15 are averaged over at least 20 runs with different randomly generated initial phases.

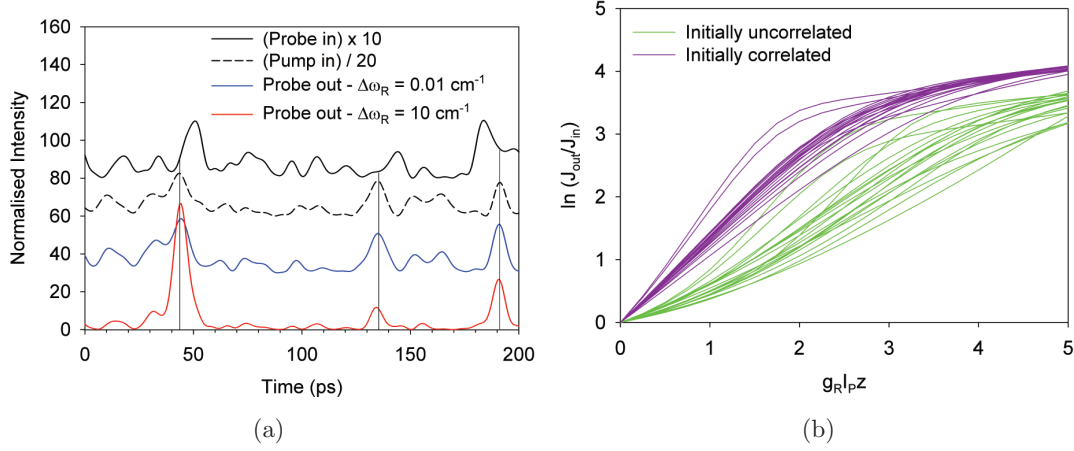


FIGURE 5.6: (a) Gain dynamics for uncorrelated beams - Intensity structure of the probe after amplification by an uncorrelated pump. Conditions are the same as Fig. 5.5, except that the crystal length is 1.2 cm. A longer crystal length was used to more clearly show the developing correlations of the probe. Traces have been scaled and offset for clarity. (b) 20 correlated and 20 uncorrelated amplification calculations where the starting longitudinal mode phases are randomly generated for each run. The pump, probe and Raman linewidths are all 1 cm^{-1} .

Similar to a pump-probe experiment, the Raman amplification for three material linewidths is displayed in Fig. 5.7. Curves are calculated for initially correlated and uncorrelated pump and probe. The model includes pump depletion, which leads to a roll-over above 20 times amplification ($\ln(J_{out}/J_{in}) > 3$). The amplification required to induce roll-over is proportional to the ratio of the initial pump and probe pulse energies. When the pump and probe are correlated beams and $\Delta\omega_R < \Delta\omega_{P,S}$, the amplification is equal to the SLM gain until pump saturation. For uncorrelated beams, phase noise suppresses the initial small-signal gain to less than 2% of the SLM value. As correlations develop during amplification the instantaneous gain (i.e. the slope) increases towards the SLM value. These results are consistent with the literature on hydrogen Raman lasers, but are not relevant for pump probe experiments with crystalline Raman materials. In the case where $\Delta\omega_R \gtrsim \Delta\omega_{P,S}$ a large proportion of the intensity variations are in the steady-state regime and the gain for correlated beams initially exceeds the SLM value. Subsequent amplification accentuates the probe intensity spikes leading to even higher gain, until pump depletion intervenes. Conversely

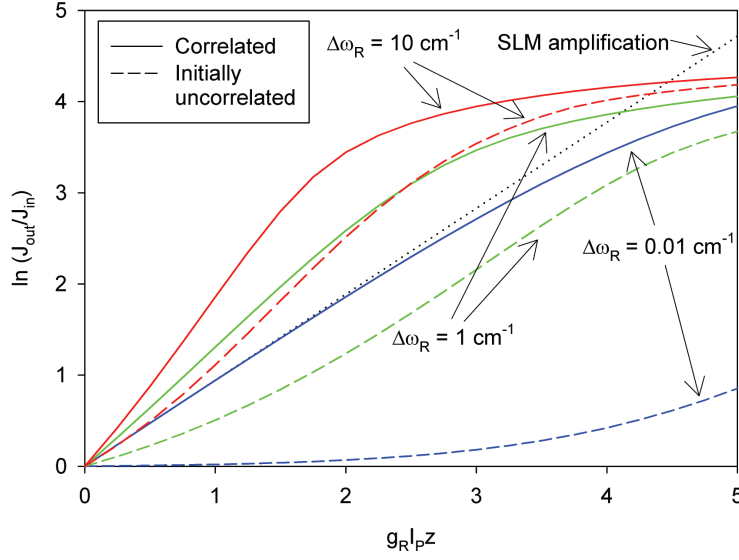


FIGURE 5.7: Amplification of a probe beam by correlated and uncorrelated pumps for three different $\Delta\omega_R$. The dotted line is the SLM amplification with no pump depletion. The laser linewidths are both 1 cm^{-1} .

for uncorrelated beams, phase noise suppresses the small-signal gain proportional to η . The subsequent development of correlations during amplification however increases the instantaneous gain beyond the SLM value.

The slope of the small signal amplification region near the origin is the most relevant to pump-probe g_R measurements. It is also with respect to this region that the linewidth correction factors are applied (Eqs. (5.4) and (5.5)). Where the pump and probe are initially correlated, the amplification is equal to or greater than the SLM case. Thus the use of linewidth correction factors will only exacerbate the error in the measurement. This leaves the application of a linewidth correction factor to experiments where the pump and probe are initially uncorrelated. Figure 5.8 shows the measured g_R relative to the SLM case as amplification is increased. Also shown is the calculated gain after Eq. (5.5) has been used to scale the values, to compensate for the broad linewidths. The corrected g_R is approximately equal to the SLM case as desired, but only for small levels of amplification. As amplification increases, correlations develop and the linewidth corrected gain overestimates the SLM value.

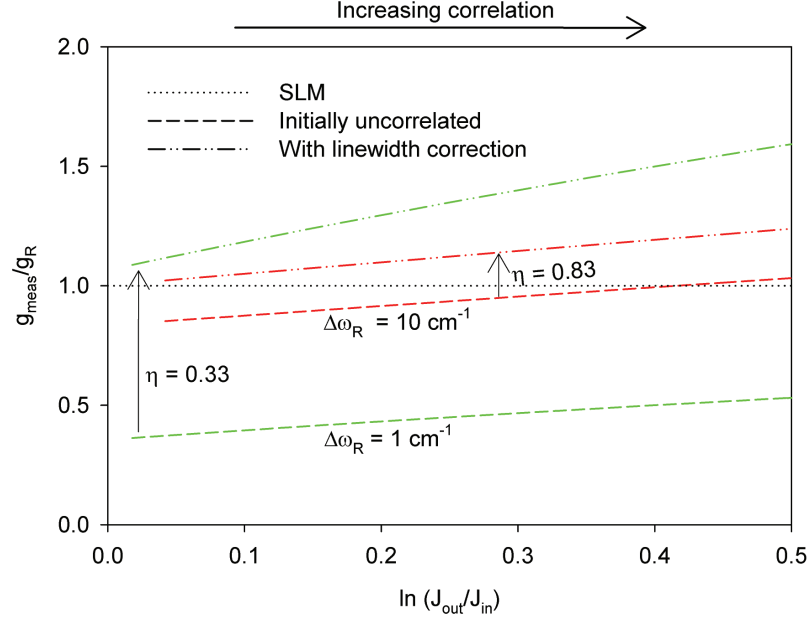


FIGURE 5.8: The Raman gain coefficient that would be measured normalised to the SLM value as a function of probe amplification. The traces are obtained by taking a subset of the uncorrelated data in Fig. 5.7, up to a given $\ln(J_{out}/J_{in})$ value, and calculating the line of best fit. The dot-dashed lines include a linewidth correction factor.

These results imply that amplification factors no greater than 10-20% should be used in multi-longitudinal-mode pump-probe measurements, particularly when the pump linewidth is not significantly narrower than the Raman linewidth. From an experimental perspective, only measuring small amplification factors may be challenging due to the inherent noise in multi-longitudinal-mode Raman amplification.

5.2.2 Broadband pump-probe experiment

The effect of correlations on pump-probe measurements was investigated by adjusting the initial correlation and laser linewidth of the pump and probe beams. The OPO laser developed for the mid-IR DRL experiments provided a convenient means of varying the pump-probe linewidth and correlation (Fig. 5.9), and details on the design are presented in Chapter 6 and Appendix C. Tuning the signal and idler frequency separation to match the Raman frequency of diamond generated the pump and probe beams. Given that a signal/idler photon pair are created from a common pump photon, a high

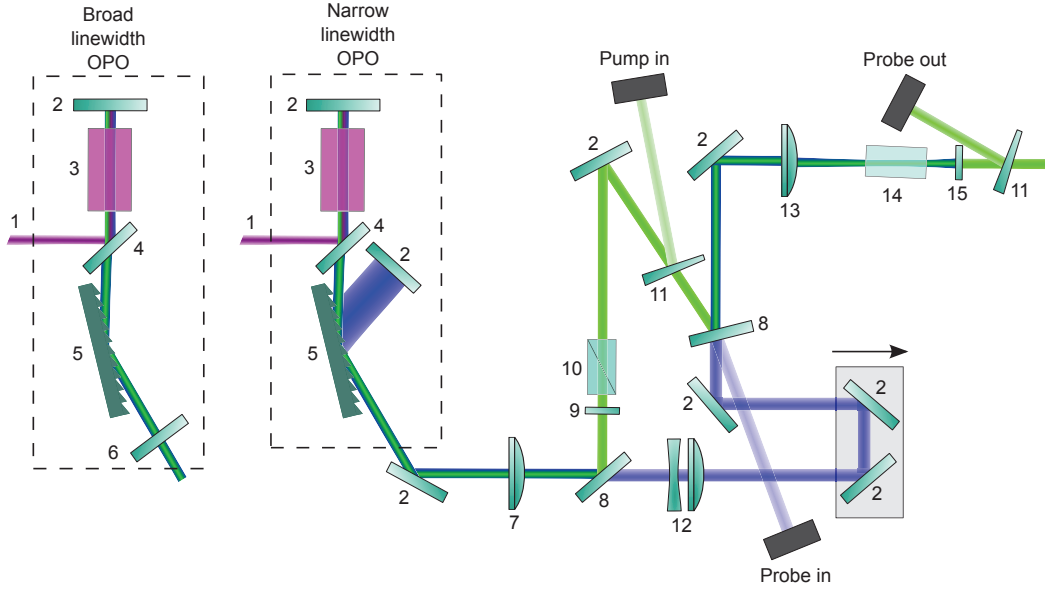


FIGURE 5.9: Layout for the pump-probe experiment. (1) Nd:YAG pump input, (2) HR mirror, (3) KTP crystal, (4),(8) dichroic mirrors, (5) diffraction grating, (6) output coupler, (7) collimating lens, (9) half-waveplate, (10) polariser, (11) wedge, (12) 2x telescope, (13) focussing lens (14) 8 mm diamond crystal, (15) 2.5 μm bandpass filters.

degree of correlation was expected. Adjusting the relative path length between the two wavelengths changed the degree of correlation in the diamond amplifier.

Blocking the light diffracted from the grating and inserting a broadly reflective output-coupling mirror in the OPO, switched the output linewidth from narrow ($\Delta\omega_{P,S} < \Delta\omega_R$) to broad ($\Delta\omega_{P,S} > \Delta\omega_R$). Representative spectral traces of the signal and idler for both configurations are displayed in Fig. 5.10. The approximate FWHM linewidths for the narrow and broad idler are 0.5 cm^{-1} and 3 cm^{-1} , respectively. Similarly, the narrow and broad signal linewidths are 1 cm^{-1} and 3 cm^{-1} .

A dichroic mirror split the signal and idler of the OPO into the pump and probe, respectively. The pump beam passed through a half-waveplate and polariser to make its polarisation parallel to the probe and simultaneously allow variable attenuation of the energy. The probe beam propagated through a delay line before recombining with the pump and focussing into the diamond sample. The effective area of the overlapping pump and probe spots was determined by numerical analysis of magnified images captured on a Pyrocam III camera. A_{eff} for the narrow and broad linewidth

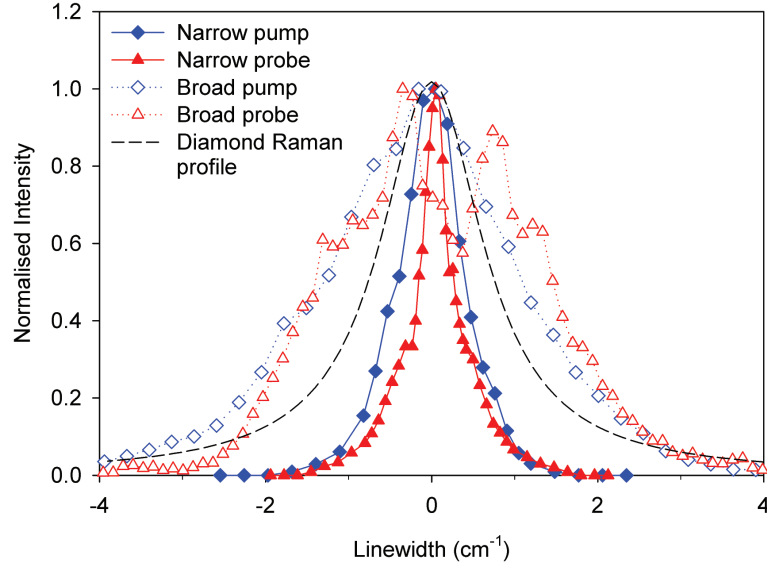


FIGURE 5.10: Representative linewidths of the OPO in narrowed and free-running operation. The broader, free-running traces are single-shot spectra, captured by imaging the monochromator output (Acton 2500 monochromator with 600 lines/mm grating) on a Pyrocam III camera (0.53 cm^{-1} instrument resolution). The linewidth narrowed traces are captured with a detector behind $20 \mu\text{m}$ monochromator slits (0.29 cm^{-1} instrument resolution) and each point is the averaged over >50 pulses. Further details are in Appendix C. The central wavelengths of the pump and probe are $1.864 \mu\text{m}$ and $2.480 \mu\text{m}$, respectively.

spots was $1.52 \times 10^{-4} \text{ cm}^2$ and $1.42 \times 10^{-4} \text{ cm}^2$, respectively. Translating the variable delay mirrors by 25 mm (50 mm change in path length), did not change the measured size of the focussed spots. Maximising the observed amplification of the probe in the diamond crystal confirmed a signal and idler frequency separation of ω_R . The pump and probe polarisation was aligned to the $[01\bar{1}]$ crystal axis and the crystal was tilted slightly to reduce the influence of Fresnel reflections. The pump and probe energy values were measured using PbS detectors (Thorlabs PDA30G). Calibration of the peak-recorded voltage against energy meter readings (Coherent J10MB-HE) confirmed a linear relationship.

In order to adapt the model in the previous section to the experiment, the pump and probe spectral profiles were set to have Gaussian profiles, with linewidths of 1 cm^{-1} and 0.5 cm^{-1} , respectively, for the narrow linewidth case, and 3 cm^{-1} each, for the broad linewidth case. Based on an OPO cavity length of 10 cm , the longitudinal mode spacing

for both beams is assumed to be 0.05 cm^{-1} . This is not an entirely valid assumption as the OPO signal is non-resonant and its spectral profile is the convolution of the resonant idler and the Nd:YAG pump laser. It will therefore contain additional spectral features with a spacing equal to the Nd:YAG laser. An estimated Nd:YAG laser cavity optical path length of 75 cm equates to a mode spacing of 0.0067 cm^{-1} . This corresponds to modelling over 1000 modes and impractical computational requirements, as the number of times Eqs. (5.8) and (5.9) are run is proportional to the number of modes cubed. Increasing the mode spacing, while decreasing the number of modes to keep the overall linewidth constant, decreases the round trip time, but has little impact on the duration of the phase and intensity features. As such, varying the modelled mode spacing did not change the average amplification significantly and for computational convenience a 0.05 cm^{-1} mode spacing was retained.

5.2.3 Broadband pump-probe results

5.2.3.1 Correlation measurement

Translating the delay line through the path matching condition confirmed the presence of correlations between the pump and probe. With the pump and probe average energies held constant (200 μJ and 11 μJ , respectively), Fig. 5.11 shows that there is a region of enhanced gain due to correlating structure in the electric field of the OPO signal and idler. Fitting $g_R = 3.5 \text{ cm/GW}$ gave excellent agreement between the narrow linewidth model and experimental data, suggesting Eqs. (5.8) and (5.9) are suitable.

Unlike the model predictions and published results [179, 190], the width of the enhanced region did not narrow with the broader linewidth pump and probe. In theory, the broader linewidth leads to higher frequency phase and amplitude fluctuations, which reduces the tolerable path mismatch before the electric field structure misaligns. An additional disagreement is in the magnitude of the Raman amplification for zero delay. The lower than expected experimental gain suggests that the correlation between the broad pump and probe is not perfect prior to entering the diamond crystal.

The difference between the expected and observed results arises from the method of

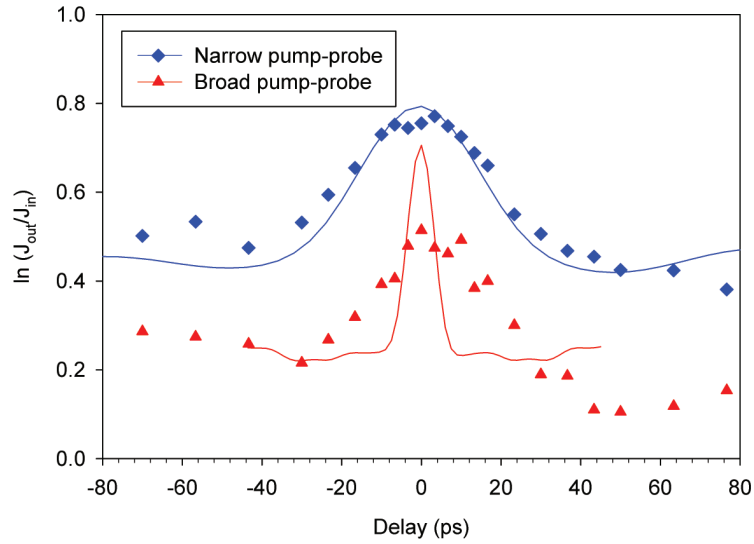


FIGURE 5.11: Measured (points) and modelled (lines) Raman amplification as the relative delay between the pump and probe is varied.

generating the pump and probe beams. Published examples generate the probe beam by Raman shifting a fraction of the pump beam [179, 190]. Any increase in the pump linewidth reduces the timescale of the temporal fluctuations which are subsequently mapped onto the probe beam. In the case here, the timescale of the fluctuations of the pump and probe is partially determined by the fluctuations of the Nd:YAG laser used to pump the OPO. Since obtaining direct measurements of the spectral and temporal fine structure of the pump and probe was not possible, the broadband nanosecond OPO model in the SNLO software package was used to provide some insight [193]. A $1.064\mu\text{m}$ input pulse with 0.8cm^{-1} linewidth and 0.0067cm^{-1} longitudinal mode spacing was injected into a model of a singly resonant KTP broadband OPO. Figure 5.12(a) shows the modelled Nd:YAG pump, signal and idler temporal structure for broadband operation. The signal and idler have rapidly oscillating components, but they are contained under a more slowly varying envelope corresponding to the longitudinal mode interference of the Nd:YAG laser. The timescale of the Nd:YAG oscillations is independent of the OPO linewidth and thus there is structure in the signal and idler intensity that is also independent of the linewidth. This provides an

explanation as to why the width of the observed correlation peak does not decrease for the broadband OPO. Correspondingly, the width of the calculated Nd:YAG self-correlation, shown in Fig. 5.12(b), is consistent with the observed correlation width in Fig. 5.11.

The alignment of the finer structure in the signal and idler did not produce the expected enhancement shown in Fig. 5.12(b) at zero delay. A proposed reason is that for a singly resonant OPO, not operating near threshold, some of the high frequency correlation is washed out. Figure 5.12(b) shows a reduction in the height of the sharp correlation peak with the addition of cavity mirrors to the simulation. Walk-off within the OPO crystal is a second proposed mechanism for washing out correlating fine structure. For the KTP crystal orientation used, the walk-off angle between the idler and the two other wavelengths is 42 mrad. This corresponds to a separation of 0.84 mm for a single pass through the 20 mm crystal. Given that the beam diameters are of the order of 1 mm, the spatial separation is a very large fraction of the total beam area. This will result in increasing degradation of correlation between the overlapping and non-overlapping regions. The spatial variation in correlation is well understood in the quantum optics domain where parametric generation is used to generate entangled signal/idler photon pairs [194, 195].

5.2.3.2 Probe amplification and g_R measurement

To demonstrate the potential pitfalls of performing g_R measurements with multi-longitudinal-mode beams, pump-probe readings were taken at combinations of high/low correlation (0 ps/60 ps delay) and narrow/broad linewidth. The average probe energy was 15 uJ and the pump was continuously varied up to 400 uJ by rotating a half-waveplate prior to a polariser.

Increasing noise in the raw data with larger amplification factors is evident in Fig. 5.13(a). Measurements of g_R are performed for small amplification factors, which avoids the high noise region. Reducing initial correlation and increasing laser linewidth both increased the degree of noise in the amplified output.

Sampled averages of the 500 pulses recorded per trace allowed the trends to be

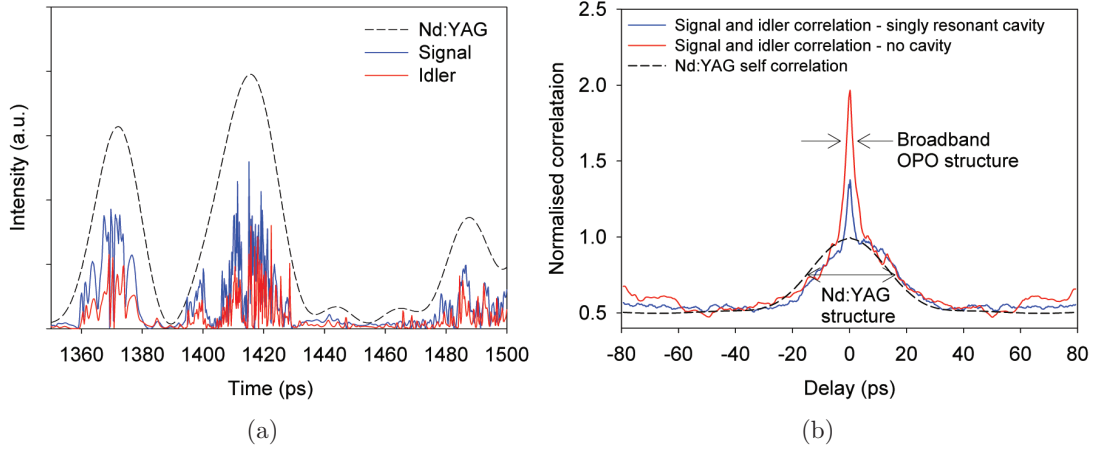


FIGURE 5.12: (a) Temporal structure of the signal and idler, overlaid with the structure of the Nd:YAG pump laser. The data is obtained using the BBOPO function of the SNLO software package [193]. (b) Modelled correlation between the signal and idler with and without a singly resonant cavity surrounding the KTP crystal. The results are compared to the self-correlation of the Nd:YAG pump laser.

more clearly observed and Fig. 5.13(b) shows the averaged probe amplification for each combination of initial correlation and linewidth. The initial slopes give g_{meas} ranging from 1.4 to 5.6 cm/GW. The slope of the narrow-correlated condition remains constant with pump intensity, confirming a high degree of initial correlation between the pump and probe, while the slopes for both uncorrelated cases increase with pump intensity, as expected. As with Fig. 5.11, applying $g_R = 3.5$ cm/GW in the modelling gave the best overall agreement, although there were several discrepancies. The broad correlated data starts out with a lower than expected slope, before the rate of amplification increases. This presumably is due to developing correlations and supports the previous suggestion that the broad linewidth pump and probe are not perfectly correlated to begin with. A second inconsistency is the faster than expected rise of the broad uncorrelated probe. Unseeded broadband OPOs contain complex spectral evolutions [196] that are not captured in the simplified static Gaussian representation used in the modelling.

The accuracy of g_R , as estimated through the modelling, is dependent on several assumptions and it is preferable to obtain a direct measurement. Figure 5.14 displays the results of pump-probe measurements limited to initially uncorrelated beams

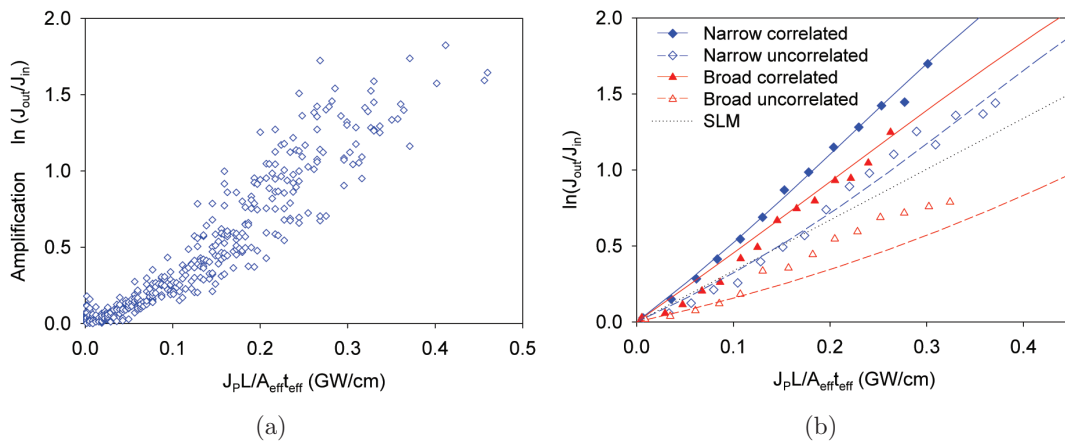


FIGURE 5.13: (a) Raw amplification data for the narrow uncorrelated case. (b) Measured (points) and modelled (lines) Raman amplification for four combinations of pump-probe linewidth and correlation.

and less than 20% amplification. Employing Eq. (5.5) with the measured narrow and broad spectral profiles returned average values of $\eta = 0.71$ ¹ and $\eta = 0.38$, respectively. Scaling the collected data by η returns $g_R = (3.6 \pm 0.6)$ cm/GW and $g_R = (4.0 \pm 0.3)$ cm/GW for the broad and narrow pump-probe linewidths, respectively. The two g_R values are consistent, within the calculated uncertainty, supporting the use of linewidth correction factors in uncorrelated pump-probe experiments. Combining both scaled data sets gives $g_R = (3.80 \pm 0.35)$ cm/GW.

¹ η of 0.85, used for modelling 2.48 μm pumped DRLs (see the list of modelling parameters in Table A.2), is calculated using only the idler spectral profile.

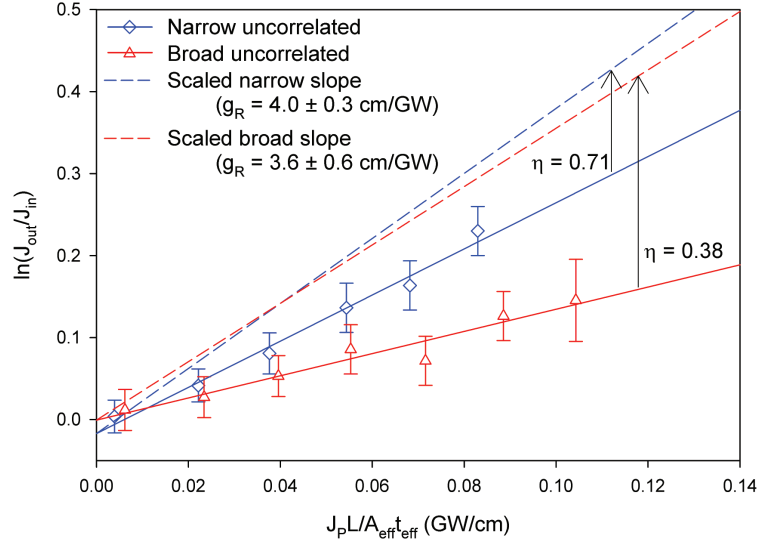


FIGURE 5.14: Small signal amplification of uncorrelated pump and probe beams, for both narrow and broad OPO output. Linear fits to the data are scaled by linewidth correction factors, η , to calculate g_R .

5.2.3.3 Implications for published g_R measurements using the pump-probe technique

All pump-probe measurements for diamond reported to date have used broadband lasers. Our preliminary g_R measurements at $1.864\ \mu\text{m}$, reported in [197], used a similar experimental set up, except the path difference between the pump and probe was fixed. Measurement of the path lengths returned a difference less than 5 mm and the higher value reported in that work ($4.8\ \text{cm/GW}$) is attributed to a partial correlation between the two input beams.

The first published pump-probe experiment in diamond split off a fraction of the pump beam from a multi-longitudinal mode Q-switched Nd:YAG laser to generate a probe in a second diamond crystal [105]. The reported g_R is notably higher than other results at $1.064\ \mu\text{m}$, but over-evaluation of t_{eff} due to insufficient detector bandwidth is the likely predominant reason, as discussed in Section 2.1.4. Additionally, a linewidth correction factor isn't used despite a pump linewidth of $\sim 1\ \text{cm}^{-1}$ [198]. For the $\langle 110 \rangle$ propagation data, the probe was amplified by a factor of 1.4, which is sufficiently high to

carry the dual risk of inflating results from both developing correlations and exceeding the region where a linear approximation to e^x is valid. This may explain the difference between the $\langle 110 \rangle$ and $\langle 100 \rangle$ propagation results (16 cm/GW cf. 14 cm/GW), which are amplified by factors of 1.4 and 1.1, respectively, whereas both measurements should yield the same result.

A second publication by the same authors measured the g_R of diamond for wavelengths spanning 0.355 μm to 1.450 μm [104]. An OPO was used to create a tuneable pump wavelength, a portion of which was used to generate a probe beam in a second diamond crystal. The linewidth of the OPO was relatively broad, with an example given of 2 cm^{-1} when the Nd:YAG pump laser was injection seeded, and 5 cm^{-1} when the Nd:YAG laser was unseeded. Pumping of broadband OPOs with injection seeded lasers may lead to purely phase noise broadened output [199], while non-seeded pumping induces both phase and intensity fluctuations. In either case the application of a linewidth correction factor is only relevant if correlations are not present between the pump and probe. Private communication with the authors indicate that the pump and probe path lengths were similar (contrary to the published layout), although it is not known if they are matched to an accuracy that will result in correlating structure, i.e. to within a few millimetres. The gain values were corrected for pump linewidth using a variant of Eq. (5.4) and, unless the pump spectra have Lorentzian profiles, there is scope for miscalculation of g_R , as noted in Section 5.1.3.1. In addition, probe linewidths were not accounted for and without further details on its spectral profile it is difficult to fully assess the accuracy of the results.

Pump-probe experiments conducted on $\text{Ba}(\text{NO}_3)_2$ and BaWO_4 used two laser sources [172, 200]. A single longitudinal mode pump laser was used for the 0.532 μm and 1.064 μm data points, which therefore are not influenced by multi-longitudinal-mode effects. The intermediate measurements from 0.74 μm to 0.9 μm employed a Ti:Sapphire laser with a 0.03 cm^{-1} linewidth. The experimental layout suggests a high chance of path matching between the pump and probe, particularly since the narrow pump linewidth requires $>5\text{ cm}$ path mismatch before complete decorrelation. A linewidth correction factor is not applied, which is appropriate, as the pump laser linewidths are

over an order of magnitude narrower than the Raman profiles. The multi-longitudinal-mode data points are in relative agreement with the SLM data, suggesting correlation effects are not significant.

5.2.3.4 Implications for published g_R measurements using the SRS threshold technique

In the SRS threshold technique for determining g_R , the large amplification factor ($\sim e^{25}$) ensures a high degree of correlation develops between the pump and Stokes well before the SRS threshold is reached. Therefore, there is a significant opportunity for enhanced gain to reduce thresholds and inflate g_R measurements. Figure 5.15 shows that the observed threshold may be lower than the monochromatic pump threshold and applying a linewidth correction factor will exacerbate the error in the measurement.

Most published crystalline SRS threshold measurements use mode-locked picosecond laser sources, e.g. [75, 103] for diamond. The phases of the longitudinal modes in a mode-locked laser are aligned, which results in the generation of a single intense spike every cavity round trip. Providing the intensity of the spike is well characterised, and transient Raman effects factored in if required, the calculated g_R should not be influenced by the multi-longitudinal-mode effects discussed here.

A measurement of g_R in diamond as a function of pump wavelength contained SRS threshold readings that used a Q-switched OPO source [104]. The threshold values are corrected for linewidths using a variant of Eq. (5.4). As correlations develop well before threshold, the application of a linewidth correction factor is unnecessary. The end effect may be inconsequential as no absolute g_R measurements are reported, instead the relative SRS thresholds are scaled until they match the pump-probe data.

Raman threshold results published by Cerny et al. [31] may have inadvertently demonstrated inflated g_R measurements obtained by non-mode-locked pumping, similar to the red or green traces in Fig. 5.15. The calculated g_R for $0.532\text{ }\mu\text{m}$ in KGW was 18.6 cm/GW using 5.1 ns Q-switched pulses. Pumping with a 35 ps mode-locked laser at the same wavelength gave 11.8 cm/GW . The phonon decay time for KGW is $\sim 1.5\text{ ps}$ [8] so both lasers should be in the steady state regime and the same g_R measured.

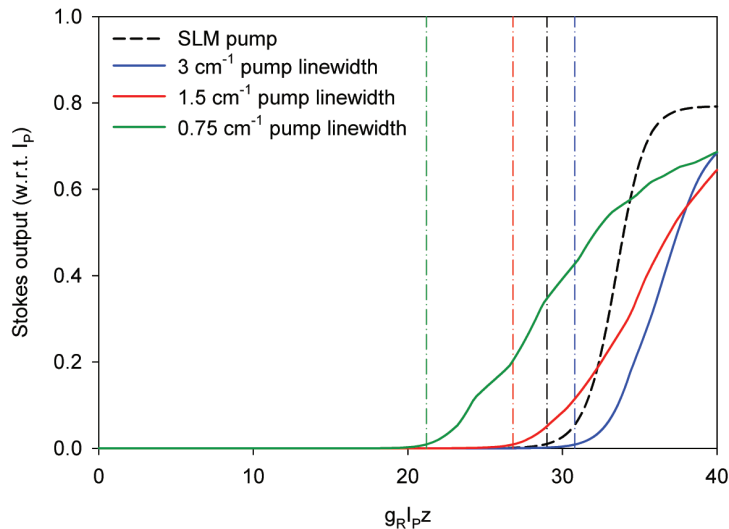


FIGURE 5.15: Modelled Raman generator thresholds for three different pump laser linewidths (Lorentzian profiles). The Raman linewidth is 1.5 cm^{-1} . The dot-dashed lines mark the point at which 1% pump conversion is reached and where the relative g_R reading would be taken.

5.2.3.5 Implications for laser thresholds

From the preceding discussion, it is clear that Raman gain values above the SLM value are obtainable when $\Delta\omega_P \gtrsim \Delta\omega_R$. It is interesting to consider how this may be applied to reduce thresholds and increase laser efficiency. For Raman oscillators, enhanced Raman gain is not generally relevant and practical benefits are only obtainable for amplification on a single pass. As the Stokes field is resonating it experiences gain from the counter propagating pump. This is effectively a case of very large dispersion, and correlations do not develop. In addition, for external cavity lasers, on each round trip the Stokes field is introduced to a fresh pump field and any previous correlations are now irrelevant. It may be possible to obtain a threshold reduction by matching the cavity round trip times of the pump laser and the Raman laser, such that the fresh pump field and the existing Raman field contain some correlations, as has been demonstrated in OPOs [201] and in synchronously pumped Raman lasers [71].

Due to the generally poor conditions for developing correlations in external cavity Raman lasers, the effective Raman gain coefficient under broadband pumping is less

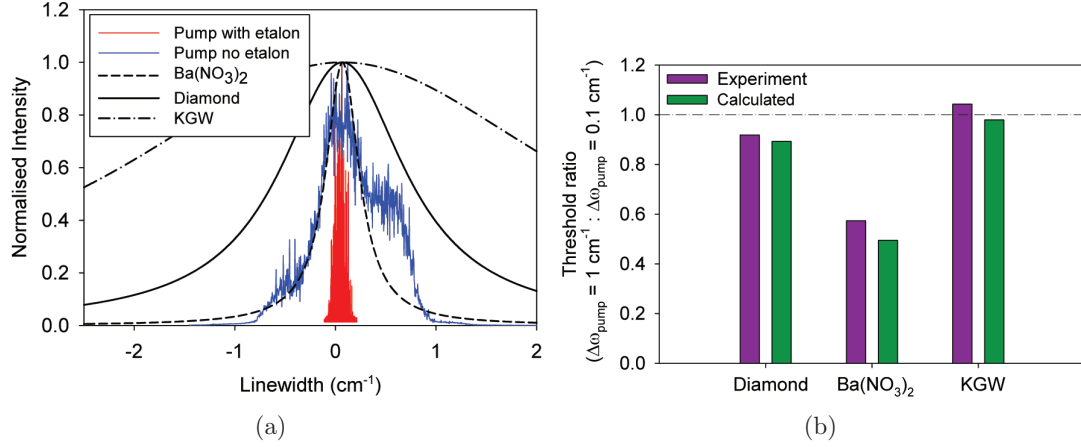


FIGURE 5.16: (a) Spectra of the free running and etalon narrowed pump compared to the Raman linewidth of diamond, KGW and $\text{Ba}(\text{NO}_3)_2$. (b) Calculated (Eq. (5.5)) and measured ratios of the laser threshold between a pump linewidth of 1 cm^{-1} and 0.1 cm^{-1} .

than g_R . An experiment was conducted to compare the change in threshold with the change in g_{meas} predicted by Eq. (5.5). Threshold intensities of first Stokes Raman lasers were compared using three different Raman crystals and two pump linewidths. External cavity Diamond, $\text{Ba}(\text{NO}_3)_2$ and KGW Raman lasers were pumped by a $1064 \mu\text{m}$ Nd:YAG laser with a removable etalon that reduced the linewidth from 1 cm^{-1} to 0.1 cm^{-1} (Fig. 5.16(a)). The measured ratio of the threshold with broad and narrow linewidth pumping is shown in Fig. 5.16(b). KGW has a Raman linewidth (5.4 cm^{-1}) broader than both pump laser linewidths and therefore should demonstrate minimal change in threshold. The KGW measurement therefore serves as a reference, as any observed changes to the threshold are likely to be from the etalon changing the spatial and temporal properties of the pump beam. Given that the KGW threshold remained relatively constant, the changes observed using other crystals can be attributed to spectral influences. $\text{Ba}(\text{NO}_3)_2$ has a narrow Raman linewidth (0.4 cm^{-1}) and the threshold halves as the pump laser linewidth is narrowed. The diamond linewidth is between those of KGW and $\text{Ba}(\text{NO}_3)_2$, and accordingly the observed threshold reduction is not as large as $\text{Ba}(\text{NO}_3)_2$. The results for all three crystals agree with the change in effective gain calculated from Eq. (5.5).

5.3 Measurement of g_R using coherent Stokes Raman scattering

Pump-probe experiments require accurate, absolute measurement of the spatial, temporal and spectral profiles of both laser beams. Characterising the beams to the required accuracy may be challenging, particularly for multimode beams. In addition, pulse-to-pulse fluctuations in amplification add uncertainty to the readings. This section describes an alternative method for determining g_R which removes the need to characterise the spatial, temporal and spectral laser profiles and requires only measurement of relative intensity and absolute wavelength.

Mixing two wavelengths in a material, as their frequency difference tunes through the Raman resonance, produces Stokes and anti-Stokes signatures. These signatures form the basis for the widely used Coherent Stokes Raman Scattering (CSRS) and Coherent Anti-Stokes Raman Scattering (CARS) spectroscopic tools [202]. In the 1970s Levenson and Bloembergen used CARS to measure the third order electronic susceptibility, $\chi_E^{(3)}$, of materials by using known spontaneous Raman scattering values to fit curves to the collected data [102]. Here, the reverse process is used. Modern measurements of $\chi_E^{(3)}$, typically made using the z-scan technique [203], are referenced to allow determination of the Raman susceptibility and hence g_R .

5.3.1 Raman Susceptibility

Spatially and temporally overlapping two beams of wavelengths ω_1 and ω_2 in a material creates Stokes and anti-Stokes photons through a degenerate four-wave-mixing (FWM) process. Considering only the Stokes photons,

$$\omega_S = 2\omega_1 - \omega_2 \quad (5.11)$$

where $\omega_2 > \omega_1$. When the frequency separation of the incident beams approaches the Raman frequency, the total induced polarisation contains terms describing both

Raman amplification and FWM. The increase in the Stokes field is then given by

$$\frac{dE_S}{dz} = \frac{3i\omega_S}{n_{sc}}\chi_R^{(3)}(\omega_S)|E_1|^2E_S + \frac{3i\omega_S}{2n_{sc}}\chi_F^{(3)}(\omega_S)E_1^2E_2^*e^{i(2k_1-k_2)z} \quad (5.12)$$

where $\chi_R^{(3)}$ and $\chi_F^{(3)}$ are the Raman and FWM susceptibilities, respectively. See Appendix A and [140] for a more detailed derivation of this equation. The degeneracy of ω_1 in the FWM process gives a factor of two difference in the definition of $\chi^{(3)}$, i.e. $\chi_F^{(3)} = 2\chi_R^{(3)}$ [140].

The field strength of the incident beams is typically much greater than the Stokes field and under the assumption of perfect phase matching ($2k_1 - k_2 = 0$), the growth of the Stokes light is largely due to the FWM term

$$\frac{dE_S}{dz} = \frac{3i\omega_S}{2n_{sc}}\chi_F^{(3)}(\omega_S)E_1^2E_2^* \quad (5.13)$$

where $\chi_F^{(3)}(\omega_S)$ is given by [140]

$$\chi_F^{(3)}(\omega_S) = \frac{N(\partial\alpha/\partial Q)^2}{3\epsilon_0 m[\omega_R^2 - (\omega_1 - \omega_2)^2 + i\Delta\omega_R(\omega_1 - \omega_2)]} \quad (5.14)$$

as the frequency difference between ω_1 and ω_2 is tuned through the Raman frequency.

The FWM-generated intensity, which is proportional to $|\chi_F^{(3)}|^2$, has a Lorentzian distribution. However, interference with non-resonant components of the nonlinearity produces an asymmetric intensity profile and background. These may originate from residual contributions from neighbouring Raman modes and the third order background electronic susceptibility, $\chi_E^{(3)}$. In the case of isolated Raman transitions (as for the first order Raman mode in diamond) only $\chi_E^{(3)}$ is relevant. Including $\chi_E^{(3)}$, the total third order susceptibility becomes

$$\chi_{Total}^{(3)}(\omega_S) = \chi_F^{(3)}(\omega_S) + \chi_E^{(3)} \quad (5.15)$$

The measured intensity at the Stokes wavelength will therefore be proportional to

$$I(\omega_S) \propto |\chi_F^{(3)}(\omega_S) + \chi_E^{(3)}|^2 \quad (5.16)$$

Over the frequency range in question, $\chi_E^{(3)}$ can be considered a real constant, giving

$$I(\omega_S) \propto |\text{Re}(\chi_F^{(3)}(\omega_S)) + \chi_E^{(3)} + i\text{Im}(\chi_F^{(3)}(\omega_S))|^2 \quad (5.17)$$

Breaking Eq. (5.14) into real and imaginary components gives

$$\text{Re}(\chi_F^{(3)}(\omega_S)) = \frac{N(\partial\alpha/\partial q)^2}{3\epsilon_0 m} \frac{\omega_R^2 - (\omega_1 - \omega_S)^2}{[\omega_R^2 - (\omega_1 - \omega_2)^2]^2 + \Delta\omega_R^2(\omega_1 - \omega_2)^2} \quad (5.18)$$

$$\text{Im}(\chi_F^{(3)}(\omega_S)) = \frac{N(\partial\alpha/\partial q)^2}{3\epsilon_0 m} \frac{-\Delta\omega_R(\omega_1 - \omega_S)}{[\omega_R^2 - (\omega_1 - \omega_2)^2]^2 + \Delta\omega_R^2(\omega_1 - \omega_2)^2} \quad (5.19)$$

Amplitudes of the real and imaginary components of $\chi_F^{(3)}$ in the vicinity of the Raman frequency, along with a constant background $\chi_E^{(3)}$, are plotted in Fig. 5.17. When the two wavelengths are resonant with the Raman frequency, the real component is zero and the Raman susceptibility is negative imaginary, with a negative peak at $\chi_{Fpk}^{(3)}$. The effect of $\chi_E^{(3)}$ in creating an asymmetry to the intensity profile is clearly seen in the lower figure. Notably, a minima is created when the non-resonant component is equal in magnitude, but opposite in sign, to the real component of the Raman resonance. At this frequency separation the imaginary component is typically negligible. If the Raman response is strong, as is the case with diamond, $|\chi_{Fpk}^{(3)}/\chi_E^{(3)}| \gg 1$ and the peak intensity will occur close to the Raman frequency. In this case the separation between the maxima and the minima is approximated by

$$\Delta\omega_{peak-trough} \approx \left(\frac{\chi_{Fpk}^{(3)}}{\chi_E^{(3)}} \right) \frac{\Delta\omega_R}{2} \quad (5.20)$$

Thus if $\chi_E^{(3)}$ and $\Delta\omega_R$ are known, $\chi_F^{(3)}$ can be calculated through only a measurement of wavelength and relative Stokes intensity.

For SRS the increase in Stokes intensity is given by the first term of Eq. (5.12).

Using the product rule and $I = 2c\epsilon_0 n|E|^2$ gives

$$\frac{dI_S}{dz} = \frac{-3\omega_S}{n_1 n_S c^2 \epsilon_0} \text{Im}(\chi_R^{(3)}(\omega_S)) I_1 I_S \quad (5.21)$$

Substituting $\chi_F^{(3)} = 2\chi_R^{(3)}$, the Raman gain coefficient on resonance is then

$$g_R = \frac{-3\omega_S}{2n_P n_S c^2 \epsilon_0} \chi_{Fpk}^{(3)} = \frac{-3\omega_S}{n_P n_S c^2 \epsilon_0} \frac{2(\Delta\omega_{peak-trough})\chi_E^{(3)}}{\Delta\omega_R} \text{ (m/W)} \quad (5.22)$$

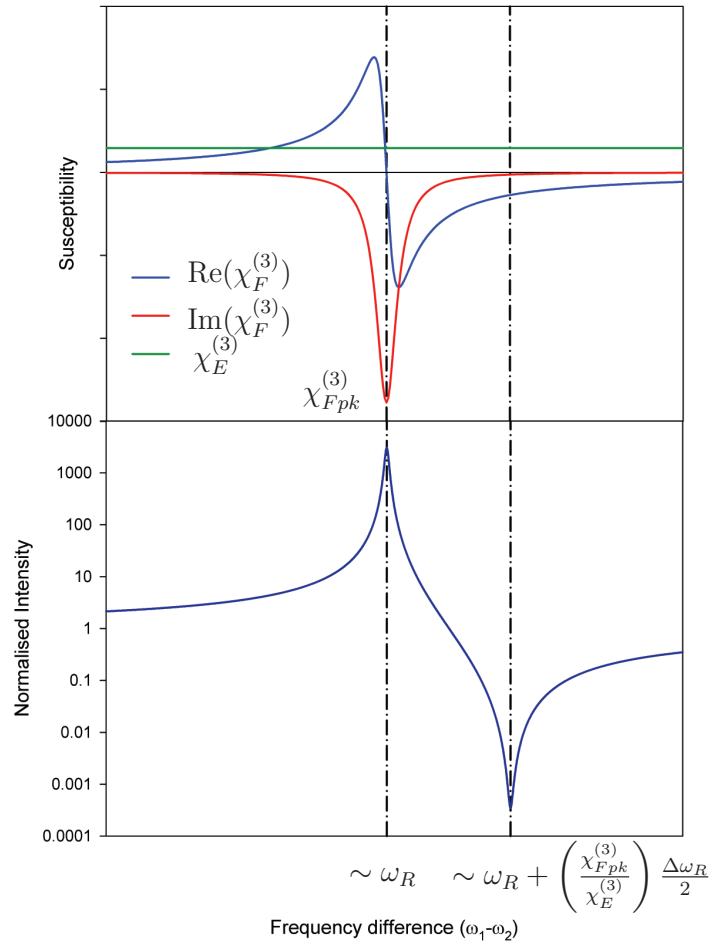


FIGURE 5.17: Top - FWM and background susceptibilities near the Raman resonance. Bottom - Intensity of the Stokes output, normalised to the background susceptibility, as the frequency difference of the mixing beams is tuned through the Raman resonance.

5.3.2 Third order background electronic susceptibility

Knowledge of $\chi_E^{(3)}$ at the wavelength of interest is essential for this technique of measuring g_R . $\chi_E^{(3)}$ is responsible for a range of non-linear processes such as self-focussing and self-phase modulation. Fortunately, diamond is a heavily studied material and several measurements of $\chi_E^{(3)}$, or equivalently the nonlinear index of refraction, are reported [68, 102, 204–206]. The conversion between $\chi_E^{(3)}$ and the intensity based nonlinear refractive index is

$$n_2^I = \frac{3\chi_E^{(3)}}{4n_0^2\epsilon_0 c} \quad (5.23)$$

The published data for $\chi_E^{(3)}$ in diamond is collated in Fig. 5.18. The results reported by [102, 205–207] assume a different definition of the electric field than that used here (see Appendix A) and therefore, require their values to be scaled up by a factor of four [208]. The values in Fig. 5.18 show discrepancies in both magnitude and sign. Particularly concerning is the difference in sign between the two z-scan measurements at 0.355 μm , as the sign of $\chi_E^{(3)}$ is an obvious feature of a z-scan trace. The limited available data at longer wavelengths does appear to be more consistent, but the longest reported wavelength for direct measurement of $\chi_E^{(3)}$ using the z-scan technique is 1.064 μm [207]. A susceptibility value for 1.550 μm , inferred from threshold measurements of diamond ring resonators [68], is also plotted. To obtain values of $\chi_E^{(3)}$ at longer wavelengths, estimations are made using a two-parabolic-band model of susceptibility [203]. This model has been used to accurately predict the dispersion of $\chi_E^{(3)}$ for numerous semiconductors [209], but it has been acknowledged that the accuracy of the model is reduced for large band gap materials, such as diamond, in the two photon absorption region [210]. In addition, the model was developed for direct band gap materials, so the short wavelength fit for diamond is expected to be poor [204]. Values far from the two photon absorption region are of interest here and the limited available data shows better agreement with the model at longer wavelengths. A calculated value of $\chi_E^{(3)} = 3.12 \times 10^{-21} \text{ m}^2 \text{ V}^{-2}$ for a pump wavelength of 2.480 μm is subsequently used to determine $\chi_F^{(3)}$.

The values presented in Fig. 5.18 are for one particular orientation of the incident wavelengths, $\chi_{Exxx}^{(3)}$, where the polarisation of the four mixing wavelengths are

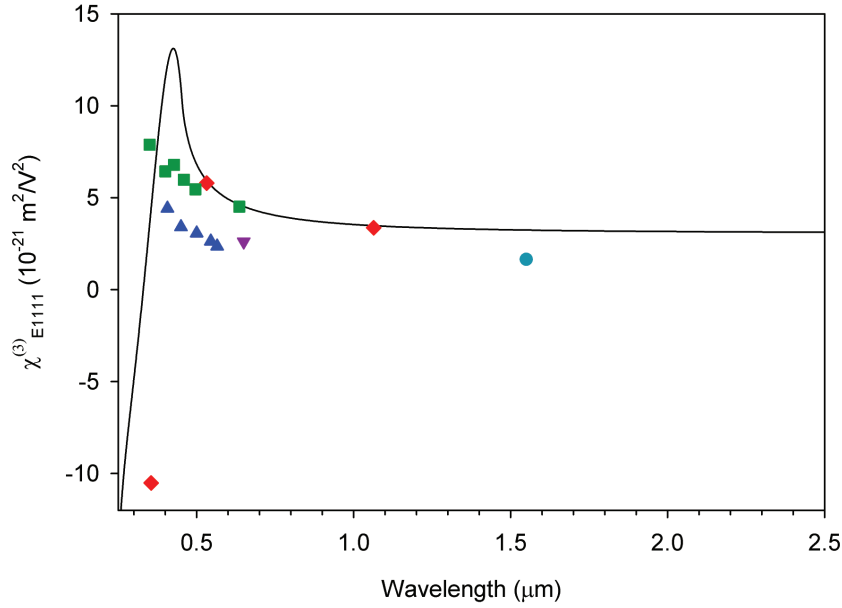


FIGURE 5.18: Modelled electronic susceptibility [203] with measured data points from the following references: Red diamonds, z-scan [207]; green squares, z-scan [205]; purple down triangle, Kerr effect measurement of $\chi_{E1212}^{(3)}$ converted assuming $\chi_{E1111}^{(3)} = 3\chi_{E1212}^{(3)}$ [206]; blue up triangles, CARS [102]; aqua circle, micro resonator threshold [68].

aligned with the $\langle 100 \rangle$ axes of the crystal. $\chi_E^{(3)}$ is a tensor and thus the resultant effective susceptibility will change depending on the relative orientation of the crystal and polarisation of the beams. The effective susceptibility used with Eq. (5.20) is

$$\chi_{Eff}^{(3)} = [d_1\chi_{xxxx}^{(3)} + d_2\chi_{xxyy}^{(3)} + d_3\chi_{xyxy}^{(3)} + d_4\chi_{xyyx}^{(3)}] \quad (5.24)$$

where the four $\chi^{(3)}$ symbols are the independent non-zero components of the susceptibility in cubic materials. The x and y subscripts denote the polarisation orientation of each of the fields. The coefficients d_{1-4} are calculated through multiplication of the $\chi_E^{(3)}$ tensor with the relevant input polarisation states, summarised in Appendix B, with the final results in Table 5.1. Equation (5.24) can be simplified further assuming Kleinman symmetry. Away from resonant features, i.e. in regions of minimal $\chi_E^{(3)}$ dispersion, the

following condition holds [211].

$$\chi_{xxxx}^{(3)} = 3\chi_{xxyy}^{(3)} = 3\chi_{xyxy}^{(3)} = 3\chi_{yyyx}^{(3)} \quad (5.25)$$

Leveneson et al. reported a factor of 2.6 instead of 3 for diamond, which may be influenced by the fact that the measurement was taken in a region of increased $\chi_E^{(3)}$ dispersion [102]. The key result in Table 5.1 is that under the condition of parallel input polarisations, the background susceptibility is approximated by $\chi_{Exxx}^{(3)}$, which allows direct comparison with the data in Fig. 5.18.

Input polarisations	d_1	d_2	d_3	d_4	$\chi_{Eeff}^{(3)}$ assuming Kleinmen symmetry
$\omega_2, \omega_1, \omega_S$ parallel to $\langle 100 \rangle$	1	0	0	0	$\chi_{xxxx}^{(3)}$
$\omega_2, \omega_1, \omega_S$ parallel to $\langle 110 \rangle$	1/2	1/2	1/2	1/2	$[1/2\chi_{xxxx}^{(3)} + 3/2\chi_{xxyy}^{(3)}] = \chi_{xxxx}^{(3)}$
$\omega_2, \omega_1, \omega_S$ parallel to $\langle 111 \rangle$	1/3	2/3	2/3	2/3	$[1/3\chi_{xxxx}^{(3)} + 6/3\chi_{xxyy}^{(3)}] = \chi_{xxxx}^{(3)}$
ω_2 parallel to $\langle 100 \rangle$, ω_1, ω_S parallel to $\langle 010 \rangle$	0	0	0	1	$\chi_{yyyx}^{(3)}$

TABLE 5.1: Effective background electronic susceptibility for several input polarisation orientations.

5.3.3 Experiment

Tuning the spectrally narrowed OPO used in the pump-probe experiment generated the required wavelengths, with $\omega_1 = \omega_{idler}$ and $\omega_2 = \omega_{signal}$. Mixing $\omega_{idler} = 2.46\text{--}2.52\text{ }\mu\text{m}$ with $\omega_{signal} = 1.88\text{--}1.84\text{ }\mu\text{m}$ produced Stokes output spanning $3.57\text{--}4.0\text{ }\mu\text{m}$. Alternatively, the anti-Stokes intensity could have been recorded, but at the time instrumentation was configured for $3.7\text{ }\mu\text{m}$ generation.

The signal and idler beams were incident on the diamond crystal with an angular separation of 50 mrad (Fig. 5.19). This results in a 21 mrad internal crossing angle, which is approximately equal to the theoretically predicted phase matching condition. Average pulse energies in each wavelength were constant throughout the experiment at $350\text{ }\mu\text{J}$, prior to the crystal. Rotating the crystal sequentially aligned the parallel signal

and idler polarisations with the $[100]$, $[11\bar{1}]$ and $[01\bar{1}]$ crystal axes. The output Stokes light passed through two longpass filters and a dichroic mirror to reject the pump wavelengths. An uncooled PbSe detector (Thorlabs PDA20H-EC) measured the signal strength around the resonant peak. The anti-resonant intensity was several orders of magnitude weaker and required the use of a liquid nitrogen cooled detector (Teledyne J10D-M204-R01M-60).

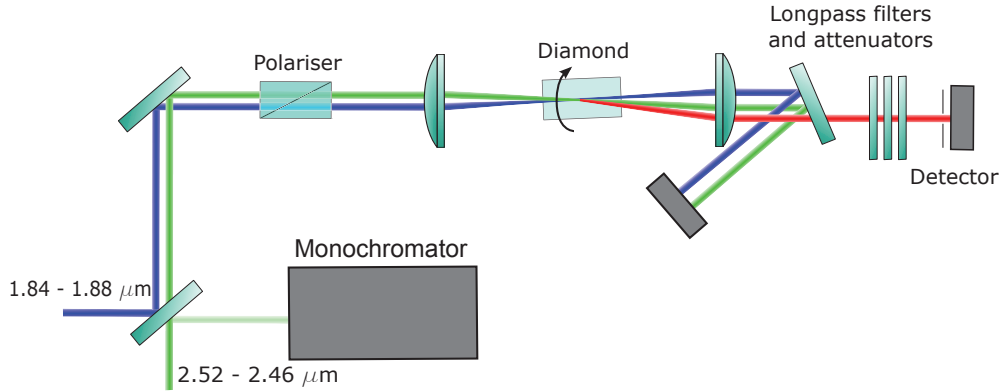


FIGURE 5.19: Experimental layout for measuring the FWM signal strength as a function of OPO signal and idler wavelength separation.

5.3.4 Results

Aligning the input polarisations with the $[11\bar{1}]$ or $[01\bar{1}]$ axes produced clearly observable resonant and anti-resonant regions of Stokes intensity in Fig. 5.20 as $\omega_{\text{signal}} - \omega_{\text{idler}}$ was tuned through ω_R . Conversely aligning polarisations with the $[100]$ axis displayed no Raman resonance, as predicted by the Raman tensors. The $[100]$ readings were used to normalise the other orientations and calibrate out losses due to multiphonon absorption, which varied from $\alpha = 0.72 \text{ cm}^{-1}$ to 4.2 cm^{-1} across the output tuning range. The measured minima are not as deep as predicted, possibly due to spontaneous Raman scattering from the OPO idler (ideally the output would be measured using a monochromator to discriminate between the spontaneous Raman and FWM photons). Fits to the data using Eqs. (5.17) to (5.19) determined the frequency separation between the maxima and minima ($\Delta\omega_{\text{peak-trough}}$), and the associated uncertainties. Calculation of g_R is then achieved by inserting $\Delta\omega_R = 1.5 \text{ cm}^{-1}$ and $\chi_E^{(3)} = 3.12 \times 10^{-21} \text{ m}^2/\text{V}^2$ into

Eq. (5.22). The results for $[01\bar{1}]$ and $[11\bar{1}]$ polarised beams are summarised in Table 5.2.

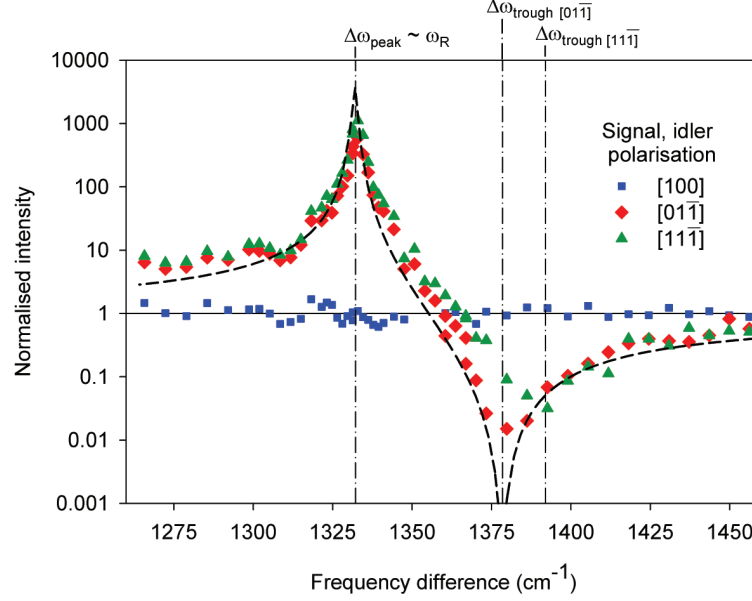


FIGURE 5.20: Measured FWM signal strength as the frequency difference of the OPO beams is tuned through the Raman resonance. The input polarisations are successively aligned with the $[100]$, $[01\bar{1}]$ and $[11\bar{1}]$ directions. The data points have been normalised to the average non-resonant $[100]$ signal strength. Each point is an average of at least 50 pulses and the uncertainty is similar to the symbol size.

Input Polarisation	$\Delta\omega_{peak-trough}$ (cm^{-1})	$\chi_{Fpk}^{(3)}/\chi_{Eeff}^{(3)}$	$\chi_{Rpk}^{(3)}$ ($10^{-20} m^2 V^{-2}$)	g_R (2.480 μm pump) (cm/GW)	
				CSRS	Pump-probe
$[01\bar{1}]$	47 ± 2	63	9.83	3.33	2.5
$[11\bar{1}]$	59 ± 3	79	12.3	4.18	3.4

TABLE 5.2: Susceptibility and g_R values in diamond measured using CSRS with pump beams tuned around 1.864 μm and 2.480 μm .

The agreement with the pump-probe measurement (scaled for wavelength) is within 25% and the ratio between g_R values with polarisations aligned with $[01\bar{1}]$ and $[11\bar{1}]$ is 1.26, which is within 5% of the theoretical value of 1.33. Uncertainties are only listed for the peak-trough separation, not calculated g_R values, as the inconsistencies in $\chi_E^{(3)}$

mentioned in Section 5.3.2 need resolving. Considering only the uncertainty of $\chi_E^{(3)}$ at $1.064\text{ }\mu\text{m}$ from [207], would give an overall uncertainty in g_R of $\pm 15\%$.

These results confirm that there is potential for CSRS to be a viable alternative technique for measuring g_R , with the important advantage of not relying on the details of the spatial, temporal and spectral properties of the interacting beams. Reducing the uncertainty in $\chi_E^{(3)}$ is required to improve confidence and further z-scan measurements of $\chi_E^{(3)}$ at infrared wavelengths would aid in resolving the inconsistencies in Fig. 5.18.

5.3.5 Application of the CSRS technique to other crystals

The application of CSRS to finding g_R is particularly suitable for diamond due to the single Raman peak and availability of published $\chi_E^{(3)}$ data. In the case of other Raman crystals, $\chi_E^{(3)}$ data is available for common Raman crystals such as $\text{Ba}(\text{NO}_3)_2$ and KGW [212, 213], but separate z-scan experiments may be required for less well studied materials. There are empirical relationships that relate the linear and nonlinear refractive indices [214, 215], but measured magnitudes often deviate several tens of percent from the predicted value. An additional factor for consideration is that the total background susceptibility includes the off-resonant contribution of any surrounding Raman modes. The 768 cm^{-1} mode of KGW for example, has a side lobe that would need to be accounted for in $\chi_{Eff}^{(3)}$ [63].

5.4 Chapter Summary

This chapter reports new considerations and approaches for making g_R measurements with multimode lasers. The pump-probe experiment examined the effect of correlations between the pump and probe fine structure. Although studied in the context of early gas Raman lasers, recent g_R measurements in crystals do not consider the possibility of correlations inflating the Raman gain. Applying this knowledge, a g_R of $(3.80 \pm 0.35)\text{ cm/GW}$ for $1.864\text{ }\mu\text{m}$ pumping was determined using uncorrelated beams and accounting for the spectral width of the pump and probe relative to the Raman profile. Summing multiple longitudinal modes to produce a modelled electric field with

phase and amplitude noise reproduced many of the experimental observations.

To overcome the challenges associated with accurately characterising the pump and probe beams, a second measurement method based on CSRS was devised. Tuning the OPO signal and idler frequency difference through ω_R produced a Stokes intensity profile with maxima and minima determined by the ratio of $\chi_R^{(3)}$ and $\chi_E^{(3)}$. Using published $\chi_E^{(3)}$ data, a g_R of 3.33 cm/GW was calculated for a pump wavelength of 2.480 μm . Scaling the value measured using the pump-probe technique to 2.480 μm returns $g_R = 2.5 \text{ cm/GW}$, which is 25% smaller. Further improvements in accuracy may be obtained in future by using single longitudinal mode sources in the case of the pump-probe technique and higher accuracy long-wavelength measurements of $\chi_E^{(3)}$ for the CSRS technique.

A comparison of results from both methods with the calculated g_R dispersion curve and previously published experimental data is presented in Fig. 5.21. Both values lie well within the boundaries defined through extrapolating shorter wavelength measurements and broadly support the applicability of the calculated g_R dispersion curve for determining mid-IR g_R values. These results will assist in developing models of mid-IR DRLs, details of which are presented in the following chapter.

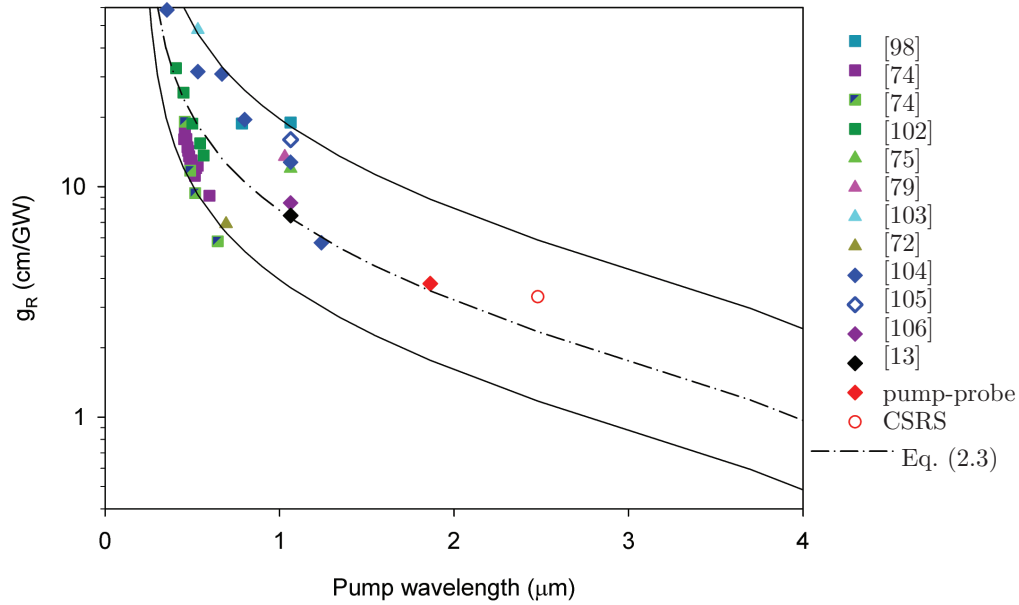


FIGURE 5.21: Reported g_R measurements as a function of wavelength. Values are scaled for $\langle 100 \rangle$ (or equivalently $\langle 110 \rangle$) pump polarisations. Measurements are made using the following techniques: diamonds – pump probe; triangles – SRS threshold; squares – spontaneous Raman scattering. The solid lines represent upper and lower limits defined by extrapolating visible and near-IR data. The dashed-dot line is calculated from Eq. (2.3).

5.4.1 Publications arising from the work in this chapter

Peer reviewed journal articles

Sabella, A., Piper, J. A., and Mildren, R. P., “Pump–Probe Measurements of the Raman Gain Coefficient in Crystals Using Multi-Longitudinal-Mode Beams”, IEEE journal of Quantum Electronics, **51**(12), 1-8, (2015).

6

Mid-IR diamond Raman laser

The excellent performance of diamond demonstrated in the near-IR is promising for extending the output wavelength in the face of decreasing g_R and increased absorption. Prior to this work, $1.6\text{ }\mu\text{m}$ was the longest wavelength reported in a DRL [157] and solid state Raman lasers had not been demonstrated beyond $3\text{ }\mu\text{m}$. This chapter investigates the feasible mid-IR wavelengths obtainable with diamond, and demonstrates a DRL with tuneable output around $3.7\text{ }\mu\text{m}$. The role of multiphonon absorption in limiting efficiency and the effect of seeding the Stokes output on thresholds are examined, before designing a second Stokes laser to Raman shift over the two phonon absorption region to produce $7.30\text{ }\mu\text{m}$ output. The chapter concludes with a discussion on the current limitations of mid-IR DRLs.

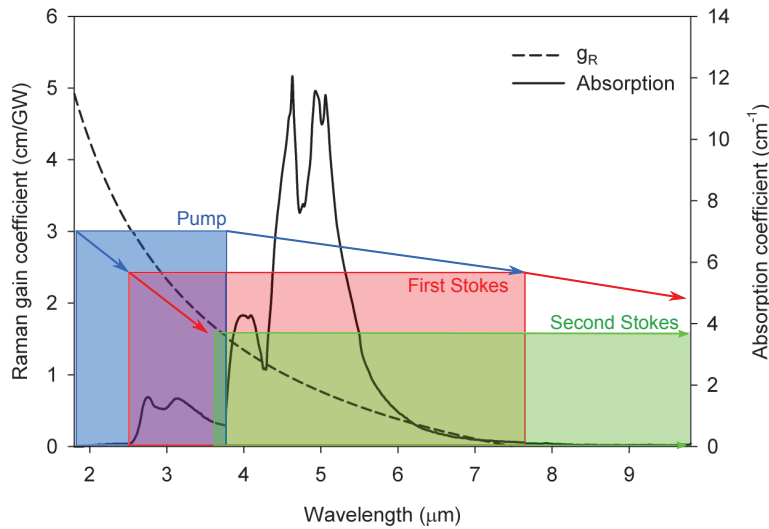


FIGURE 6.1: Measured diamond absorption and calculated g_R in the mid-IR region. The g_R curve is presented as a function of pump wavelength. The red and green boxes represent spectral regions covered by the first and second Stokes, respectively, for pump wavelengths spanning 1.8 to 3.8 μm (the blue box).

6.1 Potential mid-IR wavelengths

The challenges involved in developing a mid-IR DRL are heightened by the multi-phonon absorption region, diminishing g_R and increasing diffraction (i.e. larger cavity mode sizes). Figure 6.1 overlays the first two of these parameters with the span of potential first and second Stokes wavelengths for pump wavelengths ranging from 1.8 μm to the start of the strong two-phonon absorption region near 3.8 μm . For a Raman laser or amplifier to be feasible, the Raman gain needs to be greater than the intrinsic absorption loss at the Stokes wavelength. This condition sets a baseline for the consideration of other sources of loss, such as Fresnel reflections.

Modelling of a single pass Raman amplifier using Eq. (4.1) with the g_R and absorption parameters in Fig. 6.1 returns the relative performance for different pump/Stokes pairs shown in Fig. 6.2. With the pump intensity set near the facet damage threshold, the results demonstrate that there are several regions where strong amplification is possible. Stokes wavelengths less than 3.75 μm show the highest gain, followed by a

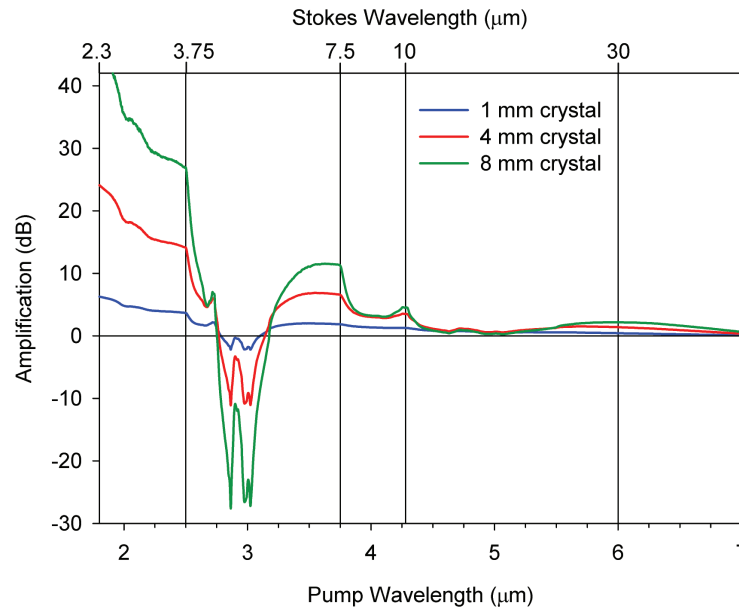


FIGURE 6.2: Modelled single pass SRS amplification of a low power, 12.7 W/cm^2 , seed beam by a 3 GW/cm^2 pump beam with the wavelength tuned from 1.8 to $7 \mu\text{m}$.

band spanning 6.2 – $7.5 \mu\text{m}$. When the Stokes seed is in the two-phonon absorption region (3.8 – $6 \mu\text{m}$) the Raman amplification is unable to compete and net loss occurs. For Stokes wavelengths from 10 – $30 \mu\text{m}$ the pump is in the two-phonon absorption region and is attenuated before it has a chance to significantly amplify the seed. Both pump and Stokes experience relatively little absorption for output wavelengths beyond $30 \mu\text{m}$, but g_R is very small and again negligible amplification occurs. Figure 6.2 confirms what is intuitively discerned from the multiphonon absorption profile in Fig. 6.1; the best mid-IR wavelengths for DRLs are at multiples of the Raman frequency ($1332 \text{ cm}^{-1} = 7.5 \mu\text{m}$ and $2664 \text{ cm}^{-1} = 3.75 \mu\text{m}$). Characterisation of DRLs at these wavelengths will provide a good foundation for determining the potential range of lasing wavelengths, and accordingly, the first mid-IR DRL was designed to produce Stokes output near the local absorption minima at $3.75 \mu\text{m}$.

6.2 Pump laser selection for 3.75 μm output

A 3.75 μm DRL requires a pump laser at 2.50 μm and the following paragraphs outline the requirements for several important laser parameters.

Pulse energy/pulse width: Increased losses in diamond at 3.75 μm necessitate high peak power pulses to reach threshold. Pulse durations in the nanosecond regime were deemed the most attractive as the required peak powers are readily available from Q-switched sources and the pulse durations are long enough to be in the steady state Raman regime. Standard external cavity configurations perform well, without the complications of synchronous pumping, as required for picosecond Raman lasers. The minimum spot size to maintain a confocal parameter longer than an 8 mm diamond crystal is 80 μm , assuming a high beam quality 2.5 μm laser. With an 80 μm pump spot, numerical modelling, coupled with g_R measurements from Chapter 5, indicated that a peak intensity of 1 GW/cm² was required to be comfortably above threshold for a 5 ns Q-switched pulse. This corresponds to 250 μJ pulse energy.

Beam quality: Given that one of the key attractions of Raman lasers is beam-clean-up, perfect beam quality is not a requirement. However, subsequent changes to the spot size and confocal parameter will increase the pulse energy requirements.

Linewidth: To achieve optimal thresholds, ideally the linewidth should be less than 1 cm⁻¹ (0.63 nm at 2.50 μm). Evaluating Eq. (5.5) returns the expected increase in threshold relative to the SLM case.

Tuneability: Whilst not a necessity, having the ability to tune the pump wavelength allows for investigation of performance as a function of wavelength and a more detailed analysis of the role of multiphonon absorption.

6.2.1 Pump laser options

In the context of evaluating diamond as a mid-IR material, an OPO is a flexible pump source that meets the previously listed requirements. The ability to generate the required pulse energies, with narrow linewidths, across a broad tuning range, is well documented [216–218]. It also is a simple addition to an existing 1.064 μm laser, which

reduced development time and cost, and allowed for the research effort to be primarily focussed on the mid-IR performance of diamond. A fortunate consequence of converting 1.064 μm to 2.480 μm , which is close to 2.50 μm , is that the signal-idler frequency difference is equal to the Raman frequency of diamond, as shown in Fig. 6.3(a). The dual wavelength output was exploited to produce a seed at 3.70 μm through FWM as well as used to conduct the g_R measurements in Chapter 5.

Several directly emitting laser technologies were considered as alternatives. Cr:ZnSe naturally lases in the vicinity of 2.5 μm and has been the subject of significant recent research [2]. Thulium doped lasers on the other hand lase near 1.9 μm and thus could act as a pump source where the second Stokes is 3.75 μm . Each of these technologies are able to generate high peak power nanosecond pulses with the potential for broadly tuneable output wavelength. Published examples of tuneable, narrow linewidth operation however, are almost exclusively CW [219–222]. Commonly used birefringent Lyot filters have insufficient out of band suppression for high gain pulsed operation [223], requiring investigation of alternative tuning elements, such as volume Bragg gratings. Although not selected here, extending the spectral coverage of these pump sources using diamond remains a potential research path, and the OPO pumped results provide an excellent measure of potential performance.

6.2.2 OPO output parameters

The experiments detailed in this chapter used the same custom built OPO as in Chapter 5. A summary of the output parameters is listed in Table 6.1, with further details on the OPO design and performance presented in Appendix C. Maintaining a suitably narrow linewidth was the main challenge, with the final design using a diffraction grating in a Littman-Metcalf configuration to narrow the resonant idler linewidth to less than the diamond Raman profile, as shown in Fig. 6.3(b). A linewidth correction factor of 0.85 was calculated from the idler profile using Eq. (5.5). The width of the non-resonant signal was broader as it is approximated by the convolution of the resonant idler and 1.064 μm Nd:YAG pump spectra.

The type II phase matching present in the OPO creates orthogonal signal and idler

	Signal	Idler
Wavelength span (μm) *	1.84 – 1.96	2.33 – 2.53
Linewidth (cm^{-1}) **	1.2	0.55
Pulse Energy (mJ)	1.9	1.3
Pulsewidth (ns)	4	4
M^2 **	2.5	1.7

TABLE 6.1: Littman-Metcalf OPO output parameters. * Represents the tuning range tested, not the maximum possible tuning range. ** At approximately 1 mJ idler pulse energy.

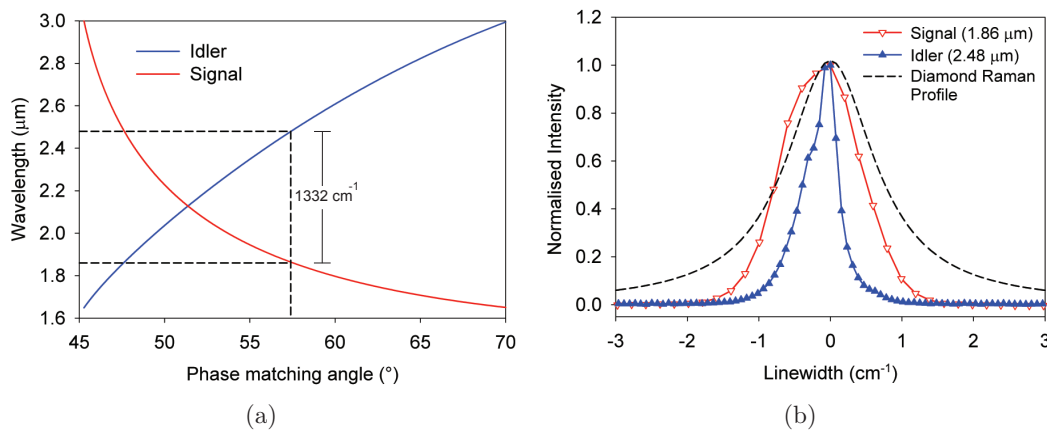


FIGURE 6.3: (a) Angular tuning curve for KTP with Type II phase matching in the XZ principal plane. The $1.064\mu\text{m}$ pump and the signal are polarised parallel, while the idler is perpendicular. (b) Littman-Metcalf OPO signal ($1.864\mu\text{m}$) and idler ($2.480\mu\text{m}$) linewidths for 1 mJ idler output.

polarisation. Whilst this could be used to pump a DRL, it is advantageous to have both polarisations aligned with a $\langle 111 \rangle$ axis. The signal and idler wavelengths were split using a dichroic mirror to allow independent adjustment of the polarisation and energy. The two wavelengths were then recombined and focussed into the DRL.

6.3 3.70 μm diamond Raman laser

Although the prior analysis highlighted $3.75\mu\text{m}$ as the desired Stokes wavelength, the ability to seed the DRL through mixing the OPO signal and idler wavelengths changed the design wavelength to $3.70\mu\text{m}$. The development of a $3.70\mu\text{m}$ DRL drew on several

important lessons in the near-IR, such as gain enhancement when the pump polarisation is aligned with a $\langle 111 \rangle$ axis and laser alignment techniques. Operating at longer wavelengths also introduced new challenges associated with the higher required intensities, increased loss and lower coating damage thresholds. In particular, the required pump intensities were deemed too high for AR coating the diamond facets. The use of an uncoated rectangular crystal provided a performance benchmark from which future design concepts, such as those discussed later in Chapter 7, could be compared.

In the progression to longer wavelengths, diffraction increases cavity mode sizes by $\sqrt{\lambda}$. The subsequent reduction in intracavity Stokes intensity increases SRS thresholds, as Stokes amplification depends both on pump and Stokes intensity. Employing cavity designs with strong confinement such as concentric and hemispheric resonators is therefore beneficial to achieving the gain required to overcome multiphonon absorption. These cavity types have a secondary benefit, in that the surrounding cavity optics are in a region of low intensity. This is critical for mid-IR DRLs where the increased thickness of the dielectric coatings reduces the damage threshold to many times less than the threshold intensity of the laser.

Numeric modelling of near-concentric and hemispheric cavities assumed a constant spot size within the cavity. Whilst this is clearly not valid for the cavity as a whole, as Figs. 6.5(a) and 6.5(b) show, the predicted intensity within the diamond crystal is relatively constant.

6.3.1 Concentric cavity results

The first successfully implemented mid-IR DRL had a concentric cavity, as shown in the inset of Fig. 6.4 and Fig. 6.5(a). The 8 mm, uncoated diamond crystal was rotated along the long edge by 35° to align the $[11\bar{1}]$ axis with the horizontal polarisations of both OPO pump wavelengths. The CaF_2 , 50 mm ROC cavity mirrors resonated the 3.70 μm Stokes with an out-coupling of 40% and double passed the 2.48 μm pump. CaF_2 lenses were placed either side of the diamond crystal to decrease the effective radius of curvature of the cavity mirrors. The increase in intracavity loss from the lenses is minor compared to the diamond multiphonon absorption and was offset by

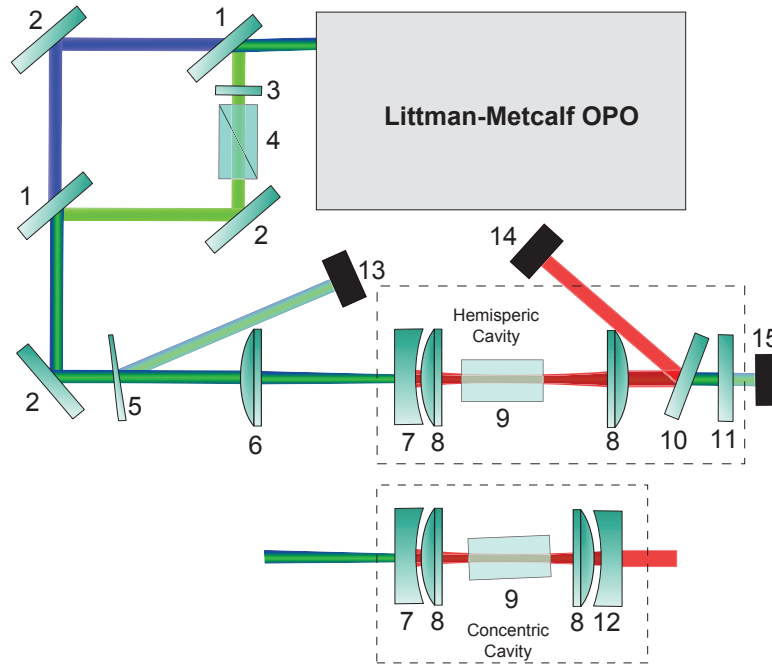


FIGURE 6.4: OPO pumped mid-IR DRL layout. (1) HT $1.864\mu\text{m}$, HR $2.480\mu\text{m}$; (2) HR mirror; (3) half-waveplate; (4) polariser; (5) wedge; (6) CaF_2 singlet; (7) ROC=50 mm, HT $1.864\mu\text{m}$, $2.480\mu\text{m}$, HR $3.70\mu\text{m}$; (8) $f=20\text{ mm}$ CaF_2 singlet; (9) 8 mm uncoated CVD single diamond crystal; (10) HT $2.480\mu\text{m}$, HR $3.70\mu\text{m}$; (11) HR $2.480\mu\text{m}$; (12) ROC=50 mm, HR 2.480 , 60%R at $3.70\mu\text{m}$; Energy meters: (13) Double-pass residual pump, (14) $3.70\mu\text{m}$ output, (15) Single-pass residual pump.

reducing the cavity length, which aids in threshold reduction.

The output of the Raman laser is shown in Fig. 6.6(a). The high intracavity loss restricted the slope efficiency to 13% and the conversion efficiency to 10%. Both values are presented with respect to the pump energy entering the crystal. It was proposed that the laser performance would improve by increasing the output coupling fraction and thus reducing the average time Stokes photons spent in the cavity. Numeric modelling in Fig. 6.6(b), using the model outlined in Chapter 4 and Appendix A, clearly demonstrates that with the higher cavity losses in the mid-IR, lower output coupler reflectivities are favourable. This is in contrast to a near-IR first Stokes DRL, where the modelled optimal reflectivities range from 30 to 60%.

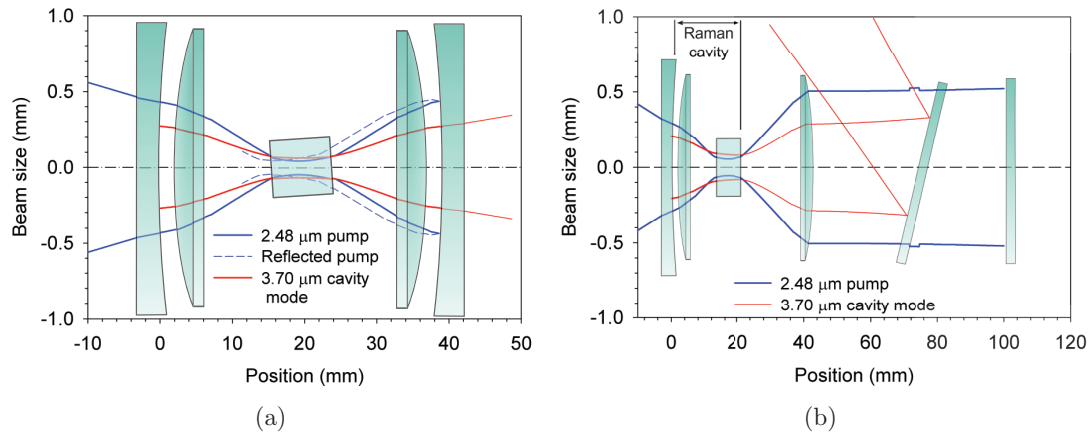
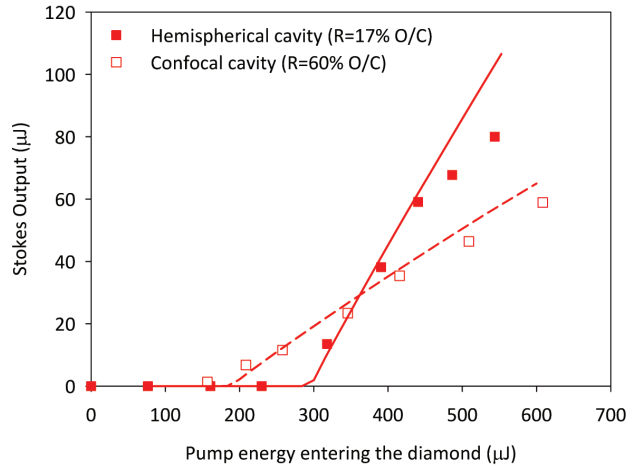


FIGURE 6.5: Modelled pump propagation and Stokes cavity mode for the (a) near concentric cavity and (b) near hemispheric cavity configurations. Optical component heights are not drawn to scale.

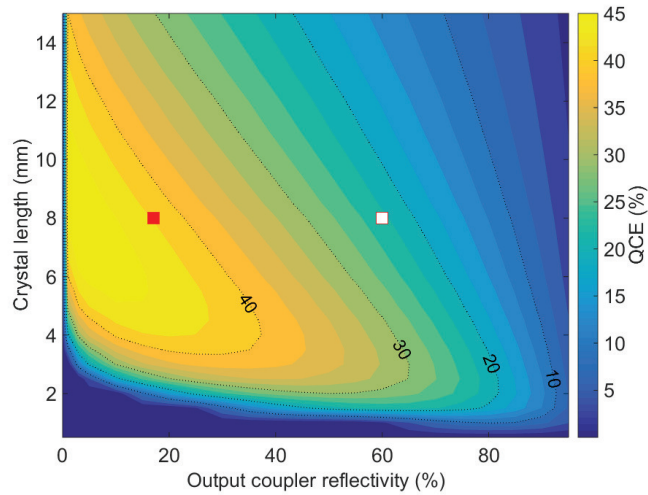
6.3.2 Hemispheric cavity results

To improve the output performance, the Raman cavity was redesigned to reduce losses from multiphonon absorption. In the absence of a lower reflectivity output coupler, the Fresnel reflection from a diamond facet (16.7%) formed a viable alternative. Figure 6.6(b) indicates that the combination of a 16.7% reflectivity output coupler and an 8 mm crystal is close to optimal. Forming a hemispheric cavity with the facet maintains a high cavity intensity in the crystal and reduces the Raman cavity length. In addition, only one diamond facet now acts as a parasitic loss. To compensate for the low pump reflection from the facet, an external lens and mirror was used to more efficiently double pass the pump. Figure 6.5(b) shows the relative sizes of the pump and Stokes beams in the cavity. The pump waist remained in the centre of the crystal, while the Stokes waist is now on the right hand facet. Output Stokes light that originated from the left hand facet reflection could be spatially filtered out due to the different distance from the pump-collimating lens. For modelling of this cavity, a partially reflecting output coupler was placed at the diamond facet and a second output coupler that only reflected pump light was moved 8 cm further back.

The laser performance displayed in Fig. 6.6(a) improved as expected with the increased output coupling. The slope efficiency more than doubled to 29%, while the



(a)



(b)

FIGURE 6.6: (a) Measured and modelled $3.70\text{ }\mu\text{m}$ output with the concentric and hemispherical cavities. The parameters used in the modelling are listed in Table A.2. (b) Modelled quantum conversion efficiency (%) of a $3.70\text{ }\mu\text{m}$ first Stokes DRL for varying output coupler reflectivity and crystal length. The 4 cm near-concentric cavity is assumed to have ideal mirror coatings, low loss facets and a SLM pump. $700\text{ }\mu\text{J}$ of $2.48\text{ }\mu\text{m}$ pump energy is focussed to a $110\text{ }\mu\text{m}$ diameter spot and double passed. The two squares are indicative of the experimental cavity configurations.

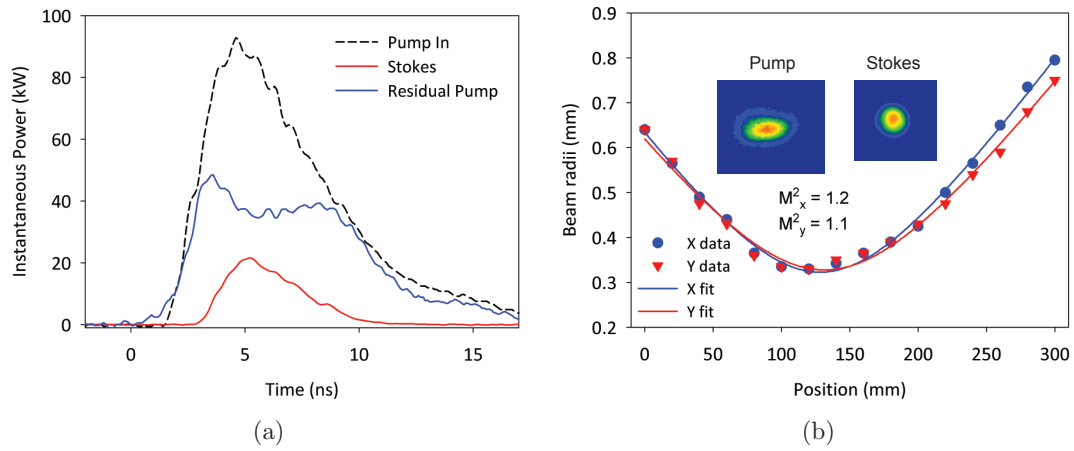


FIGURE 6.7: (a) Temporal pulse profiles for 535 μJ pump input at 2.480 μm and the subsequent double passed residual pump and Stokes output. (b) M^2 measurement for the same conditions. Insets show imaged focus profiles for the pump and Stokes beams.

threshold only increased moderately by 150 μJ . The combined effect was an improved average output energy of 80 μJ and a conversion efficiency of 15%. Taking into account the large change in photon energy the quantum slope and conversion efficiencies are 44% and 22%, respectively.

The temporal and spatial properties exhibited a similar profile to the near-IR DRLs. The Stokes temporal pulse profile had a 4 ns FWHM and peak power in the vicinity of 20 kW (Fig. 6.7(a)). The beam quality, shown in Fig. 6.7(b), was excellent and the Stokes output was circular, in contrast to the elliptical, astigmatic pump input.

6.3.3 Effect of multiphonon absorption loss

The Stokes output wavelength of 3.70 μm is in the three-phonon-absorption band and subsequently laser performance is degraded compared to the near-IR results. Calculating the amount of Stokes light lost through multiphonon absorption requires knowledge of the amount of pump light that has been converted. The double passed residual pump was measured using a wedge prior to the Raman cavity to sample the returning pump beam. The portion of this energy that had reflected from surfaces up to and including the first diamond facet was subtracted from the measurement to provide an estimation

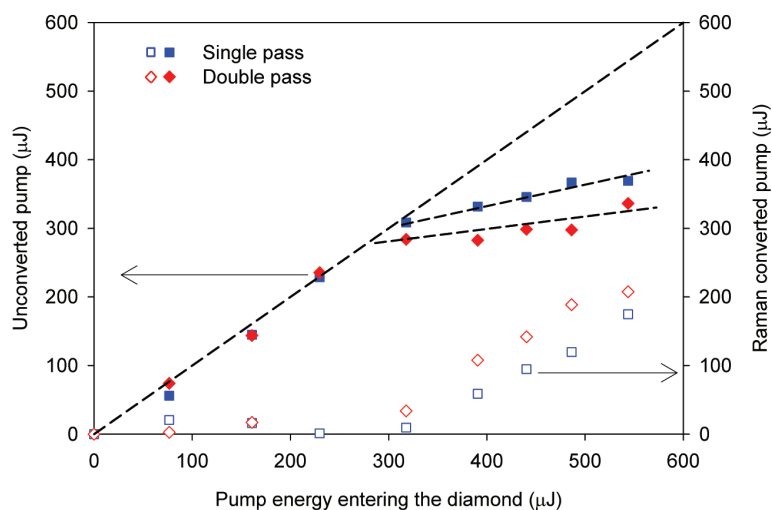


FIGURE 6.8: Unconverted pump (solid points) and the complementary converted pump (hollow points) after a single and double pass through the DRL. Values have been scaled to account for reflective and absorptive losses.

of the energy that had passed twice through the crystal. The data points were then scaled such that the slope prior to threshold with respect to the pump entering the crystal was unity. In this way an absolute scale is obtained that factors out all losses due to reflections after the first facet and any deviation from the initial slope is due to depletion from Raman conversion. There is a complicating factor however, as the portion of the conversion that occurs on the second pass has now been scaled for losses in the pump retro-reflection optics, when those losses are not relevant in this case. This leads to the residual pump data over estimating the amount of pump that has been converted. To make a more accurate determination of the converted pump the ratio of the Raman conversion that occurs on the first pass to the second pass needs to be known. The single pass residual pump was measured via leakage through the pump reflecting mirror and is also shown in Fig. 6.8. The energy difference between the measured single and double pass data above threshold is scaled by the loss factor of the rear of the cavity to give the final double pass values presented.

For the highest input pump energy point in Fig. 6.8, 207 μJ of pump is calculated to have been depleted due to the Raman process from 543 μJ entering the crystal.

This corresponds to 139 μJ of Stokes light after accounting for the change in photon energy. The measured Stokes output is 80 μJ , which leaves 59 μJ (42%) that has been lost primarily due to multiphonon absorption, with a secondary contribution from facet losses. Comparing the areas under the input pump, residual pump and Stokes pulse traces (Fig. 6.7(a)) in a similar manner, confirmed that approximately 40% of the generated Stokes light was missing. Correspondingly, given the low cavity Q , the magnitude of the loss is similar to the 44% single pass absorption loss at 3.70 μm .

6.3.4 Tuneable output

Tuning the OPO idler wavelength continuously varied the Raman wavelength. Figure 6.9(a) shows tuneable Stokes output from 3.38 μm to 3.80 μm , for 700 μJ average pulse energy incident on the Raman laser. The linewidth of the Stokes output was less than the 0.55 cm^{-1} resolution of the monochromator. On the long wavelength side of the tuning curve the limiting factor was increasing two phonon absorption. Multiphonon absorption coefficients above 2 cm^{-1} prevented the SRS threshold from being reached. On the short wavelength side of the tuning curve, a combination of increasing three-phonon absorption and reduced reflectivity of the input coupler at the Stokes wavelength defined the tuning limit. Given the three-phonon absorption coefficient is below 2 cm^{-1} , it should be possible, with improved cavity optics, to tune across the three-phonon band.

Figure 6.9(b) shows the outcome of numeric modelling for several scenarios. The blue curve is for a case that closely matches the experimental conditions and the prediction of the tuning range is good. Changing the input coupler to one that remains reflective at all Stokes wavelengths gives the green tuning curve, confirming that it is possible to traverse the three-phonon region. Finally the purple curve presents the predicted output energies for an idealised scenario with ideal optics, low loss on the first diamond facet and a SLM linewidth pump. The conversion efficiency at 3.70 μm is approximately doubled compared to the current case.

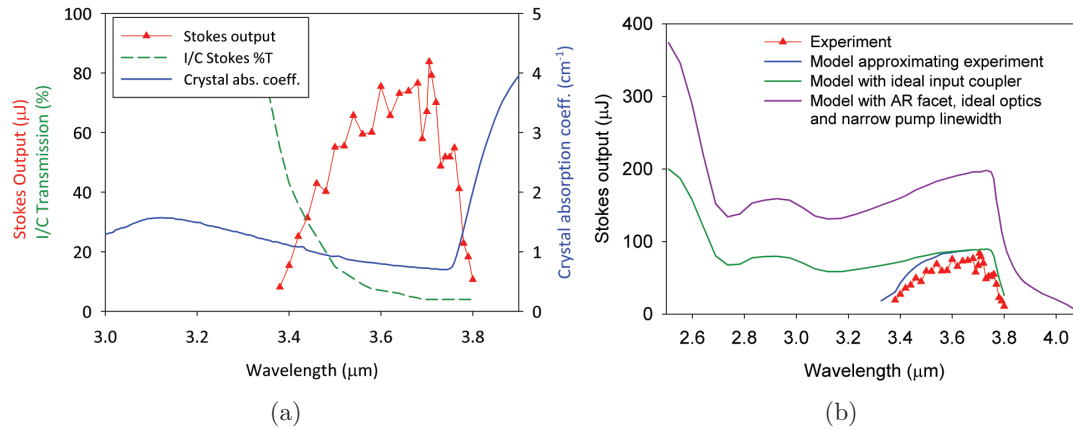


FIGURE 6.9: (a) tuning capability of the DRL for 700 μJ average pump energy. Also shown is the multiphonon absorption and input coupler reflectivity. (b) Comparison of experimental and modelled tuning capability for three cavity optic scenarios.

6.3.5 Threshold reduction through four-wave-mixing

The reduced g_R and substantial Stokes absorption lead to high threshold pump intensities in mid-IR DRLs. Typically the Stokes intensity in Raman lasers needs to build up from very weak sources such as spontaneous scattering. Tuning the OPO wavelengths such that their frequency separation equals ω_R produces seed photons at 3.70 μm through FWM. Seeding of Raman lasers through FWM processes has been investigated for higher order Raman generation [149, 224] and secondary pump lasers ([25, 46] and Section 7.2). The approach here is a combination, where the secondary pump is also at the anti-Stokes wavelength.

6.3.5.1 SRS modelling with four-wave-mixing

The intensity based Raman model used prior is not suitable for modelling FWM as it does not include the relative phases of the propagating beams. An equivalent set of equations expressed in terms of the electric field is given by [149, 225].

$$\begin{aligned}
\frac{dE_j^\pm}{dz} = & -g_j^E[(|E_{j+1}^+|^2 + |E_{j+1}^-|^2)(E_j^\pm + \sigma_{SP}^E(E_{j-1}^+ + E_{j-1}^-)) + E_{j+1}^\pm{}^2 E_{j+2}^\pm{}^* e^{\pm\Delta k_{j+1}z}] \\
& + g_j^E[(|E_{j-1}^+|^2 + |E_{j-1}^-|^2)(E_j^\pm + \sigma_{SP}^E(E_{j-1}^+ + E_{j-1}^-)) + E_{j-1}^\pm{}^2 E_{j-2}^\pm{}^* e^{\pm\Delta k_{j-1}z}] \\
& - E_j^\pm \alpha_j^E
\end{aligned} \tag{6.1}$$

where j is the Stokes order and the momentum vector mismatch, Δk_j , is given by $k_{j-2} + k_j - 2k_{j-1}$. The $E^2 E^* e^{\Delta k z}$ term describes the FWM process and the superscript E on the Raman gain, spontaneous Raman and loss coefficients indicates that these variables are converted to their electric field form. Table A.1 in Appendix A lists the conversion factors. Only degenerate mixing is considered, as in regions of normal dispersion, non-degenerate mixing has a larger Δk [149]. Similarly FWM between counter propagating waves is not considered as Δk is extremely high and the net impact negligible.

Dispersion in the crystal refractive index leads to poor phase matching between the collinear pump and Stokes beams. The usual cyclical flow of energy between wavelengths is however strongly biased by the Raman process, which does not rely on the same phase matching requirements. Figure 6.10(a) shows the large change in second and higher Stokes thresholds in a Raman generator with and without FWM included in the modelling. Strong FWM coupling, as is often found in Raman gases, is not always beneficial. It disperses the energy among several Stokes and anti-Stokes orders instead of the desired Stokes wavelength [226]. Higher normal dispersion found in crystals might actually be beneficial in some scenarios. The energy flow to shorter wavelengths with high dispersion is hindered, while lower thresholds are achieved at higher Stokes orders where dispersion is lower [149].

Unlike the commonly encountered case of the pump and first Stokes mixing to seed the second Stokes, the experiments here used two pump wavelengths. Stokes seed photons are immediately created and the large modelled threshold reduction compared to a single pump wavelength is apparent in Fig. 6.10(b).

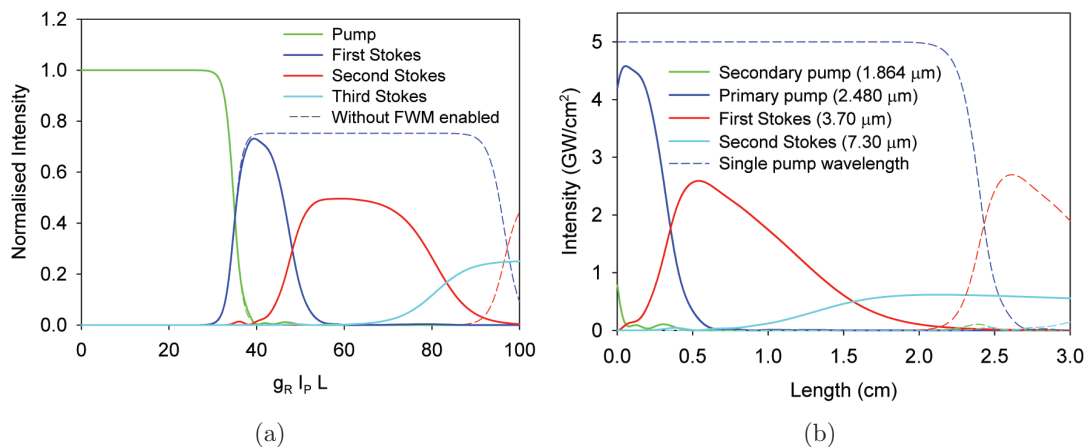


FIGURE 6.10: (a) Single pass SRS intensities with and without FWM included in the modelling. The model does not include absorption, and dispersion is equivalent to diamond in the mid-IR. (b) Modelled single pass Stokes output as a function of crystal length for 5 GW/cm² of total pump input. Dispersion and absorption are indicative of actual diamond values. Dashed lines are for a single 2.480 μm pump, while solid lines represent pumping with 1.864 μm and 2.480 μm , in an experimentally representative 1:6 ratio.

6.3.5.2 Results with FWM

Laser performance with and without the Stokes seed was performed concurrently with the previous experiments by blocking and unblocking the separated 1.864 μm beam (see Fig. 6.4). The threshold pump intensity, shown in Fig. 6.11, approximately halved, even after accounting for the energy in both pump wavelengths. For the higher efficiency hemispheric cavity, the maximum 3.70 μm output increased by 44% to 115 μJ and the conversion efficiency, including both wavelengths, was 18%.

In the current OPO based scenario where the 1.864 μm wavelength is available as a by-product, it would be ideal to focus as much energy as possible into the crystal to maximise 3.70 μm output. Laser damage to the facet and bulk of the diamond crystal however place a limitation on the total intensity. The slope efficiency for increasing 2.480 μm energy was higher than for increasing 1.864 μm energy (29% cf. <16%). Thus, the decision was made to attenuate the 1.864 μm energy relative to the incident 2.480 μm energy.

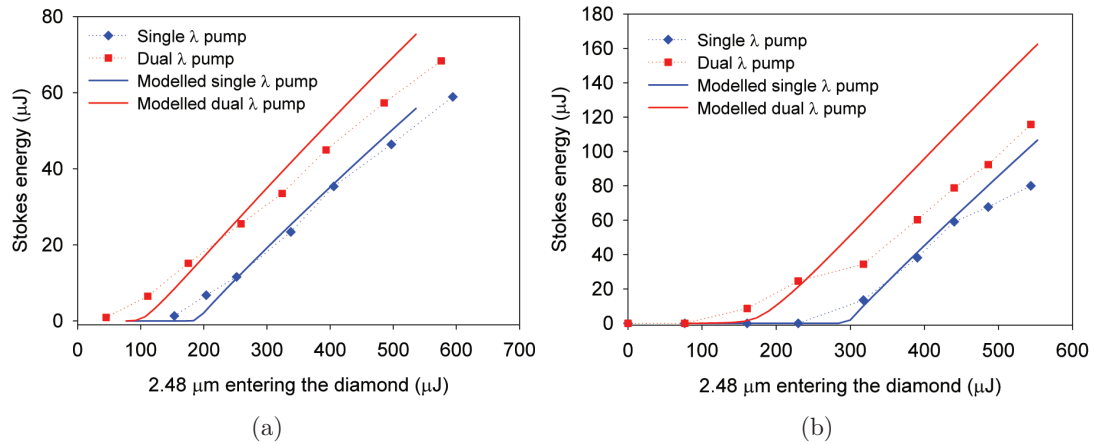


FIGURE 6.11: Comparison of modelled and experimental data with and without the FWM seed. (a) Concentric cavity with 60% reflectivity output coupler (b) Hemispheric cavity with diamond facet output coupler.

The controlled FWM conditions available with the dual wavelength pumping assisted in validating the numeric models used for predicting the performance of DRLs operating beyond 6 μm . At these longer wavelengths the reduced dispersion and lower g_R in diamond increase the importance of incorporating FWM in the modelling. Figure 6.11 shows the ability of the electric field based model to calculate the relative changes in laser output with and without FWM. The agreement, while not perfect, is sufficient to assess the viability of different techniques for longer wavelength Raman lasers.

6.3.6 Laser induced damage of the diamond crystal

The high pump intensities required for mid-IR DRLs create a high risk of damage to the diamond crystal, and limits energy output. For example, the peak pump power incident on the facet at threshold for the hemispherical cavity configuration exceeded 1.5 GW/cm² (3 GW/cm² in the centre of the beam profile). Damage was observed on input and output facets, depending on numerous factors such as surface contaminants and the exact location of the incident and reflected pump waists. Damage became increasingly likely as the total estimated intracavity peak intensity exceeded 6 GW/cm².

Complete cleavage of the crystal was observed on three occasions along a $\langle 111 \rangle$

plane, the weakest plane of diamond for sheer stress fracture [227]. The consistent factor on each occasion was the creation of a beam waist in the crystal that had a confocal parameter shorter than the crystal length. This led to intensities surpassing the bulk damage threshold prior to the surface damage threshold. Internal graphitisation leads to the formation of large stresses, as graphite is less dense than diamond by a factor of 1.6 [228]. It also is highly absorbing, which is presumed to cause a chain reaction of damage, leading to the propagation of large planar cracks or crystal splitting (Fig. 6.12).

The first incidence of cleavage occurred after tightening the pump focus in an attempt to reduce thresholds. Both OPO wavelengths were focused into the crystal and as the damage was unexpected, exact details on the intensities are not known. The second and third cases were related to the formation an unstable cavity whilst adjusting the input coupler. Each time the damage occurred at relatively low pump energies ($\sim 100 \mu\text{J}$) as the input coupler was brought into alignment. Subsequent analysis revealed that the spacing between the crystal and the input lens/mirror was too great leading to an unstable cavity. It is hypothesised that any reflections from the output facet were tightly re-focussed in a strongly pumped region of the crystal and subsequently amplified to damaging levels (see Fig. 6.13). The intensity of the amplified $3.70 \mu\text{m}$ beam is unknown and again there is insufficient data to obtain a damage threshold. Due to the destructive nature of the testing and limited available samples, no further systematic study of this damage mechanism was conducted.

6.3.7 Mid-IR DRL performance comparison

In order to evaluate the mid-IR performance of diamond it is important to benchmark it against nonlinear frequency conversion with other materials. Given the challenges associated with solid-state mid-IR Raman conversion there is a limited list of published examples with which to compare diamond (Table 6.2). KGW and BaWO_4 have reported good efficiencies to wavelengths less than $3 \mu\text{m}$ [54, 229]. Both crystals are transparent out to $5 \mu\text{m}$, so providing the Raman gain remains high enough to avoid damage, there is scope to extend their wavelengths further.

Numerous proposals exist for waveguide based mid-IR silicon Raman lasers [48–51],

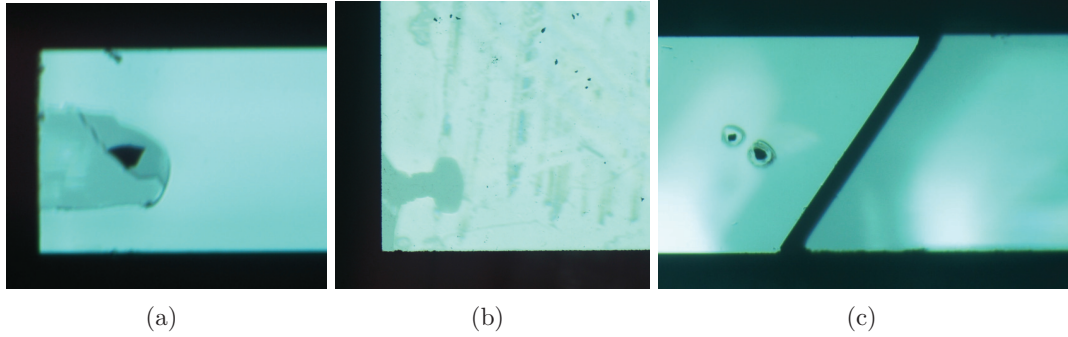


FIGURE 6.12: : (a),(b) End and top view of bulk damage, initiated approximately $750\text{ }\mu\text{m}$ behind the facet. In this instance, the damage did not lead to a complete cleavage of the crystal. (c) End view of cleavage of the crystal due to internal damage. Also seen are two previously existing facet damage spots.

Material	Length (mm)	Pump λ (μm)	Stokes λ (μm)	QCE	Ref.
Diamond	8	2.48	3.70	22 (48)	this work
KGW	50	1.9	2.3, 2.9	46	[54]
BaWO ₄	20	2.1	2.6	17	[229]
Silicon amplifier	25	2.88	3.39	neg.	[49]
As ₂ S ₃ fibre	3000	3.0	3.34	22	[56]
As ₂ S ₃ fibre	2800	3.0	3.77	3	[57]
ZGP OPO	14	2.1	3.55	62	[230]
QPM LiNbO ₃ OPO	40	1.06	3.84	58	[17]

TABLE 6.2: Quantum conversion efficiencies (QCE) for solid-state mid-IR Raman lasers. The value in brackets for diamond is the predicted efficiency with an optimal hemispheric cavity. Also included are examples of efficient $1\text{ }\mu\text{m}$ and $2\text{ }\mu\text{m}$ pumped mid-IR OPOs.

but small-signal amplification of a $3.4\text{ }\mu\text{m}$ HeNe laser in bulk silicon is the only experimental report [49]. A possible reason for the lack of experimental results could be that higher than expected threshold intensities are leading to damage of coatings and crystals. Numeric analysis of mid-IR silicon Raman lasers typically scale the referenced near-IR g_R with pump frequency, using 20 cm/GW at $1.427\text{ }\mu\text{m}$ [99]. Measurements of g_R near $1.5\text{ }\mu\text{m}$ vary substantially, with reported values ranging from 9.5 cm/GW to 37 cm/GW [99, 231] and are complicated by nonlinear absorption [232] and waveguide losses. Scaling g_R values obtained at $1.5\text{ }\mu\text{m}$ with frequency potentially overestimates the mid-IR value, due to the proximity of the silicon bandgap at $1.1\text{ }\mu\text{m}$. The only

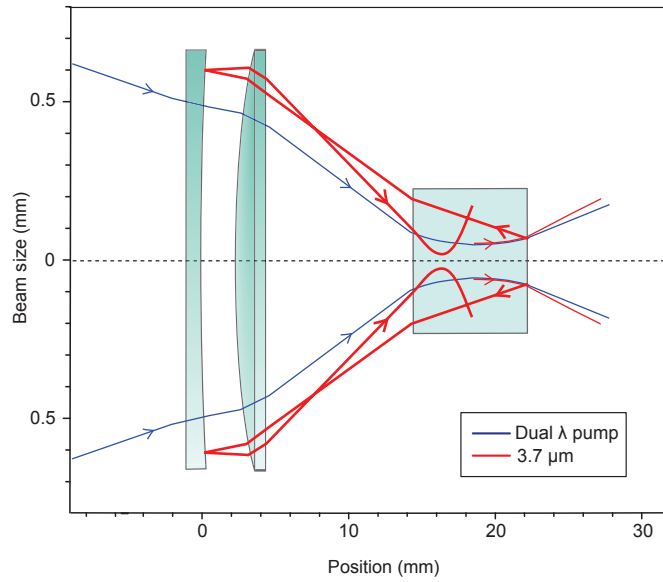


FIGURE 6.13: Proposed route to internal damage of the diamond crystal due to the formation of an unstable cavity.

measurement at mid-IR wavelengths estimated g_R to be 5 cm/GW for a pump wavelength of 2.88 μm [49], which after scaling for wavelength, is at the low end of reported values.

Chalcogenide fibre Raman lasers are suitable for low peak and average power Raman conversion of CW lasers. Spectral broadening degrades conversion to second and higher Stokes orders and high average powers are likely to be challenging due to the low melting point of the glass [57]. Raman conversion in chalcogenide glass micro-resonators has also recently been reported [58], with 3rd Stokes conversion of a 1.88 μm pump out to 2.35 μm . Thresholds are low (sub-mW), but conversion efficiencies are a fraction of a percent.

Frequency conversion to mid-IR wavelengths using OPOs has demonstrated high average powers [45] and broad tuning across the mid-IR and longwave regions [44]. The maximum reported quantum conversion efficiencies from 1 μm and 2 μm pump sources is around 60% [17, 230].

An optimised DRL is a competitive option for wavelength conversion of pulsed lasers, such as those based on Tm^{3+} , Ho^{3+} and Cr:ZnSe, to longer mid-IR wavelengths.

The larger Raman frequency gives diamond a deeper extension into the mid-IR per Raman shift compared to other solid-state Raman materials. The larger fractional change in photon energy when converting longer pump wavelengths increases the heat load, which diamond is better placed to handle. Clearly the multiphonon absorption is disadvantageous, but the demonstrated quantum conversion efficiency of 22% is predicted to more than double to 48% under optimal conditions (see Figs. 6.6(b) and 6.9(b)), placing it on par with the other efficient mid-IR Raman results [54]. In the near-IR, Raman and OPO conversion efficiencies are similar, however in the mid-IR, absorption of Stokes light reduces optimised DRL performance by $\sim 25\%$. Although less efficient, mid-IR DRLs do have beam quality and linewidth advantages. As previously described, the beam quality of high power OPOs are generally worse than the pump [17, 45, 233, 234], compared to the improved quality discussed in Chapter 4 and Fig. 6.7(b). The free running linewidth here was less than 0.55 cm^{-1} compared to linewidths up to 150 cm^{-1} in OPOs [45].

6.4 Wavelengths longer than the two-phonon absorption region

Previously, Raman lasers operating with Stokes wavelengths beyond $5\text{ }\mu\text{m}$ have been limited to a few demonstrations using gases [25, 46, 47], liquids [47] and atomic vapours [235]. Each of these approaches require large ($> 30\text{ cm}$) Raman cells and are limited to low average powers. Most high performing solid-state Raman materials are not transparent in this wavelength region and the results listed in Table 6.2 represent the longest reported wavelengths.

Raman shifting over the two-phonon absorption features in diamond accesses the transparent region beyond $6.5\text{ }\mu\text{m}$. Developing a DRL beyond $6.5\text{ }\mu\text{m}$ is challenging as coupled with diminishing g_R , it necessitates pumping in a region of multiphonon absorption. Using the equation set described by Eq. (6.1), the predicted range of wavelengths for ideal first and second Stokes lasers ($\sim 3.75\text{ }\mu\text{m}$ and $\sim 2.5\text{ }\mu\text{m}$ pump

lasers, respectively) is shown in Fig. 6.14. As expected, targeting the local absorption minima at multiples of the Raman frequency provides the greatest output. The effects of two phonon absorption bound both the upper and lower limits of the tuning range. On the short wavelength side, increasing two-phonon absorption directly depletes the output. Conversely, the long wavelength tuning limit is set by increasing absorption of pump wavelengths beyond $3.75\text{ }\mu\text{m}$. The larger pulse energy shown for the first Stokes case is due to the reduced quantum defect; the quantum conversion efficiencies are similar.

The $6\text{--}8\text{ }\mu\text{m}$ tuning range is in a region of high atmospheric absorption as shown in the upper plot of Fig. 6.14. The atmosphere will also attenuate sunlight and a laser in the $6\text{--}8\text{ }\mu\text{m}$ band may be of interest for short range outdoor sensing applications, where the reduced background light will reduce detector noise. Laser wavelengths between 6.1 and $6.45\text{ }\mu\text{m}$ are also in demand for surgical applications, where the overlap of water and protein absorption bands result in tissue ablation with reduced collateral damage and improved healing [236].

While pumping with $3.75\text{ }\mu\text{m}$ is conceptually the simplest option, a second Stokes laser pumped at $2.5\text{ }\mu\text{m}$ offers several advantages. FWM between the $2.5\text{ }\mu\text{m}$ pump and the $3.75\text{ }\mu\text{m}$ first Stokes aids in reducing the threshold intensity. A second Stokes laser is also compatible with the previously developed OPO.

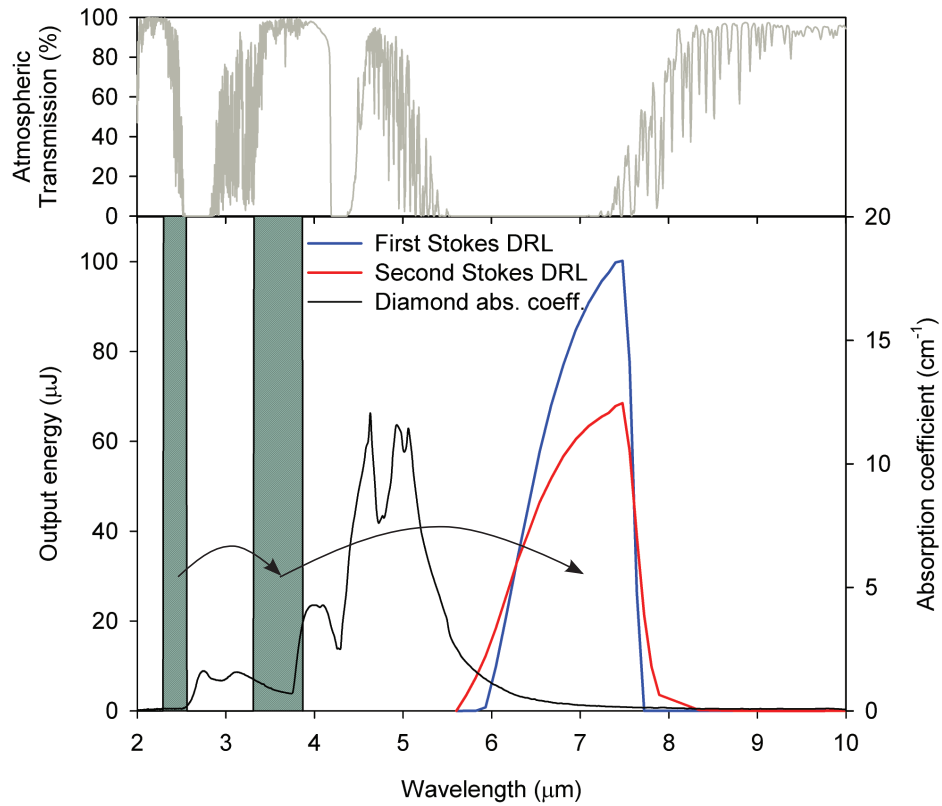


FIGURE 6.14: (Lower) Modelled tuning ranges of first and second Stokes DRLs near 7 μm under optimised conditions (4 cm cavity, low loss facets and narrow pump linewidth). The shaded rectangles indicate the span of the tuneable pump lasers. Pump energy is constant at 700 μJ . (Upper) Atmospheric transmission for a 1 km path 2 m above the ground. Data generated with MODTRAN 5.

6.4.1 7.30 μm laser experiment

The design of the 7.30 μm DRL cavity, shown in Fig. 6.15, was similar to the original concentric 3.70 μm DRL (see Fig. 6.5(a)). The cavity mirrors were changed to be highly reflective at 3.70 μm to encourage conversion to the second Stokes. To reduce absorption losses, the output mirror substrate was ZnS, while the input coupler substrate remained as CaF_2 . Once again the goal of the concentric cavity was to maximise the intensity in the crystal to reduce thresholds, while reducing the intensity on the mirrors to prevent damage. Another difference with the 3.70 μm DRL was the removal of the intracavity CaF_2 lenses to lengthen the cavity and further reduce the intensity on

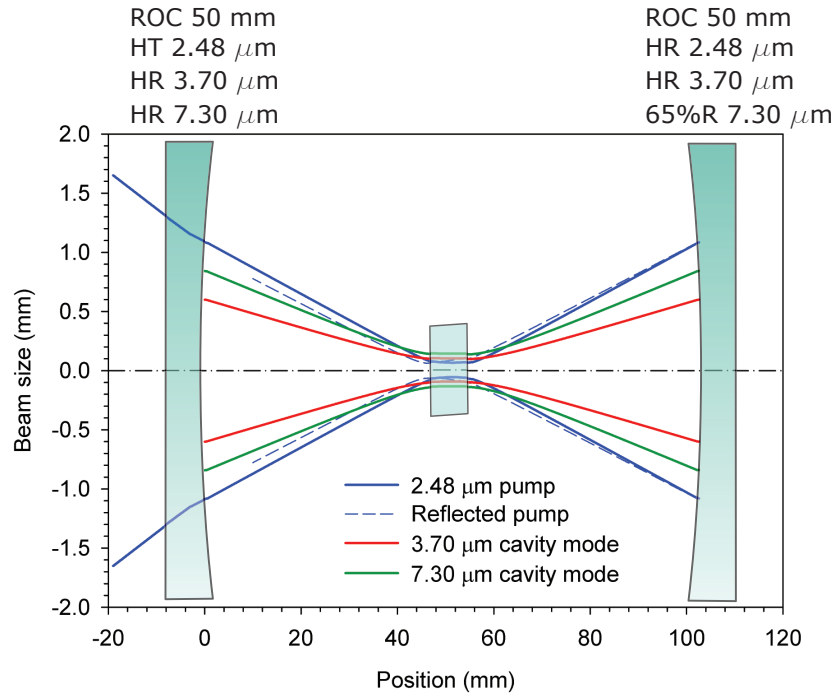


FIGURE 6.15: Calculated pump and cavity beam sizes in the 7.30 μm Raman laser cavity. Optic heights are not to scale.

the input coupler. Although the modelling indicated that this would increase the SRS threshold, it was necessary to compensate for the very low measured mirror coating damage threshold of approximately $30 \text{ MW}/\text{cm}^2$. Without the intracavity lenses, the focal length of the main focussing lens (item (6) in Fig. 6.4) was reduced from 100 mm to 50 mm to maintain a similar pump spot size in the crystal ($120 \mu\text{m}$ diameter). As with previous experiments, the pump polarisation was aligned with the diamond $[11\bar{1}]$ axis.

Prior analysis of the near-IR second Stokes DRLs demonstrated that low reflectivity output couplers improved performance (Section 4.3). In the present case, since the operation point will be close to threshold, the higher output mirror reflectivity of 65% is advantageous. Coarse alignment and length adjustment of the cavity was performed by initially using an output coupler designed for $3.70 \mu\text{m}$ and maximising the first Stokes energy. The second Stokes output coupler was then inserted and a detector monitored for evidence of $7.30 \mu\text{m}$ output.

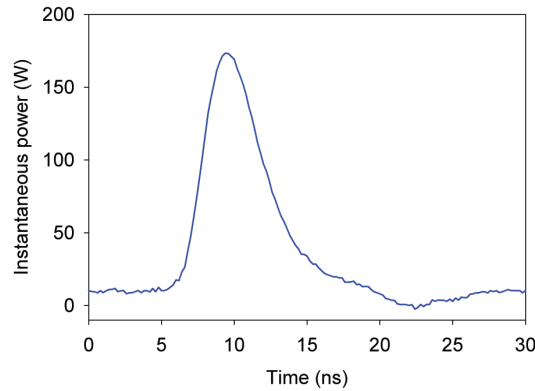


FIGURE 6.16: Measured 7.30 μm pulse profile with 700 μJ pump.

For 700 μJ of pump energy incident on the cavity, Fig. 6.16 shows the observed signal on a fast detector (Vigo PEM 10.6, 1 ns rise time). Insertion of additional longpass filters confirmed that the signal was not leakage of shorter wavelengths. With the signal maximised, the energy meter readings were of the order of 1 μJ . Accurate readings were inhibited by the proximity of the readings to the lower limit of the energy meter (0.3 μJ for a Coherent J-10MB-LE sensor). Attempts to increase the confinement of the cavity mode in the crystal by increasing the cavity length, resulted in the damage of the crystal and prevented further measurements. The results agree with the modelling in Fig. 6.17 which shows that for the current experimental conditions, the threshold intensity is similar to the damage threshold.

Despite the low efficiency, this result demonstrates, for the first time, that it is possible to make a DRL at wavelengths on the long wavelength side of the two-phonon absorption peak. Prospects for improving performance are discussed in Chapter 7.

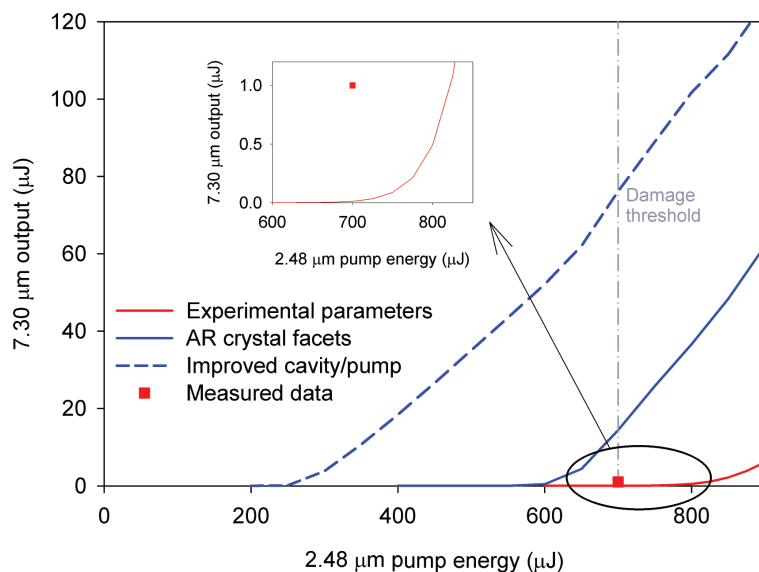


FIGURE 6.17: Modelled second Stokes output for experimentally representative parameters (red line), with AR facets (blue line), and a 4 cm cavity length with a SLM pump (blue dashed line). The inset enlarges the region near threshold.

6.5 Current limits of mid-IR performance

Intracavity loss is the main factor impeding mid-IR DRL performance. The loss of approximately 40% of the $3.70\text{ }\mu\text{m}$ Stokes light through multiphonon absorption was discussed in Section 6.3.3 and the rapid increase in absorption beyond $3.75\text{ }\mu\text{m}$ also limited the tuning range of the DRLs. A second large factor was Fresnel reflections from the crystal facets. The uncoated facets degraded the $7.30\text{ }\mu\text{m}$ DRL performance in particular, as three wavelengths are each experiencing $\sim 17\%$ per facet loss entering and leaving the crystal. Figure 6.17 demonstrates the calculated improvement in output if the facet reflections are eliminated. Fresnel reflections from the CaF_2 intracavity lenses used in the first Stokes DRLs also introduced an additional 3% per surface loss. Unlike the diamond facets, the lenses are not placed in the beam waist and dielectric AR coatings are feasible. Two alternative options for reducing diamond facet reflections, that also have high damage thresholds, are presented in Chapter 7.

The mid-IR DRLs required longer cavity lengths, compared to the near-IR experiments, to reduce the laser intensity on the mirrors and compensate for the increased cavity mode size at longer wavelengths (through the use of concentric and hemispheric cavity designs). Lengthening the cavity increases the build up time of the Stokes photons and subsequently raises the SRS threshold. Shortening the total cavity length from 10 cm to 4 cm by reducing the mirror ROC from 50 mm to 16 mm is the dominant factor behind the improved performance seen with the dashed line in Fig. 6.17. A drawback of a shorter cavity is that the mirrors are closer to the pump waist and subject to higher pump intensities. The damage threshold of the mirrors would need to increase by a factor of 5 over the current samples to accommodate the modelled change in cavity length.

Efficiency and average power were also limited by the pump laser. The 2.5 μm OPO output had a measured linewidth correction factor of 0.85, which indicates that a further 15% reduction in the SRS threshold is possible through further linewidth narrowing. The pump average power was also six orders of magnitude below the potential diamond power limits discussed in Chapter 4. High peak and average power holmium and thulium lasers available near 2 μm generate up to 100 W of average power [45, 237] and are potential sources to combine with diamond to generate new wavelengths from 2.5 to 2.9 μm with high average power and brightness.

Modelled examples in Figs. 6.6(b), 6.9(b), 6.14 and 6.17 demonstrate that combining the improvements to loss, cavity length and pump linewidth results in maximum quantum conversion efficiencies in excess of 40% for both first and second Stokes lasers. Multiphonon absorption accounts for the remainder of the difference between the quantum conversion efficiencies in excess of 70% demonstrated in the near-IR. While multiphonon absorption is an unavoidable intrinsic property of the crystal, some concepts for manipulating the absorption profile are explored in Chapter 7.

6.6 Chapter Summary

This chapter describes the performance of first and second Stokes mid-IR DRLs. Both output wavelengths are the longest demonstrated from a solid State Raman laser. The first Stokes laser had a tuning range spanning 3.38 μm to 3.80 μm and at the local minima between the two and three phonon absorption features the quantum conversion efficiency was 22%. The Raman conversion of the pump was actually much more efficient, with approximately 40% of the Stokes light absorbed in the crystal prior to exiting the cavity. The output beam quality was near diffraction limited, in contrast to the pump which had lower beam quality and substantial astigmatism. Modelling and experiments confirmed that increasing the output coupling fraction lowered the Stokes absorption and improved performance.

The smaller g_R and increased losses at mid-IR wavelengths led to high pump intensities to reach threshold. Damage to the crystal facet limited the maximum permissible intensity to approximately 6 GW/cm². As a means to reduce the required pump intensity to reach threshold, seeding the Stokes output through FWM between the OPO signal and idler approximately halved thresholds and led to a 50% increase in the Stokes output.

A second Stokes 7.30 μm DRL was demonstrated, with output pulses of the order of 1 μJ (175 W peak power) generated near the facet damage threshold. Modelling suggests that with reduced Fresnel losses, a shorter cavity, and a SLM pump, a quantum conversion efficiency in excess of 40% may be possible.

6.6.1 Publications arising from the work in this chapter

Peer reviewed journal articles

Sabella, A., Piper, J. A., and Mildren, R. P., “Diamond Raman laser with continuously tunable output from 3.38 to 3.80 μm ”, *Optics letters*, **39**(13), 4037-4040, (2014).

Conference presentations

Sabella, A., Piper, J. A., and Mildren, R. P., “Mid-infrared diamond Raman laser with tuneable output”, at SPIE LASE, San Francisco, USA, (2014). *Oral Presentation*

7

Strategies for improving mid-IR performance

The mid-IR DRL quantum conversion efficiencies were considerably less than achieved in the near-IR (Chapter 4). While reduced g_R and increased absorption will always affect performance, there are opportunities to improve the Stokes output. The crystals used in the experiments were uncoated rectangular samples, which led to large Fresnel losses. Brewster cut facets and anti-reflecting microstructures are considered as two high damage threshold options for reducing loss. Multiphonon absorption is an intrinsic property of the diamond crystal and therefore impossible to completely remove. It is however possible to manipulate the absorption profile by changing the isotopic content and cryogenic cooling. These approaches are examined as means to alter the span and strength of the absorption, respectively. The previous chapter demonstrated that FWM

was an effective means to reduce SRS thresholds, but required a specific secondary pump wavelength. Modelling of an alternative pumping scheme with an arbitrary second pump wavelength is investigated as a method to reduce the threshold of long wavelength DRLs.

7.1 Modification of the diamond crystal

7.1.1 $\langle 111 \rangle$ Brewster cut crystal

In conjunction with multiphonon absorption, facet reflections are the largest source of loss (16.7% loss per surface). The high pump intensities required at longer wavelengths however, are not compatible with traditional AR coatings. Cutting laser crystals with facets at Brewsters angle is a well-known method for reducing Fresnel losses for a single polarisation that does not require coating the crystal [133]. The first reported DRL of substantial efficiency used a Brewster cut crystal that was low loss for $[01\bar{1}]$ polarised light [69]. Cutting the diamond crystal such that the low loss polarisation aligns with an $\langle 111 \rangle$ axis will maximise g_R and reduce the SRS threshold compared to the $[01\bar{1}]$ cut crystal.

Figure 7.1(a) compares the cut of the original $[01\bar{1}]$ Brewster crystal to one that is low loss for $[11\bar{1}]$ polarisation. Rotating the crystal 35.3° , whilst maintaining the same geometric ‘Brewster planes’ defines the revised end facets. Relative to the optical table, the pump is horizontally polarised in both cases.

Whilst Brewster facets offer broadband low loss, the penalty is that the beam diameter is expanded by a factor of 2.6 in the p-polarised plane (horizontal plane in Fig. 7.1(a)). As gain is proportional to intensity in Raman lasers, SRS thresholds also increase by a factor of 2.6. Figure 7.2 compares the modelled performance of an uncoated rectangular crystal and a Brewster cut crystal with the ideal case of an AR coated rectangular crystal. Figures 7.2(a) and 7.2(b) show that for high gain, low absorption cases, such as in the near-IR, the Brewster crystal offers improved performance over the uncoated rectangular crystal. For a first Stokes laser, the larger

threshold penalty is quickly overcome by the higher slope efficiency. For a second Stokes laser the Brewster crystal is also clearly more favourable. The rapid increase in first Stokes intensity in the high Q cavity (recall Fig. 4.10) leads to a minimal additional penalty from the expanded spot size. The uncoated square crystal on the other hand experiences Fresnel losses at all three wavelengths and performance suffers.

The situation is different in the mid-IR. The higher absorptive losses, coupled with lower g_R , lead to lasers that cannot be operated as high above threshold before crystal damage becomes a concern. Pump pulse energies higher than possible with normal incidence pumping are required to achieve larger pulse energies with a Brewster crystal. In theory this should be achievable due to the elongated pump spot in the crystal. If the Bettis-House-Guenther (BHG) scaling law outlined in Chapter 2 holds, the 2.6 times increase in beam area results in $\sqrt{2.6} = 1.6$ times reduction in damage threshold intensity. Thus the predicted maximum pulse energy for Brewster's angle under the current conditions is 1120 μJ .

An 8 mm long, low birefringence crystal with low loss for $[11\bar{1}]$ polarisation was manufactured by Element 6. Unfortunately the crystal damaged at less than half the expected pump intensity, based on the BHG scaling law, and no significant mid-IR results were obtained. The reason for the lower than expected damage threshold is unknown and further investigation of the surface condition is required.

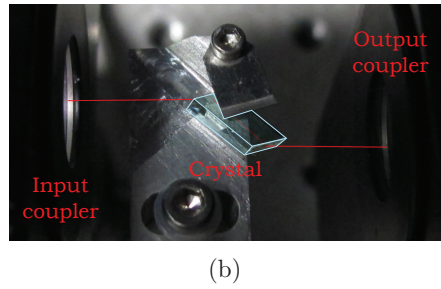
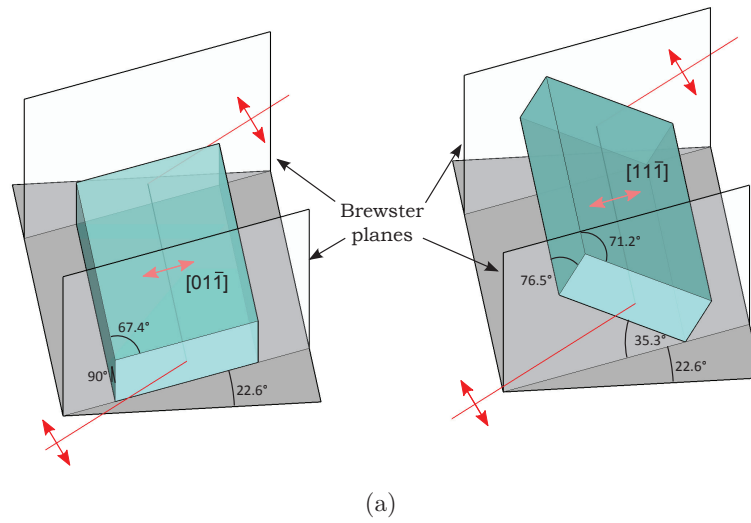


FIGURE 7.1: (a) LHS: Original Brewster cut used in [69]. RHS: Enhanced g_R Brewster crystal. The red polarisation arrows are all horizontally polarised with respect to the grey table plane. (b) Photo of the revised Brewster crystal in an external Raman laser cavity. Note that the crystal has been highlighted using photo editing software to increase visibility.

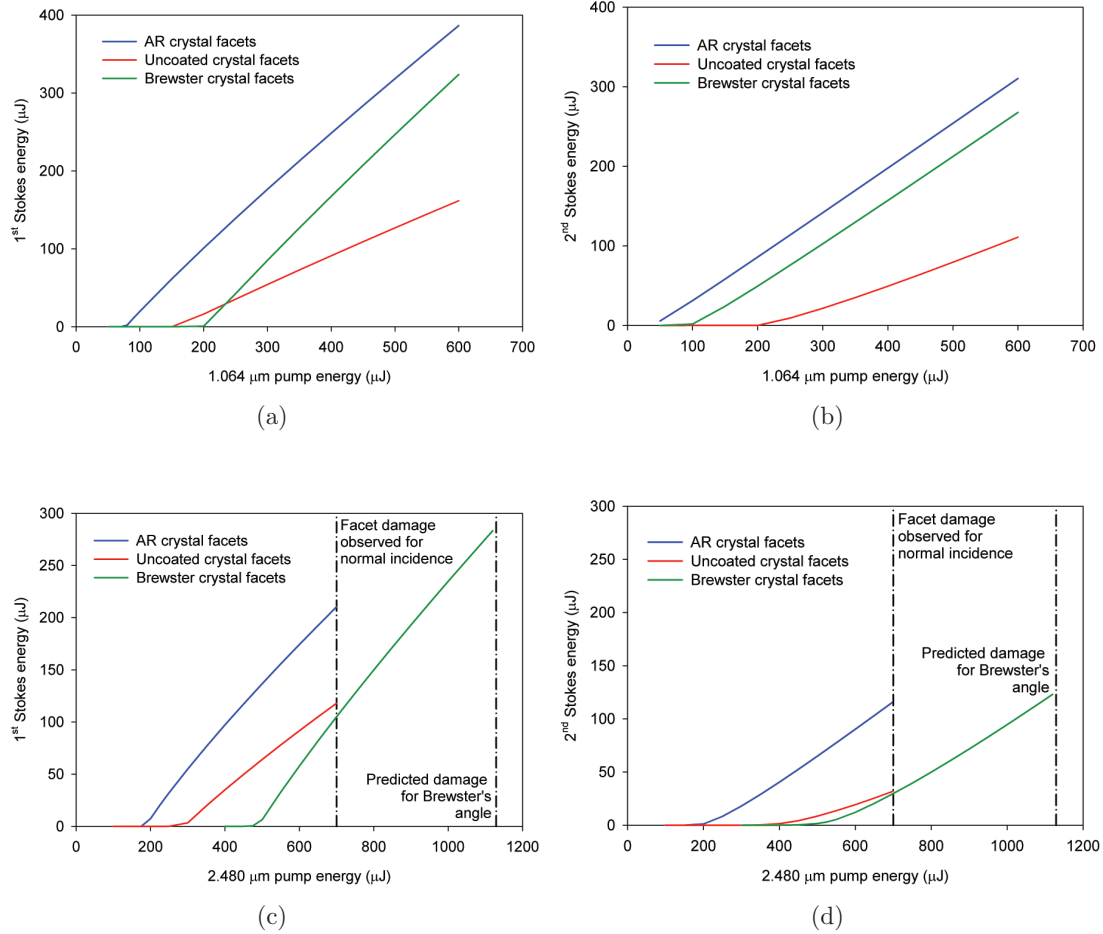


FIGURE 7.2: Modelled first Stokes (LHS) and second Stokes (RHS) DRLs pumped at 1.064 μm (top) and 2.48 μm (bottom). Note that the pump and cavity parameters are different between the two pump wavelengths. The near-IR DRL parameters are as used in Chapter 4. The mid-IR DRL model uses the parameters in Table A.2, with a short 4 cm cavity and a SLM pump.

7.1.2 Anti-reflecting microstructures

Anti-reflection micro-structures (ARMS) are a technology that offers broadband AR performance with damage thresholds similar to the bulk material [238]. Figure 7.3(c) displays the improved transmission for several diamond windows with ARMS surfaces designed for an incident wavelengths from 8-12 μm . Unlike Brewster facets there is no expansion of the spot size or restrictions on polarisation, and the improved modelled performance is shown by the blue curves in Fig. 7.2.

Abrupt changes in refractive index are the source of Fresnel reflections as light is incident on the diamond facet. ARMS surfaces are designed to present a gradual change in the effective refractive index seen by the light and thus suppress reflections. To avoid diffraction effects, the period of the structured features must be sub-wavelength, i.e. $p < \lambda/n_2$, as labelled in Fig. 7.3(a). The height of the features must also be greater than half the design wavelength ($h > \lambda/2$). For optimum performance there should be a high fill factor of the surface features, and Fig. 7.3(b) shows several commonly used profiles. Taking the 2.48 μm pumped second Stokes DRL as an example, broadband AR performance is required from 2.48 μm to 7.3 μm . This requires a feature period less than $2.48 \mu\text{m}/2.38 = 1.04 \mu\text{m}$ and feature heights greater than $7.3 \mu\text{m}/2 = 3.65 \mu\text{m}$.

A key benefit of ARMS surfaces is a potentially high damage threshold. The limited data presented in [238] shows variation in the structured surface damage thresholds of diamond, ranging from a third to double the untreated surface. More comprehensive studies of other materials show laser damage thresholds of AR structured surfaces are comparable to the untreated surface [238].

Difficulty of fabrication is the main drawback of ARMS surfaces. This is particularly true of diamond, which is difficult to machine or etch. Laser ablation [240], ion beam milling [241], substrate patterning [242] and plasma etching [243] have all been used to create AR structures in diamond. Of these, plasma etching appears to be the most promising for creating large uniform arrays on single crystal diamond facets.

ARMS technology has the capability to benefit DRLs of all wavelengths, not just the mid-IR, as it provides increased laser damage thresholds, chemical inertness and scratch resistance, compared to dielectric coatings. The recent commercial availability

of polycrystalline diamond windows with ARMS surfaces for high power CO₂ laser applications is promising for incorporating ARMS technology in future DRLs [244].

Similar microstructured features may also be designed to create photonic band gaps that act as a filter and reflect certain wavelengths [245, 246]. This approach may be an option for overcoming the low damage thresholds typical of the thick dielectric coatings used on the mid-IR cavity mirrors. The thickness and number of deposited layers required for microstructured reflectors is greatly reduced compared to standard dielectric coatings [246]. Initial trials in the visible and near-IR reported damage thresholds lower than standard thin film coatings [247], but the authors predict improvements by utilising techniques proven for high damage threshold thin film coatings.

7.1.3 Waveguides

Waveguides have been proposed in the near-IR to reduce thresholds and improve efficiency of CW DRLs by tightly confining the pump and Stokes field over extended lengths [67, 248]. Although a CW DRL in a racetrack waveguide structure has been recently demonstrated at 1.9 μm with a 100 mW pump threshold [67], analysis suggests that waveguides are unlikely to offer significant benefits in the mid-IR, where intrinsic absorption losses dictate the minimum waveguide loss and hence limit the cavity Q . For linear waveguides that have their length limited by the crystal dimensions, facet damage limits the minimum pump spot diameter, and since the confocal parameter in Chapter 6 is already longer than typical crystal lengths, linear waveguides provide little benefit. In the case where pump peak powers are significantly lower, smaller spot sizes are required and linear waveguides may provide an advantage. As a means to reduce the facet intensity, tapered waveguides are a potential path to restrict the highest intensity to within the bulk crystal, where the damage threshold may be higher.

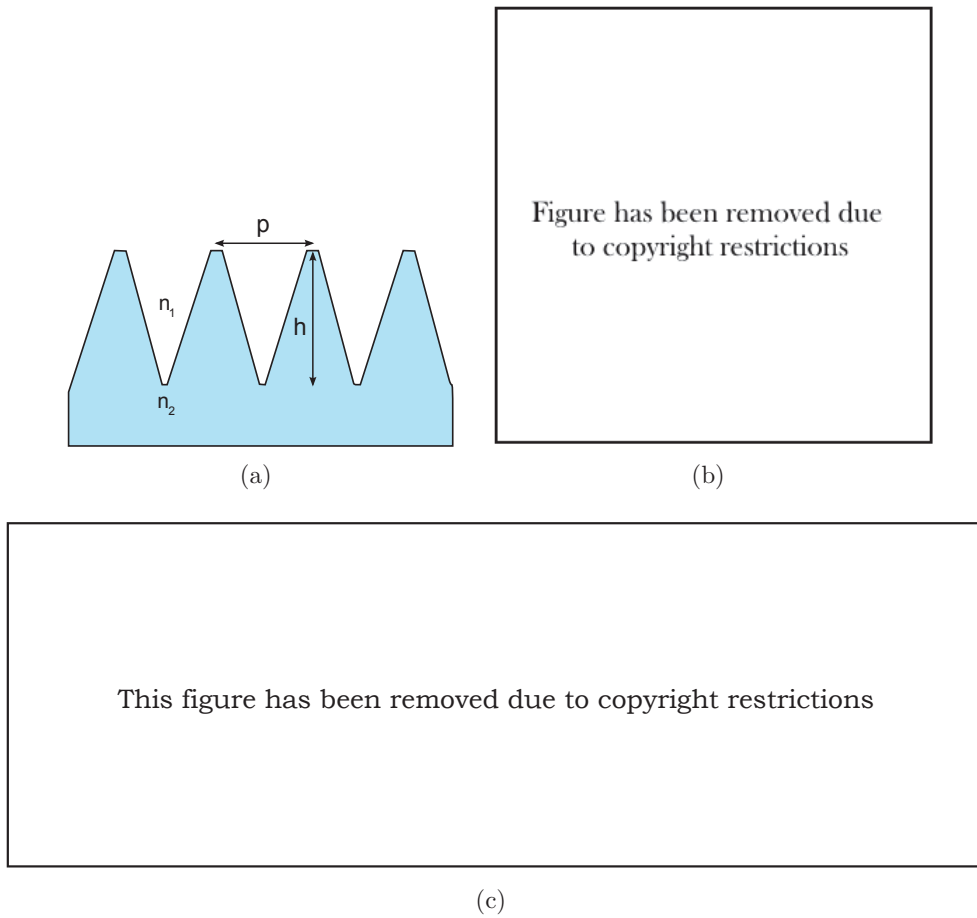


FIGURE 7.3: (a) Potential AR micro-structure cross section. (b) Overhead and elevation scanning electron microscope images of AR micro-structures in several optical materials (diamond is top left). The figure is copied from [238]. (c) Transmission through diamond windows with AR micro-structures designed for 8-12 μm light. The window is only treated on a single side so the maximum possible transmission is 83.4%. The figure is copied from [239].

7.1.4 Carbon-13 crystal

Changing the carbon isotope in the diamond crystal changes the Raman frequency and hence shifts the multiphonon absorption spectrum to slightly longer wavelengths [249, 250]. There are two stable isotopes of carbon, ^{12}C and ^{13}C . Natural diamond, and the CVD grown crystals used here, are predominantly ^{12}C based (98.9%). Using $^{13}\text{CH}_4$ methane in the CVD growth process will result in diamond comprised of ^{13}C atoms. The additional nuclear mass from the extra neutron reduces the Raman frequency from 1332 cm^{-1} to 1282 cm^{-1} (scaled by $m^{-0.5}$). The multiphonon absorption region will also shift accordingly (see Fig. 7.4), and the absorption minima previously targeted for Raman lasers will shift from $2.5\text{ }\mu\text{m}$, $3.75\text{ }\mu\text{m}$ and $7.5\text{ }\mu\text{m}$ to $2.6\text{ }\mu\text{m}$, $3.9\text{ }\mu\text{m}$ and $7.8\text{ }\mu\text{m}$, respectively. The higher atomic mass will also reduce g_R , but this is only expected to be by a few percent, as given by Eq. (2.3)

Using a ^{13}C crystal, an efficient DRL could be operated with minimal absorption loss out to $2.6\text{ }\mu\text{m}$. The corresponding pump wavelength of $1.95\text{ }\mu\text{m}$ is also at the peak of the thulium gain profile [222, 251], facilitating the use of existing high average power laser technology. A possible application is in the pumping of gain-switched iron doped chalcogenide lasers, which are attracting interest for generating $4\text{--}5\text{ }\mu\text{m}$ laser output [2]. Fe:ZnS and Fe:ZnSe crystals have stronger pump absorption at $2.6\text{ }\mu\text{m}$ compared to $2.5\text{ }\mu\text{m}$ [2] and extending the DRL wavelength should improve device efficiency.

7.1.5 Cryogenic cooling

Cryogenic cooling reduces or narrows the multiphonon absorption region in many materials including related group IV crystals, silicon and germanium [252]. Whilst heating increases the degree of absorption in diamond, unfortunately the temperature dependence is relatively weak below room temperature [95, 96, 252–254]. Figure 7.5 shows the variation in multiphonon absorption with temperature for several wavelengths. The three phonon absorption region is of particular relevance in this thesis and the $3\text{ }\mu\text{m}$ data points in the lower right of Fig. 7.5 show minimal improvement below 300 K .

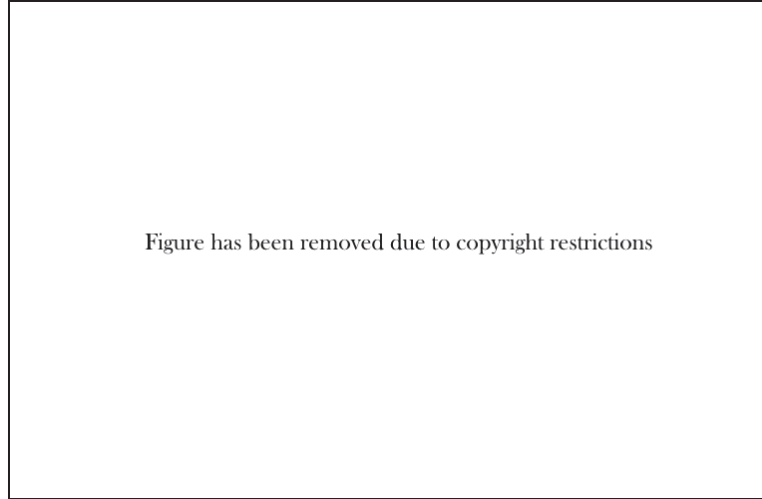


FIGURE 7.4: : Comparison of the two phonon absorption spectrum of natural diamond and a diamond with $>99\%$ ^{13}C content. The figure is copied from [249].

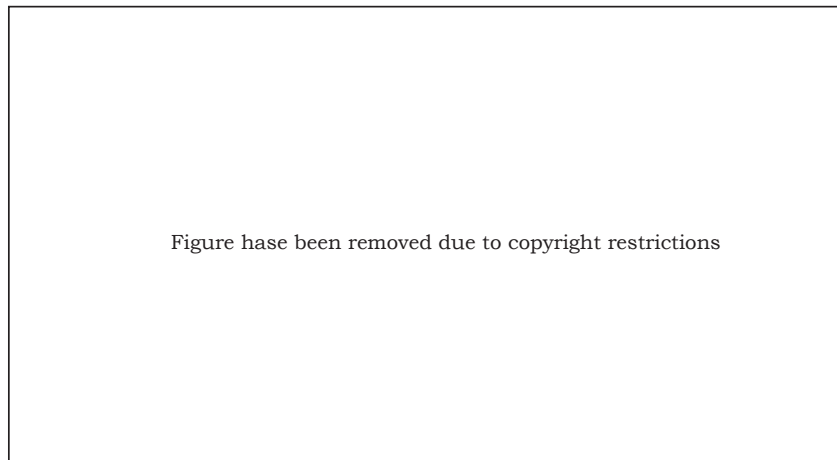


FIGURE 7.5: Measured (points) and modelled (lines) of crystal absorption for several fixed wavelengths with varying temperature. The figure is copied from [253].

7.2 Coherent Raman mixing

So far, reducing the SRS threshold through FWM in Section 6.3.5 required a second pump at the anti-Stokes wavelength. Coherent Raman mixing is an approach to reduce thresholds of first Stokes Raman lasers through FWM, without the requirement for a specific second pump wavelength, and has been used to overcome the low g_R of long wavelength gas Raman lasers [25, 46]. Two Raman lasers operate simultaneously in the same medium; the first Raman laser is pumped by a shorter wavelength pump (short pump) and readily generates first Stokes output due to the higher gain. The two shorter wavelengths mix through FWM with a longer wavelength pump (long pump) to create a seed at the required output wavelength.

$$\begin{aligned}\omega_{\text{FWM output}} &= \omega_{\text{Long pump}} - (\omega_{\text{Short pump}} - \omega_{\text{Short Stokes}}) \\ &= \omega_{\text{Long pump}} - \omega_{\text{Raman}}\end{aligned}\tag{7.1}$$

As the individual pump wavelengths are not important to the mixing process, the laser used for the short pump can be chosen for convenience, providing it is suitable for pumping a DRL. Equivalently the long pump can be tuneable and the frequency mixing will generate photons at the appropriate wavelength.

Figure 7.6 shows a conceptual example to extend the tuning range of an OPO beyond 7 μm . A single Nd:YAG laser pumps both the OPO and the short wavelength DRL. With all the wavelengths collinear, perfect phase matching is not achieved, but as discussed in Section 6.3.5, this is not required for significant threshold reductions. One drawback is the complexity of the cavity mirror and crystal coatings. The 1.240 μm DRL does not need to be efficient, allowing for the assignment of very loose tolerances on the coatings. It also would be possible to pump the short and long wavelength Raman lasers along different optical axes, each having separate optics. In this case, the effect of the relative propagation directions on the FWM phase matching condition becomes an additional parameter.

To model coherent Raman mixing requires a slight modification of the electric field based equations used previously in Section 6.3.5. The main difference is that there

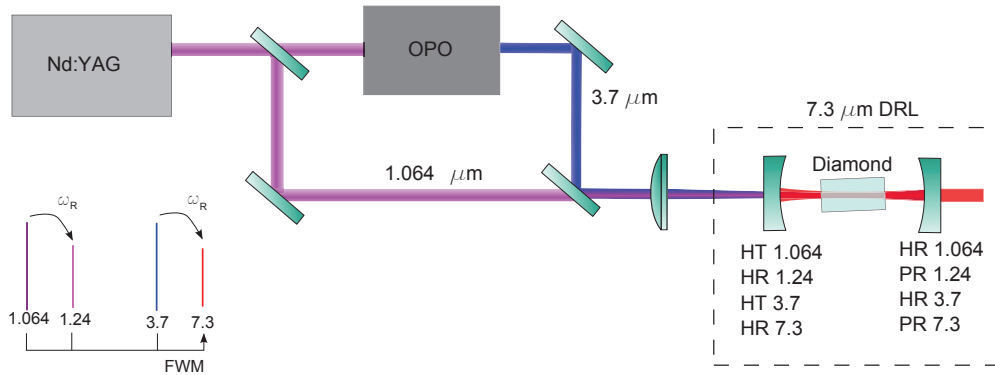


FIGURE 7.6: Possible layout for a 7.3μm DRL with coherent Raman mixing to reduce thresholds.

is no Raman relationship between the two shorter wavelengths and the two longer wavelengths. A second difference is that only non-degenerate FWM is relevant which changes the phase mismatch parameter, ΔK , defined below. The adjusted set of equations becomes

Short λ Raman pair

$$\begin{aligned} \frac{dE_{1.064}^{\pm}}{dz} &= -g_{1.064}^E \left[(|E_{1.24}^{+}|^2 + |E_{1.24}^{-}|^2) E_{1.064}^{\pm} + E_{1.24}^{\pm} E_{3.7}^{\pm} (E_{7.3}^{\pm})^* e^{\pm \Delta K z} \right] - E_{1.064}^{\pm} \alpha_{1.064}^E \\ \frac{dE_{1.24}^{\pm}}{dz} &= +g_{1.24}^E \left[(|E_{1.064}^{+}|^2 + |E_{1.064}^{-}|^2) (E_{1.24}^{\pm} + \sigma_{SP}^E (E_{1.064}^{+} + E_{1.064}^{-})) \right. \\ &\quad \left. + E_{1.064}^{\pm} E_{7.3}^{\pm} (E_{3.7}^{\pm})^* e^{\pm \Delta K z} \right] - E_{1.24}^{\pm} \alpha_{1.24}^E \end{aligned}$$

Long λ Raman pair

$$\begin{aligned} \frac{dE_{3.7}^{\pm}}{dz} &= -g_{3.7}^E \left[(|E_{7.3}^{+}|^2 + |E_{7.3}^{-}|^2) E_{3.7}^{\pm} + E_{7.3}^{\pm} E_{1.064}^{\pm} (E_{1.24}^{\pm})^* e^{\pm \Delta K z} \right] - E_{3.7}^{\pm} \alpha_{3.7}^E \\ \frac{dE_{7.3}^{\pm}}{dz} &= +g_{7.3}^E \left[(|E_{3.7}^{+}|^2 + |E_{3.7}^{-}|^2) (E_{7.3}^{\pm} + \sigma_{SP}^E (E_{3.7}^{+} + E_{3.7}^{-})) \right. \\ &\quad \left. + E_{3.7}^{\pm} E_{1.24}^{\pm} (E_{1.064}^{\pm})^* e^{\pm \Delta K z} \right] - E_{7.3}^{\pm} \alpha_{7.3}^E \\ \Delta K &= k_{1.064} + k_{7.3} - (k_{3.7} + k_{1.24}) \end{aligned} \tag{7.2}$$

The modelled performance of a DRL with a configuration similar to Fig. 7.6, for an uncoated crystal and a crystal with reduced facet reflections is presented in Fig. 7.7. The greatest benefit is obtained near threshold, as the FWM process diffuses energy

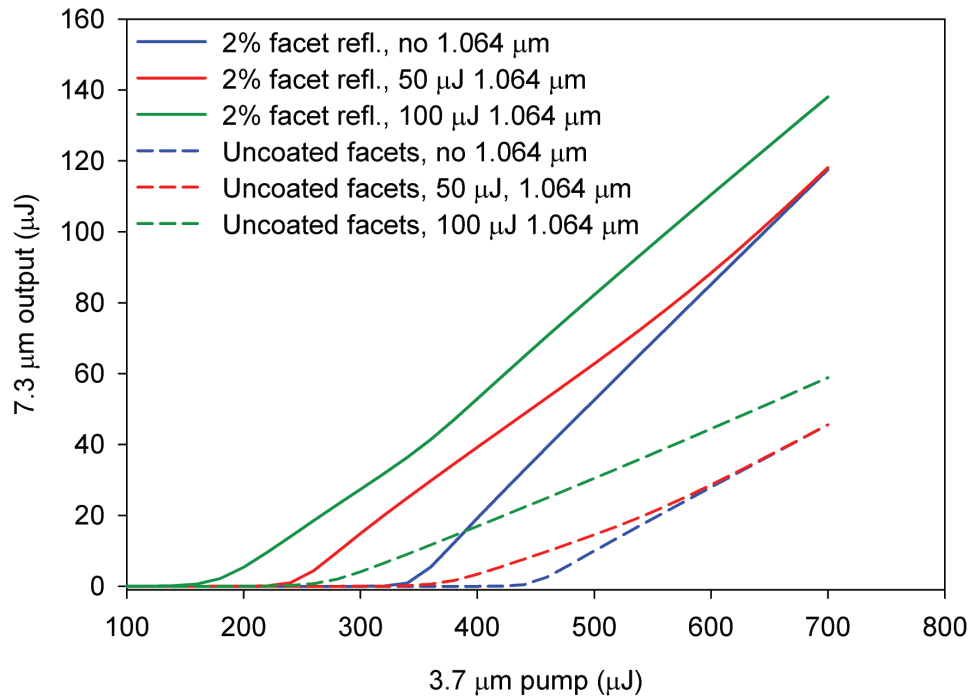


FIGURE 7.7: Modelled 7.3 μm DRL output energy using coherent Raman mixing for three secondary 1.064 μm pump levels.

amongst multiple wavelengths, leading to an initial reduction of the 7.3 μm slope efficiency. As the 3.7 μm pump is increased, the slope efficiency asymptotically approaches the single pump case. The utility of coherent Raman mixing will likely depend on the planned operating point of the laser.

7.3 Chapter Summary

This chapter has considered several strategies for improving the performance of mid-IR DRLs. With multiphonon absorption a largely unavoidable impediment, the greatest benefit comes from reducing Fresnel reflections from the facets. Brewster cut facets provide a broadband reduction in Fresnel loss for a single polarisation and have a high damage threshold. The main drawback is the threshold penalty from the expanded spot size. Orientating the facets such that the low loss polarisation aligns with a $\langle 111 \rangle$ axis

optimises g_R and mitigates part of the threshold penalty. Etching microstructured features on the crystal facet also provides broadband AR performance with high damage thresholds, but with the advantage of not expanding the spot size in the crystal.

Using the existing diamond samples, strong increases in absorption at 2.5 μm and 3.75 μm hinder or even prevent operation at longer wavelengths. Applications that require slightly longer wavelength output may benefit from changing the isotope of the carbon atoms to ^{13}C . The reduction of ω_R from 1332 cm^{-1} to 1282 cm^{-1} shifts the two and three phonon absorption limits to 3.9 μm and 2.6 μm , respectively.

Waveguides and cryogenic cooling were two other approaches considered as they have demonstrated benefits at shorter wavelengths and in other materials. Unfortunately the absorption properties of diamond are likely to prevent these techniques from improving performance in high peak power mid-IR DRLs.

Finally, coherent Raman mixing is investigated as an approach to reduce the threshold of long wavelength DRLs. By introducing an arbitrary second, shorter DRL pump wavelength, seed photons at a longer Stokes wavelength are generated through FWM. Modelling demonstrated significant reductions in thresholds for a 7.3 μm first Stokes DRL, but initial slope efficiencies were reduced due to FWM distributing energy amongst several wavelengths. The requirement for a secondary pump laser and challenges associated with cavity optics are drawbacks of this approach.

8

Conclusion

High optical quality synthetic diamond is a ‘new’ material with an array of exceptional properties able to extend the capability of Raman lasers. The transmission band, Raman gain coefficient, Raman frequency and thermal conductivity equal or exceed alternative nonlinear frequency conversion materials, enabling the generation of new wavelengths at high power, across a broad spectral range. This thesis describes the design, characterisation and optimisation of the first efficient infrared DRLs and the extension of the Stokes output to mid-IR wavelengths. In addition to the laser demonstrations, the thesis also expands and refines g_R measurement techniques, and describes the first investigation of polarisation effects in DRLs.

The polarisation properties of DRLs were studied in detail in Chapter 3 and considered the tensor properties of Raman scattering in diamond. Unlike prior experiments that were restricted by the crystal cut used [69, 70, 121], probing a rectangular crystal

along a $\langle 110 \rangle$ axis allowed the excitation of all three degenerate phonon modes. Mueller matrix modelling and experimental results demonstrated several important advantages of understanding DRL polarisation behaviour. Aligning the input polarisation with a $\langle 111 \rangle$ axis increased g_R by a factor of 1.33 over $\langle 100 \rangle$ or $\langle 110 \rangle$ polarised pumping and thus reduced SRS thresholds by the same factor. Modelling confirmed that alignment with a $\langle 111 \rangle$ axis gives the highest possible g_R , over all crystal orientations. Since the publication of this result, pumping with polarisation aligned to a $\langle 111 \rangle$ axis has been incorporated in many DRL designs [36, 69, 80, 81, 84, 121, 131, 132]. Varying the phase between the horizontal and vertical components of a $\langle 111 \rangle$ polarised pump produces a series of elliptically polarised states that also experience optimal gain. While not exactly optimal, circularly polarised pumping produces a g_R 98% of the maximum and is compatible with quarter-wave-plate isolators subsequently used in high average power experiments [81]. In addition to improving the spatial brightness of pump lasers, DRLs are also able to improve polarisation purity. Pumping with an unpolarised pump laser, when propagating along a $\langle 110 \rangle$ direction, produces linearly polarised Stokes output. A recent demonstration reported minimal efficiency difference with linearly polarised pumping [134]. Finally, in progressing DRLs to chip based architectures, the ability to predict the changing polarisation interactions as the beams propagate around curved waveguides will be important to optimising designs.

The 1.064 μm pumped DRLs in Chapter 4 represent the first reported efficient infrared DRLs and confirmed diamond as a high performing nonlinear conversion material. As both Stokes wavelengths provide a substantial increase in eye-safety over the pump laser, the results are of interest for converting existing 1 μm laser sources for lidar and remote sensing applications. The first Stokes laser had quantum limited slope efficiency and both first and second Stokes lasers demonstrated quantum conversion efficiencies in excess of 70%, equivalent to prior high performing Raman crystal and OPO results. The beam qualities were excellent, as expected for the modest output powers. Scaling the results presented in this thesis to high average output powers, whilst maintaining high efficiencies and beam quality, is an area where diamond has a

distinct advantage over alternative materials, and is a future research direction. Simplified analysis suggests detrimental thermal effects are not expected until output powers reach the kilowatt level. This is commensurate with the record held by fibre Raman lasers, but with the advantage of reduced spectral broadening and increased compatibility with high peak powers. Successive research has demonstrated over an order of magnitude increase in pulsed first and second Stokes output (~ 20 W) [12, 79] and 154 W of CW first Stokes power [81]. Each of these results have reported no evidence of detrimental thermal effects, in contrast to multi-Watt examples in other Raman crystals [18, 136, 255].

Having established diamond as an efficient frequency conversion material in the near-IR, research efforts were directed to the more challenging mid-IR region. There are very few reports of crystalline Raman lasers operating in the mid-IR due to reducing g_R and the absorption cutoff of many materials.

In extending DRLs to longer wavelengths, the gap between SRS and damage thresholds is decreased. Determining an accurate value of g_R for diamond in the mid-IR is therefore important for modelling and designing mid-IR DRLs. Published values in the visible and near-IR vary by up to a factor of 5 and extrapolating to the mid-IR produces similar discrepancies. Chapter 5 refines the existing pump-probe method for measuring g_R and proposes a new technique based on FWM. Prior measurements of g_R in diamond using the pump-probe method employed multi-longitudinal-mode beams [104, 105]. Modelling and experiments show that such measurements may be susceptible to errors through enhanced gain caused by correlations in the pump and probe mode structure. Ensuring mismatched pump and probe path lengths and amplifying the probe by less than $\sim 20\%$ minimises the influence of correlating structure.

A drawback of the pump-probe approach is that accurate knowledge of the spatial, spectral and temporal properties of the beams is required. The novel FWM approach to measuring g_R circumvents many of these requirements, providing $\chi_E^{(3)}$ and $\Delta\omega_R$ are known. The technique based on coherent Stokes Raman spectroscopy (CSRS) only requires the measurement of the frequency spacing between the maxima and minima in the CSRS spectrum (or the equivalent anti-Stokes CARS spectrum). While diamond

is a heavily studied material and several studies of $\chi_E^{(3)}$ are available, their values vary substantially.

The g_R measured using the pump-probe technique was 25% smaller than the CSRS value (2.5 cm/GW cf. 3.3 cm/GW at 2.48 μm). Compared to the factor of 5 variation in g_R obtained through extrapolating values at shorter wavelengths, the 25% difference is relatively minor. Within the uncertainties, the values agree with the semi-empirical g_R dispersion curve of Grimsditch et al. reported in 1981 [74]. Future refinements to improve the accuracy include performing the pump-probe measurements with SLM beams and conducting additional measurements of $\chi_E^{(3)}$.

With assistance from the measured g_R values, several mid-DRL designs were modelled in Chapter 6 and tested. The Raman cavities used concentric and hemispheric architectures to increase the Stokes intensity and overcome the combined challenges of reduced g_R , increased absorption, increased diffraction and weak mirror coatings. Tuning the wavelength of a custom OPO pump, a DRL generated narrow linewidth tuneable output spanning 3.4-3.8 μm , with the range limited by multiphonon absorption and cavity coatings. In conjunction with subsequent results at 7.30 μm , they are the longest wavelengths ever reported from a solid state Raman laser. The combination of a reduced g_R , increased absorption and facet reflections led to conversion efficiencies less than an equivalent near-IR DRL. Analysis of the pump depletion and Stokes output in fact revealed that the conversion of pump to Stokes is actually quite efficient, but almost half the Stokes is absorbed prior to exiting the Raman cavity. Modelling indicated that under improved operating conditions, quantum conversion efficiencies for 3.70 μm Stokes output could exceed 40%. Whilst the efficiency of an optimised mid-IR DRL is less than an equivalent OPO, a DRL is likely to have beam quality and linewidth advantages, particularly for high pulse repetition rates, without thermal degradation.

The OPO laser was an excellent pump source for characterising the performance of diamond in the mid-IR, but did not take advantage of the average power capability of diamond. Extending the spectral coverage of existing high power $\sim 2 \mu\text{m}$ sources, such as Tm^{3+} or Ho^{3+} doped lasers, is a possible future research direction. For example,

the first Stokes shift of a 2.1 μm Ho:YAG laser is 2.9 μm , which is near the peak of the water absorption profile and is beneficial for several surgical applications [59].

Advancing the Stokes wavelength beyond the two-phonon absorption enters a novel and challenging spectral region for solid-state Raman lasers. A maximum recorded output of $\sim 1 \mu\text{J}$ was demonstrated at 7.30 μm using an uncoated crystal in a second Stokes cavity. Although the second Stokes wavelength was in a region of low loss, absorption of the first Stokes and Fresnel losses increased the SRS threshold to an intensity similar to the crystal facet damage threshold.

Chapter 7 reviews several possible approaches to increasing 7.30 μm output and improving mid-IR DRL outputs in general. Fresnel reflections represent a large source of loss, and of the available options to reduce reflections, ARMS surfaces offer the best outcomes. They provide broadband reductions in reflectivity with high damage thresholds, and unlike Brewster cut facets, there is no SRS threshold increase from expanded beam spot sizes. ARMS technology is also likely to benefit DRLs at shorter wavelengths through increased robustness of the facet surface over dielectric coatings. Seeding the Stokes output is another path to reducing threshold intensities and improving efficiency. The approach demonstrated in Chapter 6 used a second pump wavelength at the anti-Stokes frequency, but degenerate FWM with an arbitrary shorter wavelength pump and its first Stokes will also seed a long wavelength DRL. Although modelling indicated improved 7.30 μm output, increased cavity complexity and the requirement for a second pump wavelength are limitations of this approach.

In the six years since the commencement of the research for this thesis there have been great developments in DRL technology. The results presented here, in conjunction with parallel research, have made it clear that diamond outperforms other materials in many aspects of Raman laser design. DRLs set the benchmark for average power, efficiency and spectral coverage in a number of Raman laser categories. In the coming years average powers will inevitably increase alongside improved capability for incorporating the performance demonstrated with bulk diamond into on-chip designs. This long studied material will continue to capture the imagination of researchers for years to come.



Classical stimulated Raman scattering theory

Raman interactions have been analysed using quantum mechanical, semi-classical and classical approaches [109]. The classical method derives the key Raman relationships relevant to this thesis, and is presented in the following section. Steady state conditions are assumed as the experimentally representative pulse widths (4–10 ns) are significantly longer than the decay time of the phonon field in diamond (7 ps) [8]. The equations define the electric field as $E(z, t) = Ee^{i(kz - \omega_P t)} + c.c.$, which follows the conventions used in textbooks by Boyd [140] and Sutherland [211]. An alternative definition, $E(z, t) = E/2e^{i(kz - \omega_P t)} + c.c.$, used by some authors (e.g. [102, 203]), results in a factor of four reduction in derived third-order susceptibilities and thus a scale factor difference for several of the equations derived below.

A.1 Raman Susceptibility

Linear and nonlinear optical effects may be described by the interaction of the electric field component of an electromagnetic wave with the charged particles in a material. At optical frequencies, the oscillations are too fast for the heavy nuclei to follow. However, the lower mass electrons strongly follow the rapid field oscillations. The displacement of the electrons induces an electric dipole moment, $\mu(t) = -e r(t)$, where e is the charge of an electron and $r(t)$ is the displacement. The macroscopic polarisation, P , is obtained by adding up all N electric dipoles per unit volume and leads to the introduction of the material susceptibility, χ .

$$P(t) = N\mu(t) = \epsilon_0\chi E(t) \quad (\text{A.1})$$

In the presence of a sufficiently strong driving electric field, a linear relationship can no longer be assumed and an accurate description of the polarisation requires the inclusion of nonlinear electron motions.

$$P(t) = \epsilon_0 [\chi^{(1)} E(t) + \chi^{(2)} E^2(t) + \chi^{(3)} E^3(t) + \dots] \quad (\text{A.2})$$

The first order term, $\chi^{(1)}$, governs linear interactions such as refraction. The higher order terms describe nonlinear interactions. Second order, $\chi^{(2)}$, effects are responsible for the nonlinear processes in harmonic generation and OPOs. $\chi^{(2)}$ is only non-zero in non-centrosymmetric materials and therefore not relevant to diamond. Third order non-linearities, governed by $\chi^{(3)}$, are present in all materials and importantly for this work include stimulated Raman scattering and four-wave-mixing.

As previously mentioned, the incident light is usually at a much higher frequency than the natural vibration of the material and thus the nuclei oscillations are not driven efficiently and the scattering response is very weak. However in the presence of two light fields with different frequencies, the slower beat frequency may induce a strong interaction. Perturbations to the nuclei will affect the potential seen by the electrons and thus the induced polarisation. The effect of nuclear motion on the polarisation

can be described by

$$P(t) = N\alpha(t)E(t) \quad (\text{A.3})$$

where $\alpha(t)$ is the polarisability of the material. The change in polarisability with nuclei vibration is given by

$$\alpha(t) = \alpha_0 + \frac{\partial\alpha}{\partial Q}Q(t) \quad (\text{A.4})$$

where Q is a coordinate describing normal modes of vibration. A key requirement for Raman scattering is that the polarisability changes during the nuclear motion, i.e. $(\partial\alpha/\partial Q) \neq 0$. Here $(\partial\alpha/\partial Q)$ is treated as a scalar, but for most crystalline materials, such as diamond, it is necessary to consider its tensor properties. This is explored in more depth in Chapter 3.

Describing the motion of the nucleus as a simple harmonic oscillator, with damping constant $\Delta\omega_R$, the time varying solution depends on the frequency difference between the two light fields,

$$Q(t) = Q(\omega_P - \omega_S)e^{i((k_P - k_S)z - (\omega_P - \omega_S)t)} + c.c. \quad (\text{A.5})$$

where the amplitude function is

$$Q(\omega_P - \omega_S) = \frac{(\partial\alpha/\partial Q)}{m[\omega_R^2 - (\omega_P - \omega_S)^2 - i\Delta\omega_R(\omega_P - \omega_S)]}E_P E_S^* \quad (\text{A.6})$$

Substituting the motion of the nucleus back in to Eq. (A.3) via Eq. (A.4) and only considering the second non-linear polarisation term in Eq. (A.4) we obtain an expression for the interaction with two light fields

$$\begin{aligned} P^{NL}(z, t) = & N \frac{\partial\alpha}{\partial Q} [Q(\omega_P - \omega_S)e^{i((k_P - k_S)z - (\omega_P - \omega_S)t)} + c.c.] \\ & \times [E_P e^{i(k_P - \omega_P t)} + E_S e^{i(k_S - \omega_S t)} + c.c.] \end{aligned} \quad (\text{A.7})$$

Isolating the Stokes frequency component leaves us with.

$$P(\omega_S) = \frac{N(\partial\alpha/\partial Q)^2}{m[\omega_R^2 - (\omega_P - \omega_S)^2 + i\Delta\omega_R(\omega_P - \omega_S)]}E_P E_P^* E_S e^{ik_S z} \quad (\text{A.8})$$

We now have an expression in the form of the third order term in Eq. (A.2), $P(\omega_S) = D\epsilon_0\chi^{(3)}E_1E_2E_3$. D is a degeneracy factor, which accounts for the number of distinct permutations of the electric fields. Since we have 3 distinguishable fields: E_P , E_{P^*} and E_S , D is equal to 6 [140]. We can now define the third order susceptibility due to Raman interactions,

$$\chi_R^{(3)}(\omega_S) = \frac{N(\partial\alpha/\partial Q)^2}{6\epsilon_0 m[\omega_R^2 - (\omega_P - \omega_S)^2 + i\Delta\omega_R(\omega_P - \omega_S)]} \quad (\text{A.9})$$

Near resonance this is approximated by

$$\chi_R^{(3)}(\omega_S) = \frac{N(\partial\alpha/\partial Q)^2}{12\epsilon_0 m\omega_R[\omega_R - (\omega_P - \omega_S) + i\Delta\omega_R/2]} \quad (\text{A.10})$$

The Raman susceptibility is complex and the real and imaginary components are plotted in Fig. A.1. When the beat frequency between the incident pump and Stokes light is equal to the resonant frequency, the susceptibility is negative imaginary. This leads to a positive feedback scenario where Stokes light beats with the pump to increase the vibrations, which then leads to the creation of additional Stokes photons.

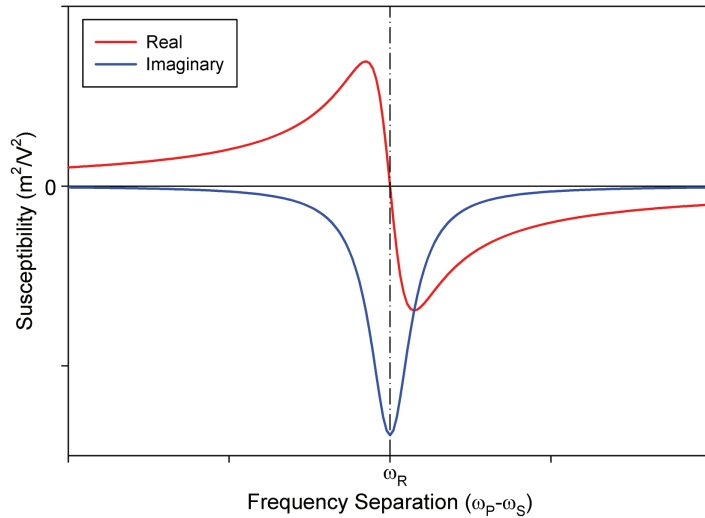


FIGURE A.1: Real and imaginary components of the Raman susceptibility.

A.2 Coupled Raman Intensity Equations

Having defined the Raman susceptibility, the next step is to derive the evolution of the pump and Stokes beams as they propagate through a material. Setting Eq. (A.8) to act as the driving term in the wave equation, delivers solutions of the form [140]

$$\frac{dE_S}{dz} = -i \frac{3\omega_S}{n_{Sc}} \chi_R^{(3)}(\omega_S) |E_P|^2 E_S \quad (\text{A.11})$$

Using the product rule and $I = 2c\epsilon_0 n |E|^2$ to convert to intensity¹ we obtain

$$\frac{dI_S}{dz} = \frac{-3\omega_S}{n_P n_{Sc}^2 \epsilon_0} \text{Im}(\chi_R^{(3)}(\omega_S)) I_P I_S \quad (\text{A.12})$$

The change in Stokes intensity is proportional to the imaginary component of the Raman susceptibility. Using $\text{Im}(x) = 1/2i(x - x^*)$ with Eq. (A.10)

$$\text{Im}(\chi_R^{(3)}(\omega_S)) = \frac{-N(\partial\alpha/\partial Q)^2}{12\epsilon_0 m \omega_R} \frac{\Delta\omega_R/2}{[[\omega_R - (\omega_P - \omega_S)]^2 + (\Delta\omega_R/2)^2]} \quad (\text{A.13})$$

This is a Lorentzian distribution centred at ω_R and with a FWHM equal to $\Delta\omega_R$. Substituting into Eq. (A.12) we get

$$\frac{dI_S}{dz} = \frac{\omega_S N(\partial\alpha/\partial Q)^2}{4n_P n_{Sc}^2 m \epsilon_0^2 \omega_R} \frac{\Delta\omega_R/2}{[[\omega_R - (\omega_P - \omega_S)]^2 + (\Delta\omega_R/2)^2]} I_P I_S \quad (\text{A.14})$$

When the pump and Stokes are resonant with the Raman vibration ($\omega_P - \omega_S = \omega_R$) Eq. (A.14) reduces to

$$\frac{dI_S}{dz} = \frac{\omega_S N(\partial\alpha/\partial Q)^2}{4n_P n_{Sc}^2 m \epsilon_0^2 \omega_R \Delta\omega_R/2} I_P I_S \quad (\text{A.15})$$

This allows us to define the Raman gain coefficient,

$$g_R = \frac{\omega_S N(\partial\alpha/\partial Q)^2}{2n_P n_{Sc}^2 m \epsilon_0^2 \Delta\omega_R \omega_R} \quad (\text{A.16})$$

¹ $I = c\epsilon_0 n |E|^2/2$ is used in some publications due to an alternative definition of the electric field.

and we now have

$$\frac{dI_S}{dz} = g_R I_P I_S \quad (\text{A.17})$$

which we can solve to obtain the classic expression relating the Raman amplification of an initial Stokes intensity, $I_S(0)$, along a Raman medium with length L .

$$I_S(L) = I_S(0)e^{g_R I_P L} \quad (\text{A.18})$$

Thus far, we have ignored the pump field and assumed that it remains constant. In reality, at some point the magnitude of the Stokes wave will be such that the depletion of the pump becomes significant. Following the same set of steps that were used to derive the change in Stokes intensity the change in pump intensity is

$$\frac{dI_P}{dz} = -\frac{\omega_P}{\omega_S} g_R I_P I_S \quad (\text{A.19})$$

Equations (A.17) and (A.19) form a pair of coupled equations that describe the interaction between two wavelengths. In a practical laser there are additional factors that influence the output behaviour. As the Stokes intensity builds it may reach a level intense enough to act as a pump in its own right, leading to further coupled equations describing the energy flow into higher order Stokes wavelengths. In addition, since phase matching is not required for SRS, both the forward and backwards travelling beams contribute to the Stokes output and need to be accounted for. Including spontaneous Raman scattering is also important for most Raman lasers where there is no incident Stokes beam to seed the process. Finally, any practical system has sources of loss, such as absorption or non-ideal mirrors. Introducing these additional factors to Eqs. (A.17) and (A.19), we arrive at the set of coupled intensity equations in Chapter 4 (Eq. (4.1)) that form the basis for much of the modelling conducted. To complement the description of the modelling in Chapter 4, the following section lists the variables used, in addition to the conversion factors for using the modelling in the electric field domain.

A.3 Modelling parameters

Variable	Intensity model	Electric field model
Field conversion	$I = 2c\epsilon_0 n_0 E ^2$	$E = \sqrt{\frac{I}{2c\epsilon_0 n_0}}$
Reflectivity	R_i	$\sqrt{R_i}$
Raman gain coefficient, g_R	$g'_R = g_R/n$	$g_R^E = g'_R c\epsilon_0$
Loss coefficient, α_i	$\alpha'_i = \alpha_i/n$	$\alpha_i^E = \alpha'_i/2$
Spontaneous scattering coefficient, σ_{SP}	$\sigma'_{SP} = \sigma_{SP}/n$	$\sigma_{SP}^E = \sqrt{\sigma'_{SP}}$

TABLE A.1: Conversion between intensity and electric field based variables. Note that the crystal parameters are divided by the refractive index to compensate for the crystal being modelled in terms of optical path length.

Variable	Symbol	Units	Near-IR model	Mid-IR model
Pump wavelength	λ	μm	1.064	2.480
Raman frequency	ω_R	cm^{-1}	1332	1332
Raman gain coefficient - $\langle 100 \rangle$	g_R	cm/GW	8.5	2.9
Crystal length	L	cm	6.9	8
Pump linewidth correction	η		0.83	0.85
Pump spot diameter		μm	120	100
Pump pulse length (FWHM)		ns	10	4
Spontaneous scattering rate	σ_{SP}	cm^{-1}	10^{-13}	$10^{-13}/2$
Refractive index - pump	n_P		2.391	2.3824
1 st Stokes	n_{S1}		2.389	2.3813
2 nd Stokes	n_{S2}		2.386	2.3806
1 st anti-Stokes	n_{AS}			2.3839
Absorption - pump	α_P	cm^{-1}	0.003	0.1
1 st Stokes	α_{S1}	cm^{-1}	0.003	0.72
2 nd Stokes	α_{S2}	cm^{-1}	0.003	0.18
1 st anti-Stokes	α_{AS}	cm^{-1}		0.003
Facet Loss - pump		%	2	17
1 st Stokes		%	0.4	17
2 nd Stokes		%	1	17
1 st anti-Stokes		%		17
Grid size	dz	cm	0.01-0.04	0.01-0.04

TABLE A.2: Baseline variables used in the intensity based DRL modelling.

B

Tensor form of the third order susceptibility

In the context of Raman lasers, FWM between two or more wavelengths may affect the laser threshold and Stokes polarisation. FWM also forms the basis for the g_R measurement technique described in Section 5.3. The intensity and polarisation of the generated light depend on the polarisation of the mixing wavelengths and the orientation of the crystal, and therefore the tensor form of $\chi_E^{(3)}$ is required.

The third order polarisation at $\omega_4 = \omega_2 + \omega_3 + \omega_1$ is given by

$$P_i^{(3)}(\omega_4) = \epsilon_0 D \sum_{jkl} \chi_{ijkl}^{(3)}(-\omega_4; \omega_1, \omega_2, \omega_3) E_j(\omega_1) E_k(\omega_2) E_l(\omega_3) \quad (\text{B.1})$$

where i, j, k, l are the orientation of the polarisations of $\omega_4, \omega_1, \omega_2, \omega_3$, respectively. D is a degeneracy factor that takes into account scenarios where ω_1, ω_2 and ω_3 may be

representing the same field.

$$D^{(3)} = \begin{cases} 1 & \text{all fields indistinguishable} \\ 3 & \text{two fields indistinguishable} \\ 6 & \text{all fields distinguishable} \end{cases}$$

Equivalently the nonlinear polarisation can be written in matrix form.

$$\begin{bmatrix} P_x^{(3)}(\omega) \\ P_y^{(3)}(\omega) \\ P_z^{(3)}(\omega) \end{bmatrix} = \epsilon_0 D \begin{bmatrix} \chi_{xxxx}^{(3)} & \chi_{xxxy}^{(3)} & \cdots & \chi_{xzzz}^{(3)} \\ \chi_{yyxx}^{(3)} & \chi_{yyxy}^{(3)} & \cdots & \chi_{yzzz}^{(3)} \\ \chi_{zxxx}^{(3)} & \chi_{zxxy}^{(3)} & \cdots & \chi_{zzzz}^{(3)} \end{bmatrix} \begin{bmatrix} E_x(\omega_1)E_x(\omega_2)E_x(\omega_3) \\ E_x(\omega_1)E_x(\omega_2)E_y(\omega_3) \\ \vdots \\ E_z(\omega_1)E_z(\omega_2)E_y(\omega_3) \\ E_z(\omega_1)E_z(\omega_2)E_z(\omega_3) \end{bmatrix} \quad (\text{B.2})$$

where the directions i, j, k, l have been replaced with the coordinates x, y, z that correspond to the $[100]$, $[010]$ and $[001]$ crystal axes, respectively. In general $\chi_{ijkl}^{(3)}$ is a tensor with 81 elements. Due to symmetries in the diamond lattice only 21 are non-zero and of these only 4 are independent values. Applying

$$\begin{aligned} e &= \chi_{xxxx}^{(3)} = \chi_{yyyy}^{(3)} = \chi_{zzzz}^{(3)} \\ f &= \chi_{yyzz}^{(3)} = \chi_{zzyy}^{(3)} = \chi_{zzxx}^{(3)} = \chi_{xxzz}^{(3)} = \chi_{xxyy}^{(3)} = \chi_{yyxx}^{(3)} \\ g &= \chi_{yzzy}^{(3)} = \chi_{zyzy}^{(3)} = \chi_{zxzx}^{(3)} = \chi_{xxzz}^{(3)} = \chi_{xyxy}^{(3)} = \chi_{yxxy}^{(3)} \\ h &= \chi_{yzzz}^{(3)} = \chi_{zyyz}^{(3)} = \chi_{zxzx}^{(3)} = \chi_{xxzz}^{(3)} = \chi_{xyyz}^{(3)} = \chi_{yxxy}^{(3)} \end{aligned} \quad (\text{B.3})$$

reduces the $\chi^{(3)}$ tensor to

$$\chi^{(3)} = \begin{bmatrix} e & 0 & 0 & 0 & f & 0 & 0 & 0 & f & 0 & g & 0 & g & 0 & 0 & 0 & 0 & 0 & 0 & g & 0 & 0 & 0 & h & 0 & 0 \\ 0 & d & 0 & g & 0 & 0 & 0 & 0 & 0 & f & 0 & 0 & 0 & e & 0 & 0 & 0 & f & 0 & 0 & 0 & 0 & g & 0 & h & 0 \\ 0 & 0 & h & 0 & 0 & 0 & g & 0 & 0 & 0 & 0 & 0 & 0 & 0 & h & 0 & c & 0 & f & 0 & 0 & 0 & f & 0 & 0 & 0 & e \end{bmatrix} \quad (\text{B.4})$$

If the four wavelengths are away from resonant features, Kleinmann symmetry reduces the number of independent values to one.

$$\chi_{xxxx}^{(3)} = 3\chi_{xxyy}^{(3)} = 3\chi_{xyxy}^{(3)} = 3\chi_{yyyx}^{(3)} \quad (\text{B.5})$$

Example 1: Effective susceptibility calculations

The g_R measurements in Section 5.3 require the effective susceptibility for a given combination of input polarisations and crystal orientations, which is defined as [211].

$$\chi_{Eff}^{(3)} = [d_1\chi_{xxxx}^{(3)} + d_2\chi_{xxyy}^{(3)} + d_3\chi_{xyxy}^{(3)} + d_4\chi_{yyyx}^{(3)}] \quad (\text{B.6})$$

As an example, aligning all polarisations along the $\langle 111 \rangle$ direction gives

$$\begin{bmatrix} E_x(\omega_1) \\ E_y(\omega_1) \\ E_z(\omega_1) \end{bmatrix} = \begin{bmatrix} E_x(\omega_2) \\ E_y(\omega_2) \\ E_z(\omega_2) \end{bmatrix} = \begin{bmatrix} E_x(\omega_3) \\ E_y(\omega_3) \\ E_z(\omega_3) \end{bmatrix} = \begin{bmatrix} 1/\sqrt{3} \\ 1/\sqrt{3} \\ 1/\sqrt{3} \end{bmatrix} \quad (\text{B.7})$$

where $\omega_2 = \omega_3 = \omega_{idler}$ and $\omega_1 = \omega_{signal}$. Substituting Eq. (B.7) into Eq. (B.2) gives

$$\begin{bmatrix} P_x^{(3)}(\omega) \\ P_y^{(3)}(\omega) \\ P_z^{(3)}(\omega) \end{bmatrix} = \epsilon_0 D \begin{bmatrix} 3^{-3/2}(\chi_{xxxx}^{(3)} + 2\chi_{xxyy}^{(3)} + 2\chi_{xyxy}^{(3)} + 2\chi_{yyyx}^{(3)}) \\ 3^{-3/2}(\chi_{xxxx}^{(3)} + 2\chi_{xxyy}^{(3)} + 2\chi_{xyxy}^{(3)} + 2\chi_{yyyx}^{(3)}) \\ 3^{-3/2}(\chi_{xxxx}^{(3)} + 2\chi_{xxyy}^{(3)} + 2\chi_{xyxy}^{(3)} + 2\chi_{yyyx}^{(3)}) \end{bmatrix} \quad (\text{B.8})$$

From Eq. (B.8) we can see that changes to $\chi_{xxxx}^{(3)}$ will change the ‘length’ of the nonlinear

polarisation vector by a factor of $\sqrt{(3^{-3/2})^2 + (3^{-3/2})^2 + (3^{-3/2})^2} = 1/3$. Therefore $d_1 = 1/3$. Similarly we get $d_2 = d_3 = d_4 = 2/3$ for changes to $\chi_{xxyy}^{(3)}$, $\chi_{xyxy}^{(3)}$ and $\chi_{xyyx}^{(3)}$.

Following the same approach for different input polarisation combinations gives the values listed in Table 5.1.

Example 2: Second Stokes DRL polarisation for [100] polarised pumping

The second Stokes DRL in Section 4.3 produced [100] linearly polarised light when pumped with a [100] polarised pump beam. In this configuration the first Stokes output is $[01\bar{1}]$ polarised and Mueller matrix analysis indicates the second Stokes output is therefore ‘randomly’ polarised. It is hypothesised that degenerate FWM between the pump and first Stokes is seeding the second Stokes output.

For degenerate FWM, second Stokes photons are created via $\omega_{S2} = 2\omega_{S1} - \omega_P$, which gives $\omega_4 = \omega_{S2}$, $\omega_2 = \omega_3 = \omega_{S1}$ and $\omega_1 = -\omega_P$ in Eq. (B.1). With respect to the standard cubic basis vectors, the corresponding normalised electric field vectors for a [100] polarised pump and $[01\bar{1}]$ polarised first Stokes are

$$\begin{bmatrix} E_x(\omega_2) \\ E_y(\omega_2) \\ E_z(\omega_2) \end{bmatrix} = \begin{bmatrix} E_x(\omega_3) \\ E_y(\omega_3) \\ E_z(\omega_3) \end{bmatrix} = \begin{bmatrix} 0 \\ 1/\sqrt{2} \\ -1/\sqrt{2} \end{bmatrix} \quad \begin{bmatrix} E_x(\omega_1) \\ E_y(\omega_1) \\ E_z(\omega_1) \end{bmatrix} = \begin{bmatrix} 1 \\ 0 \\ 0 \end{bmatrix} \quad (\text{B.9})$$

Substituting Eq. (B.9) and Eq. (B.4) into Eq. (B.2) we get

$$P^{(3)}(\omega_4) = 3\epsilon_0 \begin{bmatrix} 0.5f + 0.5f \\ 0 \\ 0 \end{bmatrix} \quad (\text{B.10})$$

The generated light is polarised in the [100] direction and thus seeds the second Stokes laser to operate on this polarisation.



OPO development

Underpinning the experiments in Chapters 5 and 6 was a custom OPO laser, designed to produce tuneable narrow-linewidth output near $2.5\text{ }\mu\text{m}$. For most of the experiments the idler wavelength was set to $2.48\text{ }\mu\text{m}$, so that the signal wavelength was at the diamond anti-Stokes wavelength of $1.86\text{ }\mu\text{m}$.

Obtaining the desired pulse energy ($\sim 1\text{ mJ}$) was straightforward, and the main challenge was restricting the linewidth to less than 1 cm^{-1} . The linewidth of an OPO depends on many factors including dispersion and reflection properties of the cavity, spectral bandwidth of the crystal, in addition to the linewidth, pulse duration and divergence properties of the pump [217]. Obtaining narrow spectral output from a relatively broad pump is possible for the resonant wavelength in a singly-resonant-OPO. However the non-resonant wavelength will have a broader linewidth approximated by the spectral convolution of the pump and resonant wavelength. Given that the $1.064\text{ }\mu\text{m}$

pump laser had a linewidth of approximately 1 cm^{-1} it is important that the OPO resonate at $2.48\text{ }\mu\text{m}$ to ensure it is the wavelength with the narrower linewidth.

The OPO cavities constructed were plane-plane with a diffraction grating acting as a linewidth narrowing element. Both Littrow and Littman-Metcalf architectures were investigated (see Fig. C.1) and used a blazed 600 lines/mm grating (Thorlabs GR25-0616). The AR coated KTP crystal was $10 \times 10 \times 20\text{ mm}$ and was cut at 57° to the crystal axis for type II phase matching at $2.46\text{ }\mu\text{m}$. To operate at $2.48\text{ }\mu\text{m}$ the crystal was rotated $\sim 0.4^\circ$ from normal. As Fig. C.2 shows, the crystal could also have been cut at 47.6° to obtain the same wavelength combination. A 57° cut was chosen as it had an increased nonlinear coefficient (2.79 c.f. 2.4 pV/m) and reduced gain bandwidth ($16\text{ c.f. } 29\text{ cm}^{-1} \cdot \text{cm}$), to reduce thresholds and encourage narrow linewidth operation, respectively. The output coupling mirror was HR at $1.064\text{ }\mu\text{m}$ and 67% reflective at $2.48\text{ }\mu\text{m}$. To protect the diffraction grating from the pump intensity a dichroic mirror was used at 45° to reflect the pump light, and pass the p-polarised idler with low loss.

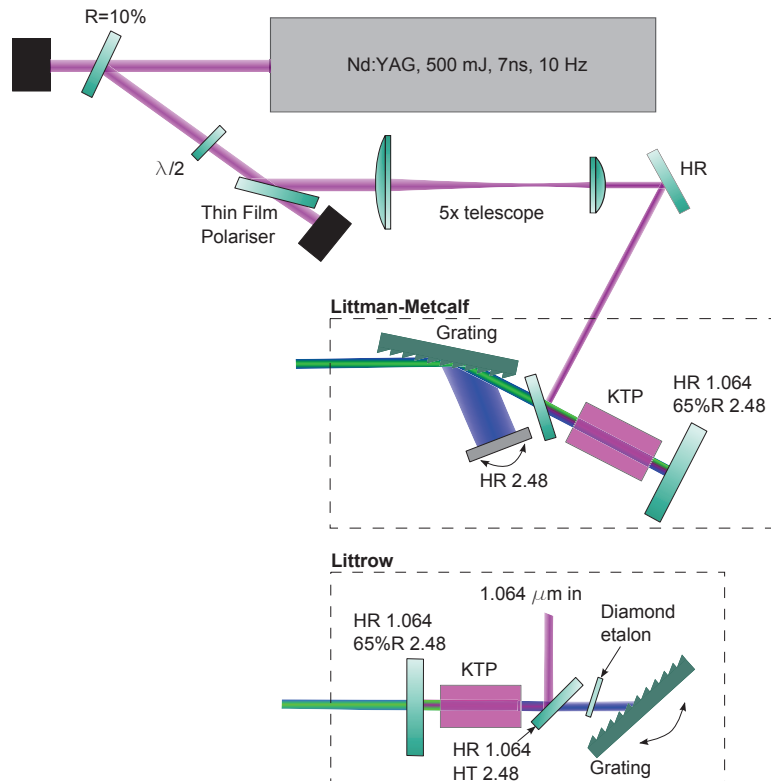


FIGURE C.1: $1.064\text{ }\mu\text{m}$ pumped Littman-Metcalf and Littrow OPO designs.

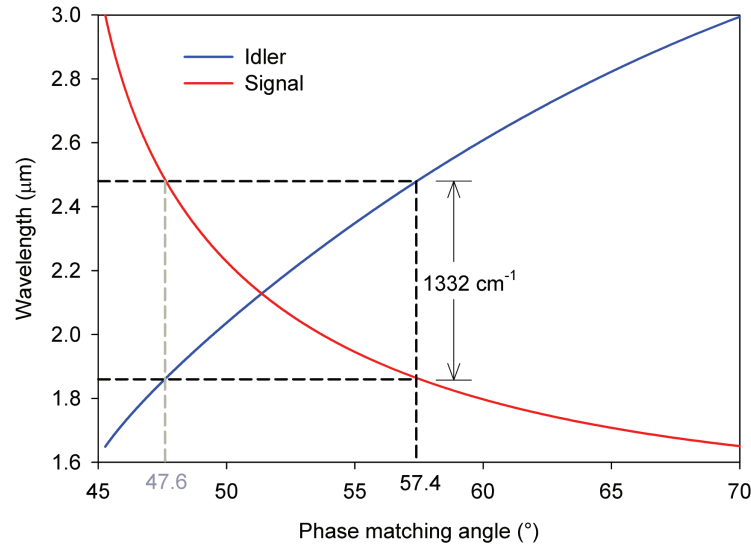


FIGURE C.2: Angular tuning curve for KTP with Type II phase matching in the XZ principal plane. The $1.064\text{ }\mu\text{m}$ pump and the signal are parallel polarised, while the idler is perpendicular.

The pump laser for the OPO was a Surelite Nd:YAG laser capable of delivering 500 mJ , 7 ns pulses at 10 Hz . A dichroic mirror diverted approximately 10% of the pulse energy, which was sufficient to obtain several millijoules of output from the OPO. The linewidth of the Nd:YAG laser was measured to be approximately 1 cm^{-1} and the M^2 was 2 in both axes. A waveplate and a thin film polariser were used to control the pulse energy incident on the OPO. This was followed by a $5\times$ telescope to reduce the diameter of the beam to 1.2 mm , prior to directing the laser into the OPO (see Fig. C.1).

An Acton 2500 monochromator with a 600 lines/mm grating was used to measure the OPO linewidths. Imaging the dispersed output on a Pyrocam III camera gave pulse-by-pulse linewidth measurements, while higher resolution averaged readings were taken with a detector behind $20\text{ }\mu\text{m}$ slits. The resolution limit of the Pyrocam and slit based detector methods was 0.53 cm^{-1} and 0.29 cm^{-1} FWHM, respectively, when measured using a single longitudinal mode fibre laser at $2.1\text{ }\mu\text{m}$. The narrowest idler linewidth measured (slit detection) had a FWHM of 0.43 cm^{-1} . If both the instrument profile and measured profile are assumed to be Gaussian, the deconvolved linewidth is

0.32 cm^{-1} . A change in linewidth from 0.32 cm^{-1} to 0.43 cm^{-1} results in a 5% change in the calculated effective g_R for diamond (Eq. (5.5) in Chapter 5). The non-resonant OPO signal linewidths were broader and thus the uncertainties in measurement were lower. Given the small impact on the final results, the data presented in this section is uncorrected for the influence of the measurement system.

The OPO evolved through several designs to achieve the required laser parameters. Initially a broadband silver rear mirror provided a performance reference and assisted with optimising the alignment of the cavity elements. Once the cavity was aligned, the broadband mirror was replaced with a diffraction grating in the Littrow configuration (Fig. C.1). The pulse energies and linewidths are shown in Figs. C.3(a) and C.4. Although the linewidth narrowed significantly, it was still broader than desired. In particular the idler spectra often contained two peaks, separated by approximately 1 cm^{-1} . A possible source of the dual peak output is Fabry-Perot effects in the output coupler, the second side of which was uncoated. To suppress the second peak a spare 1 mm thick diamond crystal was used as an etalon. The 2 cm^{-1} free spectral range conveniently placed a transmission minima on the second peak, suppressing the majority of its intensity, as shown in Fig. C.4(b). The FWHM measured linewidth was $0.6\text{--}0.8\text{ cm}^{-1}$, with a small remnant of the second peak still present.

Whilst the OPO could now be operated with the desired characteristics, it was an impractical source. Any tuning of the wavelength required adjustment of the KTP crystal, the diffraction grating and the diamond etalon. In addition the stability of the single peak operation was poor, particularly at higher pump powers. The etalon had to be continually adjusted to suppress the second peak.

To improve the stability of the linewidth, the OPO cavity was changed to a Littmann-Metcalf configuration. With the light now striking the grating at grazing incidence the number of lines illuminated, and hence spectral selectivity, is enhanced. In addition the resonated light diffracts off the grating twice per round trip, further narrowing the linewidth. Whilst grating angle in the Littrow configuration is fixed (for a given wavelength), in the Littmann-Metcalf design there is some flexibility in the grating angle. Using a shallower angle of incidence on the grating will, up to the limit of the

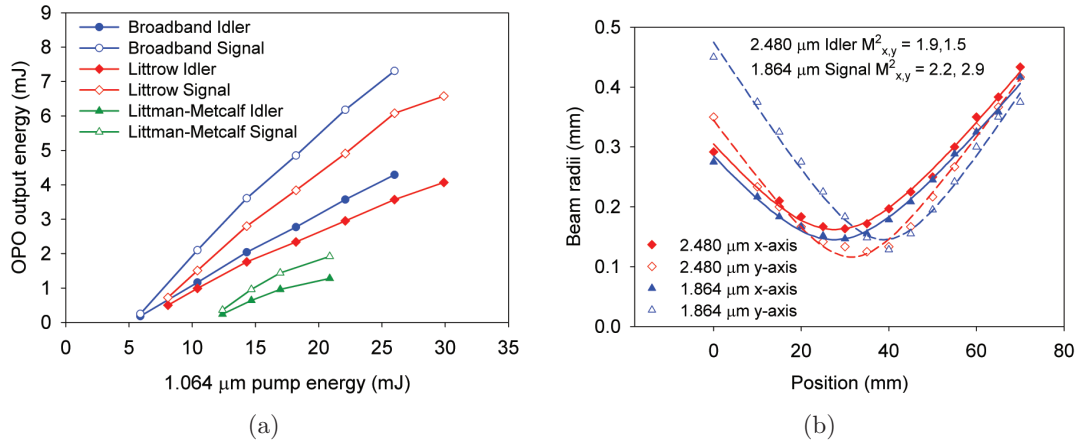


FIGURE C.3: (a) Signal (1.864 μm) and idler (2.480 μm) pulse energies for three OPO cavity configurations. Note that the Littrow results presented do not include the etalon. b) M^2 measurement for the signal and idler in the Littman-Metcalf cavity.

physical grating size, decrease the linewidth of the output, but at the expense of higher thresholds. An incident angle of 80° resulted in a good balance between linewidth and pulse energy. The measured FWHM linewidth at 2.48 μm was approximately 0.6 cm^{-1} , which was similar to the Littrow case with an ideally aligned etalon. The main advantage was the increased spectral stability. Figure C.5 shows the improved pulse to pulse linewidth stability, for a small sample of 9 consecutive pulses. The long-term stability was also greatly improved, with the Littmann-Metcalf cavity able to operate for long periods without the need to constantly readjust the OPO alignment.

The beam quality of the signal and idler was 1.7 and 2.5 times diffraction limited, respectively, similar to the 1.064 μm pump (Fig. C.3(b)).

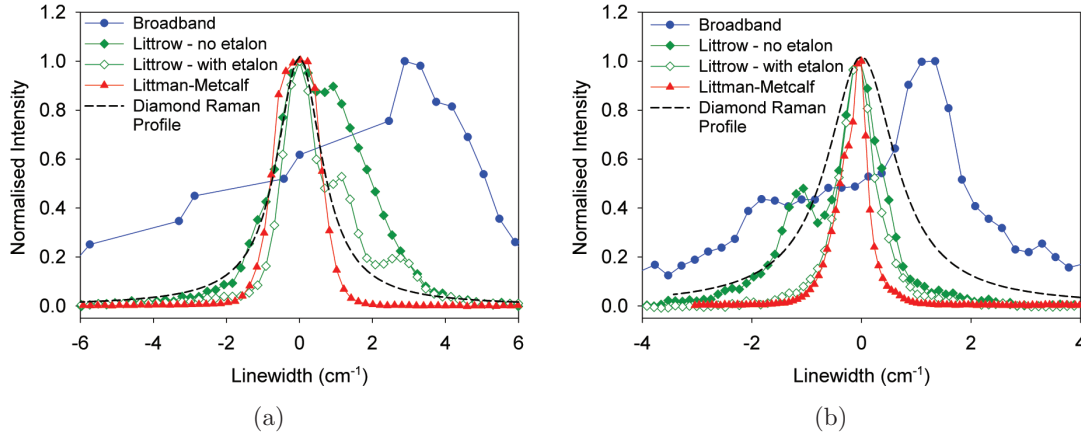


FIGURE C.4: Sample measurements of the spectral profiles of the (a) signal and (b) idler for four OPO cavity configurations. Idler pulse energy is approximately 1 mJ.

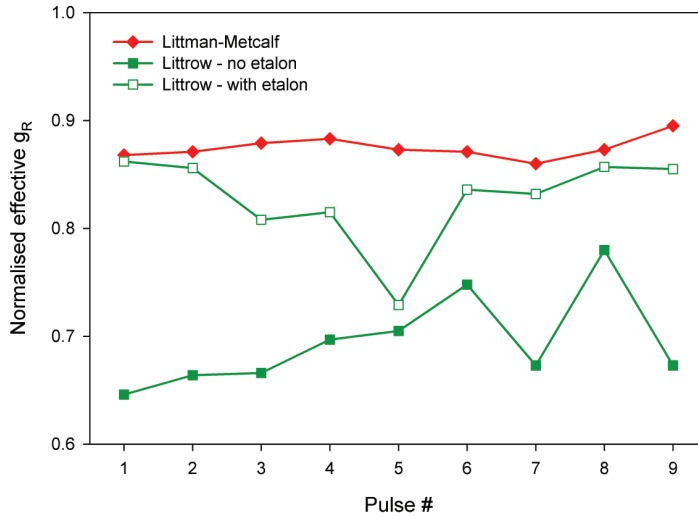


FIGURE C.5: Effective g_R for 9 consecutive pulses for three OPO cavity configurations. The values are normalised to the SLM pump case. Calculations are performed using Eq. (5.5) in Chapter 5.

D

Related Publications

This appendix includes a full list of relevant publications that I have authored and contributed to.

Peer-reviewed journal papers

1. A. Sabella, J. A. Piper, and R. P. Mildren. *1240 nm diamond Raman laser operating near the quantum limit*. Optics Letters **35**(23), 3874 (2010)
2. A. Sabella, J. A. Piper, and R. P. Mildren. *Efficient conversion of a 1.064 μm Nd:YAG laser to the eye-safe region using a diamond Raman laser*. Optics Express **19**(23), 23554 (2011)
3. A. Sabella, J. A. Piper, and R. P. Mildren. *Diamond Raman laser with continuously tunable output from 3.38 to 3.80 μm* . Optics letters **39**(13), 4037 (2014)

4. A. Sabella, D. J. Spence, and R. P. Mildren. *Pump-Probe Measurements of the Raman Gain Coefficient in Crystals Using Multi-Longitudinal-Mode Beams*. Quantum Electronics, IEEE Journal of **51**(12), 1 (2015)
5. A. McKay, A. Sabella, and R. P. Mildren. *Polarization conversion in cubic Raman crystals*. Scientific Reports **7** (2017)

Book Chapter

1. R. P. Mildren, A. Sabella, O. Kitzler, D. J. Spence, and A. M. McKay. *Optical Engineering of Diamond*, chap. Diamond Raman Laser Design and Performance, pp. 239–276 (Wiley-VCH Verlag GmbH & Co., Boschstr, 2013)

Conference presentations

1. A. Sabella, J. A. Piper, and R. P. Mildren. *84% slope efficiency 1240 nm diamond Raman laser*. In *Europhoton* (2010)
2. A. Sabella, J. A. Piper, and R. Mildren. *Efficient diamond Raman lasers operating at 1240 nm and 1485 nm*. In *Australian Institute of Physics Congress* (2010)
3. A. Sabella, J. Piper, and R. P. Mildren. *Efficient 1064 nm conversion to the eye-safe region using an external cavity diamond Raman laser*. In *Conference on Lasers and Electro-Optics (CLEO) Pacific Rim* (2011). Paper C725
4. A. Sabella, J. A. Piper, and R. Mildren. *Impact of pump polarisation and linewidth on the Raman gain coefficient of diamond*. In *Australian Institute of Physics Congress* (2012)
5. A. Sabella, J. A. Piper, and R. P. Mildren. *Mid-infrared diamond Raman laser with tuneable output*. In *Proc. SPIE*, vol. 8959 (2014). Paper 89590B
6. R. P. Mildren, A. Sabella, E. Granados, and D. J. Spence. *Diamond Raman Lasers*. In *Conference on Lasers and Electro-Optics (CLEO)* (2010). Paper

CTuJ1

7. O. Kitzler, A. Sabella, B. Johnston, A. McKay, and R. Mildren. *Design and characterisation of optical quality single crystal diamond for Raman laser applications*. In *Conference on Lasers and Electro-Optics (CLEO) Pacific Rim* (2011). Paper C1064

Symposia

1. A. Sabella, J. A. Piper, and R. P. Mildren. *573nm Diamond Raman laser*. In *Rank Prize symposium on diamond photonics* (2010)
2. A. Sabella, J. A. Piper, and R. P. Mildren. *Polarisation dynamics in diamond Raman lasers*. In *MMI-Harvard Diamond Photonics Symposium* (2012)

References

- [1] H. Injeyan and G. Goodno. *High Power Laser Handbook* (McGraw-Hill Education, 2011).
- [2] S. B. Mirov, V. V. Fedorov, D. Martyshkin, I. S. Moskalev, M. Mirov, and S. Vasilyev. *Progress in Mid-IR Lasers Based on Cr and Fe-Doped II–VI Chalcogenides*. Selected Topics in Quantum Electronics, IEEE Journal of **21**(1), 292 (2015).
- [3] R. P. Mildren. *Optical Engineering of Diamond*, chap. Intrinsic Optical Properties of Diamond, pp. 1–34 (Wiley-VCH Verlag GmbH & Co. KGaA, 2013).
- [4] A. Zaitsev. *Optical Properties of Diamond* (Springer-Verlag, Berlin, 2001).
- [5] I. Friel, S. L. Geoghegan, D. J. Twitchen, and G. A. Scarsbrook. *Development of high quality single crystal diamond for novel laser applications*. In *Proc. SPIE*, vol. 7838 (2010). Paper 783819.
- [6] D. C. Harris. *Materials for infrared windows and domes: properties and performance* (SPIE press, 1999).
- [7] F. Van Loon, A. J. Kemp, A. J. Maclean, S. Calvez, J. M. Hopkins, J. E. Hastie, M. D. Dawson, and D. Burns. *Intracavity diamond heatspreaders in lasers: The effects of birefringence*. Optics Express **14**(20), 9250 (2006).
- [8] K. Lee, B. J. Sussman, J. Nunn, V. Lorenz, K. Reim, D. Jaksch, I. Walmsley, P. Spizzirri, and S. Prawer. *Comparing phonon dephasing lifetimes in diamond*

- using transient coherent ultrafast phonon spectroscopy*. *Diamond and Related Materials* **19**(10), 1289 (2010).
- [9] J. T. Murray, W. L. Austin, and R. C. Powell. *Intracavity Raman conversion and Raman beam cleanup*. *Optical Materials* **11**(4), 353 (1999).
- [10] R. Chang, R. Lehmberg, M. Duignan, and N. Djeu. *Raman beam cleanup of a severely aberrated pump laser*. *IEEE journal of quantum electronics* **21**(5), 477 (1985).
- [11] J. Reintjes, R. Lehmberg, R. Chang, M. Duignan, and G. Calame. *Beam cleanup with stimulated Raman scattering in the intensity-averaging regime*. *JOSA B* **3**(10), 1408 (1986).
- [12] A. McKay, O. Kitzler, and R. P. Mildren. *Simultaneous brightness enhancement and wavelength conversion to the eye-safe region in a high-power diamond Raman laser*. *Laser & Photonics Reviews* **8**(3), L37 (2014).
- [13] A. McKay, D. J. Spence, D. W. Coutts, and R. P. Mildren. *Non-Collinear Beam Combining of Kilowatt Beams in a Diamond Raman Amplifier*. In *Advanced Solid State Lasers* (2014). Paper ATu5A.1.
- [14] L. R. Marshall and A. Kaz. *Eye-safe output from noncritically phase-matched parametric oscillators*. *J. Opt. Soc. Am. B* **10**(9), 1730 (1993).
- [15] L. S. Lingvay, N. Angert, and M. Roth. *High-average-power KTP ring OPO*. In *Proc. SPIE*, vol. 3928, pp. 52–56 (2000).
- [16] G. Hansson, H. Karlsson, and F. Laurell. *Unstable resonator optical parametric oscillator based on quasi-phase-matched RbTiOAsO_4* . *Applied optics* **40**(30), 5446 (2001).
- [17] Y. Peng, W. Wang, X. Wei, and D. Li. *High-efficiency mid-infrared optical parametric oscillator based on PPMgO : CLN*. *Optics letters* **34**(19), 2897 (2009).

-
- [18] A. McKay, O. Kitzler, and R. P. Mildren. *Thermal lens evolution and compensation in a high power KGW Raman laser*. Optics express **22**(6), 6707 (2014).
- [19] M. S. Webb, P. F. Moulton, J. J. Kasinski, R. L. Burnham, G. Loiacono, and R. Stolzenberger. *High-average-power KTiOAsO₄ optical parametric oscillator*. Optics letters **23**(15), 1161 (1998).
- [20] N. Takei, S. Suzuki, and F. Kannari. *20-Hz operation of an eye-safe cascade Raman laser with a Ba(NO₃)₂ crystal*. Applied Physics B: Lasers and Optics **74**(6), 521 (2002).
- [21] G. Eckhardt, R. Hellwarth, F. McClung, S. Schwarz, D. Weiner, and E. Woodbury. *Stimulated Raman scattering from organic liquids*. Physical Review Letters **9**(11), 455 (1962).
- [22] R. Minck, R. Terhune, and W. Rado. *Laser-Stimulated Raman Effect and Resonant Four-Photon Interactions in Gases H₂, D₂, and CH₄*. Applied Physics Letters **3**(10), 181 (1963).
- [23] G. Eckhardt, D. P. Bortfeld, and M. Geller. *Stimulated emission of stokes and anti-stokes raman lines from diamond, calcite, and sulfur single crystals*. Applied Physics Letters **3**(8), 137 (1963).
- [24] J. Duardo, F. Johnson, and L. Nugent. *Some new aspects in stimulated Raman scattering from hydrogen gas*. IEEE Journal of Quantum Electronics **4**(6), 397 (1968).
- [25] R. L. Byer and W. R. Trutna. *16 μ m generation by CO₂-pumped rotational Raman scattering in H₂*. Optics letters **3**(4), 144 (1978).
- [26] V. Wilke and W. Schmidt. *Tunable coherent radiation source covering a spectral range from 185 to 880 nm*. Applied Physics A: Materials Science & Processing **18**(2), 177 (1979).

-
- [27] D. Hanna, D. Pointer, and D. Pratt. *Stimulated Raman Scattering of Picosecond Light Pulses in Hydrogen, Deuterium, and Methane*. IEEE Journal of Quantum Electronics **22**(2), 332 (1986).
- [28] H. M. Pask. *The design and operation of solid-state Raman lasers*. Progress in Quantum Electronics **27**(1), 3 (2003).
- [29] M. N. Islam. *Raman amplifiers for telecommunications*. IEEE journal of selected topics in quantum electronics **8**(3), 548 (2002).
- [30] V. R. Supradeepa and J. W. Nicholson. *Power scaling of high-efficiency 1.5 μ m cascaded Raman fiber lasers*. Optics Letters **38**(14), 2538 (2013).
- [31] P. Cerny, H. Jelinkova, T. T. Basiev, and P. G. Zverev. *Properties of transient and steady-state stimulated Raman scattering in KGd (WO₄)₂ and BaWO₄ tungstate crystals*. In *Proc. SPIE*, vol. 4268, pp. 101–108 (2001).
- [32] A. Kaminskii, H. Rhee, H. Eichler, L. Bohatý, P. Becker, and K. Takaichi. *Wide-band Raman Stokes and anti-Stokes comb lasing in a BaF₂ single crystal under picosecond pumping*. Laser Physics Letters **5**(4), 304 (2008).
- [33] V. A. Lisinetskii, T. Riesbeck, H. Rhee, H. J. Eichler, and V. A. Orlovich. *High average power generation in barium nitrate Raman laser*. Applied Physics B: Lasers and Optics **99**(1-2), 127 (2010).
- [34] I. S. Grudinin and L. Maleki. *Ultralow-threshold Raman lasing with CaF₂ resonators*. Optics letters **32**(2), 166 (2007).
- [35] Y. Takahashi, Y. Inui, M. Chihara, T. Asano, R. Terawaki, and S. Noda. *A micrometre-scale Raman silicon laser with a microwatt threshold*. Nature **498**(7455), 470 (2013).
- [36] O. Kitzler, A. McKay, and R. P. Mildren. *Continuous-wave wavelength conversion for high-power applications using an external cavity diamond Raman laser*. Optics letters **37**(14), 2790 (2012).

- [37] H. Zhang, R. Tao, P. Zhou, X. Wang, and X. Xu. *1.5-kW Yb-Raman Combined Nonlinear Fiber Amplifier at 1120 nm*. Photonics Technology Letters, IEEE **27**(6), 628 (2015).
- [38] F. Couny, B. J. Mangan, A. V. Sokolov, and F. Benabid. *High power 55 watts CW Raman fiber-gas-laser*. In *Conference on Lasers and Electro-Optics (CLEO)* (2010). Paper CTuM3.
- [39] D. H. Titterton. *Military laser technology and systems* (Artech House, 2015).
- [40] F. K. Tittel, D. Richter, and A. Fried. *Mid-infrared laser applications in spectroscopy*, pp. 458–529 (Springer, 2003).
- [41] J. Faist. *Quantum cascade lasers* (Oxford University Press, 2013).
- [42] S. B. Mirov, V. Fedorov, D. Martyshkin, I. Moskalev, M. Mirov, and S. Vasilyev. *High average power Fe: ZnSe and Cr: ZnSe mid-IR solid state lasers*. In *Advanced Solid State Lasers* (Optical Society of America, 2015). Paper AW4A–1.
- [43] I. Sorokina and K. Vodopyanov. *Solid-State Mid-Infrared Laser Sources*. Physics and Astronomy Online Library (Springer, 2003).
- [44] K. Vodopyanov, F. Ganikhanov, J. Maffetone, I. Zwieback, and W. Ruderman. *ZnGeP₂ optical parametric oscillator with 3.8–12.4 μ m tunability*. Optics Letters **25**(11), 841 (2000).
- [45] B.-Q. Yao, Y.-J. Shen, X.-M. Duan, T.-Y. Dai, Y.-L. Ju, and Y.-Z. Wang. *A 41-W ZnGeP₂ optical parametric oscillator pumped by a Q-switched Ho: YAG laser*. Optics letters **39**(23), 6589 (2014).
- [46] S. Brosnan, R. Fleming, R. Herbst, and R. Byer. *Tunable infrared generation by coherent Raman mixing in H₂*. Applied Physics Letters **30**(7), 330 (1977).
- [47] A. Martino, R. Frey, and F. Pradere. *Near-to far-infrared tunable Raman laser*. Quantum Electronics, IEEE Journal of **16**(11), 1184 (1980).

-
- [48] B. Jalali, V. Raghunathan, R. Shori, S. Fathpour, D. Dimitropoulos, and O. Stafsudd. *Prospects for silicon mid-IR Raman lasers*. IEEE Journal on Selected Topics in Quantum Electronics **12**(6), 1618 (2006).
- [49] V. Raghunathan, D. Borlaug, R. R. Rice, and B. Jalali. *Demonstration of a mid-infrared silicon Raman amplifier*. Optics Express **15**(22), 14355 (2007).
- [50] M. Krause, R. Draheim, H. Renner, and E. Brinkmeyer. *Cascaded silicon Raman lasers as mid-infrared sources*. Electronics Letters **42**(21), 1224 (2006).
- [51] J. Ma and S. Fathpour. *Pump-to-Stokes relative intensity noise transfer and analytical modeling of mid-infrared silicon Raman lasers*. Optics Express **20**(16), 17962 (2012).
- [52] D. Borlaug, R. R. Rice, and B. Jalali. *Raman beam cleanup in silicon in the mid infrared*. Optics Express **18**(12), 12411 (2010).
- [53] J. Zhao, X. Zhang, X. Guo, X. Bao, L. Li, and J. Cui. *Diode-pumped actively Q-switched Tm, Ho:GdVO₄/BaWO₄ intracavity Raman laser at 2533 nm*. Optics Letters **38**(8), 1206 (2013).
- [54] Y. Zakharenkov, V. Shkunov, and D. Rockwell. *Tunable Solid-State Mid-IR Raman Laser Scalable to High Power*. Unpublished document, Raytheon Space & Airborne Systems, (2012).
- [55] T. T. Basiev, M. N. Basieva, M. E. Doroshenko, V. V. Fedorov, V. V. Osiko, and S. B. Mirov. *Stimulated Raman scattering in mid IR spectral range 2.31-2.75-3.7 μ m in BaWO₄ crystal under 1.9 and 1.56 μ m pumping*. Laser Physics Letters **3**(1), 17 (2006).
- [56] M. Bernier, V. Fortin, N. Caron, M. El-Amraoui, Y. Messaddeq, and R. Valle. *Mid-infrared chalcogenide glass Raman fiber laser*. Optics Letters **38**(2), 127 (2013).

- [57] M. Bernier, V. Fortin, M. El-Amraoui, Y. Messaddeq, and R. Vallée. *3.77 μm fiber laser based on cascaded Raman gain in a chalcogenide glass fiber*. Optics Letters **39**(7), 2052 (2014).
- [58] F. Vanier, Y.-A. Peter, and M. Rochette. *Cascaded Raman lasing in packaged high quality As_2S_3 microspheres*. Optics express **22**(23), 28731 (2014).
- [59] M. L. Wolbarsht. *Laser surgery: CO_2 or HF*. Quantum Electronics, IEEE Journal of **20**(12), 1427 (1984).
- [60] J. T. Walsh, T. J. Flotte, and T. F. Deutsch. *Er: YAG laser ablation of tissue: effect of pulse duration and tissue type on thermal damage*. Lasers in surgery and medicine **9**(4), 314 (1989).
- [61] M. Harlander, A. Heinrich, C. Hagen, and B. Nussbaumer. *High-brightness monolithic diode-pumped Er: YAG laser system at 2.94 μm with 400W peak power*. In Proc. SPIE, vol. 8959 (2014). Paper 895908.
- [62] G. M. Hale and M. R. Querry. *Optical constants of water in the 200-nm to 200- μm wavelength region*. Applied optics **12**(3), 555 (1973).
- [63] T. Basiev, A. Sobol, P. Zverev, L. Ivleva, V. Osiko, and R. Powell. *Raman spectroscopy of crystals for stimulated Raman scattering*. Optical materials **11**(4), 307 (1999).
- [64] R. P. Mildren, A. Sabella, O. Kitzler, D. J. Spence, and A. M. McKay. *Optical Engineering of Diamond*, chap. Diamond Raman Laser Design and Performance, pp. 239–276 (Wiley-VCH Verlag GmbH & Co., Boschstr, 2013).
- [65] R. M. Wood. *Laser-induced damage of optical materials* (CRC Press, 2003).
- [66] S. Tomljenovic-Hanic, T. J. Karle, A. D. Greentree, B. C. Gibson, B. A. Fairchild, A. Stacey, and S. Praver. *Optical Engineering of Diamond*, chap. Diamond-Based Optical Waveguides, Cavities, and Other Microstructures, pp. 311–351 (Wiley Online Library, 2013).

-
- [67] P. Latawiec, V. Venkataraman, M. J. Burek, B. J. Hausmann, I. Bulu, and M. Lončar. *On-chip diamond Raman laser*. *Optica* **2**(11), 924 (2015).
- [68] B. Hausmann, I. Bulu, V. Venkataraman, P. Deotare, and M. Lončar. *An on-chip diamond optical parametric oscillator*. *Nat. Photonics* **8**, 369 (2014).
- [69] R. P. Mildren and A. Sabella. *Highly efficient diamond Raman laser*. *Optics Letters* **34**(18), 2811 (2009).
- [70] R. P. Mildren, J. E. Butler, and J. R. Rabeau. *CVD-diamond external cavity Raman laser at 573 nm*. *Optics Express* **16**(23), 18950 (2008).
- [71] D. J. Spence, E. Granados, and R. P. Mildren. *Mode-locked picosecond diamond raman laser*. *Optics Letters* **35**(4), 556 (2010).
- [72] A. K. McQuillan, W. R. L. Clements, and B. P. Stoicheff. *Stimulated Raman emission in diamond: Spectrum, gain, and angular distribution of intensity*. *Physical Review A* **1**(3), 628 (1970).
- [73] W. Lubeigt, P. Millar, J. A. Kemp, E. J. Hastie, D. M. Dawson, and D. Burns. *Raman lasers using low birefringence synthetic diamond: Material characterisation, device design, and an initial demonstration*. In *Conference on Lasers and Electro-Optics (CLEO) Europe* (2009). Paper CD5.3.
- [74] M. Grimsditch, M. Cardona, J. Calleja, and F. Meseguer. *Resonance in the Raman scattering of CaF_2 , SrF_2 , BaF_2 and diamond*. *Journal of Raman Spectroscopy* **10**(1), 77 (1981).
- [75] A. A. Kaminskii, R. J. Hemley, J. Lai, C. S. Yan, H. K. Mao, V. G. Ralchenko, H. J. Eichler, and H. Rhee. *High-order stimulated Raman scattering in CVD single crystal diamond*. *Laser Physics Letters* **4**(5), 350 (2007).
- [76] N. M. Lawandy and R. Afzal. *Solid State Diamond Raman Laser* (2005). US Patent App. 10/971,661.

-
- [77] A. A. Demidovich, A. S. Grabtchihov, V. A. Orlovich, M. B. Danailov, and W. Kiefer. *Diode pumped diamond Raman microchip laser*. In *Conference on Lasers and Electro-Optics (CLEO) Europe*, p. 251 (2005).
- [78] I. Friel, S. L. Clewes, H. K. Dhillon, N. Perkins, D. J. Twitchen, and G. A. Scarsbrook. *Control of surface and bulk crystalline quality in single crystal diamond grown by chemical vapour deposition*. *Diamond and Related Materials* **18**(5-8), 808 (2009).
- [79] J. P. M. Feve, K. E. Shortoff, M. J. Bohn, and J. K. Brasseur. *High average power diamond Raman laser*. *Optics Express* **19**(2), 913 (2011).
- [80] A. McKay, H. Liu, O. Kitzler, and R. P. Mildren. *An efficient 14.5 W diamond Raman laser at high pulse repetition rate with first (1240 nm) and second (1485 nm) Stokes output*. *Laser Physics Letters* **10**(10) (2013).
- [81] R. J. Williams, J. Nold, M. Strecker, O. Kitzler, A. McKay, T. Schreiber, and R. P. Mildren. *Efficient Raman frequency conversion of high-power fiber lasers in diamond*. *Laser & Photonics Reviews* **9**(4), 405 (2015).
- [82] E. Granados, D. J. Spence, and R. P. Mildren. *Deep ultraviolet diamond Raman laser*. *Optics Express* **19**(11), 10857 (2011).
- [83] M. Murtagh, J. Lin, R. P. Mildren, G. McConnell, and D. J. Spence. *Efficient diamond Raman laser generating 65 fs pulses*. *Optics express* **23**(12), 15504 (2015).
- [84] D. C. Parrotta, A. J. Kemp, M. D. Dawson, and J. E. Hastie. *Multi-watt, continuous-wave, tunable diamond Raman laser with intracavity frequency-doubling to the visible region*. *Selected Topics in Quantum Electronics, IEEE Journal of* **19**(4), 1400108 (2013).
- [85] S. Reilly, V. G. Savitski, H. Liu, E. Gu, M. D. Dawson, and A. J. Kemp. *Monolithic diamond Raman laser*. *Optics letters* **40**(6), 930 (2015).

- [86] C. Ramaswamy. *Raman effect in diamond*. Nature **125**(3158), 704 (1930).
- [87] A. C. Menzies. *Raman effect in solids*. Reports on Progress in Physics **16**(1), 83 (1953).
- [88] D. Kirillov and G. Reynolds. *Linewidths of phonon lines of natural and synthetic diamonds*. Applied physics letters **65**(13), 1641 (1994).
- [89] N. Surovtsev, I. Kupriyanov, V. Malinovsky, V. Gusev, and Y. N. Pal'yanov. *Effect of nitrogen impurities on the Raman line width in diamonds*. Journal of Physics: Condensed Matter **11**(24), 4767 (1999).
- [90] F. Waldermann, B. J. Sussman, J. Nunn, V. Lorenz, K. Lee, K. Surmacz, K. Lee, D. Jaksch, I. Walmsley, P. Spizziri, *et al.* *Measuring phonon dephasing with ultrafast pulses using Raman spectral interference*. Physical Review B **78**(15), 155201 (2008).
- [91] M. S. Liu, L. A. Bursill, S. Prawer, and R. Beserman. *Temperature dependence of the first-order Raman phonon line of diamond*. Physical Review B **61**(5), 3391 (2000).
- [92] K.-H. Chen, Y.-L. Lai, L.-C. Chen, J.-Y. Wu, and F.-J. Kao. *High-temperature Raman study in CVD diamond*. Thin Solid Films **270**(1), 143 (1995).
- [93] K. De Corte, A. Anthonis, J. Van Royen, M. Blanchaert, J. Barjon, and B. Willems. *Overview of Dislocation Networks in Natural Type IIa Diamonds*. Gems & Gemology **42**(3) (2006).
- [94] C. A. Klein, T. M. Hartnett, and C. J. Robinson. *Critical-point phonon frequencies of diamond*. Physical Review B **45**(22), 12854 (1992).
- [95] M. E. Thomas and W. J. Tropf. *Optical properties of diamond*. In *Proc. SPIE*, vol. 2286, pp. 144–151 (1994).
- [96] C. Piccirillo, G. Davies, A. Mainwood, S. Scarle, C. M. Penchina, T. P. Mollart, K. L. Lewis, M. Nesldek, Z. Remes, and C. S. J. Pickles. *Temperature dependence*

- of intrinsic infrared absorption in natural and chemical-vapor deposited diamond.* Journal of Applied Physics **92**(2), 756 (2002).
- [97] T. T. Basiev, A. A. Sobol, P. G. Zverev, V. V. Osiko, and R. C. Powell. *Comparative spontaneous Raman spectroscopy of crystals for Raman lasers.* Applied Optics **38**(3), 594 (1999).
- [98] R. Aggarwal, L. Farrar, S. Saikin, X. Andrade, A. Aspuru-Guzik, and D. Polla. *Measurement of the absolute Raman cross section of the optical phonons in type Ia natural diamond.* Solid State Communications **152**(3), 204 (2012).
- [99] R. Claps, D. Dimitropoulos, V. Raghunathan, Y. Han, and B. Jalali. *Observation of stimulated Raman amplification in silicon waveguides.* Optics Express **11**(15), 1731 (2003).
- [100] J. M. Ralston and R. K. Chang. *Spontaneous-raman-scattering efficiency and stimulated scattering in silicon.* Physical Review B **2**(6), 1858 (1970).
- [101] H. Rhee, O. Lux, S. Meister, U. Woggon, A. A. Kaminskii, and H. J. Eichler. *Operation of a Raman laser in bulk silicon.* Optics letters **36**(9), 1644 (2011).
- [102] M. D. Levenson and N. Bloembergen. *Dispersion of the nonlinear optical susceptibility tensor in centrosymmetric media.* Physical Review B **10**(10), 4447 (1974).
- [103] H. Jelínková, O. Kitzler, V. Kubecek, M. Jelínek, M. Cech, J. Šulc, and M. Němec. *Single pass SRS Threshold and Gain from Diamond under 532 nm picosecond Nd:YAG pulse pumping.* In *Europhoton*, vol. WeP14 (2010).
- [104] V. G. Savitski, S. Reilly, and A. J. Kemp. *Steady-state Raman gain in diamond as a function of pump wavelength.* IEEE Journal of Quantum Electronics **49**(2), 218 (2013).
- [105] V. G. Savitski, I. Friel, J. E. Hastie, M. D. Dawson, D. Burns, and A. J. Kemp. *Characterization of single-crystal synthetic diamond for multi-watt continuous-wave Raman lasers.* Quantum Electronics, IEEE Journal of **48**(3), 328 (2012).

-
- [106] A. Sabella, J. A. Piper, and R. Mildren. *Impact of pump polarisation and linewidth on the Raman gain coefficient of diamond*. In *Australian Institute of Physics Congress* (2012).
- [107] M. Grimsditch and A. Ramdas. *Brillouin scattering in diamond*. *Physical Review B* **11**(8), 3139 (1975).
- [108] A. Kaminskii, C. McCray, H. Lee, S. Lee, D. Temple, T. Chyba, W. Marsh, J. Barnes, A. Annanenko, V. Legun, *et al.* *High efficiency nanosecond Raman lasers based on tetragonal PbWO₄ crystals*. *Optics communications* **183**(1), 277 (2000).
- [109] A. Penzkofer, A. Laubereau, and W. Kaiser. *High intensity Raman interactions*. *Progress in Quantum Electronics* **6**(2), 55 (1979).
- [110] V. A. Lisinetskii, D. N. Bus'ko, R. V. Chulkov, A. S. Grabchikov, P. A. Apanasevich, and V. A. Orlovich. *Low-threshold lasing in stimulated Raman lasers with nanosecond pumping*. *Journal of Applied Spectroscopy* **75**(2), 300 (2008).
- [111] A. Sabella, J. A. Piper, and R. P. Mildren. *1240 nm diamond Raman laser operating near the quantum limit*. *Optics Letters* **35**(23), 3874 (2010).
- [112] B. Heinen, T.-L. Wang, M. Sparenberg, A. Weber, B. Kunert, J. Hader, S. Koch, J. V. Moloney, M. Koch, and W. Stolz. *106 W continuous-wave output power from vertical-external-cavity surface-emitting laser*. *Electronics letters* **48**(9), 516 (2012).
- [113] H. P. Godfried, S. E. Coe, C. Hall, C. S. Pickles, R. S. Sussmann, X. Tang, and W. van der Voorden. *Use of CVD diamond in high-power CO₂ lasers and laser diode arrays*. In *Proc. SPIE*, vol. 3889, pp. 553–563 (2000).
- [114] P. K. Schelling, L. Shi, and K. E. Goodson. *Managing heat for electronics*. *Materials Today* **8**(6), 30 (2005).

-
- [115] C. A. Klein. *Laser-induced damage to diamond: dielectric breakdown and BHG scaling*. In *Proc. SPIE*, vol. 2428, pp. 517–530 (1995).
- [116] A. Sabella, J. A. Piper, and R. P. Mildren. *Diamond Raman laser with continuously tunable output from 3.38 to 3.80 μm* . *Optics letters* **39**(13), 4037 (2014).
- [117] O. Kitzler. *External cavity diamond Raman lasers for high-power continuous-wave beam conversion*. Ph.D. thesis, Department of Physics and Astronomy, Macquarie University (2015).
- [118] P. M. Martineau, S. C. Lawson, A. J. Taylor, S. J. Quinn, D. J. Evans, and M. J. Crowder. *Identification of synthetic diamond grown using chemical vapor deposition (CVD)*. *Gems & Gemology* **40**(1), 2 (2004).
- [119] U. Willamowski, D. Ristau, and E. Welsch. *Measuring the absolute absorptance of optical laser components*. *Applied optics* **37**(36), 8362 (1998).
- [120] A. A. Kaminskii, V. G. Ralchenko, and V. I. Konov. *Observation of stimulated raman scattering in CVD-diamond*. *JETP Letters* **80**(4), 267 (2004).
- [121] W. Lubeigt, G. M. Bonner, J. E. Hastie, M. D. Dawson, D. Burns, and A. J. Kemp. *Continuous-wave diamond Raman laser*. *Optics Letters* **35**(17), 2994 (2010).
- [122] R. Loudon. *The Raman effect in crystals*. *Advances in Physics* **13**(52), 423 (1964).
- [123] N. Colthup. *Introduction to infrared and Raman spectroscopy* (Elsevier, 2012).
- [124] C. Raman. *The vibration spectra of crystals. Part II. The case of diamond*. In *Proceedings of the Indian Academy of Sciences, Section A*, vol. 26, pp. 356–369 (Indian Academy of Sciences, 1947).
- [125] N. N. Nath. *The dynamical theory of the diamond lattice. I*. In *Proceedings of the Indian Academy of Sciences-Section A*, vol. 1, pp. 333–345 (Springer, 1934).

- [126] V. Chandrasekharan. *Scattering matrix for Raman effect in cubic crystals*. Zeitschrift für Physik **175**(1), 63 (1963).
- [127] R. Claps, D. Dimitropoulos, Y. Han, and B. Jalali. *Observation of Raman emission in silicon waveguides at 1.54 μm* . Optics Express **10**(22), 1305 (2002).
- [128] T. Saito, K. Suto, J.-i. Nishizawa, and M. Kawasaki. *Spontaneous Raman scattering in [100],[110], and [11-2] directional GaP waveguides*. Journal of Applied Physics **90**(4), 1831 (2001).
- [129] I. L. Snetkov, A. V. Voitovich, O. V. Palashov, and E. A. Khazanov. *Review of Faraday isolators for kilowatt average power lasers*. IEEE Journal of Quantum Electronics **50**(6), 434 (2014).
- [130] J. Feve, J. Bohn, K. Brasseur, and K. Shortoff. *High power Raman diamond laser*. In *Proc. SPIE*, vol. 7912 (2011). Paper 79121P.
- [131] A. Sabella, J. A. Piper, and R. P. Mildren. *Efficient conversion of a 1.064 μm Nd:YAG laser to the eye-safe region using a diamond Raman laser*. Optics Express **19**(23), 23554 (2011).
- [132] P. J. Schlosser, D. C. Parrotta, V. G. Savitski, A. J. Kemp, and J. E. Hastie. *Intracavity Raman conversion of a red semiconductor disk laser using diamond*. Optics express **23**(7), 8454 (2015).
- [133] W. Koechner. *Solid-state laser engineering*, vol. 1 (Springer, 2013).
- [134] A. McKay, A.; Sabella and R. P. Mildren. *Polarization conversion in cubic Raman crystals*. Currently under review.
- [135] V. A. Lisinetskii, A. S. Grabtchikov, I. A. Khodasevich, H. J. Eichler, and V. A. Orlovich. *Efficient high energy 1st, 2nd or 3rd Stokes Raman generation in IR region*. Optics Communications **272**(2), 509 (2007).

-
- [136] T. T. Basiev, A. V. Gavrilov, V. V. Osiko, S. N. Smetanin, and A. V. Fedin. *High-average-power SRS conversion of radiation in a BaWO₄ crystal*. Quantum Electronics **34**(7), 649 (2004).
- [137] Y. Feng, L. R. Taylor, and D. B. Calia. *150 W highly-efficient Raman fiber laser*. Optics express **17**(26), 23678 (2009).
- [138] I. Bufetov, M. Bubnov, Y. Larionov, O. Medvedkov, S. Vasiliev, M. Melkounov, A. Rybaltovsky, S. Semjonov, E. Dianov, A. Guryanov, *et al.* *Highly efficient one-and two-cascade Raman lasers based on phosphosilicate fibers*. Laser Physics **13**(2), 234 (2003).
- [139] R. Chulkov, V. Lisinetskii, O. Lux, H. Rhee, S. Schrader, H. Eichler, and V. Orlovich. *Thermal aberrations and high power frequency conversion in a barium nitrate Raman laser*. Applied Physics B **106**(4), 867 (2012).
- [140] R. Boyd. *Nonlinear Optics* (Academic Press, 2008), 3rd ed.
- [141] S. Ding, X. Zhang, Q. Wang, F. Su, S. Li, S. Fan, Z. Liu, J. Chang, S. Zhang, S. Wang, and Y. Liu. *Theoretical and experimental research on the multi-frequency Raman converter with KGd(WO₄)₂ crystal*. Optics Express **13**(25), 10120 (2005).
- [142] J. Richards and A. McInnes. *Versatile, efficient, diode-pumped miniature slab laser*. Optics letters **20**(4), 371 (1995).
- [143] O. Kitzler, A. McKay, D. J. Spence, and R. P. Mildren. *Modelling and optimization of continuous-wave external cavity Raman lasers*. Optics express **23**(7), 8590 (2015).
- [144] H. M. Pask, S. Myers, J. A. Piper, J. Richards, and T. McKay. *High average power, all-solid-state external resonator Raman laser*. Optics Letters **28**(6), 435 (2003).

- [145] V. Pashinin, V. Ralchenko, A. Bolshakov, E. Ashkinazi, M. Gorbashova, V. Y. Yurov, and V. Konov. *External-cavity diamond Raman laser performance at 1240 nm and 1485 nm wavelengths with high pulse energy*. Laser Physics Letters **13**(6), 065001 (2016).
- [146] P. G. Zverev, T. T. Basiev, and A. M. Prokhorov. *Stimulated Raman scattering of laser radiation in Raman crystals*. Optical Materials **11**(4), 335 (1999).
- [147] C. Zhang, X. Y. Zhang, Q. P. Wang, S. Z. Fan, X. H. Chen, Z. H. Cong, Z. J. Liu, Z. Zhang, H. J. Zhang, and F. F. Su. *Efficient extracavity Nd:YAG/BaWO₄ Raman laser*. Laser Physics Letters **6**(7), 505 (2009).
- [148] S. Ding, X. Zhang, Q. Wang, F. Su, S. Li, S. Fan, Z. Liu, J. Chang, S. Zhang, S. Wang, and Y. Liu. *Highly efficient Raman frequency converter with strontium tungstate crystal*. IEEE Journal of Quantum Electronics **42**(1), 78 (2006).
- [149] T. T. Basiev, S. N. Smetanin, A. S. Shurygin, and A. V. Fedin. *Parametric coupling of frequency components at stimulated Raman scattering in solids*. Physics-Uspekhi **53**(6), 611 (2010).
- [150] S. Ding, X. Zhang, Q. Wang, P. Jia, C. Zhang, and B. Liu. *Numerical optimization of the extracavity Raman laser with barium nitrate crystal*. Optics Communications **267**(2), 480 (2006).
- [151] A. McKay, O. Kitzler, and R. P. Mildren. *High power tungstate-crystal Raman laser operating in the strong thermal lensing regime*. Optics express **22**(1), 707 (2014).
- [152] J. Vanderslice. *1.5 mmicro Raman laser* (1972). US Patent 3,668,420.
- [153] E. Gregor, D. E. Nieuwsma, and R. D. Stultz. *20 Hz eyesafe laser rangefinder for air defense*. In *Proc. SPIE*, vol. 1207, pp. 124–135 (1990).
- [154] V. Orlovich, P. Apanasevich, S. Batishche, V. Belyi, A. Bui, A. Grabchikov, N. Kazak, and A. Kachinskii. *High-power sources of eye-safe radiation, based*

- on nonlinear-optical conversion of the radiation of YAG: Nd lasers.* Journal of Optical Technology **67**(11), 984 (2000).
- [155] *Safety of Laser Products. Part 1: Equipment classification and requirements* (2011). AS/NZS IEC 60825.1:2011.
- [156] *Safety of Laser Products. Part 1: Equipment classification and requirements* (2014). AS/NZS IEC 60825.1:2014.
- [157] M. Jelínek Jr, O. Kitzler, H. Jelínková, J. Šulc, and M. Němec. *CVD-diamond external cavity nanosecond Raman laser operating at 1.63 μm pumped by 1.34 μm Nd: YAP laser.* Laser Physics Letters **9**(1), 35 (2012).
- [158] T. T. Basiev, M. N. Basieva, A. V. Gavrilov, M. N. Ershkov, L. I. Ivleva, V. V. Osiko, S. N. Smetanin, and A. V. Fedin. *Efficient conversion of Nd: YAG laser radiation to the eye-safe spectral region by stimulated Raman scattering in BaWO₄ crystal.* Quantum Electronics **40**(8), 710 (2010).
- [159] Z. P. Wang, D. W. Hu, X. Fang, H. J. Zhang, X. G. Xu, J. Y. Wang, and Z. S. Shao. *Eye-safe raman laser at 1.5 μm based on BaWO₄ crystal.* Chinese Physics Letters **25**(1), 122 (2008).
- [160] M. Roth, N. Angert, E. Gold, and M. Tseitlin. *High conversion efficiency of an eye-safe KTP monolithic OPO.* In *Advanced Solid State Lasers* (2002). Paper MB12.
- [161] C. A. Ebbers and S. P. Velsko. *Optical and thermo-optical characterization of KTP and its isomorphs for 1.06- μm -pumped OPOs.* In *Proc. SPIE*, vol. 2700, pp. 227–239 (1996).
- [162] A. Fix and R. Wallenstein. *Spectral properties of pulsed nanosecond optical parametric oscillators: experimental investigation and numerical analysis.* JOSA B **13**(11), 2484 (1996).

- [163] J. W. Kim, D. Y. Shen, J. K. Sahu, and W. A. Clarkson. *Fiber-Laser-Pumped Er:YAG lasers*. IEEE Journal on Selected Topics in Quantum Electronics **15**(2), 361 (2009).
- [164] I. S. Moskalev, V. V. Fedorov, V. P. Gapontsev, D. V. Gapontsev, N. S. Platonov, and S. B. Mirov. *Highly efficient, narrow-linewidth, and single-frequency actively and passively Q-switched fiber-bulk hybrid Er: YAG lasers operating at 1645 nm*. Optics express **16**(24), 19427 (2008).
- [165] J. W. Kim, J. Sahu, and W. Clarkson. *Impact of energy-transfer-upconversion on the performance of hybrid Er: YAG lasers*. In *Proc. SPIE*, vol. 6871 (2008). Paper 68710W.
- [166] Sol30 Nd:YAG laser specifications, Bright Solutions. Retrieved from <http://brightsolutions.it/wp-content/uploads/2015/06/SOL.pdf>, (Dec 2015).
- [167] S. C. Tidwell, J. F. Seamans, M. S. Bowers, and A. K. Cousins. *Scaling CW diode-end-pumped Nd: YAG lasers to high average powers*. Quantum Electronics, IEEE Journal of **28**(4), 997 (1992).
- [168] Y. Chen. *Design criteria for concentration optimization in scaling diode end-pumped lasers to high powers: influence of thermal fracture*. Quantum Electronics, IEEE Journal of **35**(2), 234 (1999).
- [169] A. M. Warrier, J. Lin, H. M. Pask, R. P. Mildren, D. W. Coutts, and D. J. Spence. *Highly efficient picosecond diamond Raman laser at 1240 and 1485 nm*. Optics express **22**(3), 3325 (2014).
- [170] A. A. Kaminskii, T. Kaino, T. Taima, A. Yokoo, K.-i. Ueda, K. Takaichi, J. Hulliger, H. J. Eichler, J. Hanuza, J. Fernandez, *et al.* *Monocrystalline 2-Adamantylamino-5-Nitropyridine (AANP)—a Novel Organic Material for Laser Raman Converters in the Visible and Near-IR*. Japanese journal of applied physics **41**(6A), 603 (2002).

-
- [171] J. J. Ottusch and D. A. Rockwell. *Measurement of Raman gain coefficients of hydrogen, deuterium, and methane*. IEEE Journal of Quantum Electronics **24**(10), 2076 (1988).
- [172] V. A. Lisinetskii, S. V. Rozhok, D. N. Bus'ko, R. V. Chulkov, A. S. Grabtchikov, V. A. Orlovich, T. T. Basiev, and P. G. Zverev. *Measurements of Raman gain coefficient for barium tungstate crystal*. Laser Physics Letters **2**(8), 396 (2005).
- [173] R. Stegeman, C. Rivero, G. Stegeman, P. Delfyett Jr, K. Richardson, L. Jankovic, H. Kim, *et al.* *Raman gain measurements in bulk glass samples*. JOSA B **22**(9), 1861 (2005).
- [174] A. Georges and S. Dixit. *Dependence of broadband Raman amplification in dispersive media on the pump–Stokes input correlation*. JOSA B **8**(4), 780 (1991).
- [175] G. M. Bonner, J. Lin, A. J. Kemp, J. Wang, H. Zhang, D. J. Spence, and H. M. Pask. *Spectral broadening in continuous-wave intracavity Raman lasers*. Optics express **22**(7), 7492 (2014).
- [176] V. V. Bocharov, A. Z. Grasyuk, I. G. Zubarev, and V. F. Mulikov. *Stimulated Raman Scattering of Neodymium Laser Radiation in Liquid Nitrogen*. Soviet Journal of Experimental and Theoretical Physics **29**, 235 (1969).
- [177] W. Trutna Jr, Y. K. Park, and R. L. Byer. *The dependence of Raman gain on pump laser bandwidth*. IEEE Journal of Quantum Electronics **15**, 648 (1979).
- [178] M. Raymer, J. Mostowski, and J. Carlsten. *Theory of stimulated Raman scattering with broad-band lasers*. Physical Review A **19**(6), 2304 (1979).
- [179] E. Stappaerts, W. Long, and H. Komine. *Gain enhancement in Raman amplifiers with broadband pumping*. Optics letters **5**(1), 4 (1980).
- [180] J. Eggleston and R. L. Byer. *Steady-state stimulated Raman scattering by a multimode laser*. Quantum Electronics, IEEE Journal of **16**(8), 850 (1980).

-
- [181] J. Rifkin, M. Bernt, D. MacPherson, and J. Carlsten. *Gain enhancement in a XeCl-pumped Raman amplifier*. JOSA B **5**(8), 1607 (1988).
- [182] A. Berry and D. Hanna. *Dependence of stimulated Raman threshold on the pump bandwidth*. Optical and Quantum Electronics **15**(4), 367 (1983).
- [183] T. Takasaki, A. Tsunemi, K. Nagasaka, A. Suda, and H. Tashiro. *Enhanced Raman conversion by a two-longitudinal-mode beam in the para-hydrogen Raman laser*. Journal of applied physics **79**(1), 45 (1996).
- [184] A. Georges. *Statistical theory of Raman amplification and spontaneous generation in dispersive media pumped with a broadband laser*. Physical Review A **39**(4), 1876 (1989).
- [185] A. Georges. *Theory of stimulated Raman scattering in a chaotic incoherent pump field*. Optics Communications **41**(1), 61 (1982).
- [186] M. Trippenbach, K. Rzażewski, and M. G. Raymer. *Stimulated Raman scattering of colored chaotic light*. JOSA B **1**(4), 671 (1984).
- [187] C. Warner and B. Bobbs. *Effects of off-resonant Raman interactions on multi-mode Stokes conversion efficiency and output wave front*. JOSA B **3**(10), 1345 (1986).
- [188] J. P. Partanen and M. J. Shaw. *High-power forward Raman amplifiers employing lowpressure gases in light guides. I. Theory and applications*. J. Opt. Soc. Am. B **3**(10), 1374 (1986).
- [189] G. Dzhotyan, Y. E. D'yakov, I. G. Zubarev, and A. Mironov. *Influence of the spectral width and statistics of a Stokes signal on the efficiency of stimulated Raman scattering of nonmonochromatic pump radiation*. Soviet Journal of Quantum Electronics **7**(6), 783 (1977).
- [190] M. Bashkansky and J. Reintjes. *Correlation effects in pump-depleted broadband stimulated Raman amplification*. Optics communications **83**(1), 103 (1991).

-
- [191] A. Grabtchikov, A. Vodtchits, and V. Orlovich. *Pulse-energy statistics in the linear regime of stimulated Raman scattering with a broad-band pump*. Physical Review A **56**(2), 1666 (1997).
- [192] M. G. Raymer, K. Rzażewski, and J. Mostowski. *Pulse-energy statistics in stimulated Raman scattering*. Optics letters **7**(2), 71 (1982).
- [193] SNLO nonlinear optics code available from A. V. Smith, AS-Photonics, Albuquerque, NM.
- [194] M. I. Kolobov. *Quantum imaging* (Springer Science & Business Media, 2007).
- [195] R. Zambrini, A. Gatti, L. Lugiato, and M. San Miguel. *Polarization quantum properties in a type-II optical parametric oscillator below threshold*. Physical Review A **68**(6), 063809 (2003).
- [196] G. Anstett and R. Wallenstein. *Experimental investigation of the spectro-temporal dynamics of the light pulses of Q-switched Nd: YAG lasers and nanosecond optical parametric oscillators*. Applied Physics B **79**(7), 827 (2004).
- [197] A. Sabella, J. A. Piper, and R. P. Mildren. *Mid-infrared diamond Raman laser with tuneable output*. In *Proc. SPIE*, vol. 8959 (2014). Paper 89590B.
- [198] Minilite specifications, Continuum Lasers. Retrieved from <http://www.continuumlasers.com/files/products/minilite/minilite.pdf>, (Dec 2015).
- [199] D. Armstrong and A. Smith. *Tendency of nanosecond optical parametric oscillators to produce purely phase-modulated light*. Optics letters **21**(20), 1634 (1996).
- [200] V. A. Lisinetskii, I. I. Mishkel, R. V. Chulkov, A. S. Grabtchikov, P. A. Apanasevich, H. J. Eichler, and V. A. Orlovich. *Raman gain coefficient of barium nitrate measured for the spectral region of Ti:Sapphire laser*. Journal of Nonlinear Optical Physics and Materials **14**(1), 107 (2005).

-
- [201] M. Henriksson, L. Sjöqvist, V. Pasiskevicius, and F. Laurell. *Cavity length resonances in a nanosecond singly resonant optical parametric oscillator*. Optics express **18**(10), 10742 (2010).
- [202] M. Levenson and S. Kano. *Introduction to Nonlinear Laser Spectroscopy. Revised Edition* (Academic Press, 1988).
- [203] M. Sheik-Bahae, A. A. Said, T.-H. Wei, D. J. Hagan, and E. W. Van Stryland. *Sensitive measurement of optical nonlinearities using a single beam*. IEEE Journal of Quantum Electronics **26**(4), 760 (1990).
- [204] M. Sheik-Bahae, R. J. DeSalvo, A. A. Said, D. J. Hagan, M. Soileau, and E. W. Van Stryland. *Nonlinear refraction in UV transmitting materials*. In *Proc. SPIE*, vol. 1624, pp. 25–29 (1992).
- [205] M. Kozák, F. Trojánek, B. Dzurňák, and P. Malý. *Two-and three-photon absorption in chemical vapor deposition diamond*. JOSA B **29**(5), 1141 (2012).
- [206] J. Zhao, G. Jia, X. Liu, Z. Chen, J. Tang, and S. Wang. *Measurement of third-order nonlinear optical susceptibility of synthetic diamonds*. Chinese Optics Letters **8**(7), 685 (2010).
- [207] M. Sheik-Bahae, R. J. DeSalvo, A. A. Said, D. J. Hagan, M. Soileau, and E. W. Van Stryland. *Optical nonlinearities in diamond*. In *Proc. SPIE*, vol. 2428, pp. 605–609 (1995).
- [208] N. Bloembergen. *Nonlinear Optics*. Advanced book classics (Addison-Wesley Publishing Company, 1991).
- [209] M. Sheik-Bahae, D. C. Hutchings, D. J. Hagan, and E. W. Van Stryland. *Dispersion of bound electronic nonlinear refraction in solids*. IEEE Journal of Quantum Electronics **27**(6), 1296 (1991).
- [210] R. DeSalvo, A. A. Said, D. J. Hagan, E. W. Van Stryland, and M. Sheik-Bahae. *Infrared to ultraviolet measurements of two-photon absorption and n_2 in wide bandgap solids*. IEEE Journal of Quantum Electronics **32**(8), 1324 (1996).

- [211] R. L. Sutherland. *Handbook of nonlinear optics* (CRC press, 2003).
- [212] P. Zverev, T. Basiev, V. Osiko, A. Kulkov, V. Voitsekhovskii, and V. Yakobson. *Physical, chemical and optical properties of barium nitrate Raman crystal*. Optical Materials **11**(4), 315 (1999).
- [213] A. Vodchits, V. Kozich, V. Orlovich, and P. Apanasevich. *Z-Scan studies of KYW, KYbW, KGW, and Ba (NO₃)₂ crystals*. Optics communications **263**(2), 304 (2006).
- [214] C. C. Wang. *Empirical relation between the linear and the third-order nonlinear optical susceptibilities*. Physical Review B **2**(6), 2045 (1970).
- [215] N. L. Boling, A. J. Glass, and A. Owyong. *Empirical relationships for predicting nonlinear refractive index changes in optical solids*. Quantum Electronics, IEEE Journal of **14**(8), 601 (1978).
- [216] F. Ganikhanov, T. Caughey, and K. Vodopyanov. *Narrow-linewidth middle-infrared ZnGeP₂ optical parametric oscillator*. JOSA B **18**(6), 818 (2001).
- [217] P. Schlup. *Passive optical bandwidth control of quasi-phase matched optical parametric oscillators*. Ph.D. thesis, University of Otago (2003).
- [218] S. Das. *Nd: YAG pumped tunable singly resonant optical parametric oscillator in mid-infrared*. Journal of Physics D: Applied Physics **42**(8), 085107 (2009).
- [219] J. W. Evans, P. A. Berry, and K. L. Schepler. *A broadly tunable continuous-wave Fe: ZnSe laser*. In *Proc. SPIE*, vol. 8599 (2013). Paper 85990C.
- [220] J. Kernal, V. Fedorov, A. Gallian, S. Mirov, and V. Badikov. *3.9-4.8 μ m gain-switched lasing of Fe:ZnSe at room temperature*. Optics Express **13**(26), 10608 (2005).
- [221] Y. Li, Y. Wang, and B. Yao. *Comparative optical study of thulium-doped YAlO₃ and GdVO₄ single crystals*. Laser Physics Letters **5**(1), 37 (2008).

- [222] J. Šulc, H. Jelínková, P. Koranda, P. Černý, J. K. Jabczyński, W. Żendzian, J. Kwiatkowski, Y. Urata, and M. Higuchi. *Comparison of tunable lasers based on diode pumped Tm-doped crystals*. In *Proc. SPIE*, vol. 7141 (2008). Paper 71410C.
- [223] L. Gorajek, J. Jabczyński, W. Żendzian, J. Kwiatkowski, H. Jelinkova, J. Sulc, and M. Nemec. *High repetition rate, tunable, Q-switched diode pumped Tm: YLF laser*. *Opto-Electronics Review* **17**(4), 309 (2009).
- [224] V. S. Butylkin, G. V. Venkin, L. L. Kulyuk, D. I. Maleev, Y. G. Khronopulo, and M. F. Shalyaev. *Role of the parametric and Raman processes in the generation of the second axial Stokes component of the stimulated Raman scattering*. *Sov J Quantum Electron* **7**(7), 867 (1977).
- [225] N. Vermeulen, J. E. Sipe, L. G. Helt, and H. Thienpont. *Opportunities for wavelength conversion with on-chip diamond ring resonators*. *Laser and Photonics Reviews* **6**(6), 793 (2012).
- [226] J. H. Newton and G. Schindler. *Numerical model of multiple-Raman-shifting excimer lasers to the blue-green in H_2* . *Optics letters* **6**(3), 125 (1981).
- [227] R. Telling, C. Pickard, M. Payne, and J. Field. *Theoretical strength and cleavage of diamond*. *Physical Review Letters* **84**(22), 5160 (2000).
- [228] V. I. Konov. *Laser in micro and nanoprocessing of diamond materials*. *Laser & Photonics Reviews* **6**(6), 739 (2012).
- [229] O. Kuzucu. *Watt-level, mid-infrared output from a $BaWO_4$ external-cavity Raman laser at 2.6 μm* . *Optics letters* **40**(21), 5078 (2015).
- [230] P. Budni, L. Pomeranz, M. Lemons, C. Miller, J. Mosto, and E. Chicklis. *Efficient mid-infrared laser using 1.9- μm -pumped Ho:YAG and $ZnGeP_2$ optical parametric oscillators*. *JOSA B* **17**(5), 723 (2000).

- [231] R. Jones, H. Rong, A. Liu, A. Fang, M. Paniccia, D. Hak, and O. Cohen. *Net continuous wave optical gain in a low loss silicon-on-insulator waveguide by stimulated Raman scattering*. Optics Express **13**(2), 519 (2005).
- [232] X. Gai, Y. Yu, B. Kuyken, P. Ma, S. J. Madden, J. Van Campenhout, P. Verheyen, G. Roelkens, R. Baets, and B. Luther-Davies. *Nonlinear absorption and refraction in crystalline silicon in the mid-infrared*. Laser & Photonics Reviews **7**(6), 1054 (2013).
- [233] C. Kieleck, M. Eichhorn, A. Hirth, D. Faye, and E. Lallier. *High-efficiency 20–50 kHz mid-infrared orientation-patterned GaAs optical parametric oscillator pumped by a 2 μ m holmium laser*. Optics letters **34**(3), 262 (2009).
- [234] A. Dergachev, D. Armstrong, A. Smith, T. Drake, and M. Dubois. *3.4- μ m ZGP RISTRA nanosecond optical parametric oscillator pumped by a 2.05- μ m Ho:YLF MOPA system*. Optics express **15**(22), 14404 (2007).
- [235] D. Cotter, D. Hanna, and R. Wyatt. *A high power, widely tunable infrared source based on stimulated electronic Raman scattering in caesium vapour*. Optics Communications **16**(2), 256 (1976).
- [236] V. Serebryakov, E. Boiko, N. Petrishchev, and A. Yan. *Medical applications of mid-IR lasers. Problems and prospects*. Journal of Optical Technology **77**(1), 6 (2010).
- [237] F. Stutzki, F. Jansen, C. Jauregui, J. Limpert, and A. Tünnermann. *2.4 mJ, 33 W Q-switched Tm-doped fiber laser with near diffraction-limited beam quality*. Optics letters **38**(2), 97 (2013).
- [238] D. S. Hobbs. *Laser damage threshold measurements of anti-reflection microstructures operating in the near UV and mid-infrared* (2010).
- [239] D. S. Hobbs. *Study of the environmental and optical durability of AR microstructures in sapphire, ALON, and diamond*. In *Proc. SPIE*, vol. 7302 (2009). Paper 73020J.

- [240] S. S. Chan, F. Raybould, G. Arthur, F. Goodall, and R. B. Jackman. *Laser projection patterning for the formation of thin film diamond microstructures*. Diamond and related materials **5**(3), 317 (1996).
- [241] M. Tarutani, Y. Takai, and R. Shimizu. *Application of the focused-ion-beam technique for preparing the cross-sectional sample of chemical vapor deposition diamond thin film for high-resolution transmission electron microscope observation*. Japanese Journal of Applied Physics, Part 2: Letters & Express Letters **31**, L1305 (1992).
- [242] V. Ralchenko, A. Khomich, A. Baranov, I. Vlasov, and V. Konov. *Fabrication of CVD diamond optics with antireflective surface structures*. physica status solidi (a) **174**(1), 171 (1999).
- [243] M. Karlsson and F. Nikolajeff. *Diamond micro-optics: Microlenses and antireflection structured surfaces for the infrared spectral region*. Optics Express **11**(5), 502 (2003).
- [244] Element 6 website, (Accessed Feb 2016), URL http://www.e6.com/wps/wcm/connect/E6_Content_EN/Home/Applications/Optics/High+power+laser+optics/Diamond+PureOptics.
- [245] S. Wang and R. Magnusson. *Theory and applications of guided-mode resonance filters*. Applied optics **32**(14), 2606 (1993).
- [246] D. S. Hobbs. *Laser-line rejection or transmission filters based on surface structures built on infrared transmitting materials*. In *Proc. SPIE*, vol. 5786, pp. 319–334 (2005).
- [247] D. S. Hobbs. *Laser damage threshold measurements of microstructure-based high reflectors*. In *Proc. SPIE*, vol. 7132 (2008). Paper 71321K.
- [248] L. J. McKnight, M. D. Dawson, and S. Calvez. *Diamond Raman waveguide lasers: Completely analytical design optimization incorporating scattering losses*. Quantum Electronics, IEEE Journal of **47**(8), 1069 (2011).

- [249] R. Vogelgesang, A. Alvarenga, H. Kim, A. Ramdas, S. Rodriguez, M. Grimsditch, and T. Anthony. *Multiphonon Raman and infrared spectra of isotopically controlled diamond*. Physical Review B **58**(9), 5408 (1998).
- [250] A. Kaminskii, V. Ralchenko, A. Bolshakov, and A. Khomich. *CVD-diamond ^{13}C : A new SRS-active crystal*. In *Doklady Physics*, vol. 60, pp. 529–532 (Springer, 2015).
- [251] Q. Wang, J. Geng, T. Luo, and S. Jiang. *Q-switched pulses amplified with short thulium-doped silicate fibers*. In *Proc. SPIE*, vol. 8237 (2012). Paper 82371W.
- [252] R. Collins and H. Fan. *Infrared lattice absorption bands in germanium, silicon, and diamond*. Physical Review **93**(4), 674 (1954).
- [253] D. V. Hahn, M. E. Thomas, D. W. Blodgett, and S. G. Kaplan. *Characterization and modeling of the infrared properties of diamond and SiC*. In *Proc. SPIE*, vol. 5078, pp. 148–158 (2003).
- [254] G. Davies, A. Mainwood, C. Piccirillo, K. Lewis, T. Mollart, M. Nesládek, and Z. Remes. *Why Does Diamond Absorb Infra-Red Radiation?* physica status solidi (a) **193**(3), 442 (2002).
- [255] V. A. Lisinetskii, H. J. Eichler, H. Rhee, X. Wang, and V. A. Orlovich. *The generation of high pulse and average power radiation in eye-safe spectral region by the third stokes generation in barium nitrate Raman laser*. Optics Communications **281**(8), 2227 (2008).
- [256] A. Sabella, D. J. Spence, and R. P. Mildren. *Pump-Probe Measurements of the Raman Gain Coefficient in Crystals Using Multi-Longitudinal-Mode Beams*. Quantum Electronics, IEEE Journal of **51**(12), 1 (2015).
- [257] A. McKay, A. Sabella, and R. P. Mildren. *Polarization conversion in cubic Raman crystals*. Scientific Reports **7** (2017).

-
- [258] A. Sabella, J. A. Piper, and R. P. Mildren. *84% slope efficiency 1240 nm diamond Raman laser*. In *Europhoton* (2010).
- [259] A. Sabella, J. A. Piper, and R. Mildren. *Efficient diamond Raman lasers operating at 1240 nm and 1485 nm*. In *Australian Institute of Physics Congress* (2010).
- [260] A. Sabella, J. Piper, and R. P. Mildren. *Efficient 1064 nm conversion to the eye-safe region using an external cavity diamond Raman laser*. In *Conference on Lasers and Electro-Optics (CLEO) Pacific Rim* (2011). Paper C725.
- [261] R. P. Mildren, A. Sabella, E. Granados, and D. J. Spence. *Diamond Raman Lasers*. In *Conference on Lasers and Electro-Optics (CLEO)* (2010). Paper CTuJ1.
- [262] O. Kitzler, A. Sabella, B. Johnston, A. McKay, and R. Mildren. *Design and characterisation of optical quality single crystal diamond for Raman laser applications*. In *Conference on Lasers and Electro-Optics (CLEO) Pacific Rim* (2011). Paper C1064.
- [263] A. Sabella, J. A. Piper, and R. P. Mildren. *573nm Diamond Raman laser*. In *Rank Prize symposium on diamond photonics* (2010).
- [264] A. Sabella, J. A. Piper, and R. P. Mildren. *Polarisation dynamics in diamond Raman lasers*. In *MMI-Harvard Diamond Photonics Symposium* (2012).